Henry Hirvonen

Probing Properties of Quark-Gluon Plasma Using Machine Learning

UNIVERSITY OF JYVÄSKYLÄ

FACULTY OF MATHEMATICS
AND SCIENCE

Henry Hirvonen

Probing Properties of Quark-Gluon Plasma Using Machine Learning

JYVÄSKYLÄN YLIOPISTO
UNIVERSITY OF JYVÄSKYLÄ

Editors
Ilari Maasilta
Department of Physics, University of Jyväskylä
Ville Korkiakangas
Open Science Centre, University of Jyväskylä

ABSTRACT

Hirvonen, Henry
Probing Properties of Quark-Gluon Plasma Using Machine Learning

This thesis focuses on a phenomenological modeling of ultrarelativistic heavy-ion collisions. The primary objective is to investigate and constrain the properties of the quark-gluon plasma (QGP) by comparing fluid-dynamical simulation results with various flow observables measured at CERN-LHC and BNL-RHIC. To achieve this, the existing EKRT+fluid dynamics heavy-ion collision framework is further developed, and machine learning techniques are utilized to reduce the computational cost of complex simulations. These types of advancements are crucial for the improving understanding of the QGP properties. The introduction of the thesis provides a general description of the employed heavy-ion collision framework and discusses the novel features introduced in this thesis.

The main contributions of this work can be categorized into three development areas: dynamical decoupling, neural networks, and the Monte-Carlo EKRT initial state model. Firstly, incorporating a dynamical decoupling into the fluid-dynamical framework improved the description of peripheral collision systems, resulting in a better agreement with the measured flow coefficients compared to constant temperature decoupling. Secondly, neural networks were trained to predict flow observables directly from the initial state, effectively replacing the computationally expensive hydrodynamic simulations and reducing the required computation time by several orders of magnitude. Finally, a new Monte-Carlo EKRT initial state model was introduced and successfully applied to the studies of rapidity distributions of charged particles and their flow coefficients, as well as midrapidity flow observables.

Keywords: relativistic heavy-ion collisions, quark-gluon plasma, relativistic hydrodynamics, machine learning

TIIVISTELMÄ (ABSTRACT IN FINNISH)

Hirvonen, Henry
Kvarkki-gluoniplasman ominaisuuksien tutkiminen koneoppimisen avulla

Tämä väitöskirja keskittyy ultrarelativististen raskasionitörmäysten mallintamiseen. Ensisijainen tavoite on tutkia ja määrittää kvarkki-gluoniplasman (QGP) ominaisuuksia vertaamalla fluididynaamisten simulaatioden tuloksia useiden CERN-LHC:ssä ja BNL-RHIC:ssä mitattujen virtausobservaabelei-den kanssa. Tämän saavuttamiseksi olemassa olevaa EKRT+fluididynamiikka -raskasionitörmäysmallia on jatkokehitetty ja koneoppimista hyödynnetty monimutkaisten simulaatioiden nopeuttamiseksi. Tälläiset edistysaskeleet ovat erittäin tarpeellisia QGP:n ominaisuuksien ymmärtämisen parantamiseksi. Väitöskirjan johdanto antaa yleiskatsauksen raskasioinitörmäysten kyseisellä mallilla simuloimisesta ja keskustelee tässä väitöskirjassa esitellyistä mallin uusista ominaisuuksista.

Tämän työn päätulokset jakautuvat kolmelle kehitysalueelle: dynaaminen irtikytkeytyminen, neuroverkot ja Monte-Carlo EKRT -alkutilamalli. Ensinnäkin, dynaamisen irtikytkeytymisen lisääminen malliin paransi perifeeristen törmäys-systeemien kuvausta, mikä johti parempaan yhtenäväisyyteen mitattujen virtaus-kertoimien kanssa. Toiseksi, neuroverkkoja koulutettiin ennustamaan virtausob-servaabeleita suoraan alkutilasta, mikä efektiivisesti korvasi laskennallisesti ras-kaat virtausmekaniikkasimulaatiot ja vähensi tarvittavaa laskenta-aikaa useilla kertaluokilla. Viimeiseksi, uusi Monte Carlo EKRT -alkutilamalli esiteltiin ja si-tä sovellettiin menestyksellisesti varattujen hiukkasten rapiditeettijakaumien ja virtauskertoimien sekä myös keskirapiditeetin mittaussuureiden tarkasteluun.

Avainsanat: relativistiset raskasionitörmäykset, kvarkki-gluoniplasma, relativis-
tinen virtausmekaniikka, koneoppiminen

Author   Henry Hirvonen
                    Department of Physics
                    University of Jyväskylä
                    Finland

Supervisors   University Researcher Harri Niemi
                    Department of Physics
                    University of Jyväskylä
                    Finland

                    Professor Kari J. Eskola
                    Department of Physics
                    University of Jyväskylä
                    Finland

Reviewers   Research Director Jean-Yves Ollitrault
                    CNRS, CEA
                    Institut de Physique Théorique
                    Université Paris Saclay
                    France

                    Associate Professor Matthew Luzum
                    Department of Mathematical Physics
                    Institute of Physics
                    University of São Paulo
                    Brazil

Opponent   Distinguished Scientist Bjoern P. Schenke
                    Physics Department
                    Brookhaven National Laboratory
                    NY, USA

PREFACE

The research presented in this thesis has been carried out at the Department of Physics at the University of Jyväskylä during the years 2020-2024. This work is not entirely my doing and could not have been done without the support of many other people.

First and foremost, I want to thank my supervisors Dr. Harri Niemi and Prof. Kari J. Eskola for introducing me to the intriguing field of heavy-ion collisions and guiding me throughout this journey. Our countless meetings over the past years have helped enormously and none of this would have been possible without your help. Moreover, I wish to thank my collaborators Dr. Jussi Auvinen, Dr. Yuuka Kanakubo, and MSc. Mikko Kuha for their immense efforts, especially during the final stretch of this project. I would also like to thank Prof. Matthew Luzum and Dr. Jean-Yves Ollitrault for agreeing to review the thesis manuscript, and Dr. Bjoern P. Schenke for agreeing to be my opponent.

I have enjoyed my time at the physics department throughout my studies, and a big reason for that is the colleagues and friends I have made during these years. I want to especially thank Harri and Jani, with whom I have spent countless memorable hours during the last nine years. Your friendship has been invaluable, and I am grateful for each moment we shared. I am also grateful for the memories made with Tatu, Kasperi, Sami, Jouni, and Joona. It has been a pleasure. I also want to give special thanks to the Holvi people for the enjoyable discussions during the lunch and coffee breaks, and to everyone in the table tennis group for the fun time spent playing.

Finally, I want to thank my family and my partner, Pragya, for all the support you have given me. It has meant a lot to me, and I will miss you all immensely when I move to the US.

Jyväskylä, June 2024

Henry Hirvonen

LIST OF INCLUDED ARTICLES

PI Henry Hirvonen, Kari J. Eskola and Harri Niemi. *Flow correlations from a hydrodynamics model with dynamical freeze-out and initial conditions based on perturbative QCD and saturation.* Physical Review C 106 **no.4** 044913 (2022).

PII Henry Hirvonen, Kari J. Eskola and Harri Niemi. *Deep learning for flow observables in ultrarelativistic heavy-ion collisions.* Physical Review C 108 **no.3** 034905 (2023).

PIII Henry Hirvonen, Kari J. Eskola and Harri Niemi. *Deep learning for flow observables in high energy heavy-ion collisions.* arXiv: 2404.02602 [hep-ph] (2024), to appear in the Proceedings of the 30th International Conference on Ultrarelativistic Nucleus-Nucleus Collisions (Quark Matter 2024) (2024).

PIV Mikko Kuha, Jussi Auvinen, Kari J. Eskola, Henry Hirvonen, Yuuka Kanakubo and Harri Niemi. *MC-EKRT: Monte Carlo event generator with saturated minijet production for initializing 3+1 D fluid dynamics in high energy nuclear collisions.* arXiv: 2406.17592 [hep-ph] (2024), submitted to Physical Review C (2024).

PV Henry Hirvonen, Mikko Kuha, Jussi Auvinen, Kari J. Eskola, Yuuka Kanakubo and Harri Niemi. *Effects of saturation and fluctuating hotspots for flow observables in ultrarelativistic heavy-ion collisions.* arXiv: 2407.01338 [hep-ph] (2024), submitted to Physical Review C (2024).

Author's contribution

In Articles [PI, PII, PIII, PV] the author performed all numerical calculations, implemented the bulk viscosity and the dynamical decoupling conditions into the existing codes, and constructed and trained all the neural networks. For Article [PIV], the author participated in the development of the Monte-Carlo EKRT model. The author wrote the first drafts for Articles [PI, PII, PIII, PV], and participated in the completion of all the articles.

CONTENTS

INCLUDED ARTICLES

1 INTRODUCTION

The elementary particles are the smallest construction blocks of matter. During the past decades, we have managed to gain a deeper understanding of how these particles interact with each other and form matter. All of the visible matter on Earth is primarily constructed from electrons, protons, and neutrons. The electrons have been known to be point-like elementary particles since the early 1900s and for a long time the same was thought to apply to protons and neutrons as well. This turned out not to be the case when in the 1960s smaller electrically charged constituents, named quarks, were discovered [1–3]. Later it was experimentally confirmed that the nucleons also consisted of charge-neutral particles called gluons [4–6]. Gluons play an important role in high-energy nuclear collisions since the nucleon structure is dominantly gluons when probing a nucleon at small nucleon momentum fractions [7].

Nowadays, it is established that quarks and gluons, collectively known as partons, are elementary particles that experience the strong interaction. The fundamental quantum field theory that describes these interactions is Quantum Chromodynamics (QCD). QCD is a gauge theory and an essential component of the standard model of particle physics which has been very successful in explaining numerous phenomena. In QCD, particles carry a color charge, analogous to the electric charge in electrodynamics. However, instead of a single type of charge, there are three types of color charges: green, red, and blue.

Compared to simpler gauge theories, such as Quantum Electrodynamics, QCD has certain unique properties due to the non-Abelian nature of the theory. First, the strong interaction mediators, gluons, carry a color charge and can thus interact with each other. Second, there is confinement of color, which states that under normal conditions the quarks and gluons are confined inside hadrons, color singlet bound states of the strong interaction, and cannot be isolated. The third interesting property of QCD is the asymptotic freedom, which means that the strong interaction strength decreases asymptotically as the energy scale of the interaction increases.

One consequence of the asymptotic freedom is that when creating a dense system at a high enough temperature, the interaction strength is weak enough

for quarks and gluons to exist in an unconfined phase of matter. This phase of the QCD matter is called quark-gluon plasma (QGP). The first-principle lattice simulations of QCD have proven the existence of this new phase, and it has been shown that a cross-over type phase transition from ordinary hadronic matter to QGP happens when the temperature is around 155 MeV [8–11]. This corresponds to temperatures $\sim 10^{12}$ K in SI units.

Since the formation of the hot quark-gluon plasma requires such extreme conditions, it existed in large quantities only in the very early universe[1]. However, the QGP can be created in accelerator laboratories by colliding two heavy nuclei at ultra-relativistic energies. The detectors can only measure properties of final state particles, so the QGP cannot be measured directly, but its existence must be deduced from the measured particles. The first compelling experimental evidence of the formation of QGP in heavy-ion collisions was found at the Relativistic Heavy Ion Collider (RHIC) at Brookhaven National Laboratory by colliding gold nuclei with a nucleon-nucleon center of mass energy of 200 GeV [12–16]. It was found that the measured particle spectrum showed signs of collective behavior and that the measured momentum space anisotropy matched well with the hydrodynamic simulations of heavy-ion collisions with a very small shear viscosity to entropy ratio [17–21], implying that a thermalized medium was indeed formed in the collisions.

The construction of the Large Hadron Collider (LHC) at CERN in Geneva was finished in 2010, and one of its goals is to study the properties of the QGP. The ALICE detector is specially designed with heavy-ion collisions in mind, and it is constructed in such a way that it can accurately identify different particle species, and measure the momentum space anisotropies of the final state particles. The first heavy-ion run was successfully done in late 2010, and the first results from the ALICE, CMS, and ATLAS Collaborations were published shortly after [22–24].

The increased number of high-precision measurements of observables has necessitated more systematic approaches to simultaneously study multiple low-transverse-momentum observables across different collision systems. These so-called global analyses have significantly advanced our understanding of the transport properties of QCD matter [25–27]. More recently, global analyses have incorporated modern statistical methods, such as Bayesian analysis, which offer robust uncertainty estimates and correlations for matter properties [28–37]. However, a significant challenge in these analyses is the enormous computational cost associated with performing millions or even billions of collision simulations. Therefore, the development of faster numerical methods to conduct these simulations is crucial for future progress.

The development of new tools, and refining existing heavy-ion collision simulation frameworks to get a better understanding of the properties of the QGP has been the primary focus of this thesis work. Article [PI] introduced dynamical decoupling conditions offering an alternative hydrodynamic description for the

---

[1] The QCD matter in the cores of neutron stars might also exist in an unconfined phase due to a high net-baryon density, but this is not discussed in this thesis.

evolution of QCD matter that does not rely on a kinetic theory in the hadronic phase. Articles [PII, PIII] addressed the issue of computational cost, presenting a novel approach using neural networks to accelerate heavy-ion collision simulations, thereby reducing the computation time by several orders of magnitude. The Monte Carlo version of the EKRT initial state model, capable of producing three-dimensional initial states, was introduced in Article [PIV]. This model was further utilized in a study of midrapidity observables in Article [PV], where neural networks were employed to perform the simulations efficiently.

This thesis is organized as follows. The general framework of heavy-ion collisions is briefly discussed in Chapter 2 and a short review of hydrodynamics and QCD matter properties is given in Chapter 3. Chapter 4 then goes more into detail by discussing the initial state of heavy-ion collision, while Chapter 5 discusses the decoupling phase of the collision. A brief introduction to the neural networks and their application to heavy-ion collisions is presented in Chapter 6. In Chapter 7, the main results from Article [PV], which demonstrate the importance of the interplay between saturation and nucleon substructure in the initial state, are discussed. The final conclusions and remarks of this thesis are then presented in Chapter 8.

2   HEAVY-ION COLLISIONS

The computational modeling of a collision of two nuclei at ultra-relativistic ener-
gies is complicated, as it consists of many stages, each of them having their own
difficulties and uncertainties. A schematic presentation of a heavy-ion collision
is shown in Fig. 1, where two Lorenz contracted nuclei collide along the z-axis
with an impact parameter **b**. At very early times, $\tau \lesssim 1.0$ fm, the quark-gluon
plasma is created and thermalized. This stage is usually referred to as an initial
or a pre-hydrodynamic stage.

After formation, the thermalized, or nearly thermalized, QGP expands and
cools according to viscous hydrodynamics. Eventually, the temperature of the
system has decreased enough so that partons can no longer exist isolated in the
QGP, and the system hadronizes forming gas of hadrons. The consequent hadron
gas continues to expand and cool. In the context of this thesis, the hadron gas
stage is still modeled using relativistic hydrodynamics, even though switching
to the hadronic kinetic theory approach [38–40] at some fixed temperature has
become a more standard approach during the past decade [41–45]. The advantage
of a purely hydrodynamic description is that it avoids unwanted discontinuities
that easily occur when switching from one description to another.

When the system gets more dilute, the rate of collisions decreases, and in
the end, essentially on a kinetic decoupling surface, the particles stop colliding.
This typically occurs at $\tau \sim 10 - 20$ fm after the formation of QGP. From this
point on, the unstable hadrons decay into more stable particles, until eventually,
at $\tau \sim 10^{15}$ fm, the hadrons finally reach the detector.

2.1   Collision kinematics and flow observables

Before the collision, the two nuclei have a large momentum along the z-axis and
no momentum at all in the transverse direction. Thus, in the final state, the trans-
verse momenta of all the particles should still sum up to zero. However, in prac-
tice, all of the final-state particles cannot be measured due to the practical limita-
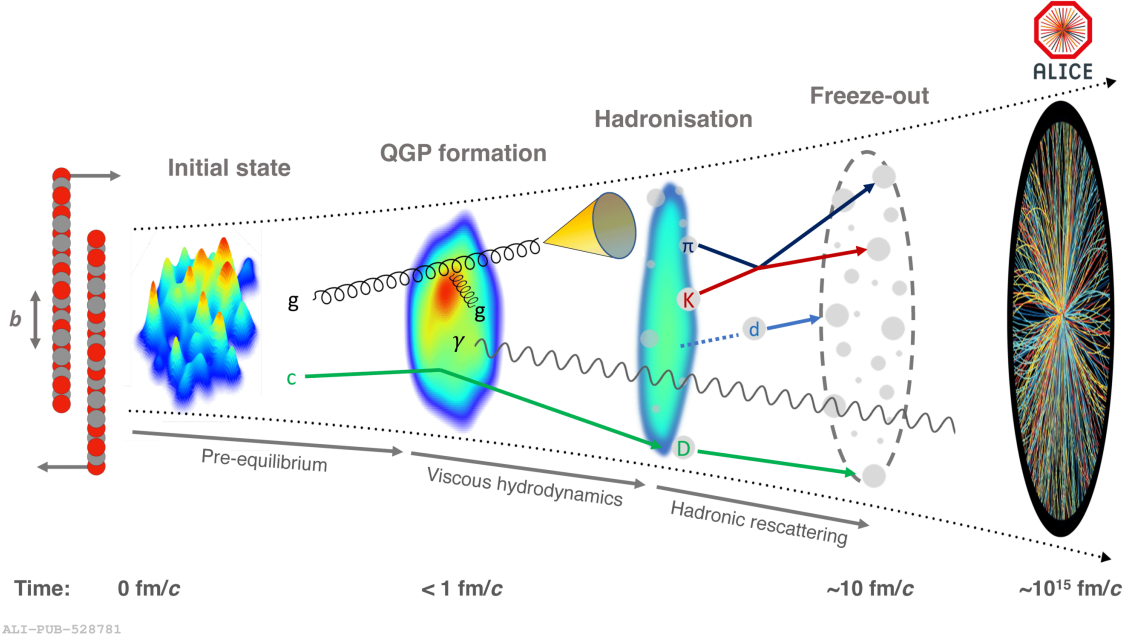
FIGURE 1   A visualization from stages of heavy-ion collisions. Figure from the ALICE
review article [46], reprinted under the license CC BY 4.0.

tions of detectors. The detectors cannot measure particles at very low transverse
momentum p_T or those that travel almost parallel to a beam pipe. For exam-
ple, the TPC detector at the ALICE experiment, which is especially designed for
detecting low-p_T particles, can accurately measure $p_T \gtrsim 0.2$ GeV. The accurate
measurement of the low-p_T particles is crucial for the QGP studies since the aver-
age p_T of charged particles is around 0.7 GeV. The measurements designed with
the heavy-ion collision in mind also measure the direction of the momentum in
the transverse plane, i.e. the azimuthal angle ϕ.

Besides the transverse momentum and azimuthal angle, the detectors also
measure rapidity y which is related to the longitudinal momentum p_z,

$$y = \frac{1}{2} \ln \left(\frac{E + p_z}{E - p_z} \right), \tag{1}$$

where E is the energy of the particle. The rapidity is analogous to longitudinal
velocity $v_z = p_z/E$, but it is more convenient in high-energy collider physics
because differences in rapidities are invariant under longitudinal boosts. Unfor-
tunately, rapidity cannot be measured for unidentified particles, since the masses
of the particles are not known. In this case, one instead measures so-called pseu-
dorapidity,

$$\eta = \frac{1}{2} \ln \left(\frac{|\mathbf{p}| + p_z}{|\mathbf{p}| - p_z} \right), \tag{2}$$

which is independent of the particle mass.

The transverse geometry of a heavy-ion collision varies significantly de-
pending on the impact parameter. Therefore, it would be beneficial to classify
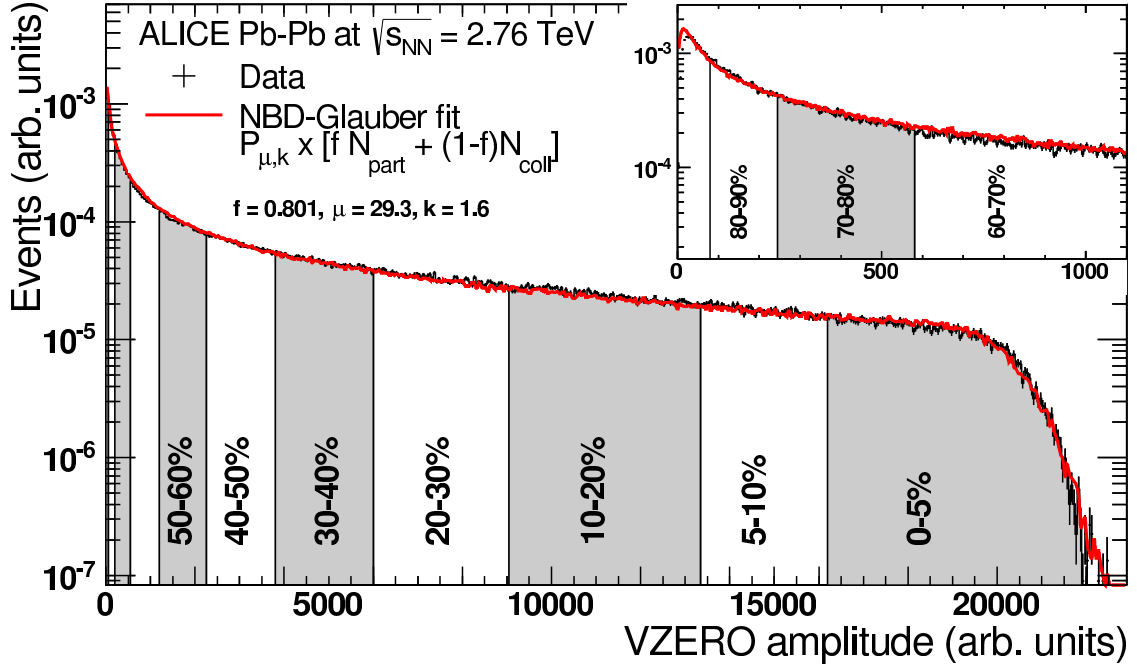
FIGURE 2   The distribution of the V0 amplitude measured by ALICE Collaboration. The red line indicates the Monte Carlo Glauber fit done to the experimental data. Figure from [47], reprinted under the license CC BY 3.0.

the collision events based on their impact parameters. However, the impact parameter cannot be measured. In practice, the events are categorized into centrality classes, which are based on multiplicity or total transverse energy E_T. In the case of the ALICE experiment, the events are categorized in terms of the V0 amplitude, which is proportional to combined charged particle multiplicity at the $-3.7 < \eta < -1.7$ and $2.8 < \eta < 5.1$ pseudorapidity ranges. The centrality classes are constructed by sorting events in decreasing yield and then binned into percentile bins. This is demonstrated in Fig. 2, where the ALICE measurement for the V0 amplitude distribution is shown. The 5% of the events that produce the largest yields are therefore placed into a centrality bin 0-5%, and 20% of the events that produce the smallest yields go into a bin 80-100%. The collisions that belong to the centrality percentiles 0-20% and 60-100% are called central, and peripheral events respectively. The centrality provides a nice probe for a collision geometry, but larger centrality does not always imply a larger impact parameter, due to event-by-event fluctuations of the nucleon positions. This is especially true in small collision systems, such as p+Pb collisions, where there is only a weak correlation between centrality and impact parameters.

In practice, ALICE does not directly determine the centrality classes from the measured events, because the fluctuations in the distribution are quite large and the small amplitude tail of the distribution is sensitive to triggering of the events [1]. Instead, ALICE has performed a Monte-Carlo Glauber fit to the distribution where the multiplicity is estimated from the number of participants and

---

[1]   Triggering hadronic events is challenging due to a large electromagnetic background from ultra-peripheral collisions, where two nuclei interact only by exchange of photons.

binary collisions by a negative binomial distribution [48]. The centrality classes are then determined based on the Glauber fit instead of the actual measured data.

When studying the properties of quark-gluon plasma, the most typically analyzed observables are the particle multiplicities, the average transverse-momenta, and various observables related to anisotropic flow. An anisotropic flow is generated when the initial spatial inhomogeneity gets converted into a momentum space anisotropy through the work done by the pressure gradients. Formally, the magnitude of the anisotropic flow can be described by flow coefficients $v_n(p_T, y)$, which are Fourier components of the single-particle transverse momentum spectrum, i.e.

$$\frac{dN}{dy\,dp_T^2\,d\phi} = \frac{1}{2\pi}\frac{dN}{dy\,dp_T^2}\left(1 + \sum_{n=1}^{\infty} v_n(p_T, y)\cos[n\left(\phi - \Psi_n(p_T, y)\right)]\right), \qquad (3)$$

where $\Psi_n(p_T, y)$ are the event-plane angles. Most of the time it is more convenient to study flow coefficients that are integrated over p_T, since these are less sensitive to the exact form of the viscous corrections used when converting the fluid into the particle spectra. The integrated flow coefficients v_n and event-plane angles Ψ_n can be written in a compact form

$$v_n(y)e^{in\Psi_n(y)} = \langle e^{in\phi}\rangle_{\phi, p_T} \qquad (4)$$

where

$$\langle e^{in\phi}\rangle_{\phi, p_T} = \left(\frac{dN}{dy}\right)^{-1}\int\limits_{0}^{2\pi} d\phi \int\limits_{p_{T,\text{min}}}^{p_{T,\text{max}}} dp_T^2 \frac{dN}{dy\,dp_T^2\,d\phi}e^{in\phi}. \qquad (5)$$

The $p_{T,\text{min}}$ and $p_{T,\text{max}}$ are the integration ranges introduced to match the kinematic cuts of the experimental measurements. Here, the dN/dy must be computed using this same p_T integration range.

Numerical simulations done in the context of this thesis give continuous particle distributions as an output, but the real measurements always measure a finite number of particles. Thus, here the observables are computed as a continuum limit of the discrete observable. For example, the flow coefficients defined in Eq. (4) cannot be easily measured, but the magnitude of flow is measured through a two-particle flow correlation coefficient [49–51]

$$v_n\{2\}^2 = \frac{1}{N_h(N_h - 1)}\sum_{\text{pairs}\,i\neq j}e^{in\phi_1}e^{-in\phi_2}, \qquad (6)$$

where N_h is the number of hadrons in the event. At the continuum limit, this observable can be written as:

$$v_n\{2\}^2 = \frac{1}{N_2}\int d\phi_1 d\phi_2 \frac{dN_2}{d\phi_1 d\phi_2}e^{in\phi_1}e^{-in\phi_2}. \qquad (7)$$

The $dN_2/d\phi_1 d\phi_2$ is the two-particle distribution function, which can be decomposed as

$$\frac{dN_2}{d\phi_1 d\phi_2} = \frac{dN}{d\phi_1}\frac{dN}{d\phi_2} + \delta_2(\phi_1, \phi_2), \qquad (8)$$

where the first term is just a product of single-particle distributions, and $\delta_2(\phi_1, \phi_2)$ describes correlations between particles, that are caused e.g. by particle decays. The $\delta_2(\phi_1, \phi_2)$ part is usually referred to as a non-flow since it vanishes when the correlations between particles come only from the collective flow. The experimental measurements try to suppress such non-flow effects, e.g. by requiring rapidity gaps between hadron pairs in the sum (6). When ignoring non-flow, the two-particle flow coefficient can be written as

$$v_n\{2\}^2 = v_n e^{in\Psi_n} v_n e^{-in\Psi_n} = v_n^2 \tag{9}$$

This expression holds for one event. When considering a large number of events, the $v_n\{2\}^2$ is averaged over events. This gives

$$v_n\{2\} = \sqrt{\langle v_n^2 \rangle_{ev}}, \tag{10}$$

where $\langle \dots \rangle_{ev}$ denotes the average over events.

The same procedure can be used to obtain expressions for higher-order flow correlations as well. It is also interesting to study different correlations between the flow coefficients since these can provide additional constraints for the models, and thereby help extract the QCD matter properties more accurately. The observable quantifying 4-particle correlation between different flow coefficients is called symmetric cumulant, which can be expressed as [52]

$$SC(n, m) = \langle v_n^2 v_m^2 \rangle_{ev,N^4} - \langle v_n^2 \rangle_{ev,N^2} \langle v_m^2 \rangle_{ev,N^2}, \tag{11}$$

where the event average is performed with the indicated power of multiplicity as a weight. The symmetric cumulant has an advantage that the $\delta_2(\phi_1, \phi_2)$ correlations explicitly cancel out. Unfortunately, the symmetric cumulant depends on the magnitude of the flow coefficients, so it is not a genuine correlation. The absolute correlation can be measured through normalized symmetric cumulants,

$$NSC(n, m) = \frac{SC(n, m)}{\langle v_n^2 \rangle_{ev,N^2} \langle v_m^2 \rangle_{ev,N^2}}, \tag{12}$$

but in this case $\delta_2(\phi_1, \phi_2)$ correlations do not cancel out in the denominator.

The symmetric cumulants are four-particle correlations, but even six- and eighth-particle correlations have been measured [53, 54]. The advantage of the multi-particle cumulants is that all the lower order non-flow correlations are canceled, e.g. four-particle non-flow is canceled in the six-particle correlation. One type of such multi-particle correlation is known as the mixed harmonic cumulant. For six-particle correlations, they are defined as [55]

$$MHC(v_n^4, v_m^2) = \langle v_n^4 v_m^2 \rangle_6 - 4\langle v_n^2 v_m^2 \rangle_4 \langle v_n^2 \rangle_2 - \langle v_n^4 \rangle_4 \langle v_m^2 \rangle_2 + 4\langle v_n^2 \rangle_2^2 \langle v_m^2 \rangle_2, \tag{13}$$

$$\begin{aligned} MHC(v_n^2, v_m^2, v_l^2) = &\langle v_n^2 v_m^2 v_l^2 \rangle_6 - \langle v_n^2 v_m^2 \rangle_4 \langle v_l^2 \rangle_2 - \langle v_n^2 v_l^2 \rangle_4 \langle v_m^2 \rangle_2 \\ &- \langle v_m^2 v_l^2 \rangle_4 \langle v_n^2 \rangle_2 + 2\langle v_n^2 \rangle_2 \langle v_m^2 \rangle_2 \langle v_l^2 \rangle_2. \end{aligned} \tag{14}$$

where $\langle\dots\rangle_k = \langle\dots\rangle_{ev,N^k}$. Similarly, the expressions of the mixed harmonic cumulants for the eight-particle correlations are defined as

$$
\begin{aligned}
MHC(v_n^6, v_m^2) =& \langle v_n^6 v_m^2 \rangle_8 - 9\langle v_n^4 v_m^2 \rangle_6 \langle v_n^2 \rangle_2 - \langle v_n^6 \rangle_6 \langle v_m^2 \rangle_2 - 9\langle v_n^4 \rangle_4 \langle v_n^2 v_m^2 \rangle_4 \\
& - 36\langle v_n^2 \rangle_2^3 \langle v_m^2 \rangle_2 + 18\langle v_n^2 \rangle_2 \langle v_m^2 \rangle_2 \langle v_n^4 \rangle_4 + 36\langle v_n^2 \rangle_2^2 \langle v_n^2 v_m^2 \rangle_4,
\end{aligned}
$$

$$
\begin{aligned}
MHC(v_n^4, v_m^4) =& \langle v_n^4 v_m^4 \rangle_8 - 4\langle v_n^4 v_m^2 \rangle_6 \langle v_m^2 \rangle_2 - 4\langle v_n^2 v_m^4 \rangle_6 \langle v_n^2 \rangle_2 - \langle v_n^4 \rangle_4 \langle v_m^4 \rangle_4 \\
& - 8\langle v_n^2 v_m^2 \rangle_4^2 - 24\langle v_n^2 \rangle_2^2 \langle v_m^2 \rangle_2^2 + 4\langle v_n^2 \rangle_2^2 \langle v_m^4 \rangle_4 \\
& + 4\langle v_n^4 \rangle_4 \langle v_m^2 \rangle_2^2 + 32\langle v_n^2 \rangle_2 \langle v_m^2 \rangle_2 \langle v_n^2 v_m^2 \rangle_4.
\end{aligned}
\tag{15}
$$

As in the case of the symmetric cumulants, the absolute correlation is described by the normalized versions of the mixed harmonic cumulants,

$$
\begin{aligned}
nMHC(v_n^k, v_m^l) =& \frac{MHC(v_n^k, v_m^l)}{\langle v_n^k \rangle_k \langle v_m^l \rangle_l}, \\
nMHC(v_n^k, v_m^l, v_p^q) =& \frac{MHC(v_n^k, v_m^l, v_p^q)}{\langle v_n^k \rangle_k \langle v_m^l \rangle_l \langle v_p^q \rangle_q}.
\end{aligned}
\tag{16}
$$

The other way to probe the properties of QGP is through the correlation between the mean p_T and the flow coefficients. In Ref. [56] it was noticed that the correlation between v_2 and mean p_T was very sensitive to the initial state structure and especially to the transverse size of the nuclear overlap area. The flow-transverse-momentum correlation is defined as a modified Pearson correlation coefficient [57, 58],

$$
\rho(v_n^2, [p_T]) = \frac{\langle \hat{\delta} v_n^2 \hat{\delta}[p_T] \rangle_{ev}}{\sqrt{\langle (\hat{\delta} v_n^2)^2 \rangle_{ev} \langle (\hat{\delta}[p_T])^2 \rangle_{ev}}},
\tag{17}
$$

where the event-by-event variance at a fixed multiplicity for an observable O is given by

$$
\hat{\delta} O = \delta O - \frac{\langle \delta O \delta N \rangle_{ev}}{\sigma_N} \delta N, \quad \delta O = O - \langle O \rangle_{ev}, \quad \sigma_O^2 = \langle (\delta O)^2 \rangle_{ev},
\tag{18}
$$

where N is the multiplicity of an event.

2.2 Boost invariance

The particle spectrum observed in the ultra-relativistic heavy-ion collisions has an interesting symmetry. The rapidity distributions of hadrons remain nearly constant around midrapidity when $|y| < 1.0$, while at larger rapidities, the number of particles drops quite rapidly. This finding indicates that the system in the midrapidity region could be approximated as an invariant under Lorentz boosts along the collision axis.

Approximating the collision system as boost invariant was first introduced by J. D. Bjorken in Ref. [59], where he argued that the boost invariance leads to a longitudinal flow velocity $v_z = z/t$, which in the absence of transverse dynamics is many times referred to as Bjorken flow. The approximation of boost invariance is still widely used today when studying observables at the midrapidity since it greatly reduces the complexity of the simulations by making it possible to replace the full 3+1D hydrodynamic simulations with computationally less expensive 2+1D simulations. The most natural coordinate system for a boost-invariant collision system are the Milne coordinates (τ, x, y, η_s), where

$$\tau = \sqrt{t^2 - z^2} \tag{19}$$

is the longitudinal proper time, and

$$\eta_s = \frac{1}{2} \ln \left(\frac{t + z}{t - z} \right) \tag{20}$$

is the spacetime rapidity. The convention $g_{\mu\nu} = \mathrm{diag}(+, -, -, -)$ for the Minkowski metric is used in this thesis. Then, in the Milne coordinates, the metric tensor is given by $g_{\mu\nu} = \mathrm{diag}(1, -1, -1, -\tau^2)$. The spacetime rapidity η_s is connected to the momentum space rapidity y in the sense that if a freely moving particle starts traveling from $t = z = 0$ with rapidity y, it will travel along a $\eta_s = $ constant curve. In the boost invariant approximation, the initial conditions, and the evolution are independent of the η_s component, so the transverse dynamics determine the system behavior. Finally, we note that even though the boost invariance has proven to be a great approximation in symmetric nucleus-nucleus collisions, it starts to fail when the collision is asymmetric, e.g. in the case of proton-lead collisions.

3   HYDRODYNAMICS

Relativistic viscous hydrodynamics has become the standard way of describing the evolution of the quark-gluon plasma in ultrarelativistic heavy-ion collisions. The earliest works that utilize relativistic hydrodynamics in heavy-ion collisions date back to the 20th century when ideal hydrodynamics was used [59, 60]. Viscous hydrodynamics entered the picture early 2000s, and after that viscous hydrodynamics has been successfully used to describe a large number of soft (small-p_T) heavy-ion observables [27, 30–32, 35, 37].

The reason for the usefulness of hydrodynamics is its simplicity compared to a full QCD theory description. Even though in principle the QCD kinetic theory with quantum fluctuations would be a more accurate way to describe the system, developing such a theory is challenging, and most of the state-of-the-art QCD kinetic theories are weakly coupled effective theories [61–65]. Simulating the full space-time evolution of the system even with these effective kinetic theories is still not very practical, since in a typical heavy-ion collision the system consists of several thousands of partons making numerical computations very expensive. Additionally, a realistic description of the cross-over phase transition from QGP to hadronic matter is a challenge for weakly coupled kinetic theories. Fortunately, the quick thermalization of QGP after the initial collision of the nuclei causes the system to be reasonably close to thermal equilibrium for most of its evolution, which allows the hydrodynamic description to be sensible. The advantage of hydrodynamics is that the complicated microscopic dynamics are captured by a few macroscopic variables and properties of the matter that have a very intuitive interpretation. The numerical implementation is also significantly faster than in kinetic theories, and the details of the phase transition are encoded into the equation of state, which can be computed with lattice QCD when the baryon chemical potential is reasonably small.

However, the applicability of hydrodynamics is less clear in small collision systems like p+Pb or when collision energies are smaller, where it is unclear whether there are enough particles to form a matter or whether this matter has enough time to thermalize and become isotropic at any point. The measured signals of collectivity in small systems have been under a lot of discussion in past

years, and the explanations of the signals vary from initial state effects to the collective evolution of possibly formed matter [66–69].

3.1 Viscous hydrodynamics

The theory of viscous hydrodynamics for non-relativistic systems was already invented in the 19th century by Claude-Louis Navier and George Stokes. They developed the Navier-Stokes equations, which have proven to describe the evolution of non-relativistic viscous fluids incredibly well.

The theory for relativistic dissipative fluids has turned out to be challenging and thus far no formalism is as established as the Navier-Stokes equations in the non-relativistic case. The starting point of the covariant formulation of hydrodynamics is the conservation laws of energy-momentum tensor $T^{\mu\nu}$ and particle current N^μ:

$$
\begin{aligned}
\partial_\mu T^{\mu\nu} &= 0, \\
\partial_\mu N^\mu &= 0.
\end{aligned}
\tag{21}
$$

In thermal equilibrium, the energy-momentum tensor and particle currents are defined in terms of energy density e, pressure p, particle density n and four-velocity u^μ, such that in the rest frame of the fluid $T^{\mu\nu} = \mathrm{diag}(e, p, p, p)$ and $N^\mu = (n, 0, 0, 0)$. From these one can obtain the ideal energy-momentum tensor and particle current in a general frame:

$$
\begin{aligned}
T^{\mu\nu}_{\mathrm{eq}} &= e u^\mu u^\nu - p \Delta^{\mu\nu}, \\
N^\mu_{\mathrm{eq}} &= n u^\mu,
\end{aligned}
\tag{22}
$$

where $\Delta^{\mu\nu} = g^{\mu\nu} - u^\mu u^\nu$. To solve the hydrodynamic Eqs. (21) one also needs knowledge about the pressure as a function of energy and particle densities. This is given by the equation of state (EoS), which is determined by the interactions of a given matter in thermal equilibrium. The EoS of the strongly interacting matter is discussed in Sec. 3.2.1.

In an out-of-equilibrium case, the situation gets more complicated, since the thermodynamic quantities, like temperature T or pressure p, are no longer well defined. Thus, one needs to choose an artificial equilibrium state where thermodynamic identities are assumed to function as they do in true equilibrium. Additionally, when the system is out of equilibrium, the velocity can no longer follow both particle and energy currents simultaneously, and one also needs to define the 4-velocity u^μ, i.e. choose the fluid rest frame. The only physical observables are components of the energy-momentum tensor and particle 4-current, which need to be parametrized in terms of macroscopic hydrodynamic variables. In the literature, the way hydrodynamic variables are defined in the non-equilibrium case is referred to as a choice of hydrodynamic frame.

The first formulations of relativistic viscous hydrodynamics were done by Eckart in 1940 [70], followed by Landau and Lifshitz in 1959 [71]. Both of these

theories are relativistic generalizations of the Navier-Stokes theory, where one expands the viscous terms to first order in gradients. These kinds of theories are called first-order theories. The major difference between these two formulations is the different choice of frame. Eckart chose a frame where velocity would follow the particle flow, while in Landau's and Lifshitz's theory, the velocity was set to be parallel with the energy flow, so that

$$
\begin{aligned}
u^\mu &= \frac{T^{\mu\nu}u_\nu}{\sqrt{u_\alpha u_\beta T^\alpha_{\ \sigma} T^{\beta\sigma}}} \quad \text{(Landau frame),} \\
u^\mu &= \frac{N^\mu}{\sqrt{N^\nu N_\nu}} \quad \text{(Eckart frame).}
\end{aligned}
\tag{23}
$$

Due to the intuitive nature of these choices, they are still widely used and are often referred to as the Eckart and Landau frames. To define the artificial equilibrium state, Eckart's and Landau's theories use the so-called Landau matching conditions:

$$
\begin{aligned}
e_{\text{eq}}(T,\mu) &= e = T^{\mu\nu}u_\mu u_\nu, \\
n_{\text{eq}}(T,\mu) &= n = N^\mu u_\mu,
\end{aligned}
\tag{24}
$$

which sets energy and particle densities to follow the same definitions as in the equilibrium, while other thermodynamic quantities can then be obtained from e and n using the EoS. This defines T and μ for a non-equilibrium system. Note that the definition of velocity directly affects what one means by the equilibrium state. A different choice of the hydrodynamic frame will result in different compositions of the energy-momentum tensor and particle current. For example, in the Landau frame, the energy-momentum tensor and the particle current are given by

$$
\begin{aligned}
T^{\mu\nu} &= eu^\mu u^\nu - (p+\Pi)\Delta^{\mu\nu} + \pi^{\mu\nu}, \\
N^\mu &= nu^\mu + n^\mu.
\end{aligned}
\tag{25}
$$

where Π is the bulk viscous pressure, $\pi^{\mu\nu}$ is the shear viscous tensor, and n^μ is the particle diffusion current. In the Landau theory, these dissipative currents are expanded to first order in gradients, i.e.

$$
\begin{aligned}
\Pi &= -\zeta\theta, \\
\pi^{\mu\nu} &= 2\eta\sigma^{\mu\nu}, \\
n^\mu &= \kappa\nabla^\mu\alpha,
\end{aligned}
\tag{26}
$$

where $\theta = \partial_\mu u^\mu$ is the expansion rate, $\sigma^{\mu\nu} = \partial^{\langle\mu}u^{\nu\rangle}$ is the strain-rate tensor, $\alpha = \mu/T$ is the ratio of the chemical potential μ to the temperature T, and

$$
A^{\langle\mu\nu\rangle} = \frac{1}{2}\left[\Delta^\mu_\alpha\Delta^\nu_\beta + \Delta^\mu_\beta\Delta^\nu_\alpha - \frac{2}{3}\Delta^{\mu\nu}\Delta_{\alpha\beta}\right]A^{\alpha\beta}
\tag{27}
$$

denotes the double symmetric, traceless projection orthogonal to the fluid velocity u^μ for any 2nd rank tensor A. The proportionally coefficients ζ, η, and κ are

the first-order transport coefficients called bulk viscosity, shear viscosity, and heat conductivity, respectively.

Unfortunately, the resulting equations of motion violate causality and are unstable under small perturbations. This is a more general problem, and it has been shown that all first-order viscous theories using Landau matching conditions violate causality [72]. Just very recently, it has been shown that it is possible to find a hydrodynamic frame where the first-order theory turns out to be causal and stable [73].

3.1.1 Israel-Stewart theory

In the 1980s, Israel and Stewart published a series of papers, which introduced an alternative formalism that led to a stable and causal equation of motion [74–78]. The idea in the Israel-Stewart (IS) theory was to promote dissipative quantities Π, $\pi^{\mu\nu}$, and n^{μ} to dynamical variables, which have their own equations of motion. In the original derivation, equations of motions for dissipative currents were derived by expanding the entropy 4-current to the second order of gradients in the dissipative quantities, and then using the second law of thermodynamics [74]. This procedure leads to the following relaxation-type equations:

$$\tau_\pi \frac{d}{d\tau}\pi^{\langle\mu\nu\rangle} + \pi^{\mu\nu} = 2\eta\sigma^{\mu\nu} + \text{higher-order terms,}$$

$$\tau_\Pi \frac{d}{d\tau}\Pi + \Pi = -\zeta\theta + \text{higher-order terms,} \qquad (28)$$

$$\tau_n \frac{d}{d\tau}n^{\mu} + n^{\mu} = \kappa\nabla_\mu\alpha^{\mu} + \text{higher-order terms,}$$

where $d/d\tau = u^{\mu}\partial_{\mu}$ is the co-moving derivative, and $\nabla^{\mu} = \Delta^{\mu}_{\nu}\partial^{\nu}$ is the space-like derivative. The relaxation times τ_π, τ_Π, and τ_n describe how quickly the dissipative currents approach corresponding Navier-Stokes values. The relativistic version of the Navier-Stokes theory is recovered by setting all the relaxation times to zero, which corresponds to instantaneous signal propagation not allowed in the theory of relativity.

A few years later, Israel and Stewart derived the same relaxation-type equations from kinetic theory [76–78]. The idea was to expand the single-particle distribution function around equilibrium in the momentum space basis 1, k^{μ_1}, $k^{\mu_1}k^{\mu_2}$, ..., and truncate the series in such a way that the number of coefficients matches the independent macroscopic degrees of freedom in $T^{\mu\nu}$ and N^{μ}, i.e., having a total of 14 coefficients. The equations of motion could then be obtained by plugging this expanded particle distribution into the relativistic Boltzmann equation and integrating over momenta. The advantage of this derivation compared to one made by utilizing thermodynamics is that in this way the transport coefficients can be obtained in terms of the microscopic properties of the matter [1], and

---

[1] The microscopic properties are encoded in the collision term of the Boltzmann equation, which contains information about the particle interactions.

the results of hydrodynamics can be tested against the corresponding kinetic theory [79–82].

The applicability of hydrodynamics is typically quantified in terms of the Knudsen and inverse Reynolds numbers. The Knudsen number is defined as a ratio between microscopic and macroscopic scales. One example of a Knudsen number is

$$\text{Kn} = \tau_\pi \theta, \tag{29}$$

where the relaxation time τ_π can be interpreted as the slowest microscopic time scale appearing in the Boltzmann equation, as discussed in Sec. 3.1.2. The inverse of the expansion rate $1/\theta$ can be seen as a macroscopic time scale, which describes how fast the fluid expands locally. The inverse Reynolds number represents how far the system is from thermal equilibrium. Thus, it is defined as a ratio between the dissipative and equilibrium quantities. In a relativistic context, the inverse Reynolds number related to shear viscosity is usually defined as

$$\text{R}^{-1} = \frac{\sqrt{\pi^{\mu\nu}\pi_{\mu\nu}}}{p}. \tag{30}$$

One would expect that a successful theory of dissipative hydrodynamics could accurately reproduce kinetic theory in the region of small Knudsen and Reynolds numbers. While the IS theory achieves this in many cases, it struggles in some specific scenarios, such as when heat flow plays a significant role, leading to discrepancies with kinetic theory calculations [83]. Consequently, the IS theory has not attained a status comparable to that of the Navier-Stokes theory in the non-relativistic case.

3.1.2 DNMR theory

Many of the more recent formulations of relativistic viscous hydrodynamics have taken significant inspiration from the IS theory. One of these is the Denicol-Niemi-Molnar-Rischke (DNMR) theory [84–87]. The DNMR theory provides a microscopic explanation for the relaxation time as the longest microscopic timescale that will dominate the macroscopic dynamics. Here, I will review the most essential ingredients that go into the DNMR theory. For simplicity, the conserved particle current is neglected in the following discussions since it has no major effect on the dynamics of the highest-energy ultra-relativistic heavy-ion collisions and it has not been implemented in the hydrodynamic code used in related Articles [PI-PV]. Additionally, only classical particles which interact via elastic two-body collisions are considered. The derivation presented here is for a fluid composed of a single particle type. However, the formalism can also be generalized to a multi-component system [88, 89].

Like the Israel-Stewart theory, the DNMR theory is derived from the relativistic Boltzmann equation. However, in the DNMR theory, the reduction of the microscopic degrees of freedom is achieved by assuming that the slowest microscopic timescales dominate the macroscopic dynamics of the system [2] and then

---

[2] This can be argued to be true from the analytic structure of the microscopic theory [90].

26

performing systematic power counting in Knudsen and inverse Reynolds numbers to truncate the equations of motion. The systematic way of performing truncation in Knudsen and inverse Reynolds numbers should in principle guarantee a good agreement with the kinetic theory in the region where $\text{Kn}, \text{R}^{-1} << 1$.

In the DNMR theory, the single-particle distribution is expanded in terms of orthogonal polynomials $P_n(E_k)$ and irreducible tensors $1, k^{\langle \mu_1 \rangle}, k^{\langle \mu_1} k^{\mu_2 \rangle}, \ldots k^{\langle \mu_1} \ldots k^{\mu_n \rangle}$ [3], which form an orthogonal and complete set. Here $A^{\langle \mu_1 \ldots \mu_n \rangle} = \Delta^{\mu_1 \ldots \mu_n}_{\nu_1 \ldots \nu_n} A^{\nu_1 \ldots \nu_n}$, where $\Delta^{\mu_1 \ldots \mu_n}_{\nu_1 \ldots \nu_n}$ are projection operators orthogonal to u^μ for rank n tensors introduced in Ref. [91]. The projection operators are traceless for $n > 1$ and symmetric in exchange of any two indices. Using this basis, the single-particle distribution function f_k can be then expanded around equilibrium as $f_k = f_{0k} + \delta f_k$, where $f_{0k} = \exp((\mu - E_k)/T)$ is the distribution in local equilibrium with $E_k = u^\mu k_\mu$, and

$$\delta f_k = f_{0k} \sum_{l=0}^{\infty} \sum_{n=0}^{N_l} \mathcal{H}^{(l)}_{nk} \rho_n^{\mu_1 \ldots \mu_l} k_{\langle \mu_1} \ldots k_{\mu_l \rangle}. \tag{31}$$

The expansion includes energy-dependent coefficients $\mathcal{H}^{(l)}_{nk}$, which are constructed in terms of orthogonal polynomials in E_k. For more detailed definitions of $\mathcal{H}^{(l)}_{nk}$, see Ref. [85]. Additionally, the expansion introduced irreducible moments of δf_k

$$\rho_r^{\mu_1 \ldots \mu_n} = \int dK E_k^r k^{\langle \mu_1} \ldots k^{\mu_n \rangle} \delta f_k \tag{32}$$

where $dK = g d^3 k / [(2\pi)^3 k^0]$, with g describing the number of internal degrees of freedom. Some of the irreducible moments are directly related to fluid dynamic variables, e.g. $\Pi = -m^2 \rho_0/3$ and $\pi^{\mu\nu} = \rho_0^{\mu\nu}$, and it turns out that all of the ρ_m moments contribute to the bulk viscosity, and $\rho_m^{\mu\nu}$ moments to the shear viscosity. Because the decomposition of the energy-momentum tensor does not include any tensors higher than rank 2, the irreducible moments $\rho^{\mu_1 \mu_2 \mu_3 \ldots}$ are neglected. In Ref. [85], it was more precisely shown that these higher-rank moments have asymptotic behavior of $\mathcal{O}(\text{Kn}^2, \text{KnR}^{-1})$ and that they don't contribute to evolution equations of lower-rank moments at $\mathcal{O}(\text{Kn}^2, \text{R}^{-2})$.

There are infinitely many irreducible moments $\rho_r^{\mu_1 \ldots \mu_n}$ corresponding to an infinite number of microscopic timescales and degrees of freedom. Each irreducible moment follows a relaxation-type equation that can be derived from the Boltzmann equation. The equations with different r are coupled together by the collision term appearing in the Boltzmann equation. To find out the moments that dominate the macroscopic dynamics, it is necessary to decouple the equations. This can be done by diagonalizing the linearized collision term and finding the eigenmodes of the irreducible moments $X_r^{\mu_1 \ldots \mu_l}$ that follow uncoupled equa-

---

3   Note that this differs from the IS theory expansion with $1, k^{\mu_1}, k^{\mu_1} k^{\mu_2}, \ldots$, which is neither an irreducible nor an orthogonal basis.

tions. The uncoupled equations for the scalar and rank-2 tensor are

$$\frac{d}{d\tau}X_r + \chi_r^{(0)}X_r = \beta_r^{(0)}\theta + \text{higher-order terms,}$$

$$\frac{d}{d\tau}X_r^{\mu\nu} + \chi_r^{(2)}X_r^{\mu\nu} = \beta_r^{(2)}\sigma^{\mu\nu} + \text{higher-order terms,}$$

(33)

where $\chi_r^{(l)}$ are the eigenvalues of the collision term and $\beta_r^{(n)}$ are the thermodynamic coefficients that are defined in Ref. [85]. The inverse of eigenvalues $\chi_r^{(l)}$ can be interpreted as the microscopic timescales related to each eigenmode $X_r^{\mu_1\cdots\mu_l}$. Without loss of generality, one can rearrange the eigenmodes $X_r^{\mu_1\cdots\mu_l}$ and corresponding eigenvalues $\chi_r^{(l)}$ in such a way that $\chi_r^{(l)} < \chi_{r+1}^{(l)}$. Therefore, inverse of eigenvalues $\chi_0^{(0)}$, and $\chi_0^{(2)}$ correspond to the longest microscopic timescales related to scalar and rank-2 tensor moments, respectively. In the DNMR theory, it is assumed that only eigenmodes with the longest microscopic timescales, i.e., eigenmodes with $r = 0$, will contribute to the macroscopic dynamics, and all other timescales are significantly smaller. Thus, one can approximate the eigenmodes with $r > 0$ with their asymptotic Navier-Stokes values. With this approximation, the only dynamical equations for the eigenmodes are

$$\frac{d}{d\tau}X_0 + \chi_0^{(0)}X_0 = \beta_0^{(0)}\theta + \text{higher-order terms,}$$

$$\frac{d}{d\tau}X_0^{\mu\nu} + \chi_0^{(2)}X_0^{\mu\nu} = \beta_0^{(2)}\sigma^{\mu\nu} + \text{higher-order terms,}$$

(34)

and the eigenmodes with $r > 0$ are approximated as

$$X_r \simeq \frac{\beta_r^{(0)}}{\chi_r^{(0)}}\theta,$$

$$X_r^{\mu\nu} \simeq \frac{\beta_r^{(2)}}{\chi_r^{(2)}}\sigma^{\mu\nu}.$$

(35)

Now that the slowest microscopic timescale has been identified, it is possible to solve the irreducible moments $\rho_r^{\mu_1\cdots\mu_n}$ from their eigenmodes $X_r^{\mu_1\cdots\mu_l}$ and find out the dynamical equations for the macroscopic dissipative currents. Neglecting all terms higher than second order in Knudsen and inverse Reynolds numbers will lead to equations of motion of the form

$$\tau_\Pi \frac{d}{d\tau}\Pi + \Pi = -\zeta\theta + \mathcal{J} + \mathcal{K} + \mathcal{R},$$

$$\tau_\pi \frac{d}{d\tau}\pi^{\langle\mu\nu\rangle} + \pi^{\mu\nu} = 2\eta\sigma^{\mu\nu} + \mathcal{J}^{\mu\nu} + \mathcal{K}^{\mu\nu} + \mathcal{R}^{\mu\nu},$$

(36)

where $\tau_\Pi = 1/\chi_0^{(0)}$, and $\tau_\pi = 1/\chi_0^{(2)}$. Thus, the relaxation times for the dissipative currents are determined by the longest microscopic timescales. The tensors $\mathcal{J}$, and $\mathcal{J}^{\mu\nu}$ contain all the terms in first-order in Knudsen and inverse Reynolds

numbers. The second-order terms in the Knudsen number are contained in the tensors $\mathcal{K}$, and $\mathcal{K}^{\mu\nu}$, while $\mathcal{R}$, and $\mathcal{R}^{\mu\nu}$ contain all of the second-order terms in the inverse Reynolds number. In practice, the terms $\mathcal{K}$, and $\mathcal{K}^{\mu\nu}$ are neglected because they contain terms that are second order in spatial derivatives which would make the equations of motion parabolic and unstable [92–94]. The physical reason for this is the approximation done in Eq. (35), which sets the eigenmodes with $r > 0$ to relax instantaneously to their Navier-Stokes values and causes acausal behavior. In Ref. [95], it was shown that the equations of motion could be made hyperbolic and stable by treating two of the irreducible moments as additional dynamical variables. However, this kind of method is not implemented in the numerical code used in Articles [PI-PV], but the terms $\mathcal{O}(\text{Kn}^2)$ are simply neglected. Additionally, some of the terms $\mathcal{O}(\text{R}^{-2})$ include transport coefficients, which have not been expressed in a convenient form to implement in the code. Thus, most of the numerical codes only include the following terms:

$$
\begin{aligned}
\mathcal{J} &= -\delta_{\Pi\Pi}\Pi\theta + \lambda_{\Pi\pi}\pi^{\mu\nu}\sigma_{\mu\nu}, \\
\mathcal{J}^{\mu\nu} &= 2\tau_\pi \pi_\alpha^{\langle\mu}\omega^{\nu\rangle\alpha} - \delta_{\pi\pi}\pi^{\mu\nu}\theta - \tau_{\pi\pi}\pi_\alpha^{\langle\mu}\sigma^{\nu\rangle\alpha} + \lambda_{\pi\Pi}\Pi\sigma^{\mu\nu}, \\
\mathcal{R}^{\mu\nu} &= \varphi_7 \pi_\alpha^{\langle\mu}\pi^{\nu\rangle\alpha},
\end{aligned}
\tag{37}
$$

where the constants $\delta_{\Pi\Pi}, \lambda_{\Pi\pi}, \delta_{\pi\pi}, \tau_{\pi\pi}, \lambda_{\pi\Pi}$, and φ_7 are higher-order transport coefficients. A similar form of equations of motion for viscous tensors is also obtained from the IS theory, but there the transport coefficients would differ from the ones obtained from the DNMR theory. In Ref. [95] it was shown that the DNMR theory can describe the kinetic theory calculations in some cases where IS theory struggles. This is due to the systematic power counting in Knudsen and inverse Reynolds numbers done in the DNMR theory.

The higher-order transport coefficients in Eqs. (37), and the relaxation times τ_Π and τ_π can be written in terms of the first-order transport coefficients ζ, and η, when assuming the 14-moment approximation[4] in a massless limit. This was done for shear viscosity in Refs. [85, 87], and for bulk viscosity in Ref. [96]. The relaxation times obtained there read

$$
\tau_\pi = \frac{5\eta}{e+p}, \qquad \tau_\Pi = \left(15\left(\frac{1}{3} - c_s^2\right)^2 (e+p)\right)^{-1}\zeta,
\tag{38}
$$

and the second order-transport coefficients as

$$
\begin{aligned}
&\delta_{\Pi\Pi} = \frac{2}{3}\tau_\Pi, \qquad \lambda_{\Pi\pi} = \frac{8}{5}\left(\frac{1}{3} - c_s^2\right)\tau_\Pi, \qquad \delta_{\pi\pi} = \frac{4}{3}\tau_\pi \\
&\tau_{\pi\pi} = \frac{10}{7}\tau_\pi, \qquad \varphi_7 = \frac{9}{70p}, \qquad\qquad\qquad \lambda_{\pi\Pi} = \frac{6}{5}\tau_\pi,
\end{aligned}
\tag{39}
$$

where c_s is the speed of sound in the fluid. These coefficients are implemented in the numerical code used in Articles [PI-PV]. More recently, in Ref. [97], the

---

[4]   i.e. truncating $\delta f_{\mathbf{k}}$ expansion by setting $N_0 = 2$, $N_1 = 1$ and $N_2 = 0$.

transport coefficients have been calculated in the context of hadron-resonance gas and thermal-mass quasiparticle models. It was demonstrated that the more realistic collision term can lead to drastically different relations between transport coefficients, especially in the case of bulk viscosity. In Ref. [98], it was shown that the measured observables do not impose tight constraints on the ratios $\tau_{\pi\pi}/\tau_\pi$ or $\tau_\pi sT/\eta$, but a more comprehensive study taking into account all second-order transport coefficients would be needed to make firmer conclusions.

3.2 QCD matter properties

3.2.1 Equation of state

The equation of state describes the thermodynamic properties of matter in equilibrium, i.e., the relations between different thermodynamic variables such as temperature, chemical potential, and entropy density. From the perspective of hydrodynamics, the relation $p = p(e, n)$ is necessary to close the equations of motion. The expansion of the system is driven by pressure gradients, for which reason many observables are sensitive to the details in the equation of state. The equation of state also captures the details of phase transitions, which is why utilizing hydrodynamics near the phase transition is easier to implement than a realistic microscopic model.

For QCD matter, the most natural variables to describe the phase space are temperature and net-baryon density. The equation of state has been computed on a lattice at zero net-baryon density, for example, by the Wuppertal-Budapest [8, 9] and HotQCD Collaborations [10, 11]. Lattice computations are done by discretizing the QCD action on a lattice, where nodes correspond to fermion fields and links between nodes correspond to gauge fields. The discretization is performed on an $N_s^3 \times N_t$ grid, where N_s describes the spatial dimensions and N_t the temporal direction. In finite-temperature field theory, the temperature is defined as the upper limit of the temporal integral. On the lattice, this gives the relation $T = 1/(aN_t)$, where a is the lattice spacing. One way to obtain the equation of state from the lattice is the integral method [99–101], in which the trace anomaly $\Theta = e - 3p$ is computed from the expression

$$\Theta(T) = -\frac{T}{V}\frac{d\ln Z}{d\ln a}, \tag{40}$$

where $V = N_s^3 a$, and the partition function Z is written in terms of the field operators. The pressure can then be obtained from the trace anomaly as

$$\frac{p(T)}{T^4} = \frac{p_0}{T_0^4} + \int_{T_0}^{T} dt\frac{\Theta(t)}{t^5}. \tag{41}$$

In this expression, the value of pressure p_0 is needed at some reference temperature T_0. Since lattice computations at low temperatures are computationally very

expensive, the reference values are usually obtained from the hadron resonance gas (HRG). For example, the HotQCD Collaboration matches the equation of state to HRG at $T = 130$ MeV. When $p(T)$ is known, other thermodynamic relations, such as $e(p)$, can be obtained using basic thermodynamics.

Calculating the QCD equation of state at non-vanishing net-baryon density is challenging because, in this case, the QCD action becomes complex, and usual Monte Carlo sampling techniques are no longer usable [102]. Currently, there are two main methods to tackle the lattice equation of state at finite net-baryon density. One way is by expanding the QCD pressure as a Taylor series in the powers of net-baryon chemical potential μ_B around $\mu_B = 0$ [103, 104]. The other way is to calculate the equation of state at the imaginary chemical potential, in which case the QCD action is real, and then perform an analytic continuation to real μ_B [105, 106]. Even though both of these techniques allow probing QCD EoS at finite net-baryon densities, the applicability range of these methods is still quite limited.

Fortunately, in ultra-relativistic heavy-ion collisions, the thermalized matter created has almost zero net-baryon density. Thus, in this case, the net-baryon density can be neglected. In Articles [PI-PV], the s95p parametrization [107] of the lattice QCD results at zero net-baryon density is used. Additionally, the equation of state used includes the chemical freeze-out, which is discussed in more detail in Sec. 5.1.

3.2.2 Transport coefficients

The equation of state describes how the ideal fluid behaves in equilibrium without any dissipation, but in reality there is always some dissipation due to finite mean free path. The magnitude of these dissipative effects is described by the transport coefficients. Transport coefficients can be naively categorized into first-order and higher-order coefficients. The first-order transport coefficients usually dominate the dissipative effects in the applicability region of hydrodynamics, as they are associated with terms proportional to first-order derivatives, while the terms including higher-order transport coefficients are suppressed by higher-order derivatives.

From the perspective of heavy-ion collision simulations discussed in Articles [PI-PV], only the transport coefficients that appear in Eqs. (36, 37) can impact the observables. The first-order transport coefficients that appear are the shear viscosity η and the bulk viscosity ζ. Shear viscosity describes a fluid's ability to translate a shear strain and can be thought of as the fluid's internal friction. It originates from the momentum transfer between particles over distances of a mean free path. A larger region of momentum transfer causes more momentum diffusion in the fluid, corresponding to a high shear viscosity. Consequently, a lower shear viscosity allows the fluid to convert spatial pressure gradients into fluid velocity more efficiently. The magnitude of the shear viscosity depends on the interaction strength of the fluid. As the interaction strength increases, the mean free path decreases, resulting in a lower shear viscosity.

On the other hand, the bulk viscosity quantifies a fluid's resistance to isotropic expansion. From a microscopic perspective, it arises when part of the additional kinetic energy gained by particles in an expanding system is transformed into internal degrees of freedom, such as rotations or vibrations of fluid constituents. As a result, bulk viscosity acts as a negative correction to isotropic pressure, decreasing the average momentum of fluid constituents.

Due to their microscopic origin, both bulk viscosity (ζ) and shear viscosity (η) depend heavily on the density of the system. Therefore, comparing viscosities at different temperatures may not always provide informative results. To address this issue, dimensionless specific shear and bulk viscosities (η/s and ζ/s) are often used to quantify the first-order transport coefficients. The entropy density (s) serves as a proxy for the number density, making specific viscosities indicative of viscosity per constituent. Current understanding suggests that for the quark-gluon plasma phase of QCD matter, the η/s ratio is extremely small. Estimates from the conformal ADS/CFT formalism suggest $\eta/s \geq 1/4\pi \approx 0.08$ in the strong coupling limit [108]. Phenomenological studies of heavy-ion collisions also support low values for η/s, typically estimating its minimum value to be around $0.1 - 0.2$, depending on the study[27, 30–34, 36, 37]. While these studies consider the temperature dependence of the shear viscosity, the majority of analyses conducted do not seem to yield significant constraints on the high-temperature behavior of the specific shear viscosity

At lower temperatures, when QCD matter exists in the hadron gas (HG) phase, the η/s is expected to increase rapidly with decreasing temperature. This is because the interaction strength in the hadron gas is weaker than in the QGP phase. The η/s has been computed for a hadron gas using a transport approach, where it has been shown that in the 100-150 MeV temperature range $\eta/s = \mathcal{O}(1)$ [109–111]. This is very different from the QGP phase where $\eta/s = \mathcal{O}(0.1)$. Since the phase transition at zero net-baryon density is a cross-over type, one would expect the transport coefficients to be continuous functions of temperature. However, in many heavy-ion simulations, this is not the case, and there is a significant discontinuity in η/s at the temperature where hydrodynamics is switched to a hadronic transport. One potential explanation for this discontinuity could be that in the transport approach the actual values of the transport coefficients are significantly influenced by unknown cross-sections of various scattering processes. Moreover, the reliance solely on $2 \rightarrow 2$ scattering processes near the phase transition raises questions about the applicability of the transport approach.

In the ADS/CFT formalism, the bulk viscosity is always zero due to the conformal nature of ADS/CFT. Nevertheless, in the real QCD matter, one would expect a peak in the bulk viscosity near the phase transition temperature, i.e. when $T \approx 200$ MeV. Nowadays, bulk viscosity has been included in almost all state-of-the-art heavy-ion collision simulations, but in its values there seem to be quite large deviations between different analyses and frameworks [30–32, 34, 36, 37]. The maximum values of the ζ/s range from 0.01 to 0.3, while the temperature where this happens ranges from 170 to 300 MeV. This indicates that the optimal

Shear viscosity:	
$(\eta/s)_{min}$	0.11
T_H [MeV]	135
S_H [GeV^{-1}]	0.025
S_Q [GeV^{-1}]	0.3
W_{min} [MeV]	35
P_{HG}	8.0

Bulk viscosity:	
$(\zeta/s)_{max}$	0.09
$(\zeta/s)_{width}$ [MeV]	60
$T_{max}^{\zeta/s}$ [MeV]	240
$a_{\zeta/s}$	-0.5

TABLE 1   Numerical values of viscosity parameters used in Articles [PI, PII, PV].

values for bulk viscosity are sensitive to the model details, such as the initial state, and form of viscous corrections at the particlization. Additionally, the large values of bulk viscosity can easily cause cavitation[5] or break causality, both of which can cause instabilities to the hydrodynamic code, and lead to unphysical results [112, 113].

In Articles [PI, PII, PV], the specific shear viscosity was parametrized as

$$\eta/s(T) = \begin{cases} (\eta/s)_{min} + S_H T \left(\left(\frac{T}{T_H} \right)^{-P_{HG}} - 1 \right), T < T_H \\ (\eta/s)_{min}, \qquad\qquad\qquad T_H \leq T \leq T_Q \\ (\eta/s)_{min} + S_Q(T - T_Q), \qquad T > T_Q, \end{cases} \tag{42}$$

where $T_Q = T_H + W_{min}$. This parametrization contains three different temperature ranges:

1. Hadron gas phase $T < T_H$: power law behaviour with power P_{HG}, and slope parameter S_H. Captures the fast increase of η/s in the HG phase.

2. $T_H < T < T_Q$: η/s is constant at its minimum value.

3. Quark-gluon plasma phase $T > T_Q$: Linear increase in η/s with a slope S_Q.

The bulk viscosity was also included in these articles, and it was parametrized as

$$\zeta/s(T) = \frac{(\zeta/s)_{max}}{1 + \left(\frac{T - T_{max}^{\zeta/s}}{w(T)} \right)^2},$$

$$w(T) = \frac{2(\zeta/s)_{width}}{1 + \exp\left(\frac{a_{\zeta/s}(T - T_{max}^{\zeta/s})}{(\zeta/s)_{width}} \right)}, \tag{43}$$

so that the specific bulk viscosity is peaked at the temperature $T_{max}^{\zeta/s}$, where it reaches its maximum value $(\zeta/s)_{max}$. The width of the peak is asymmetric in temperature, and the amount of asymmetry is characterized by parameter $a_{\zeta/s}$. If $a_{\zeta/s}$ is positive (negative) the peak is wider at the lower (higher) temperatures, and if $a_{\zeta/s} = 0$ the width of the peak is determined by the parameter $(\zeta/s)_{width}$.

---

[5]   The cavitation happens when $p + \Pi < 0$, and negative-pressure bubbles are formed in the fluid.
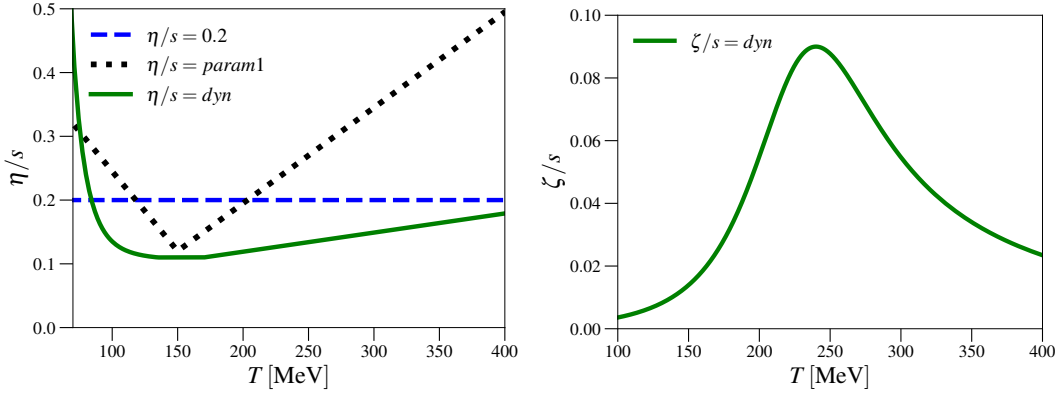
FIGURE 3   The shear and bulk viscosities as a function of temperature for $\eta/s = dyn$ parametrization, compared against two parametrizations from Ref. [27]. Figure from Article [PI], reprinted under the license CC BY 4.0.

The values of parameters used in Articles [PI, PII, PV] are shown in Table 1, and the corresponding temperature dependence of η/s, and ζ/s is illustrated in Fig. 3. At high temperatures $T > T_Q$, the temperature dependence of η/s is similar to other studies, although some include non-linear curvature at high temperatures [27, 30–32, 34, 36, 37]. At the lower temperatures, all of the other studies use hadronic transport models, which means that η/s, and ζ/s are determined by the details of the transport model. Utilizing hydrodynamics also in the hadronic phase allows continuous parametrization of the transport coefficients across the whole evolution, which is not necessarily the case when switching from hydrodynamics to hadronic transport. The continuity of the transport coefficients is one of the advantages of the approach adopted in Articles [PI-PIII, PV]. The temperature dependence of the specific bulk viscosity used is quite similar to the one obtained from the Bayesian analysis in Ref. [37], while some other studies seem to prefer bulk viscosity that reaches its maximum value at lower temperatures [30–32, 34].

4   INITIAL STATE

The initial state of a heavy-ion collision is a result of what happens during the very early moments after the two nuclei collide, and it is necessary for initializing the hydrodynamics. Modeling the initial state involves significant uncertainties. Generally, there are two main approaches to tackle these uncertainties. The first is to use a very flexible and general parametric description of the initial state and constrain the parameters from the data. An example of this kind of initial state is the TRENTO model [114], which has been widely used in determining the properties of QCD matter. The advantage of this approach is that it allows the measured data to dictate the structure of the initial state without a lot of restrictions. In a sense, this is a good feature, because it directs the focus on the most important aspect, which is determining the QCD matter properties. On the other hand, this kind of parametric approach has very little predictive power, and it is difficult to interpret the underlying physics. It is not even clear whether the parametric initial state extracted from the data can be realized according to QCD dynamics. Additionally, it might lead to less constrained matter properties, since a flexible initial state parametrization can compensate for changes in the matter properties.

Another approach is a QCD-inspired one. In this method, the initial state is modeled by some effective theory, which tries to capture the essential features of the complicated collision process. In this case, the model can have predictive power as long as the model assumptions hold, and a successful model can give some insights into underlying physics. Such successful initial state models are for example Impact parameter dependent saturation model [115, 116], EKRT (Eskola- Kajantie-Ruuskanen-Tuominen) model [117–119], EPOS (Energy conservation + Parallel scattering + factOrization + Saturation) model [120, 121], AMPT (A Multi-Phase Transport) model [122, 123], and Dynamical Core-Corona Initialization model [124, 125]. In this thesis, the EKRT initial state model is used. In Articles [PI-PIII], the initial state is determined at midrapidity by the EKRT model which includes Event-by-Event (EbyE) fluctuations [27]. Article [PIV] introduces a completely new Monte-Carlo version of the EKRT model (MC-EKRT), which can be used to generate full 3D initial state profiles. The behavior of the MC-

EKRT initial states at midrapidity was further studied in Article [PV] by looking at the effect of Monte-Carlo fluctuations and saturation on the flow observables.

4.1 Nuclear thickness function and nucleon substructure in EKRT

The nuclear thickness function describes the transverse density of nuclear matter in a nucleus, and it is a crucial input to many initial state models. In the context of the EKRT model, the overlap of the thickness functions of two nuclei affects the saturation strength. In an event-by-event simulation, the nuclear thickness function with fluctuating nucleon positions is defined as

$$T_A(\mathbf{s}) = \sum_{i=1}^{A} T_N(\mathbf{s} - \mathbf{s_i}),$$ (44)

where A is the number of nucleons in the nucleus, $\mathbf{s}$ is the coordinate vector in the transverse (x, y) plane, T_N is the nucleon thickness function, and $\mathbf{s_i}$ is the position vector of nucleon i. The positions of the nucleons are sampled from the Wood-Saxon density

$$\rho(r, \theta) \propto \frac{1}{1 + \exp((r - R(\theta))/d)},$$ (45)

where r is the radial coordinate, θ is the polar angle, d is the thickness parameter, and $R(\theta) = R_0(1 + \beta_2 Y_{20}(\theta) + \beta_3 Y_{30}(\theta) + \beta_4 Y_{40}(\theta))$, with nuclear radius R_0 and deformation parameters β_i. The functions Y_{ij} are the standard spherical harmonics. For spherically symmetric Pb and Au nuclei, the deformation parameters are zero, while for Xe nucleus $\beta_2 = 0.162$, $\beta_3 = 0$, and $\beta_4 = -0.003$ [126]. In Articles [PIV, PV], also a minimum distance of $d_{\min} = 0.4$ fm was required between the sampled nucleons inside the nucleus.

At the high collision energies, the dominant contribution to initial particle production comes from gluons, so T_N can also be interpreted as a gluonic thickness function of the nucleon. The estimation of T_N can be obtained from exclusive J/ψ photo-production in $\gamma + p \rightarrow J/\psi + p$, for which the differential cross section $d\sigma/dt \propto |F(t)|^2$ with a 2-gluon form factor $F(t)$ [127]. Since the Fourier transform of $F(t)$ with $|\mathbf{q}|^2 = t$ can be thought of as the gluonic density of the nucleon, T_N can be obtained from the $F(t)$ by taking a 3-dimensional Fourier transformation, and then integrating over longitudinal coordinate z. The 2-gluon form factor is often parameterized as $F(t) \propto \exp(-b|t|/2)$ with an energy-dependent slope parameter b. The gluonic thickness function corresponding to this parametrization is

$$T_N(\mathbf{s}) = \frac{1}{2\pi\sigma^2} e^{-\frac{|\mathbf{s}|^2}{2\sigma^2}}$$ (46)

where $\sigma = \sqrt{b}$ is the width parameter. The slope parameter b can be directly extracted from the measured differential cross section $d\sigma/dt$. The ZEUS Collabo-

ration has measured $b = 4.72\,\mathrm{GeV}^{-2}$, with the center of mass energy of photon-proton system W varying in the range of $30 < W < 220\,\mathrm{GeV}$ [128]. This corresponds to $\sigma \approx 0.43\,\mathrm{fm}$, which is the value used in Article [PI]. However, the value of b depends on W and it is often parameterized as

$$b = b_0 + 4\alpha' \ln\left(\frac{W}{90\,\mathrm{GeV}}\right). \tag{47}$$

There is no clear consensus on what values for the fit parameters b_0, and α' should be used when extrapolating to high energies. For example, in Ref. [129], the parameters $b_0 = 4.9\,\mathrm{GeV}^{-2}$, and $\alpha' = 0.06\,\mathrm{GeV}^{-2}$ are used, which are also the values used in Article [PIV]. In contrast, the H1 Collaboration has extracted values $b_0 = 4.630^{+0.043}_{-0.163}\,\mathrm{GeV}^{-2}$, and $\alpha' = 0.164^{+0.028}_{-0.030}\,\mathrm{GeV}^{-2}$ from the measurements with highest energy being $W \approx 250\,\mathrm{GeV}$ [130]. These are the b_0, and α' values used in Article [PV].

The discussion thus far has focused on the average shape of the nucleon. However, nucleons can have their own fluctuating substructure. In Ref. [131] it was demonstrated that the nucleon substructure is necessary for correctly describing the incoherent photo-production of J/ψ. The substructure can be incorporated into the nucleon thickness function as a sum of Gaussians, i.e.

$$T_N(\mathbf{s}) = \frac{1}{N_h} \sum_{i=0}^{N_h} \frac{1}{2\pi\sigma_h^2} e^{-\frac{\left|\mathbf{s}-\mathbf{s}_i^h\right|^2}{2\sigma_h^2}}, \tag{48}$$

where N_h is the number of gluonic hotspots, σ_h is the width of the hotspot, and $\mathbf{s}_i^h$ is the location of the hotspot sampled from a 2-dimensional Gaussian distribution with a width σ_s. To maintain the same average geometry as without the substructure, the total width of the nucleon needs to be σ. This means that the widths σ_h, and σ_s are not independent. The average shape of the nucleon can be obtained from σ_h, and σ_s by taking a convolution between the distribution from which the hotspots are sampled and the Gaussian thickness function of the hotspot. This results in another Gaussian with a width $\sigma = \sqrt{\sigma_h^2 + \sigma_s^2}$, giving the relation between the three widths.

Besides the structure of the nuclei, the collision geometry is determined by the impact parameter $\mathbf{b}$, which is sampled from a probability distribution $P(b) \propto b$. This means that there are a lot of events with large impact parameters. To make sure that the simulated events correspond to the ones seen in the experiments, a triggering condition is needed.

4.2 Triggering

When studying hadronic events in heavy-ion collisions, there is a huge background from large impact parameter events that happen only through electromagnetic interactions. The goal of the triggering is to filter out these events and

obtain the same inelastic nucleus-nucleus cross section as in the measurements. The triggering is especially important for peripheral collisions, where the particle multiplicity decreases rapidly, and minor changes in the triggering can have a visible impact on the observables. In the simulations, the triggering is done based on a geometrical criterion. Without any nucleon substructure, the nuclear collision event is accepted if the minimum distance between colliding nucleon-nucleon pairs $D_{\mathrm{min}}^{(NN)}$ is less than the corresponding effective distance given by the inelastic nucleon-nucleon cross-section σ_{NN}, i.e.

$$D_{\mathrm{min}}^{(NN)} < \sqrt{\frac{\sigma_{\mathrm{NN}}}{\pi}}, \tag{49}$$

The nucleon-nucleon cross sections σ_{NN} can be obtained from the measurements of $p + p$ collision with various collision energies, and various fits parameterize the energy dependence of σ_{NN}. In Article [PIV, PV], σ_{NN} is obtained as the difference between the total cross section fit from COMPETE [132] and the elastic cross section fit from TOTEM [133]. On the other hand, Articles [PI-PIII] use values $\sigma_{\mathrm{NN}} = 42$ mb at $\sqrt{s_{\mathrm{NN}}} = 200$ GeV, $\sigma_{\mathrm{NN}} = 64$ mb at $\sqrt{s_{\mathrm{NN}}} = 2.76$ TeV, $\sigma_{\mathrm{NN}} = 70$ mb at $\sqrt{s_{\mathrm{NN}}} = 5.023$ TeV, and $\sigma_{\mathrm{NN}} = 72$ mb at $\sqrt{s_{\mathrm{NN}}} = 5.44$ TeV collision energies. All these choices lead to $A + A$ inelastic cross sections that agree with the measurements [134, 135].

The triggering condition (49) treats nucleons as hard spheres with a scattering cross section σ_{NN}. This is a good approximation when the density of nucleus is distributed isotropically in azimuthal angle. However, with the nucleon substructure, the positions of hotspots fluctuate. Thus, using the triggering condition (49) may lead to situations where a collision is accepted even if any two colliding hotspots are relatively far apart, resulting in no hadronic interaction. The triggering can also be done at the substructure level with the condition

$$D_{\mathrm{min}}^{(HS)} < \sqrt{\frac{\sigma_{\mathrm{HS}}}{\pi}}, \tag{50}$$

where $D_{\mathrm{min}}^{(HS)}$ is the minimum distance between two colliding hotspots, and σ_{HS} is the effective hotspot-hotspot cross section tuned to reproduce the same nucleus-nucleus cross section as the triggering condition (49). As discussed in Article [PV], the tuning of σ_{HS} needs to be done separately for each hotspot sampling width σ_s and for all different collision systems.

4.3 Event-by-Event EKRT

The EKRT model is an initial state model based on perturbative QCD and collinear factorization combined with gluon saturation [117–119]. The collinear factorization has been very successful in predicting hard (high-p_T) observables. However, when moving towards smaller transverse momenta, it predicts that the production of gluons will increase rapidly and even unlimitedly. This growth

cannot continue forever, since at some point the density of gluons increases so much that the non-linear QCD effects start to play a role. This effect is called gluon saturation, and it is most prominent in the ultrarelativistic collisions of two nuclei, where all the nucleons interact simultaneously. At high collision energies, the nucleus consists mostly of gluons, so that the collision can be thought to be more like a collision between two gluon clouds rather than a collision of individual nucleons.

Unfortunately, the gluon saturation in this context is a non-perturbative effect and cannot be fully explained by collinear factorization alone. In the EKRT model, saturation arises when the production processes of low-p_T quarks and gluons, often referred to as minijets, start overlapping each other in the transverse coordinate plane. Many overlapping $2 \to 2$ processes would then lead to a situation where $3 \to 2$ or higher-order processes would become a more favorable production method, and thus the number of produced minijets saturates.

The EbyE variant of the EKRT model [27], is based on a perturbative production of the minijet transverse energy E_T into a midrapidity window Δy. For the $A + A$ collision of two nuclei with mass number A this can be expressed as

$$\frac{dE_T}{d^2\mathbf{r}dy}(p_0, \sqrt{s_{NN}}, A, \mathbf{r}, \mathbf{b}, \beta) = T_A(\mathbf{r} - \mathbf{b}/2)T_A(\mathbf{r} + \mathbf{b}/2)\sigma\langle E_T\rangle_{p_0,\Delta y,\beta}, \tag{51}$$

where $p_0 \gg \Lambda_{\text{QCD}}$ is a low transverse momentum cutoff scale where perturbative QCD (pQCD) is still applicable. The term $\sigma\langle E_T\rangle_{p_0,\Delta y,\beta}$ is the first E_T moment of the minijet E_T distribution (E_T being the scalar sum of the minijet p_T's), which can be computed perturbatively [118, 136, 137]. At next-to-leading order, there is some freedom in the definition of E_T with a p_T cutoff, which is quantified by the parameter β.

The perturbatively produced minijet E_T can be computed from Eq. (51), but this does not take into account saturation effects. In the EbyE EKRT model, the saturation is conjectured to take place when the transverse energy produced from $2 \to 2$ processes becomes similar to one obtained from $3 \to 2$ processes, i.e.

$$\frac{dE_T}{d^2\mathbf{r}dy}(2 \to 2) \sim \frac{dE_T}{d^2\mathbf{r}dy}(3 \to 2). \tag{52}$$

On the other hand the E_T production for $n \to 2$ processes, with $n = 2, 3$ scales as:

$$\frac{dE_T}{d^2\mathbf{r}dy}(n \to 2) \sim (T_A g)^n p_0^{4-2n}\left(\frac{\alpha_s^n}{p_0^2}\right)p_0, \tag{53}$$

where α_s is the QCD coupling constant, and g is the gluon parton distribution function. Here, the factor $T_A g$ is assigned for each incoming gluon, the factor p_0^{4-2n} is to compensate extra fm^2 dimensions of T_A, and factors α_s^n/p_0^2 and p_0 take account the partonic cross section, and E_T cutoff scale respectively. This scaling law combined with the saturation condition (52) leads to a scaling

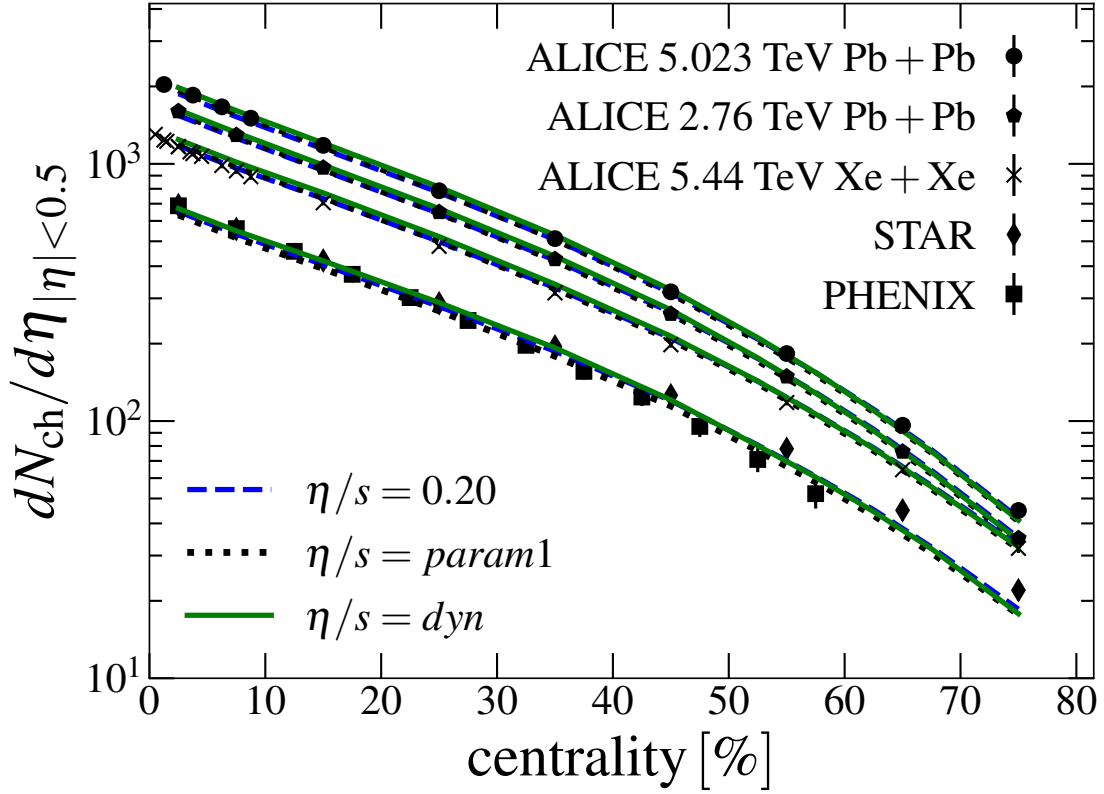$$T_A g \sim \frac{p_0^2}{\alpha_s}. \tag{54}$$

FIGURE 4 Charged hadron multiplicity as a function of centrality for 200 GeV Au+Au, 2.76 TeV Pb+Pb, 5.023 TeV Pb+Pb, and 5.44 TeV Xe+Xe collision systems. The experimental data are from the STAR [138], PHENIX [139] and ALICE [140–142] Collaborations. Figure from Article [PI], reprinted under the license CC BY 4.0.

The local saturation criterion for the minijet E_T production to the midrapidity window Δy is then obtained by feeding the scaling law (54) back to Eq. (53)

$$\frac{dE_T}{d^2\mathbf{r}}(p_0, \sqrt{s_{NN}}, A, \mathbf{r}, \mathbf{b}, \beta) = \frac{K_{\text{sat}}}{\pi} p_0^3 \Delta y, \qquad (55)$$

where the value of the proportionally constant $K_{\text{sat}} \sim 1$ needs to be determined from the measured data. The solution of Eq. (55) is the saturation scale $p_0 = p_{\text{sat}}$ [27, 119]. In principle, the saturation scale is a function of $\sqrt{s_{NN}}, A, \mathbf{r}, \mathbf{b}, \beta, K_{\text{sat}}$, and Δy. However, in practice, the nuclear geometry is contained in the nuclear overlap density $T_A T_A$, so that $p_{\text{sat}} = p_{\text{sat}}(T_A T_A(\mathbf{r}, \mathbf{b}), \sqrt{s_{NN}}, A, \Delta y, K_{\text{sat}}, \beta)$.

The 2+1D hydrodynamics requires the energy density e, the transverse velocity $\mathbf{v_T}$, and the shear stress tensor $\pi^{\mu\nu}$ as initial conditions at some constant time τ_0. In the EbyE EKRT model, the energy density at the formation time $\tau_s(\mathbf{r}) = 1/p_{\text{sat}}(\mathbf{r})$ is given by

$$e(\mathbf{r}, \tau_s(\mathbf{r})) = \frac{dE_T(p_{\text{sat}})}{d^2\mathbf{r}} \frac{1}{\tau_s(\mathbf{r})\Delta y} = \frac{K_{\text{sat}}}{\pi}[p_{\text{sat}}(\mathbf{r})]^4, \qquad (56)$$

while the transverse velocity and shear stress tensor are assumed to be zero. Since the formation time depends on the transverse coordinates, the energy density in

η/s	0.20	$param1$	dyn
K_{sat}	0.63	0.50	0.67

TABLE 2   The values of K_{sat} parameter for different η/s parametrizations.

Eq. (56) needs to be evolved to a constant initialization time τ_0. This is done using Bjorken flow, i.e.

$$e(\mathbf{r}, \tau_0) = e(\mathbf{r}, \tau_s(\mathbf{r})) \left(\frac{\tau_s(\mathbf{r})}{\tau_0} \right)^{4/3}. \tag{57}$$

In Article [PI], The initialization time was chosen as $\tau_0 = 1/p_{\text{sat,min}} \approx 0.2$ fm, with $p_{\text{sat,min}} = 1$ GeV. Below the scale $p_{\text{sat,min}}$, the perturbative QCD computation can no longer be trusted. In that region, the Bjorken evolved energy density is smoothly connected to $e \propto T_A T_A$ binary profile.

The strength of the EbyE EKRT model is its predictive power. The parameters K_{sat}, and β are (assumed to remain) constant and do not depend on the collision energy so that K_{sat}, and β determined based on the measurements from one collision system can be used to predict results for other systems. This can be seen in Fig. 4, where the charged particle multiplicity is plotted as a function of centrality for 200 GeV Au+Au, 2.76 TeV Pb+Pb, 5.023 TeV Pb+Pb and 5.44 TeV Xe+Xe collision systems. The viscosities corresponding to different parametrizations are shown in Fig. 3, and values of K_{sat}, fitted based on the charged particle multiplicity in the most central 2.76 TeV Pb+Pb collisions, are shown in Table. 2. The value $\beta = 0.8$ is used in all cases. All of the parametrizations use the nucleon width parameter $\sigma = 0.43$ fm and no nucleon substructure was introduced. The $\eta/s = dyn$ parametrization is obtained in the context of a dynamical decoupling introduced in Sec. 5.3, while the other two are obtained with a constant temperature decoupling $T_{dec} = 100$ MeV.

The charged particle multiplicity is sensitive to the initial entropy of the system and to the entropy production caused by dissipation. Therefore, different viscosity parametrizations require different values for K_{sat} to obtain the same multiplicity. Even so, all the parametrizations agree well with the measured data for all collision systems, highlighting the predictive power of the EbyE EKRT model.

4.4   Monte-Carlo EKRT

The EbyE version of the EKRT model has provided good results for the midrapidity observables, but it cannot be used to predict rapidity-dependent observables. Additionally, the EbyE EKRT does not include local fluctuations of the saturation scale that originate from local fluctuations of the minijet multiplicity, or explicit energy conservation. These weaknesses are addressed in the Monte-Carlo EKRT model introduced in Article [PIV].

4.4.1 Multiple dijet sampling

To generate an $A + B$ collision between two nuclei, the first step in the MC-EKRT model is to sample the nuclear configurations and the impact parameter, and perform event triggering, as discussed in Secs. 4.1, and 4.2. After triggering, multiple dijet production is computed from all possible nucleon pairs ab ($a \in A$, $b \in B$). The dijets from each ab pair are supposed to be produced independently, which is why Poissonian statistics is used. Thus, the probability of producing $n \geq 0$ dijets from the ab pair is given by

$$P_n(p_0, \sqrt{s_{NN}}, \{\bar{s}_a\}, \{\bar{s}_b\}) \equiv \frac{\left(\bar{N}_{\text{jets}}^{ab}\right)^n}{n!} e^{-\bar{N}_{\text{jets}}^{ab}}, \tag{58}$$

where $\bar{s}_a$, and $\bar{s}_b$ are the locations of nucleons a, and b respectively. The average number of produced dijets from the ab pair is obtained as

$$\bar{N}_{\text{jets}}^{ab}(p_0, \sqrt{s_{NN}}, \{\bar{s}_a\}, \{\bar{s}_b\}) = T_{NN}(\bar{b}_{ab}) \, \sigma_{\text{jet}}^{ab}(p_0, \sqrt{s_{NN}}, \{\bar{s}_a\}, \{\bar{s}_b\}) \tag{59}$$

where $\bar{b}_{ab} = \bar{s}_b - \bar{s}_a$, and σ_{jet}^{ab} is the integrated inclusive pQCD cross section producing dijet pair with $p_T \geq p_0$. The quantity T_{NN} is the nucleon-nucleon overlap function, calculated as

$$T_{NN}(\bar{b}_{ab}) = \int d^2\bar{s} \, T_N(\bar{s}) T_N(\bar{s} - \bar{b}_{ab}), \tag{60}$$

where T_N's are the gluonic thickness functions of the nucleons.

When the number of produced dijets is decided, the transverse momentum p_T, and the rapidities y_1 and y_2 of each final state parton in a dijet are sampled from the differential minijet cross section

$$\frac{d\sigma_{\text{jet}}(\{\bar{s}_a\}, \{\bar{s}_b\})}{dp_T^2 dy_1 dy_2} = K \sum_{i,j,k,l} x_1 f_i^{a/A}(\{\bar{s}_a\}, x_1, Q^2) x_2 f_j^{b/B}(\{\bar{s}_b\}, x_2, Q^2) \frac{d\hat{\sigma}^{ij \to kl}}{d\hat{t}}(\hat{s}, \hat{t}, \hat{u}),$$
$$\tag{61}$$

where $\frac{d\hat{\sigma}^{ij \to kl}}{d\hat{t}}$ are the differential leading-order pQCD cross sections, which depend on parton-level Mandelstam variables $\hat{s}, \hat{t}$, and $\hat{u}$. The missing higher-order pQCD contributions are taken into account by the K-factor, which is fitted from the measurements for each collision energy separately. The distribution of partons with a flavor i inside the nucleon a bound to nucleus A is described by the spatially dependent nuclear parton distribution function (snPDF) $f_i^{a/A}(\{\bar{s}_a\}, x, Q^2)$. The snPDFs depend on the position of the nucleon a, as well as the whole nucleon configuration in each event, longitudinal momentum fraction x of the parton, and factorization scale Q^2, which is set equal to p_T^2. In the MC-EKRT model, the snPDFs are implemented as

$$f_i^{a/A}(\{\bar{s}_a\}, Q^2) = f_i^p(x, Q^2) r_i^{a/A}(\{\bar{s}_a\}, Q^2), \tag{62}$$

where $f_i^p(x, Q^2)$ is the free-proton PDF, and $r_i^{a/A}$ are the spatially dependent, nucleon-configuration-dependent, nuclear modifications. As explained in Article

[PIV], $r_i^{a/A}$ are normalized so that the standard nuclear PDF modifications $R_i^{p/A}$ (here EPS09LO [143]) are obtained when taking an average over the nucleons in each nucleon configuration and an average over many nucleon configurations. That is

$$R_i^{p/A}(x, Q^2) = \left\langle \frac{1}{A} \sum_a r_i^{a/A}(\{\bar{s}_a\}, x, Q^2) \right\rangle_{\{A\}}, \tag{63}$$

where $\langle \cdots \rangle_{\{A\}}$ denotes the average over nucleon configurations. The advantage of th snPDFs constructed this way is that, unlike previous snPDFs, they can handle large nucleon density regions relevant for the event-by-event simulations. A more detailed description of the implementation of the snPDFs in MC-EKRT is found in Article [PIV].

After y_1, y_2, and p_T have been sampled from Eq. (61), the same distribution is reused to sample the parton process types, which fixes the flavors of the partons. Additionally, each participating quark is identified as a sea quark or valence quark. The azimuthal angle ϕ of the minijet pair is sampled from a uniform distribution.

Besides the momenta and the flavors, the hydrodynamics needs information about the spatial locations $\mathbf{x}_\perp$ of the formed dijets. These are obtained by sampling the nucleon-nucleon overlap function (60) for each parton produced from nucleons a and b. The space-time rapidity coordinate η_s of a parton is obtained by assuming that formed partons move along $\eta_s = y$ curves.

4.4.2 Saturation and conservation laws

The minijet sampling procedure described above does not account for the conservation of energy, momentum, or baryon number, nor does it consider saturation. Consequently, not all the sampled dijets are physical ones. Thus, the dijets sampled based on pQCD cross sections are referred to as candidates. In principle, saturation and conservation laws could be taken into account by including all multiparton processes to the differential cross-section in Eq. (61), and using multiparton distributions that would be constructed so that they would conserve energy. Obviously, this is not achievable so one needs to make some simplifying approximations. In MC-EKRT, saturation, and conservation laws are implemented as filters that are applied to the candidate dijet list. The collinear factorization has proven to work well at high p_T, and to maintain this the candidate dijets are ordered in decreasing p_T when applying filters. This way the highest p_T dijets are practically always kept after the filters, while the low-p_T dijets are removed.

Saturation is implemented as a geometrical criterion, which is motivated by the saturation criterion introduced in Ref. [117], and derivable from Eq. (55) above, replacing on the l.h.s. the E_T with the number of dijets and reducing one power of p_0 from the r.h.s. and integrating over the transverse coordinate and rapidity. Then each minijet production process occupies a transverse area $\propto 1/p_T^2$, and the candidate dijet with the transverse location $\bar{s}^{\text{cand}}$ and transverse momen-

tum p_T^{cand} is rejected if

$$\left| \bar{s} - \bar{s}^{\text{cand}} \right| < \frac{1}{\kappa_{\text{sat}}} \left(\frac{1}{p_T} + \frac{1}{p_T^{\text{cand}}} \right) \tag{64}$$

holds for any previously accepted dijet with $p_T \leq p_T^{\text{cand}}$ and $\bar{s}$. The parameter κ_{sat} is a fitting parameter that determines the proximity at which dijets can be formed from each other. Because saturation should be the main mechanism that regulates the low-p_T dijets, it is applied before the conservation laws.

The MC-EKRT can take into account the momentum and valence-quark number conservation laws. The momentum conservation is implemented for each nucleon separately, again considering the dijet candidates in a p_T ordered manner. That is, given a candidate dijet with longitudinal momentum fractions x_1^{cand} in a projectile $a \in A$, and x_2^{cand} in a target $b \in B$, the energy conservation is broken and the candidate dijet is rejected if

$$x_1^{\text{cand}} + \sum_{i=1}^{n} x_1^{(i)} > 1 \qquad \text{or} \qquad x_2^{\text{cand}} + \sum_{j=1}^{m} x_2^{(j)} > 1, \tag{65}$$

where $x_1^{(i)}$ $(x_2^{(j)})$ are the longitudinal momentum fractions of the accepted dijets associated with nucleon a (b). The valence-quark number conservation is implemented by keeping track of the number of available valence quarks in nucleons a and b. A candidate dijet is rejected if it involves a valence quark of a specific flavor from either parton a or parton b, and if either nucleon has already consumed all its valence quarks of that flavor in the previous parton scatterings.

4.4.3 Free streaming and parton smearing

At this stage, the excess minijets have been filtered away, and the remaining ones can be used to initialize hydrodynamics. For each parton i, the momentum rapidity y_i, the transverse momentum $\mathbf{p}_{T,i}$, and the transverse coordinate $\mathbf{x}_{\perp,0i}$ are known. However, the partons need to be propagated to a constant proper time τ_0 to initialize the hydrodynamics. This is done by letting partons propagate as free particles, and assuming that all the partons are produced at the longitudinal location $z_i = 0$ at time $t = 0$. This sets the spacetime and momentum rapidities equivalent, i.e. $\eta_{s,i} = y_i$. The position of a parton i at proper time τ_0 is then given by $(\tau_0, \mathbf{x}_{\perp,i}(\tau_0), \eta_{s,i})$ where $\mathbf{x}_{\perp,i}(\tau_0) = \mathbf{x}_{\perp,0i} + \tau_0 \mathbf{p}_{T,i} / p_{T,i}$.

After the free streaming, the space-time rapidity $\eta_{s,i}$, transverse momentum $\mathbf{p}_{T,i}$, and the transverse coordinate $\mathbf{x}_{\perp,i}$ of all partons i are known at the proper time τ_0. From these, it is possible to construct a distribution function for point-like partons in the Milne coordinates [144]

$$f(\tau, \vec{x}, \vec{p}) = \sum_i \delta^{(3)}(\mathbf{x} - \mathbf{x}_i)\delta^{(3)}(\mathbf{p} - \mathbf{p}_i)/|\det g|, \tag{66}$$

where $\mathbf{p}_i = (\mathbf{p}_{T,i}, p_i^\eta)$ is the three-momentum, $\mathbf{x}_i = (\mathbf{x}_{\perp,i}, \eta_{s,i})$ is the spatial location, and $\det g = -\tau^2$ is the determinant of the metric tensor in the Milne

coordinates. The energy-momentum tensor in the Milne coordinates reads

$$T^{\alpha\beta}(\tau, \mathbf{x}_\perp, \eta_s) = \int \frac{d^3\vec{p}}{p^\tau} \tau p^\alpha p^\beta f(\tau, \mathbf{x}, \vec{p}), \tag{67}$$

where $d^3\vec{p} = d^2\mathbf{p}_T dp^\eta$, and $p^\alpha = (p^\tau, \mathbf{p}_T, p^\eta)$ is the four-momentum, which can be expressed as

$$p_i^\alpha = \frac{\partial x^\alpha}{\partial x'^\mu} p'^\mu = \begin{pmatrix} p_T \cosh(y - \eta_s) \\ \mathbf{p}_T \\ \tau^{-1} p_T \sinh(y - \eta_s) \end{pmatrix}, \tag{68}$$

where x'^μ and p'^μ are the Cartesian space-time point, and four-momentum respectively. By substituting distribution (66) to the energy-momentum tensor (67), and writing the η_s integral in terms of y, it is possible to write

$$T^{\alpha\beta} = \sum_i \int d^2\mathbf{p}_T dy \frac{p^\alpha p^\beta}{p^\tau} \frac{1}{\tau} \cosh(y - \eta_s) \tag{69}$$

$$\times \delta^{(2)}(\mathbf{x}_\perp - \mathbf{x}_{\perp,i})\delta(\eta_s - \eta_{s,i})\delta^{(2)}(\mathbf{p}_T - \mathbf{p}_{T,i})\delta(y - \eta_s),$$

where $p_i^\eta = 0$ was assumed so that $\eta_{s,i} = y_i$.

The point-like nature of particles in the distribution function leads to infinite energy and momentum densities. Therefore, additional smearing is needed to smooth the density profiles. Alternatively, the smearing can be thought of as a way to account the parton shower evolution from τ_f to τ_0 which smears the particle distribution. The smearing is implemented by replacing delta functions with Gaussians in coordinate space. That is, $\delta^{(2)}(\mathbf{x}_\perp - \mathbf{x}_{\perp,i})\delta(\eta_s - \eta_{s,i}) \rightarrow g_\perp(\mathbf{x}_\perp; \mathbf{x}_{\perp,i})g_\parallel(\eta_s; \eta_{s,i})$, where the Gaussian functions are defined as

$$g_\perp(\mathbf{x}_\perp; \mathbf{x}_{\perp,i}) = \frac{C_\perp}{2\pi\sigma_\perp^2} \exp\left[-\frac{(\mathbf{x}_\perp - \mathbf{x}_{\perp,i})^2}{2\sigma_\perp^2}\right], \tag{70}$$

$$g_\parallel(\eta_s; \eta_{s,i}) = \frac{C_\parallel}{\sqrt{2\pi\sigma_\parallel^2}} \exp\left[-\frac{(\eta_s - \eta_{s,i})^2}{2\sigma_\parallel^2}\right], \tag{71}$$

where $\sigma_\perp$ and $\sigma_\parallel$ are the Gaussian widths in transverse, and longitudinal directions respectively. The Gaussians are normalized as

$$\int d^2\mathbf{x}_T d\eta_s g_\perp(\mathbf{x}_\perp; \mathbf{x}_{\perp,i})g_\parallel(\eta_s; \eta_{s,i}) = 1. \tag{72}$$

To reduce the computational cost, the smearing is done only in the $\pm 3\sigma$ range from the center of Gaussian to each direction. This together with a finite grid size causes some discretization errors in the normalization of Gaussians. Thus, the normalization constants $C_\perp$, and $C_\parallel$ are added to guarantee correct normalization. In practice, these constants are very close to unity.

With assumptions made here, the $T^{\tau\tau}$ component of the energy-momentum tensor is given as

$$T^{\tau\tau}(\tau, \mathbf{x}_\perp, \eta_s) = \frac{1}{\tau} \sum_i p_{T,i} g_\perp(\mathbf{x}_\perp; \mathbf{x}_{\perp,i}) g_\parallel(\eta_s; \eta_{s,i}). \qquad (73)$$

In Articles [PIV, PV], only the initialization of energy density is considered, ignoring the initial shear-stress tensor, bulk pressure, and transverse velocity. Thus, the initialization is determined by $e(\tau_0) = T^{\tau\tau}(\tau_0)$. This way of initializing hydrodynamics breaks the energy conservation only by around 1% with $\sigma_\parallel = 0.15$.

In Article [PV], the 2+1D hydrodynamics is used together with MC-EKRT. There, it is not necessary to perform smearing in the η direction, but instead, one can replace the smearing with the Heaviside theta function and set $\eta_s = y$, so that all the partons with $|y_i| < \Delta y/2$ are counted to the initial state in the midrapidity window Δy. With this approach one obtains

$$T^{\tau\tau}(\tau, \mathbf{x}_\perp) = \frac{1}{\tau\Delta y} \sum_i p_{T,i} g_\perp(\mathbf{x}_\perp; \mathbf{x}_{\perp,i}) \theta(\Delta y/2 - |y_i|), \qquad (74)$$

where the $g_\perp$ is normalized as

$$\int d^2\mathbf{x}_T g_\perp(\mathbf{x}_\perp; \mathbf{x}_{\perp,i}) = 1. \qquad (75)$$

4.4.4 Rapidity-dependent charged particle multiplicity

The MC-EKRT model provides full 3-dimensional initial conditions and can be used to study rapidity-dependent observables. Since 3+1 D hydrodynamic simulations are computationally very expensive and parameter tuning consequently overly slow, a large set of MC-EKRT initial conditions are averaged over in Article [PIV]. The events are first divided into centrality classes based on the total transverse energy of the minijets that survived all the filters. Within each centrality class, the energy density profiles of events are converted into entropy densities. These are then averaged and converted back to energy density profiles. Averaging is performed based on the entropy density because total entropy is a good proxy for the multiplicity of the event. Therefore, the final multiplicity obtained from the entropy-averaged initial conditions should be a good estimate of the event-averaged, event-by-event multiplicities.

Examples of the obtained charged particle multiplicities as a function of rapidity are presented in Fig. 5 for 5.023 TeV Pb+Pb, 2.76 TeV Pb+Pb, and 200 GeV Au+Au collisions. All results shown here are obtained with the MC-EKRT initial states with saturation, energy conservation, and valence quark conservation enabled. Different viscosity parametrizations and initial state parameter combinations are shown to probe uncertainties in the initial conditions. The $\eta/s = param1$ is the temperature-dependent viscosity shown in Fig. 3, while the other two parametrizations correspond to temperature-independent shear viscosities. In all cases $\sigma_\parallel = 0.15$. The 3+1 D hydrodynamic simulations performed
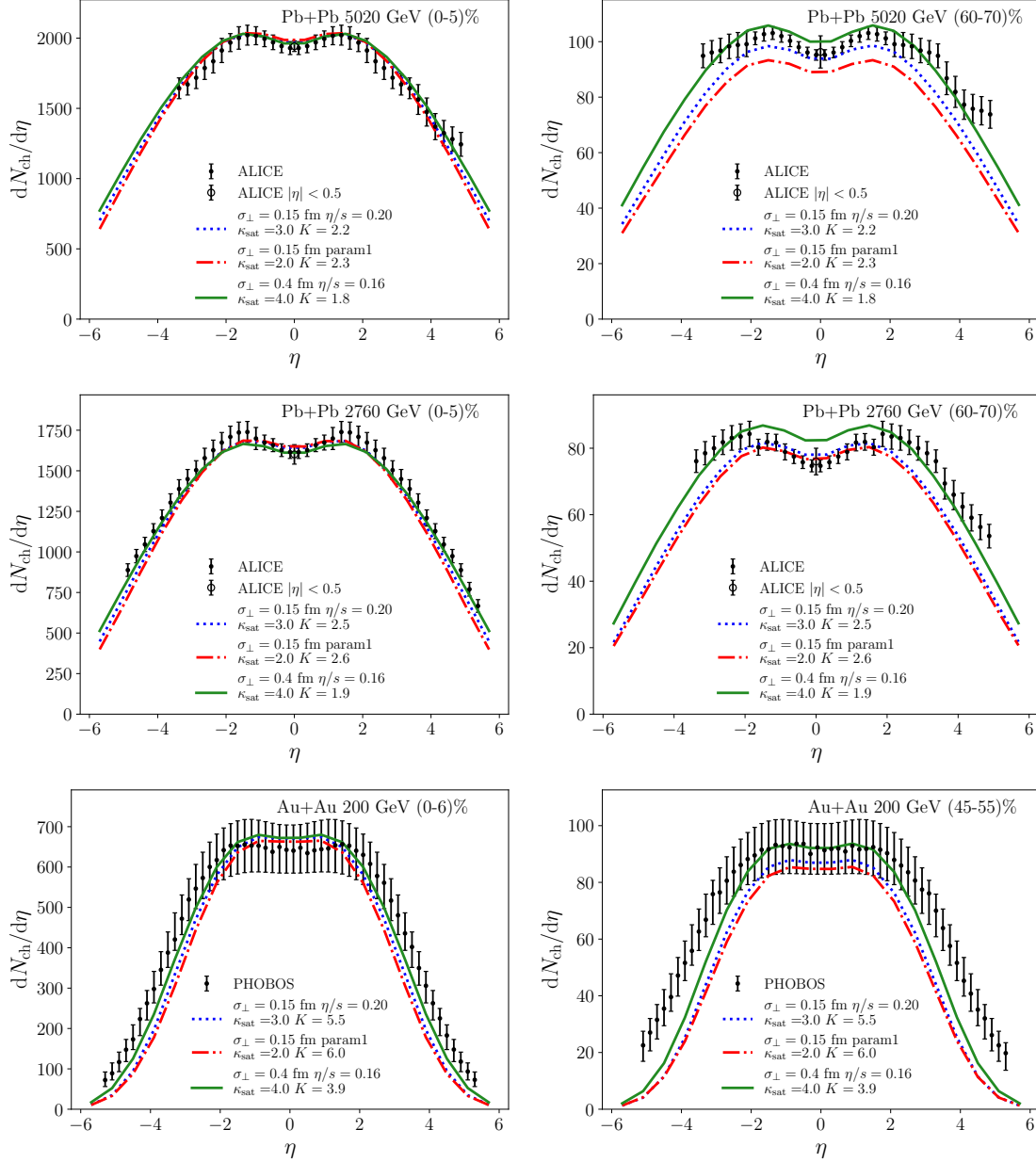
FIGURE 5   The rapidity dependence of charged particle multiplicity for 5.023 TeV Pb+Pb (top panel), 2.76 TeV Pb+Pb (middle panel), and 200 GeV Au+Au (bottom panel) collisions as obtained from the MC-EKRT model. The experimental data are from PHOBOS [145], and ALICE [140, 141, 146, 147] Collaborations. Figure from Article [PIV].

to obtain these results had chemical decoupling at the temperature $T_{\text{chem}} = 150$ MeV and the kinetic decoupling at the temperature $T_{\text{kin}} = 120$ MeV. The best overall agreement with the data is obtained with constant $\eta/s = 0.16$ and with $\sigma_\perp = 0.4$ fm. In this case, the measured rapidity distribution is reasonably well reproduced, except for peripheral RHIC collisions, where the rapidity distribution is systematically slightly narrower than the measured one. This discrepancy could be due to the lower collision energy where also approximation $\eta_s = y$ is more likely to break down. It is noteworthy that the same saturation mechanism, which previously produced a good agreement with the measured midrapidity data, also appears to work in 3+1D simulations. This emphasizes that the non-linear saturation effect is the dominant mechanism suppressing pQCD minijet production.

5 DECOUPLING

When a fluid expands and cools down, the density of matter decreases. At the same time, the rate of scatterings decreases, eventually leading to a state where there are no scatterings between fluid constituents, and the fluid decouples. The decoupling stages in heavy-ion collisions can be divided into chemical and kinetic phases.

5.1 Chemical decoupling

Chemical decoupling describes a point where all of the inelastic processes stop, and the system is no longer in a chemical equilibrium (CE). Thus, after chemical decoupling, particle species cannot be converted into each other. Without resonances, the number of hadrons would be conserved separately for each hadron species after chemical decoupling. When resonances are included, only the effective particle number $\bar{N}_i$ is conserved. The effective particle number is defined as

$$\bar{N}_i = N_i + \sum_j n_j^{(i)} N_j, \tag{76}$$

where N_i is the actual number of particles of species i, N_j is the number of resonances j, and $n_j^{(i)}$ is the number of particles i formed in the decay of the resonance j according to the branching ratios. The inclusion of resonances means that even though all the effective particle number-changing processes have ceased, the number of resonances and their constituent particles can still be in chemical equilibrium relative to each other. For example, processes like $\pi + \pi \leftrightarrow \rho$ can still take place. This approach, which includes resonances, is called partial chemical equilibrium (PCE) [148]. Additionally, there is still a small amount of entropy production in the hadron gas phase due to viscous effects, so the number of hadrons can still slightly increase after chemical decoupling, while the ratios between the effective particle numbers remain constant.

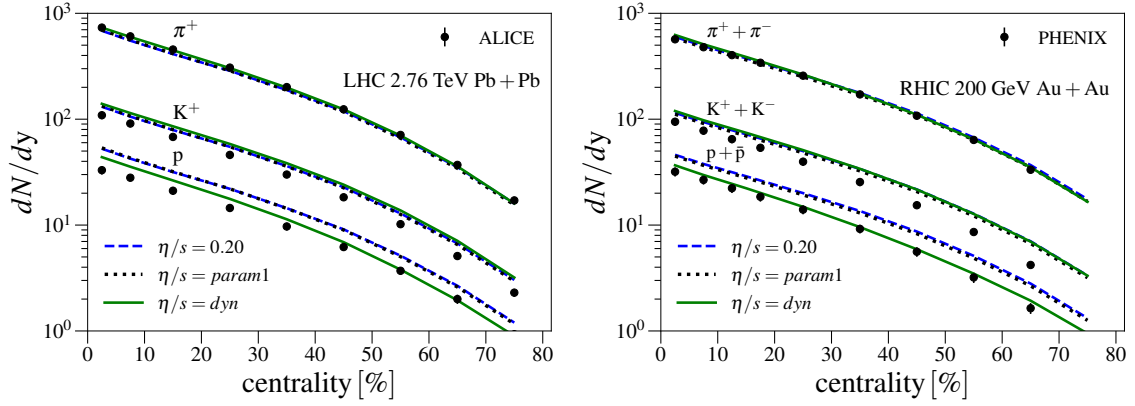Chemical decoupling can be implemented directly into the hadronic part

FIGURE 6   Identified particle multiplicities for pions, kaons and protons in 2.76 TeV Pb+Pb, and 200 GeV Au+Au collisions. The experimental data are from the ALICE [151] and PHENIX [152] Collaborations. Figure from Article [PI], reprinted under the license CC BY 4.0.

of the equation of state by introducing effective chemical potentials [148–150]. While chemical decoupling has only a slight effect on pressure as a function of energy density, the temperature decreases significantly faster as a function of energy density than in chemical equilibrium. In heavy-ion collision simulations, this means that a chemically decoupled system cools down faster than a system in chemical equilibrium. This leads to less radial flow for a given temperature, which, combined with the constant effective particle number, decreases the mean transverse momentum of the hadrons.

When using a hydrodynamic description in the hadron gas phase of QCD matter, chemical decoupling is usually assumed to take place at some constant temperature T_{chem}. In the simulations done in Articles [PI, PV], the chemical decoupling temperature was $T_{chem} = 155$ MeV, while in Article [PIV] $T_{chem} = 150$ MeV was used. The most direct consequence of chemical decoupling can be seen in the multiplicity ratios of the produced hadron species. This is illustrated in Figure 6, where the multiplicities of pion kaons, and protons are shown as a function of centrality for Pb+Pb collisions at $\sqrt{s} = 2.76$ TeV. The curve denoted with $\eta/s = dyn$ corresponds to a simulation where $T_{chem} = 155$ MeV is used, while in the other two cases $T_{chem} = 175$ MeV. In all cases, the multiplicities of the pions are quite close to each other, while the proton multiplicity clearly increases with increasing T_{chem}. The cause of this behavior is that at higher temperatures yields of the more massive particles are enhanced according to the thermal spectra.

The chemical decoupling affects the EoS and therefore the entropy density in chemical equilibrium $s_{CE}(T)$ differs from the chemically decoupled entropy density $s_{PCE}(T)$. This has to be accounted for when comparing chemically decoupled η/s or ζ/s with the corresponding specific viscosity in chemical equilibrium. This is demonstrated in figure 7, where η/s and ζ/s from Fig. 3 are compared against the same viscosities scaled with the ratio of chemically decoupled and equilibrium entropy densities. At least in the case of the simplified hadron gas, the η is not very sensitive to the chemical decomposition of the hadron gas [153].
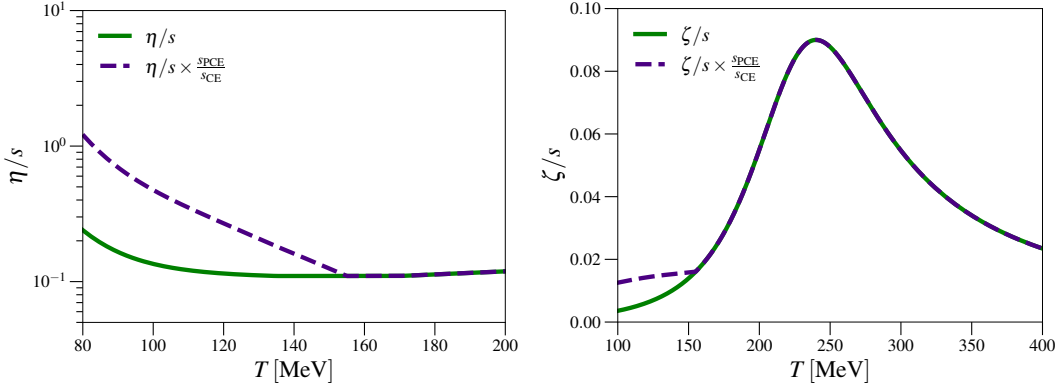
FIGURE 7   The specific shear and bulk viscosities, scaled with the ratio of chemically
decoupled and equilibrium entropy densities, as a function of temperature.

That is $(\eta/s)_{\text{CE}} \approx (\eta/s)_{\text{PCE}} \times s_{\text{PCE}}/s_{\text{CE}}$. When $T < T_{\text{chem}} = 155$ MeV, the scaled versions of η/s, and ζ/s are significantly larger than the corresponding PCE versions. At the temperatures $T \approx 100$ MeV, the scaling makes the η/s more comparable to the values obtained from the SMASH hadron transport model with the 10 mb elastic cross-sections [111].

5.2   Kinetic decoupling

The kinetic decoupling occurs when all elastic scatterings cease. After this, stable hadrons continue propagating toward the detectors without further interactions, while unstable particles decay into their daughter particles. At this stage, the system is no longer near thermal equilibrium, and fluid dynamics can no longer describe the system. Thus, the fluid needs to be converted into particles. This process can be seen as a transition from macroscopic fluid dynamic degrees of freedom to microscopic degrees of freedom. In the context of this thesis, fluid conversion into the particle spectrum is performed on the kinetic decoupling hypersurface Σ, which is found using the Cornelius algorithm [154]

Kinetic decoupling is done using the Cooper-Frye formula [155], which provides a Lorentz-invariant particle spectrum

$$E\frac{d^3 N_i}{d^3 k} = \int_{\Sigma} d^3\sigma_\mu k^\mu f_i(x,k), \tag{77}$$

where $d^3\sigma_\mu$ is a directed surface element of the hypersurface Σ, and $k^\mu = (E, \mathbf{k})$ is the four-momentum. The distribution function $f_i(x,k)$ should be chosen to reproduce the energy-momentum tensor on the decoupling surface. If the fluid was in thermal equilibrium this would be straightforward. One could simply use the equilibrium distribution

$$f_{0i}(x,k) = \left[\exp\left(\frac{k_i^\mu u_\mu - \mu_i}{T}\right) \pm 1 \right]^{-1}, \tag{78}$$

where $+(-)$ sign should be used for fermions (bosons). However, the QGP is not necessarily in thermal equilibrium on the decoupling surface. This causes an ambiguity in the choice of $f_i(x,k)$ because hydrodynamics does not contain information about all of the microscopic degrees of freedom. Since the system is expected to be reasonably close to thermal equilibrium, a standard way is to write the distribution function as a sum of the equilibrium part and the viscous correction, i.e. $f_i = f_{0i} + \delta f_i$. Various forms for the viscous corrections have been used in the past [156–159], and there is no clear consensus on the optimal form. In Articles [PI-PV] the viscous corrections are of the form [160, 161]

$$\delta f_i = -f_{0i}\tilde{f}_{0i}\frac{C_{bulk}}{T}\left[\frac{m_i^2}{3E_k} - \left(\frac{1}{3} - c_s^2\right)E_k\right]\Pi + \frac{f_{0i}\tilde{f}_{0i}}{2T^2(e+p)}\pi^{\mu\nu}k_\mu k_\nu, \qquad (79)$$

where m_i is the mass of hadron i, $E_k = \sqrt{\mathbf{k}^2 - m^2}$ is the energy, $\tilde{f}_{0i} = 1 \pm f_{0i}$, with $-(+)$ for fermions (bosons) and the fluid dynamic variables are defined in Chapter 3. The coefficient C_{bulk} is obtained by requiring that the kinetic theory definition of Π is consistent with the form of δf_i correction. Therefore,

$$\frac{1}{C_{bulk}} = \sum_i \frac{g_i m_i^2}{3T} \int \frac{d^3\mathbf{k}}{(2\pi)^3 k^0} f_{0i}\tilde{f}_{0i}\left[\frac{m_i^2}{3E_k} - \left(\frac{1}{3} - c_s^2\right)E_k\right], \qquad (80)$$

where sum goes over all included hadrons, and g_i is the degeneracy factor of a hadron i.

In Article [PI], the integral in Eq. (77) is computed numerically, leading to continuous spectra for all known hadrons with $m < 2$ GeV. The decoupling surface is determined by the dynamical decoupling conditions discussed in Sec 5.3. The two- and three-particle decays are accounted for by folding the continuous particle spectrum of an unstable particle with the single-particle decay distribution and integrating over the allowed phase space according to Ref. [162]. The decay products are assumed to be isotropically distributed in the rest frame of the particles.

On the other hand, in Article [PIV], the kinetic decoupling surface was determined as a constant temperature hypersurface with $T_{\text{kin}} = 120$ MeV. Instead of performing the folding procedure described earlier to account for particle decays, the particles were sampled from the continuous particle spectrum, after which the particle decays were performed as in Ref. [163, 164]. This sampling procedure was then repeated multiple times to obtain smooth momentum distributions.

5.3 Dynamical decoupling

In the context of the hydrodynamic description of heavy-ion collisions, the kinetic decoupling surface is often chosen as a constant temperature hypersurface. Even though temperature can be used as a proxy for the scattering rate or mean free

path, the constant temperature decoupling does not account for the expansion or the finite size of the system. These effects play a major role in heavy-ion collisions since the expansion rate and the system size are vastly different in central and peripheral collisions. Thus, one temperature scale is insufficient for describing the dynamics of kinetic decoupling accurately in different collision systems.

A usual way to solve this issue is to switch to a kinetic theory description at some constant switching temperature before the decoupling takes place and let decoupling happen automatically according to the kinetic theory. However, switching from hydrodynamics to a transport model can easily lead to unphysical discontinuities in the transport coefficients, as discussed in Sec. 3.2.2

In Article [PI], an alternative method, that keeps the transport coefficients continuous, is used. Instead of switching to the kinetic theory description, hydrodynamics is used throughout the evolution of QCD matter. The dynamics of the kinetic decoupling are then determined by two dynamical conditions that take into account the expansion and the finite size of the fluid. These conditions take inspiration from the applicability of hydrodynamics and assume that the kinetic decoupling happens when the applicability of hydrodynamics ends. This is similar to Refs.[164–167]. As discussed in Sec 3.1.1, the applicability of hydrodynamics ends occurs when the macroscopic expansion rate exceeds the microscopic scattering rate, i.e. when $\mathrm{Kn} \equiv \tau_\pi \theta \approx 1$. This is a local condition that takes into account the expansion of the fluid element. The second condition is related to the global applicability of fluid dynamics. Even though fluid dynamics would be applicable locally, it does not automatically lead to a global applicability. The global applicability requires an additional condition that the mean free path is smaller than the global size of the system R. Here, the relaxation time τ_π is used as a probe for the free mean path. Thus, kinetic decoupling can be estimated to take place based on the following dynamical conditions:

$$\mathrm{Kn} = \tau_\pi \theta = C_{\mathrm{Kn}}$$
$$\frac{\gamma \tau_\pi}{R} = C_R, \tag{81}$$

where $C_{\mathrm{Kn}}, C_R \sim 1$ are free parameters that must be adjusted to match the measured data. The additional factor $\gamma = (1 - v^2)^{-1/2}$ appears in the second equation because the size of the system is calculated in the center-of-momentum frame of the colliding nuclei, while τ_π is defined in the fluid rest frame. The size of the system R is not uniquely defined. Note that the decoupling conditions depend on η/s through the relaxation time τ_π, as they should. In Article [PI], the size of the system was calculated as

$$R = \sqrt{\frac{A}{\pi}}, \tag{82}$$

where A is the transverse plane area in which $\mathrm{Kn} < C_{\mathrm{Kn}}$, i.e., the area in which the system has not yet decoupled according to the Knudsen number criterion. If the system consists of multiple disconnected areas, then R is calculated for each
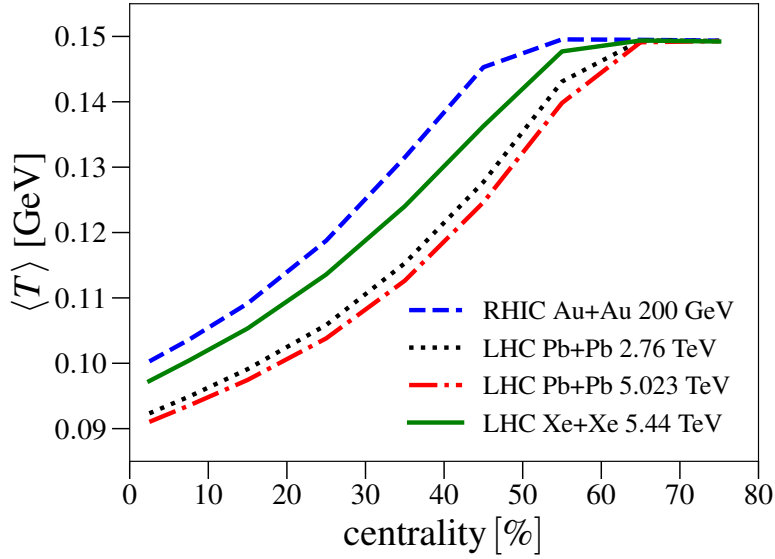
FIGURE 8   The entropy flux averaged temperature as a function of centrality for the $\eta/s = dyn$ parametrization. Figure from Article [PI], reprinted under the license CC BY 4.0.

of these areas separately. As mentioned earlier, this definition is not unique, and the definition used here corresponds close to the maximum distance a particle can travel from the center to the edges of the fluid. However, a lot of matter is distributed closer to the edges of the fluid, and most of the particles are moving toward the edges with the fluid so that the apparent size that the particles see can be smaller than the definition of R used here. Thus, the coefficient C_R might be considerably smaller than unity. Alternatively, one could define the size of the system as an entropy density weighted distance from the edges of the fluid or as a local distance that a particle needs to travel along the fluid velocity before reaching the edge of the fluid. These definitions would lead to smaller values of R so that larger values of C_R would be needed to achieve similar dynamics. In addition to the conditions (81), it is necessary to require that at the decoupling surface $T < 150$ MeV, so that the decoupling happens in the hadronic phase of the matter.

In Article [PI], it was shown that $C_{Kn} = 0.8$, and $C_R = 0.15$, together with the viscosities shown in Fig. 3 produced a good agreement with the measured data. This parametrization is referred to as $\eta/s = dyn$. The decoupling dynamics can be illustrated by looking at the entropy flux averaged decoupling temperature, which is shown for $\eta/s = dyn$ parametrization as a function of centrality for various collision systems in Fig. 8. The average temperature has a strong dependence on the centrality. The central collision systems decouple at much lower temperatures than the peripheral collisions, which practically decouple immediately when the system reaches the hadronic phase. This behavior is expected due to the smaller system sizes and larger gradients in the peripheral collisions. For the same reason, the decoupling temperature also increases when the collision energy or the radius of the colliding nuclei decreases.

The impact of the dynamical decoupling is also evident in the final state observables. The effect is most pronounced for the flow coefficients, which are shown in Fig. 9 for 5.023 TeV Pb+Pb, 2.76 TeV Pb+Pb, 5.44 TeV Xe+Xe, and 200 GeV Au+Au collision systems. Here the $\eta/s = dyn$ parametrization uses dynamical decoupling, while $\eta/s = 0.2$ and $\eta/s = param1$ from Ref. [27] use constant temperature decoupling with $T_{\text{dec}} = 100$ MeV. All of the parametrizations use EbyE EKRT initial states introduced in Sec. 4.3, with a nucleon Gaussian width $\sigma = 0.43$ fm. Therefore, the effects seen in the figure are caused by the dynamical decoupling and not the initial state. Switching from the constant temperature decoupling to the dynamical decoupling decreases flow coefficients in the peripheral collisions. The reason for this decrease is fairly easy to understand. Since the peripheral collisions decouple at higher temperatures, hydrodynamic evolution is shorter and there is less time for the work done by the pressure to convert the initial state eccentricities into the final state momentum-space anisotropies.

Due to the decrease of flow in the peripheral collisions, the $\eta/s = dyn$ parametrization can describe flow coefficients well for the LHC collision systems, while for the 200 GeV Au+Au collision system, it underestimates the amount of flow in peripheral region. There are many different reasons which might contribute to this discrepancy. The multiplicity in 200 GeV Au+Au collisions is significantly smaller than in the LHC energies, which is why the non-flow effects might be considerably larger in RHIC. Additionally, the thermalization time at the 200 GeV energy can be longer, and it is unclear if the system has enough time to thermalize sufficiently. Finally, the initial state model does not contain some of the elements that might contribute to the small systems and low collision energies, such as initial flow, finite thickness of colliding nuclei, hotspots, and non-zero initial $\pi^{\mu\nu}$. Nonetheless, the results across all collision systems are similar to the ones obtained using hadronic transport in the hadron gas phase, see e.g. Ref. [31]. This is a good indication that even though the dynamical decoupling presented here may not capture all the microscopic details of the decoupling dynamics, it manages to capture the most essential macroscopic features while keeping the transport coefficients continuous. Additionally, this method offers the potential to constrain the transport properties of QCD matter in the hadronic phase from measurements, without needing to rely on numerous unknown cross-sections that are present in the kinetic theory models.
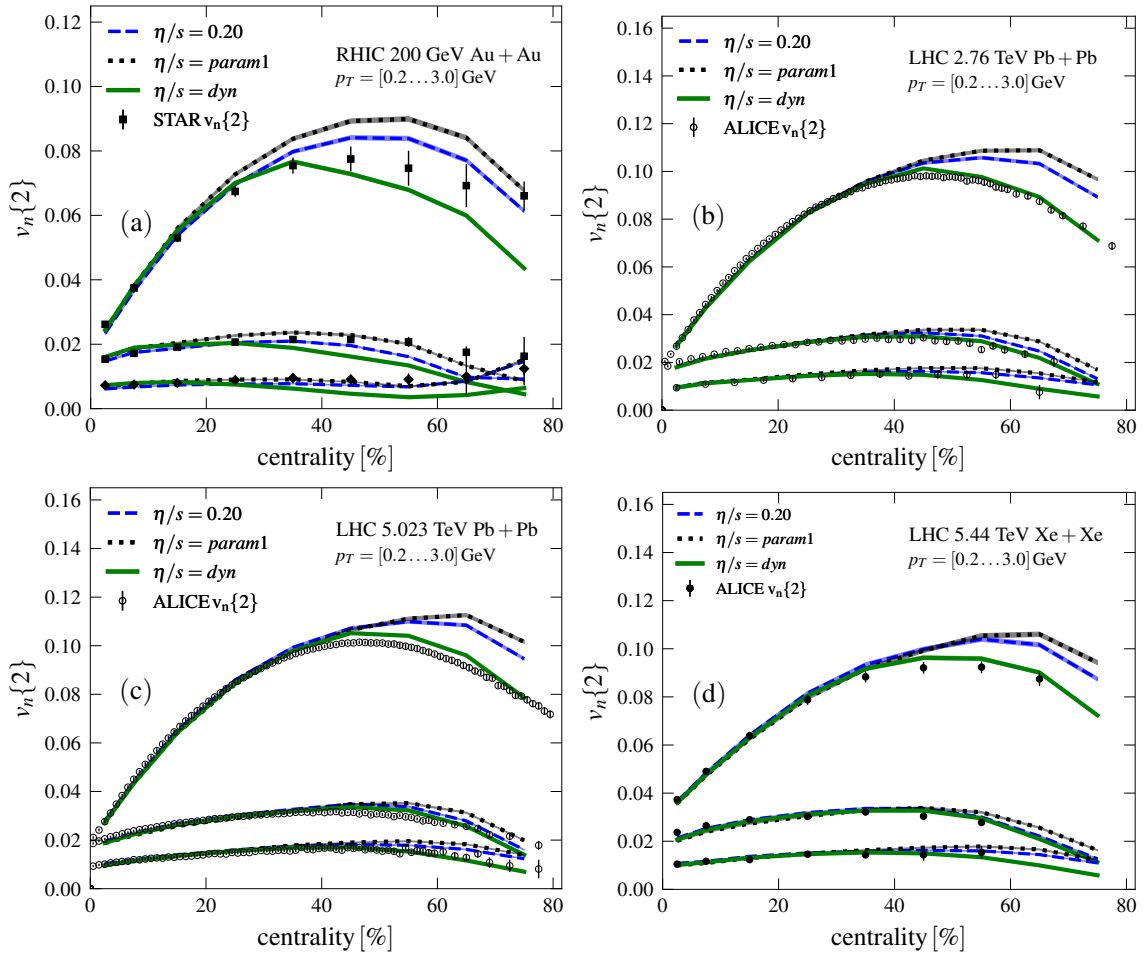
FIGURE 9   Flow coefficients as a function of centrality in 200 GeV Au+Au (a), 2.76 TeV Pb+Pb (b), 5.023 TeV Pb+Pb (c), and 5.44 TeV Xe+Xe (d) collisions. The experimental data are from the STAR [168, 169] and ALICE Collaborations [170, 171]. Figure from Article [PI], reprinted under the license CC BY 4.0.

6 MACHINE LEARNING

Machine learning is a vast field in computer science that aims to teach a machine to perform a task without explicitly programmed instructions. This enables machines to perform tasks that are beyond the guidelines given by their programmers. Typically, machine learning algorithms are divided into three classes: supervised learning, unsupervised learning, and semi-supervised learning. In supervised learning, the machine is given input and output data, and the goal of the algorithm is to make the machine learn how to produce output data from the input. The simplest example of supervised learning is linear regression, where the machine tries to find the best linear fit that maps the input to the output. Unlike supervised learning, unsupervised learning does not use any labeled data. Instead, it relies on the recognition of features and patterns from the input data alone. The most common examples of unsupervised learning are clustering algorithms and dimensionality reduction. As the name indicates, semi-supervised learning is a mixture of these two. It combines the usage of both labeled and unlabeled data, in such a way that it can more efficiently handle large datasets, while still getting some human input in the form of labeled data. Semi-supervised learning has become very popular in the context of large language models, which can contain enormous amounts of training data.

Machine learning tools have become widely used among different branches of physics, including heavy-ion physics. The main reason for the rising popularity of these tools is the increased computation times of the simulations and growing data flows in the measurements which have to be preprocessed in real-time. The first applications of machine learning in heavy-ion physics were done already in the 90s but at that time those methods did not gain that much popularity [172–174]. The second rise of machine learning in recent years has been driven by innovations in machine learning algorithms and increased computational power. Especially, the efficient usage of graphics processing units (GPUs) has boosted the available computational power significantly.

Nowadays almost all the biggest experimental heavy-ion collaborations use machine learning techniques for various applications, such as particle identification, event selection, signal/background discrimination, jet-tagging, and correct-

ing detector effects [175–178]. These methods are starting to become a necessity since the measured raw data obtained during heavy-ion runs can reach rates of over 1 TB/s.

Somewhat similar challenges are also present on the theory side. Most of the current heavy-ion collision simulations are event-by-event simulations, and to reach similar statistics as in measurements, one sometimes needs to perform millions of collision simulations. Another challenge that the simulations face is related to extracting information, like model parameters or matter properties, from the measurements through a global analysis. The statistical method that can be utilized to do this is called Bayesian inference. The implementation of Bayesian inference is usually done with the Markov chain Monte Carlo (MCMC) algorithm [179]. The drawback of MCMC is that one needs to perform simulations in tens of thousands of points in the parameter space, which is computationally very intensive. Due to this, machine learning tools, such as Gaussian process emulators, are usually used as surrogate models to decrease the computation cost of simulations [180–182]. However, even the computational cost needed to train the Gaussian process emulators can be around 100 million CPU hours if multiparticle flow correlations are included in the Bayesian analysis [34, 35]. The goal of Articles [PII, PIII] is to address this problem by replacing slow event-by-event hydrodynamic simulations with convolutional neural networks.

6.1   Neural networks

A neural network is a machine learning model originally inspired by the way biological neurons in the human brain process information. Every neural network is constructed from layers of artificial neurons, which are connected to each other. Like biological neurons, artificial neurons are activated if the signal exceeds some threshold value, after which they can forward the information to the next layer of the network. The neural networks always contain at least three layers:

1. Input layer: Contains input values given by the user,

2. Hidden layers: One or more layers that form the structure of the network,

3. Output layer: The final layer that produces the prediction of the desired output.

Each hidden layer can contain an arbitrary number of neurons, while for input and output layers, the number of neurons must match the input and output dimensions, respectively. The output of the network is determined by the weight and bias values that connect the artificial neurons to each other. The weights determine the strength of the connection between the neurons, while the biases set an offset to neuron activation. There are plenty of different ways to implement weights and biases to form various types of layers. The most basic layer type is the fully connected layer. In the fully connected layer, the output value of the

neuron k is obtained as a linear combination of the neuron values from the previous layer combined with an activation function F. If we have m neurons in a previous layer $n-1$ with outputs $x_j^{(n-1)}$, then the output of neuron k is

$$x_k^{(n)} = F\left(\sum_{j=0}^{m} w_{kj}^{(n)} x_j^{(n-1)} + b_k^{(n)} \right), \tag{83}$$

where $w_{kj}^{(n)}$ and $b_k^{(n)}$ are weights and biases of the neuron k in layer n. The activation function F is introduced to add non-linearity to the network and make it possible to describe more complex patterns. For the regression task, one often uses a linear activation $F(x) = x$ for the output layer and rectified linear unit (ReLU) activation $F(x) = \max(0, x)$ for the hidden layers. In addition to the fully connected layer, there are many other types of layers used in neural networks, each serving a distinct purpose and being designed for specific tasks. This makes it possible to efficiently tackle problems in various domains, such as computer vision, and natural language processing. Here, I will only focus on layers relevant to convolutional neural networks.

6.1.1 Convolutional neural networks

A convolutional neural network (CNN) is a type of neural network specifically designed for handling multi-dimensional structured data efficiently, and it is widely used in computer vision tasks. The neurons in a two-dimensional convolutional network are organized to form a $H \times W \times N$ grid, where each node corresponds to one neuron. In the case of an image, H, W, and N can be interpreted as the image's height, width, and number of color channels respectively.

The key ingredients of the CNN are the convolutional and the pooling layers. Convolutional layers are used to extract features from the data, and they can be thought of as applying filters to the image. Mathematically, the convolution layer is defined as a convolution between kernels $K^{k,(n)}$ and input $x^{(n-1)}$, where the index k distinguishes different kernels in the convolutional layer n. If the input has dimensions $n_h \times n_w \times n_c$, then the kernel is a $m_h \times m_w \times n_c$ tensor. The parameters m_h and m_w describe the spatial size of the filter, and they can be any numbers as long as they are smaller than the corresponding height and width of the input. In practice, odd values of m_h, and m_w are often used because the kernel then has a clear center node. One convolutional layer can contain many kernels, each producing one output channel, often referred to as feature maps. The elements of the kernel are the weights of the network, i.e., $K_{ijl}^{k,(n)} = w_{ijl}^{k,(n)}$. The output of the convolutional layer n, with odd m_h and m_w, is defined as

$$x_{ijk}^{(n)} = \sum_{x=0}^{m_h-1} \sum_{y=0}^{m_w-1} \sum_{z=0}^{n_c-1} w_{xyz}^{k,(n)} x_{x'y'z}^{(n-1)} + b_k^{(n)}, \tag{84}$$

where

$$x' = i + x - (m_h - 1)/2, \quad y' = j + y - (m_w - 1)/2. \tag{85}$$

Note that here $x' = y' = 0$ corresponds to the bottom left corner of the input. Since the convolution cannot be applied at the edges of the grid, the output tensor y has dimensions $(n_h - m_h + 1) \times (n_w - m_w + 1) \times m_c$, where m_c is the number of different kernels in the convolutional layer. Often one wants to keep the spatial dimensions of input and output equal. This can be achieved with a technique called padding. In padding, some or all elements from the previous layer that are undefined in the sum are set to a constant value. Usually, this value is chosen to be zero. With the padding P, the elements with $n_h \leq x' < n_h + P$, $-P \leq x' < 0$, $n_w \leq y' < n_w + P$, and $-P \leq y' < 0$ are defined to be zero. Usually one uses $P_h = (m_h - 1)/2$ for height, and $P_w = (m_w - 1)/2$ for the width, so the input and output have the same dimensions. The convolution layer also has a property called stride, which determines how the convolution kernel moves across the input neurons. More precisely, if the stride is set to a value S and padding is used, then Eq. (84) is applied only if $i = Sq$, and $j = Sp$, where $q, p \in \mathbb{N}$. With the padding and stride the output dimensions $O_{h/w}$ are obtained as

$$O_{h/w} = \frac{n_{h/w} - m_{h/w} + 2P_{h/w}}{S} + 1, \tag{86}$$

where the notation h/w indicates either height or width. As in the case of the fully connected layer, the activation function is usually applied after convolution to add non-linearity.

One of the variants of the convolutional layer is the depthwise separable convolution. It consists of the depthwise convolution followed by the pointwise convolution. The pointwise convolution is just a normal convolution with $m_h = m_w = 1$. On the other hand, the depthwise convolution is similar to the convolution in Eq. (84), but the kernel processes each channel independently by a separate filter, i.e. $K_{ij}^{k,(n)} = w_{ij}^{k,(n)}$, and

$$y_{ijk}^{(n)} = \sum_{x=0}^{m_h-1} \sum_{y=0}^{m_w-1} w_{xy}^{k,(n)} x_{x'y'k}^{(n-1)} + b_k^{(n)}, \tag{87}$$

where x', and y' are defined in Eq. (85). By first performing the depthwise convolution to capture spatial features, and then pointwise convolution to combine features from different channels, the depthwise separable convolution manages to reduce the number of trainable parameters compared to a traditional convolution with the same output dimensions.

Like the convolutional layer, the pooling layers are based on the kernel. However, the kernel elements of the pooling layer are not trainable weights, but instead, they are predefined. Like in the case of depthwise convolution, the pooling kernel is applied separately for each input channel, so that the number of channels remains unchanged, i.e.

$$x_{ijk}^{(n)} = \sum_{x=0}^{m_h-1} \sum_{y=0}^{m_w-1} K_{xy}^{\text{pool}} x_{x'y'k}^{(n-1)}, \tag{88}$$

where the size of the kernel K^{pool} is $m_h \times m_w$. The pooling layers almost always use no padding, and stride equal to the size of the kernel, so that the output size is $n_h / m_h \times n_w / m_w \times n_c$ The most typical pooling layers used are the average and max pooling. As the name suggests the average pooling takes the average of the input elements in the range of the kernel, i.e. $K^{\text{pool}}_{ij} = 1/(m_h m_w)$, while the max pooling takes the maximum value of the input elements.

The main function of pooling layers is to find the most relevant information from the feature maps after the convolution layer is applied and reduce the spatial dimensions of the input data. Because the pooling layers do not contain any weights or biases, they help to reduce the number of parameters in the network. Additionally, alternating between the convolution and the pooling layers helps create a feature hierarchy in the network, since the first convolutional layers probe smaller spatial areas of the original input than later ones.

In addition to the convolution and pooling layers, CNNs often utilize batch normalization [183]. The idea of batch normalization is to normalize hidden layer outputs using the mean and variance of input. The batch normalization operates slightly differently during the training and inference.

During training, the training data are divided into smaller subsets, called batches. The batch normalization layer computes batch-wise means $\mu_{ijk}^{\text{B},(n-1)}$ and variances $\left(\sigma_{ijk}^{\text{B},(n-1)} \right)^2$ for each input point $x_{ijk}^{(n-1)}$ preceding the batch normalization layer n. The output of the batch normalization is given as

$$
\begin{aligned}
x_{ijk}^{(n)} &= \gamma_{ijk}^{(n)} \tilde{x}_{ijk}^{(n-1)} + \beta_{ijk}^{(n)}, \\
\tilde{x}_{ijk}^{(n-1)} &= \frac{x_{ijk}^{(n-1)} - \mu_{ijk}^{\text{B},(n-1)}}{\sqrt{\left(\sigma_{ijk}^{\text{B},(n-1)} \right)^2 + \varepsilon}},
\end{aligned}
\tag{89}
$$

where $\gamma_{ijk}^{(n)}$, and $\beta_{ijk}^{(n)}$ are trainable parameters, which allow the network to choose an optimal normalization distribution for each input point in the layer. The parameter ε is a small constant added for numerical stability.

During the inference, there might be only a few samples, so computing the means and variances from the inference sample set could lead to unreliable results. This issue is handled by computing moving averages and variances iteratively during the training phase, and using them when performing inference. The moving mean and average describe more accurately the mean and variance of a larger sample set, and they are defined as

$$
\begin{aligned}
\mu_{ijk}^{\text{mov},(n)} &= \alpha^{\text{B}} \mu_{ijk}^{\text{mov},(n)} + (1 - \alpha^{\text{B}}) \mu_{ijk}^{\text{B},(n)} \\
(\sigma_{ijk}^{\text{mov},(n)})^2 &= \alpha^{\text{B}} (\sigma_{ijk}^{\text{mov},(n)})^2 + (1 - \alpha^{\text{B}})(\sigma_{ijk}^{\text{B},(n)})^2,
\end{aligned}
\tag{90}
$$

where the momentum parameter α^{B} determines how much the moving averages and variances lag behind their actual values. The purpose of moving averages and variances is to remove the noise due to batch-to-batch variations.

It was shown in Ref. [183], that the batch normalization makes the training of the network faster and more stable. This is especially true for deeper networks, i.e. neural networks with many hidden layers, where the output scales of the layers can vary a lot. Since the mean and variance are computed batch-wise during the training, they do not exactly reflect the true values. Therefore, the batch normalization also acts as a regularization method.

6.1.2 Training

The output of the neural network is determined by the values of the weights and biases. With proper training, these parameters are adjusted in such a way that the neural network can reproduce the results of the training and the validation data sets. Such a neural network can be used to accurately interpolate, or sometimes even slightly extrapolate the training data. In this sense, the neural network can be thought of as a fitting method with many fit parameters.

The goal of a neural network training algorithm is to to minimize the loss function L, which describes the discrepancy between the training data, and the neural network output. Thus, training a neural network is an optimization problem in a multi-dimensional space. Since neural networks can contain up to billions of trainable parameters, training is far from trivial. Most of the methods used to train CNNs are based on gradient descent and backpropagation.

The idea of gradient descent is to iteratively adjust the network parameters along the gradient of the function we want to minimize. With each iteration, the neural network parameters $\vec{\theta}$ are updated as

$$\vec{\theta} \to \vec{\theta} - \alpha \nabla L(\vec{\theta}), \tag{91}$$

where α is a learning rate that adjusts the length of the step. The algorithm is repeated as long as the loss function keeps decreasing, and the optimal values for parameters describing the training data are found. Choosing a proper value for α is essential, because if it is too large then the algorithm will not have a good enough resolution to find the minima. On the other hand, if α is too small then the algorithm will converge slowly and can get easily stuck to local minima. Some of the more sophisticated optimization algorithms, such as Adam [184], are designed to be less sensitive to the choice of the learning rate. In the Adam algorithm, this is achieved by introducing an adaptive learning rate for each individual weight. Even though the underlying optimization algorithm in the Adam is more effective and converges faster than the standard gradient descent, it still needs knowledge about the gradients $\nabla L(\vec{\theta})$.

In principle, it could be possible to form an expression for $L(\theta)$, and compute the gradient in Eq. (91) numerically. However, in practice, this is not very efficient, since the dimensionality of $\vec{\theta}$ can be enormous, and the parameters of one layer depend on the parameters of the previous layers. Therefore, the backpropagation algorithm is used. In simple terms, the backpropagation is just an application chain rule to obtain derivatives $\partial L / \partial \theta_i$. To demonstrate this in a simple way, let us assume that we have a neural network that contains an input

layer with inputs $x_j^{(0)}$, and m fully connected layers with weights $w_{kj}^{(n)}$, and an activation function $F_{(n)}$, where n denotes the layer number. For the sake of simplicity assume that all the biases are zero and that we only have one output value $y^{out} = x_0^{(m)}$. Further denoting the outputs of neuron j in layer n before and after the activation layer as $a_j^{(n)}$, and $x_j^{(n)}$ respectively. The backpropagation algorithm starts from the output layer, where we know the loss function as a function of the neural network output $L(y^{out})$. By using the chain rule and Eq. (83), the partial derivative of the loss function L with respect of the weights in the output layer w_{i1}^m can be written in a convenient form

$$\frac{\partial L}{\partial w_{0i}^{(m)}} = \frac{\partial L(y^{out})}{\partial y^{out}} \frac{\partial y^{out}}{\partial a_0^{(m)}} \frac{\partial a_0^{(m)}}{\partial w_{0i}^{(m)}} = \frac{\partial L(y^{out})}{\partial y^{out}} F'_{(m)} \left(a_0^{(m)} \right) x_i^{(m-1)}. \quad (92)$$

Note that there is only one output, so there are no other trainable weights in the output layer. For the hidden layers, the situation is only slightly more complicated. First, it is useful to notice that

$$\frac{\partial L}{\partial a_j^{(n)}} = \sum_{l=0}^{N^{n+1}} \frac{\partial L}{\partial a_l^{(n+1)}} \frac{\partial a_l^{(n+1)}}{\partial a_j^{(n)}}, \quad (93)$$

where N^n is the number of neurons in layer n. On the other hand, for the fully connected layer

$$a_l^{(n+1)} = \sum_{j=0}^{N^{n+1}} w_{lj}^{(n+1)} F_{(n)}(a_j^{(n)}), \quad (94)$$

so that

$$\frac{\partial a_l^{(n+1)}}{\partial a_j^{(n)}} = w_{lj}^{(n+1)} F'_{(n)}(a_j^{(n)}). \quad (95)$$

Now using Eqs. (93, 95), it is possible to write formula for the backpropagation

$$\frac{\partial L}{\partial a_j^{(n)}} = F'_{(n)}(a_j^{(n)}) \sum_{l=0}^{N^{n+1}} w_{lj}^{(n+1)} \frac{\partial L}{\partial a_l^{(n+1)}}. \quad (96)$$

Thus, the gradients of the layer n are related to the gradients in the next layer $n+1$. The partial derivatives for the weights can easily be obtained as

$$\frac{\partial L}{\partial w_{ij}^{(n)}} = \frac{\partial L}{\partial a_i^{(n)}} \frac{\partial a_i^{(n)}}{\partial w_{ij}^{(n)}} = \frac{\partial L}{\partial a_i^{(n)}} \frac{\partial}{\partial w_{ij}^{(n)}} \left(\sum_{l=0}^{N^{n-1}} w_{il}^{(n)} x_l^{(n-1)} \right) = \frac{\partial L}{\partial a_i^{(n)}} x_j^{(n-1)}. \quad (97)$$

In the backpropagation algorithm, one then uses Eqs. (96), and (97) iteratively to obtain all the partial derivatives of the loss function with respect to the weights for all hidden layers. Even though this example was only for a network consisting of fully connected layers, similar ideas can also be applied to more complicated structures.

Most of the time, the training data is too large to be fitted into the memory at once, which is why the training data are usually divided into smaller subsets called batches. The size of one batch typically varies between 16 and 512. The optimal value of the batch size depends on the complexity of the data. Large batch sizes can lead to a more stable and faster training process. On the other hand, with smaller batch sizes, the gradients will oscillate more, which can make the model generalize better to unseen data. The iterative process of training on batches is repeated many times for the whole training data. The period of passing the whole dataset one time is referred to as an epoch, and it usually takes at least 10 epochs to train a neural network.

One of the biggest challenges when training any supervised machine learning model is overfitting. An overfitting occurs when the model learns properties that are only specific to the training data, which leads to poor performance in the case of any other data. The neural networks suffer from this problem a lot since the number of trainable parameters can be extremely large. The large number of parameters makes it easy to describe even complex data sets precisely, with only little ability to generalize. There are many ways to try to avoid overfitting. The simplest one is to increase the training data or reduce the complexity of the model. This makes it more difficult for the model to learn features specific to the training data. However, increasing the amount of training data is not always possible, and reducing model complexity can also reduce the performance overall. One other option is data augmentation. In data augmentation one generates new training data from the existing one. This is a common technique in image classification tasks, where one can zoom, rotate, or flip images randomly during the training. However, one needs to be careful only to add data that are relevant to the problem. For example, if the goal is to recognize cars driving on a road, it is of very little use to augment data with images where the road is at the top of the image and the car is upside down.

In the context of convolutional neural networks, one popular approach to avoid overfitting is to add dropout layers to the network. The dropout layer randomly disables some of its input neurons during the training, which adds noise to the neural network. Because the disabled neurons are randomly picked each time the weights are updated, the network cannot adapt so easily to features specific to the training data. In a sense, the deactivation of neurons forces the network to try out many random subsets of the original network, making the features it learns quite robust.

In addition to the methods mentioned here, there are plenty of other methods to fight against overfitting. These include early stopping, L1/L2-regressions, and different kinds of ensemble learning methods [185, 186]. In general, it is not always easy to distinguish which methods are most suitable for a particular problem, and most of the time the best way to find the best solution is to test different available options and choose ones that lead to the best performance.

64

6.2 Predicting flow observables directly from the initial state

An investigation of the QCD matter properties requires a thorough comparison between various measured observables and those obtained from simulations. Some of the measured multi-particle correlations need up to a few million simulated collision events to obtain a statistical accuracy similar to the measurements. The computationally slowest part of these simulations is the hydrodynamic evolution and the computation of the particle spectra at the kinetic decoupling[1]. Performing one simulation takes ~ 30 minutes of CPU core time. Thus, there is a need for a way to reduce the computational cost of these simulations. One possibility is to replace the slow parts of the simulation with a neural network, which is trained to predict the final state observables directly from the initial state for each collision event separately. The input of the hydrodynamic simulations done in Article [PI] is a two-dimensional array containing the values of the energy density in the transverse-coordinate (x, y) plane. The structure of the input makes the convolutional neural network architecture ideal for replacing the hydrodynamic simulations.

6.2.1 DenseNet

The Dense Convolutional Network (DenseNet) [187] is a deep convolutional neural network architecture designed to maintain maximum information flow between multiple convolutional layers, so that the initial features of the data are not lost. Simultaneously, the DenseNet tries to address the vanishing gradients problem, which is a general challenge the deep neural network structures face. The vanishing gradient problem refers to the fact that when the number of sequential layers increases, the backpropagated gradients used in the optimization algorithm become increasingly smaller. This makes the training of the neural network inaccurate and inefficient.

The idea of the DenseNet is to replace the typical sequential structure of convolutional layers with dense connections, which are obtained by concatenating channels of the convolution layer output with all outputs of previous convolution layers in the block. That is, if C_i is the convolution layer operation with some weights then the output after n convolution layers is given by

$$\mathbf{y} = [\mathbf{x}, C_1(\mathbf{x}), C_2([\mathbf{x}, C_1(\mathbf{x})]), ..., C_n([\mathbf{x}, C_1(\mathbf{x}), C_2([\mathbf{x}, C_1(\mathbf{x})]), ...]], \tag{98}$$

where $\mathbf{x}$ is the input before the block of convolution layers. The number of feature maps each convolution layer C_i contains is called the growth rate k. Thus, the output $\mathbf{y}$ contains nk more channels than the input $\mathbf{x}$. For example, with 64 initial channels and 6 densely connected convolution layers, the factor $k = 32$ leads to an output with $64 + 6 \times 32 = 256$ channels. The DenseNet is constructed from dense blocks and transition layers. The dense blocks contain many convolution

---

[1] The hadronic transport can also use a significant amount of computational resources, but it is not used in the simulations performed in the context of this thesis.

Block	Output size	Layers
Convolution	134x134x64	7x7 conv, stride 2
Pooling	67x67x64	3x3 max pool, stride 2
Dense Block	67x67x256	$\begin{bmatrix} \text{1x1 conv} \\ \text{3x3 conv} \end{bmatrix}$ x 6
Transition Layer	67x67x128	1x1 conv
	33x33x128	2x2 average pooling, stride 2
Dense Block	33x33x512	$\begin{bmatrix} \text{1x1 conv} \\ \text{3x3 conv} \end{bmatrix}$ x 12
Transition Layer	33x33x256	1x1 conv
	16x16x256	2x2 average pooling, stride 2
Dense Block	16x16x896	$\begin{bmatrix} \text{1x1 conv} \\ \text{3x3 conv} \end{bmatrix}$ x 20
Transition Layer	16x16x448	1x1 conv
	8x8x448	2x2 average pooling, stride 2
Dense Block	8x8x1216	$\begin{bmatrix} \text{1x1 conv} \\ \text{3x3 conv} \end{bmatrix}$ x 24
Output Layer	1x1x1216	8x8 global average pooling
	N_{out}	Fully connected layer with ReLU activation

TABLE 3   The structure of the DenseNet network used in Article [PII].

layers that utilize the dense connections, while the transition layers take care of the pooling, and they consist of a 1×1 convolutional layer followed by a 2×2 average pooling layer.

The detailed structure of DenseNet used in Article [PII] is shown in Table 3, where "conv" refers to convolutional layer + batch normalization + ReLU activation and N_{out} is the number of outputs. The structure is close to the DenseNet-BC variant in which the dense block includes an additional 1×1 convolutional layer before each 3×3 convolution layer. The BC variant also includes compression in a transition layer, which is implemented by reducing feature maps in a 1×1 convolutional layer by a factor of 2. The growth rate $k = 32$ is used. There are few differences compared to the original structure from Ref. [187]. The convolution layers with kernel sizes 3×3 and 7×7 are replaced by depthwise separable convolutions, which made training slightly more stable and accurate. Additionally, at the output layer, the ReLU activation function is used.

6.2.2 Initial energy density as an input

In Article [PII], the DenseNet neural networks were trained to predict p_T integrated flow observables at the mid-rapidity directly from the initial energy density profile. The training data were obtained from hydrodynamic simulations performed in Article [PI], where the EKRT model, discussed in more detail in Sec. 4.3, was used to generate initial energy density profiles. The energy density profiles were discretized to a 269×269 grid with a resolution of 0.07 fm before passing them to the network as an input. For each initial state input, the neural network outputs one p_T integrated flow observable. A separate neural network was trained for the flow coefficients v_2, v_3, v_4, v_5, v_6, mean transverse-momentum $[p_T]$, and charged particle multiplicity $dN_{ch}/d\eta$. Each of these networks could give multiple outputs corresponding to different p_T integration ranges.

The training data consisted of 20k hydrodynamic events distributed evenly between 200 GeV Au+Au, 2.76 TeV Pb+Pb, 5.023 TeV Pb+Pb, and 5.44 TeV Xe+Xe collision systems. To make the training more efficient, neural network input was normalized so that the input of training data has a mean of zero and a standard deviation of one. The outputs of various neural networks are normalized to a common scale using a constant, ensuring that the typical value of a given output observable is approximately one. This enables the usage of the same learning rates across different observables/networks without sacrificing the quality of the training. However, the normalization was not used for the charged particle multiplicity network, since it uses a different loss function.

The loss function of the charged particle multiplicity network was chosen to be a mean squared logarithmic error (MSLE),

$$\text{Loss(MSLE)} = \frac{1}{N} \sum_i (\ln(y_{i,\text{true}} + 1) - \ln(y_{i,\text{pred}} + 1))^2, \tag{99}$$

where the sum goes over all events in the training batch of size N. In addition, $y_{i,\text{pred}}$ and $y_{i,\text{true}}$ are the predicted and true values of an observable respectively. For all other networks, the mean squared error (MSE) loss function was used:

$$\text{Loss(MSE)} = \frac{1}{N} \sum_i (y_{i,\text{true}} - y_{i,\text{pred}})^2. \tag{100}$$

All of the networks were trained using the Adam optimizer for 120 epochs with a batch size of 64. The learning rate was initially set to 0.01 for the charged particle multiplicity network while other networks used a value of 0.001. The initial learning rate was divided by a factor of ten at epochs 75 and 110. This kind of decaying learning rate would not be completely necessary due to the adaptive nature of the Adam algorithm, but in this case it seemed to speed up the learning process without sacrificing accuracy. To avoid overfitting, the training data were augmented by applying random rotations, flips, and translations to the input. This augmentation was possible because the flow observables do not depend on the orientation of the initial energy density profile.
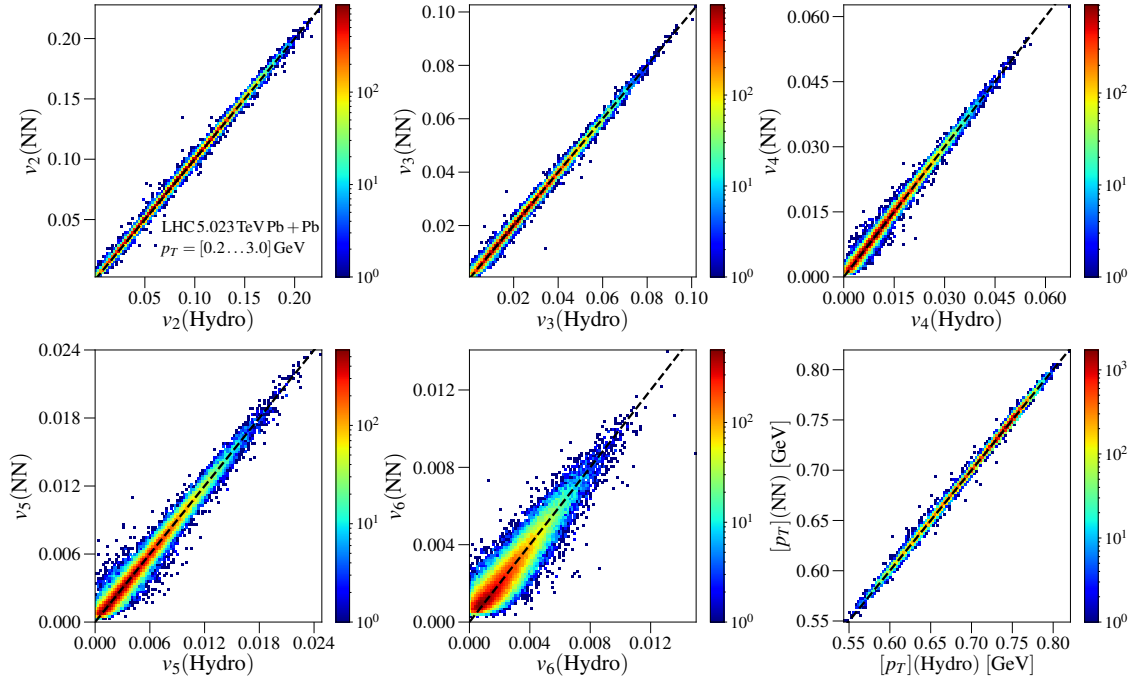
FIGURE 10   Comparison of the event-by-event predictions from the neural network (NN) with the results obtained from hydrodynamic simulations for validation events within the 0-80% centrality range. Figure from Article [PII], reprinted under the license CC BY 4.0.

The training of one network took ca. 80 minutes with an Nvidia Tesla V100 GPU. Trained neural networks can generate observables for 10 M events in $\approx$ 20 hours. This is a significant speedup compared to performing full hydrodynamic simulations, which would take $\sim$ 5 M CPU core hours. Thus, with a neural network, one can quickly generate an event-by-event distribution of flow observables. From these it is then easy to compute various measurable quantities, such as N-particle flow coefficients $v_n\{N\}$, normalized symmetric cumulants $NSC(m,n)$, normalized mixed harmonic cumulants $nMHC(n,m)$ and flow-transverse-momentum correlations $\rho(v_n^2, [p_T])$, all of which were introduced in Sec. 2.1. However, it is important to note that all events in the training data have the same parameters for hydrodynamic evolution and thus the trained neural networks cannot predict results if for example $\eta/s(T)$ changes.

The accuracy of the neural networks was validated by generating 90 k initial energy density profiles independent of the training data for the 5.023 TeV Pb+Pb collision system. These profiles were then used to compare the results of full hydrodynamic simulations with the predictions obtained from the neural networks. The accuracy of the neural network is demonstrated in Fig. 10 using 2D histograms. These histograms compare the neural network predictions against hydrodynamic computations for each event in 0-80% centrality bin, focusing on flow coefficients v_n (n ranges from 2 to 6) and the average transverse momenta $[p_T]$. The color bar indicates the number of events in a histogram bin, and the dashed black line indicates where the neural network predictions match exactly to the hydrodynamic computations.
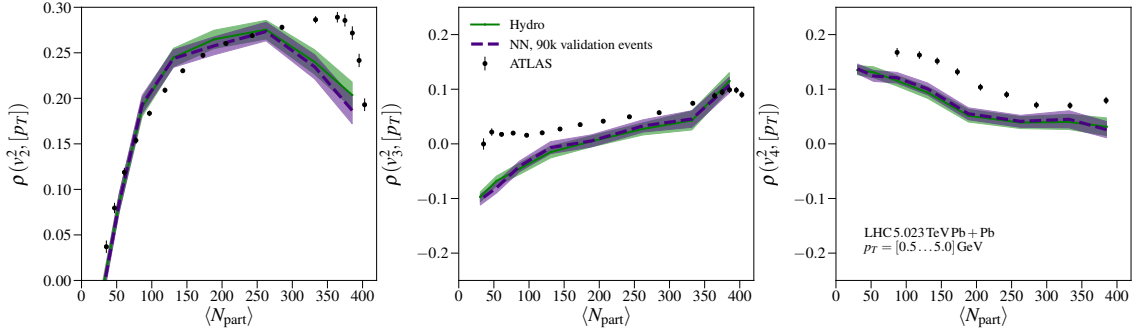
FIGURE 11   The neural network predictions of flow-transverse-momentum correlations compared against the hydrodynamic computations. The experimental data are from the ATLAS Collaboration [188]. Figure from Article [PII], reprinted under the license CC BY 4.0.

An excellent agreement between the neural network and hydrodynamic results is observed for v_2. However, when the order of flow coefficient increases, the performance slowly decreases. This behavior is expected since lower-order flow coefficients and initial-state eccentricities have quite a linear dependence and are not as sensitive to nonlinear effects arising from hydrodynamic evolution as the higher-order flow coefficients.

Regarding the average transverse momentum $[p_T]$, the hydrodynamic results are predicted very accurately by the neural network. However, it should be noted that event-by-event fluctuations of $[p_T]$ are very small compared to the absolute value of $[p_T]$. This means that relatively small errors are not necessarily a guarantee that correlations involving $[p_T]$ can be correctly predicted by the network.

Comparing the neural network and hydrodynamic results on an event-by-event basis provides insights into the accuracy of the network. However, measurements typically average the data over numerous events within centrality bins. Therefore, it is necessary to evaluate the performance of the network under these conditions. In Article [PII] it was shown that the neural network can reproduce hydrodynamic simulations accurately for 2-particle flow coefficients $v_n\{2\}$, normalized symmetric cumulants $NSC(m,n)$, normalized mixed harmonic cumulants $nMHC(n,m)$ and flow-transverse-momentum correlations $\rho(v_n^2, [p_T])$. To demonstrate this, flow-transverse-momentum correlations $\rho(v_n^2, [p_T])$ as a function of the number of participant nucleons are shown in Fig. 11.

Since the neural networks reproduce hydrodynamic simulations so accurately, it is possible to use them to generate a large number of events and see how high statistics affects flow correlations. The effect of statistics should be visible in the case of normalized mixed harmonic cumulants since there magnitude of correlation is quite weak. This is demonstrated in Fig. 12, where neural network prediction with 10 million events for $nMHC(n,m)$ is compared against full hydrodynamic results with 90 thousand events. The neural network prediction for $nMHC(v_2^2, v_3^4)$, based on 10 million events, falls within the statistical errors of the hydrodynamic results. However, in central collisions, the increased number
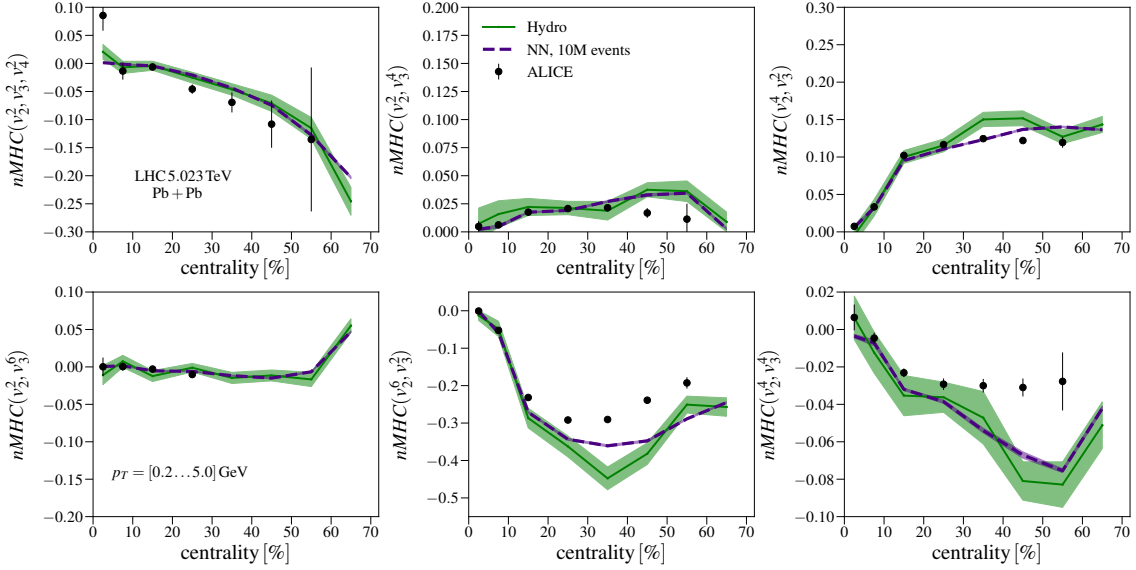
FIGURE 12   Comparison of normalized mixed harmonic cumulants between the neural network prediction with 10 M collision events and hydrodynamic results with 90 k collision events. The experimental data are from the ALICE Collaboration [53]. Figure from Article [PII], reprinted under the license CC BY 4.0.

of events reveals a significantly different centrality dependence, aligning closely with the ALICE measurements. Regarding $nMHC(v_2^2, v_3^6)$, increasing the event count from 90 thousand to 10 million evens out the sharp transitions between correlation and anti-correlation. The higher statistic outcome is nearly zero, except in most peripheral collisions. This is again consistent with the measurements from ALICE. In the cases of $nMHC(v_2^4, v_3^2)$ and $nMHC(v_2^6, v_3^2)$, there are statistically significant differences between the hydrodynamic results and the high-statistic neural network predictions. This suggests that the jackknife resampling used in the evaluation of statistical errors may sometimes substantially underestimate statistical errors.

These results emphasize that when constraining the QCD matter properties with the multi-particle flow correlations, it is necessary to include enough simulated collision events in the analysis. Otherwise, the analysis might lead to wrong conclusions. For this purpose, neural networks are ideal tools since they can be used to reduce the computational time needed to a fraction compared to conventional methods.

6.2.3 Additional inputs

The neural networks trained in Article [PII] have only the initial energy density as an input. This means that every time QCD matter properties or model parameters affecting the system evolution are changed, it would be necessary to retrain the network to correctly reproduce the results. However, this difficulty can be avoided if the neural network is trained to take additional inputs. This was demonstrated in Article [PIII], where shear and bulk viscosity parameters
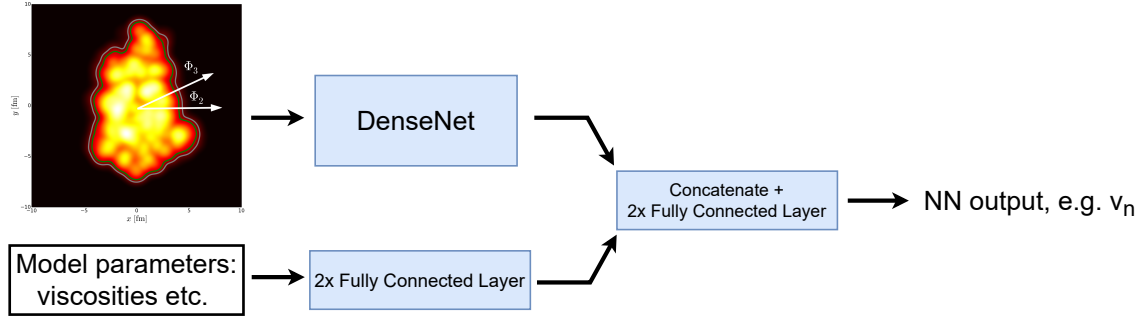
FIGURE 13 Schematic presentation of the neural network with energy density and model parameter inputs. Figure from Article. [PIII].

appearing in Eqs. (42) and (43), and decoupling parameters introduced in Sec. 5.3 were added as additional inputs. This addition makes neural networks more suitable for Bayesian analysis, where observables need to be computed with a large number of different model parameters. Unfortunately, generating a large number of events with neural networks is still too slow to be directly used in an MCMC algorithm. However, the neural networks can be used to efficiently generate the training data for the Gaussian process emulators, which in turn can reduce the computation time needed for the analysis by orders of magnitude.

With the additional inputs, the neural network structure needs to be slightly modified. The modified version is schematically illustrated in Fig. 13. The initial energy density can still be handled with the DenseNet structure like previously [2]. However, the additional inputs are no longer in a suitable form for the convolutional layers, so they need to be processed using fully connected layers. The output of this is then combined with the DenseNet output, after which two fully connected layers are applied before the output. All the fully connected layers use the ReLU activation.

The training of these neural networks was done in the same manner as the training of the networks without additional inputs, and all used hyperparameters were kept the same, with the exception of the batch size which was increased to 128. The training data consisted of 160 k training events distributed evenly between four collision systems and 2 k parameter points sampled with the Latin hypercube sampling. This results in only 80 events of training data per parameter point, which is 250 times less data than in the training approach without additional inputs.

In the case of neural networks with multiple inputs, referred to here as NN_p, the main focus lies on the accuracy of the network in generating new events with identical parameter values as those in the training data. This is because the efficient approach for Bayesian analysis involves generating a large number of events using neural networks across a range of parameter points, computing all observables within these points, and subsequently training the Gaussian process emulators for these observables. Thus, the accuracy of the NN_p networks was assessed by selecting two sets of model parameter points from the training data,

---

[2]   This structure does not include the final fully connected layer.
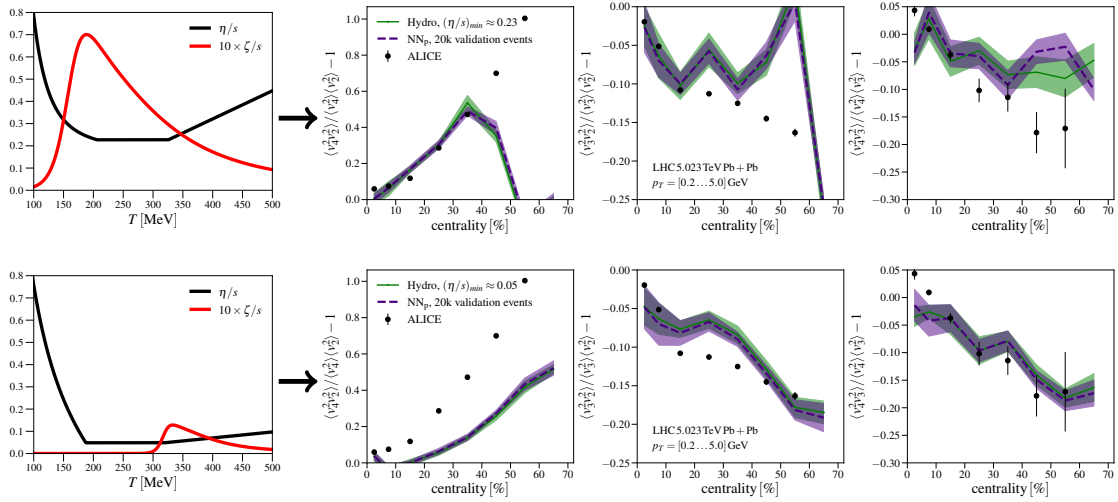
FIGURE 14   Validation tests for $NSC(m, n)$ performed using multiple input neural net-
works. The upper (lower) panels display results obtained with high (low)
specific viscosities. Both cases use 20 k validation events. The experimental
data are from the ALICE Collaboration [53]. Figure from Article [PIII].

corresponding to two vastly different viscosity values, and generating 20 k new
independent initial state profiles for both points. The validation was performed
by comparing neural network predictions with hydrodynamic computations, and
the results for the normalized symmetric cumulants are shown in Fig. 14. The
NN_p networks reproduce the results from hydrodynamic simulations with high
accuracy. The only notable deviation is observed for $NSC(3, 4)$ in the peripheral
collisions with extremely high viscosity. However, in this case, the numerical er-
rors of the hydrodynamical simulations themselves may be significant due to the
high viscosity. Thus, the neural networks with multiple inputs seem to perform
well and could be used in the Bayesian global analysis of heavy-ion observables.
This would make the addition of multi-particle correlations to the analysis much
more practical, potentially leading to more accurate constraints on QCD matter
properties.

7 SATURATION DYNAMICS OF MONTE-CARLO EKRT WITH NEURAL NETWORKS

The Monte-Carlo EKRT initial state [PIV] discussed in Sec. 4.4 introduces additional fluctuations compared to the midrapidity EbyE version of the EKRT model [27]. These fluctuations, together with the interplay between momentum conservation and saturation, lead to additional dynamics that can have an impact on the final state observables. However, investigating these effects can be slow and tedious. Fortunately, the neural networks discussed in Sec. 6.2.2 can significantly reduce the computation time needed to compute and analyze midrapidity observables.

The study performed in Article [PV], focuses on the dynamics of the MC-EKRT initial state through midrapidity observables, and it combines all major topics discussed in this thesis: Monte-Carlo EKRT initial state [PIV], dynamical decoupling [PI], and neural networks [PII, PIII]. The effect of the added fluctuations and dynamics in MC-EKRT was demonstrated by comparing the results obtained with MC-EKRT against the EbyE EKRT results from Article [PI]. The comparison was performed without altering matter properties or decoupling parameters, i.e., the MC-EKRT results use shear and bulk viscosities from Fig. 3. Therefore, the neural networks trained in Article [PII] were used to compute the final state observables. However, the training of these neural networks was performed using EbyE EKRT initial conditions, so it is necessary to ensure that the accuracy remains good even when using the MC-EKRT initial state.

The accuracy of neural networks with MC-EKRT initial state was tested in Article [PV] for 5.023 TeV Pb+Pb collisions. The validation results for flow coefficients v_2, v_3, and v_4 are illustrated in Fig 15. The validation test used the MC-EKRT initial state with $\kappa_{\mathrm{sat}} = 2.5$, $K = 2.2$, and $\sigma_\perp = 0.4$ fm. In addition, the initial state included the nucleon substructure according to Eq. (48) with parameters $N_h = 3$, and $\sigma_h = 0.2$ fm. The hotspot trigger (50) was used with $\sigma_{\mathrm{HS}} = 11.9$ mb. Despite the significantly different initial state structure, the neural networks reproduce the results from hydrodynamics simulations accurately. This is a nontrivial test, and it illustrates the neural network's ability to extrapolate beyond the training data. Thus, the neural networks can be reliably used to predict midra-
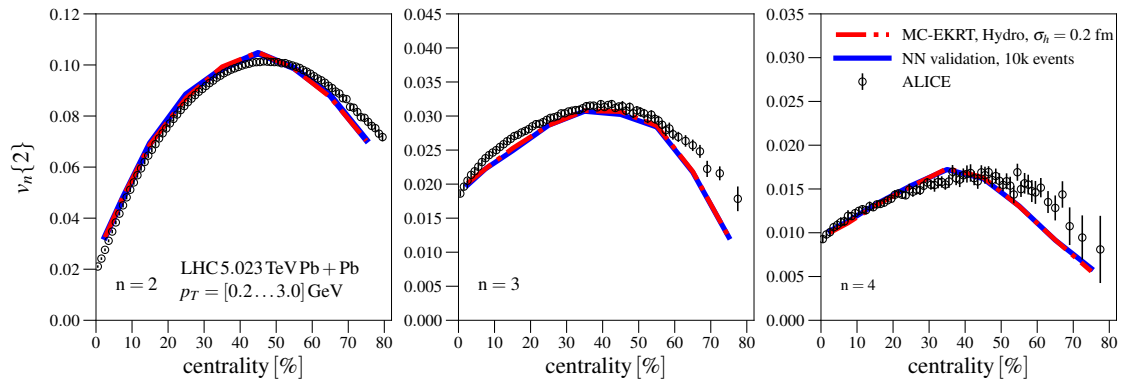
FIGURE 15   The neural network predictions of flow coefficients obtained with the MC-EKRT initial state compared against the results from hydrodynamic simulations. The experimental data are from the ALICE Collaboration [170]. Figure from Article [PV].

pidity observables from the MC-EKRT initial state.

When trying to understand initial state effects from the final state observables, it is necessary to remember that some observables are quite sensitive to the matter properties. For example, the magnitude of the flow coefficients depends heavily on the η/s. However, the ratios of the flow coefficients are less sensitive to such details, and especially the ratio between v_3 and v_2 can give valuable information about the geometry of the initial state [189]. Therefore, in Article [PV], the parameter $\sigma_\perp$ was adjusted to match the measured v_2 in 5.023 TeV collisions. This was possible because it was noticed that the $\sigma_\perp$ had only a minuscule impact on ratios between flow coefficients.

One interesting aspect of MC-EKRT is the interplay between the energy conservation and saturation filters. This is demonstrated in Fig. 16, which shows the flow coefficients computed with various filter combinations for 5.023 TeV Pb+Pb collisions. All the cases use $K = 2.5$, while the saturation parameter is adjusted to obtain similar charged particle multiplicities in central collisions. This corresponds to value $\kappa_{\text{sat}} = 1.3$ for the saturation-only case, and $\kappa_{\text{sat}} = 1.4$ for the other two cases. The nucleon width was set to $\sigma = 0.53$ fm without any substructure. The most striking feature in Fig. 16 is that the ratio between v_3 and v_2 is greatly affected by the strength of saturation. The saturation-only case seems to produce the measured v_2 and v_3 most accurately, while simultaneously applied filters lead to an underestimation of v_3. When saturation is enforced before other filters the results get closer to the saturation-only results, as one would expect. The differences come from the different geometrical nature of saturation and momentum conservation. The saturation suppresses the minijet production in locations where nuclear overlap density $T_A T_B$ is large, while the momentum conservation is less sensitive to nuclear overlap. It is also interesting to note that the v_3/v_2 ratio is very similar between the MC-EKRT with saturation-only and EbyE EKRT which does not have an explicit momentum conservation.

In Article [PV], the hotspots were introduced for the first time in the context of the EKRT model. The hotspots can play an important role in the saturation
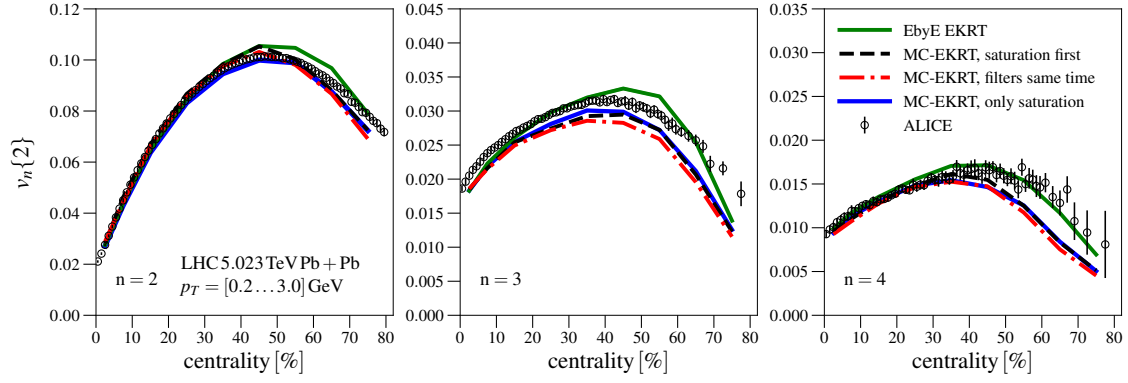
FIGURE 16   The flow coefficents as a function of centrality, computed using various filter settings in the MC-EKRT initial state for 5.023 TeV Pb+Pb collisions. The experimental data are from the ALICE Collaboration [170]. Figure from Article [PV].
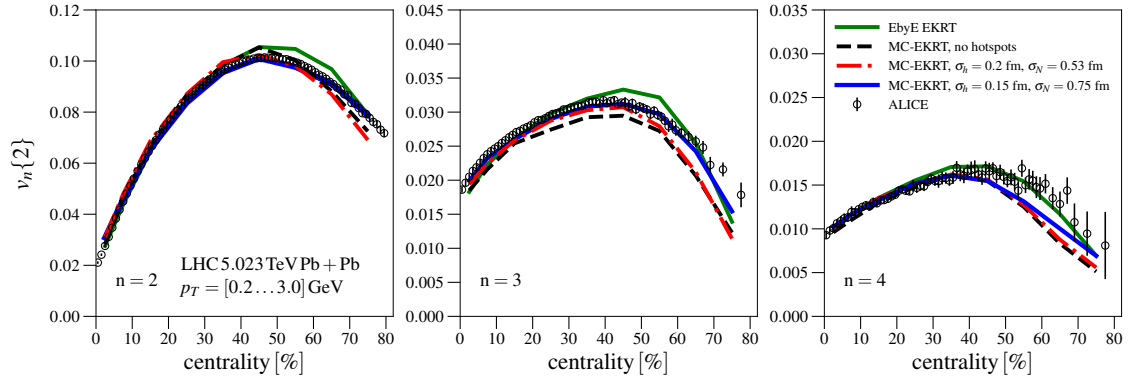

FIGURE 17   The centrality dependence of flow coefficients obtained using MC-EKRT initial state with the hotspots. The experimental data are from the ALICE Collaboration [170]. Figure from Article [PV].

dynamics since the nuclear overlap density $T_A T_B$ can reach higher values with the narrow fluctuating hotspots than with average nucleon geometry. The effect of hotspots on flow coefficients is shown in Fig. 17, where two different kinds of hotspot parameterizations are shown. One parametrization uses a wide nucleon ($\sigma = 0.75$ fm) with narrow hotspots ($\sigma_h = 0.15$ fm), while the other uses slightly wider hotspots ($\sigma_h = 0.2$ fm), and the nucleon width consistent with the H1 measurements ($\sigma = 0.53$ fm). Both parametrizations have 3 hotspots. The saturation-first case is the same as in Fig. 16. All the initial states applied saturation first, followed by momentum, and valence-quark number conservation filters. The addition of hotspots seems to increase the amount of v_3 compared to v_2, and the ratio v_3/v_2 obtained with $\sigma_h = 0.15$ fm gives the best description of the measured data. This indicates that the interplay between hotspots, and saturation is crucial for the ratio v_3/v_2.

8   CONCLUSIONS

The focus of this thesis has been the development of phenomenology and numerical tools in the field of heavy-ion collisions, aiming to eventually achieve a deeper understanding of the properties of QCD matter. The progress made in this thesis work can be divided into three parts. First, the dynamical decoupling discussed in Article [PI] provides an alternative way to describe heavy-ion collisions by relying on hydrodynamic evolution without a hadronic transport model. This way unwanted discontinuities in the transport coefficients can be avoided while capturing the essential dynamics of the kinetic decoupling. In Article [PI], it was demonstrated that the simulations done with the dynamical decoupling can well reproduce a wide range of measured flow observables in 5.023 TeV Pb+Pb, 2.76 TeV Pb+Pb, 5.44 TeV Xe+Xe, and 200 GeV Au+Au collision systems. Compared to the constant temperature decoupling, the dynamical decoupling was observed to decrease the magnitude of flow in the peripheral collisions, leading to better agreement with the measurements.

Secondly, in Article [PII], the neural networks were trained to reproduce the event-by-event flow observables obtained from hydrodynamic simulations directly from the initial state. The accuracy of the neural networks was tested by comparing the neural network predictions against the hydrodynamic simulations. The neural networks were able to reproduce the hydrodynamic results accurately, even for various multi-particle correlations. Predicting flow observables with the neural network was observed to be many orders of magnitude faster than performing full hydrodynamic simulations. For example, generating 10 million collision events with the neural network took only around 20 GPU hours of computing time.

The potential of the neural networks was further demonstrated in Article [PIII], where neural networks were extended to work with additional inputs. These inputs could contain matter properties such as shear and bulk viscosities. With this addition, the computation time needed to determine the QCD matter properties via Bayesian analysis could be reduced to a fraction compared to the current state-of-the-art methods. Thus, adding computationally costly multi-particle flow correlators to the Bayesian analysis would be more achievable.

Finally, a completely new type of Monte-Carlo version of the EKRT initial state model was introduced in Article [PIV]. The MC-EKRT set-up added additional saturation scale and minijet multiplicity fluctuations to the framework and made it possible to study rapidity-dependent observables. The rapidity dependence of charged particle multiplicity was studied in Article [PIV] with the entropy-averaged MC-EKRT initial states. The results showed a promisingly good overall agreement with the measured data across 5.023 TeV Pb+Pb, 2.76 TeV Pb+Pb, and 200 GeV Au+Au collision systems.

The fluctuating hotspots were introduced to the MC-EKRT in Article [PV], where the saturation dynamics of the initial state was studied through final state midrapidity observables. It was found that strong saturation is key for obtaining a v_3/v_2 ratio that agrees with the measurements. The narrow fluctuating hotspots were noticed to give the strongest saturation effects and provided the best agreement with the measured flow coefficients.

While this thesis addresses several challenges in the phenomenological modeling of heavy-ion collisions, there remains plenty of room for further developments. Although neural networks present an efficient method for studying QCD matter properties, they are yet to be applied in Bayesian analyses. Furthermore, the rapidity-dependent observables obviously provide further constraints to the matter properties, but the neural networks discussed in this thesis are only applicable to the midrapidity observables.

Further improvements to the MC-EKRT initial state model are also possible and foreseen. Even though the MC-EKRT model generates all initial state partons, considering high-p_T observables would necessitate the addition of parton shower evolution that couples thermalization of the produced partons and eventually with the hydrodynamic evolution. Additionally, the current implementation of the model only uses the energy density component for initializing hydrodynamics. A more detailed modeling would involve incorporating all components of the energy-momentum tensor.

REFERENCES

[1] M. Gell-Mann, "A Schematic Model of Baryons and Mesons", *Phys. Lett.*, vol. 8, pp. 214–215, 1964. DOI: 10.1016/S0031-9163(64)92001-3.

[2] E. D. Bloom *et al.*, "High-energy inelastic $e - p$ scattering at 6° and 10°", *Phys. Rev. Lett.*, vol. 23, pp. 930–934, 16 Oct. 1969. DOI: 10.1103/PhysRevLett.23.930. [Online]. Available: https://link.aps.org/doi/10.1103/PhysRevLett.23.930.

[3] M. Breidenbach *et al.*, "Observed behavior of highly inelastic electron-proton scattering", *Phys. Rev. Lett.*, vol. 23, pp. 935–939, 16 Oct. 1969. DOI: 10.1103/PhysRevLett.23.935. [Online]. Available: https://link.aps.org/doi/10.1103/PhysRevLett.23.935.

[4] D. P. Barber *et al.*, "Discovery of three-jet events and a test of quantum chromodynamics at petra", *Phys. Rev. Lett.*, vol. 43, pp. 830–833, 12 Sep. 1979. DOI: 10.1103/PhysRevLett.43.830. [Online]. Available: https://link.aps.org/doi/10.1103/PhysRevLett.43.830.

[5] R. Brandelik *et al.*, "Evidence for planar evenoctts in e+e- annihilation at high energies", *Physics Letters B*, vol. 86, no. 2, pp. 243–249, 1979, ISSN: 0370-2693. DOI: https://doi.org/10.1016/0370-2693(79)90830-X. [Online]. Available: https://www.sciencedirect.com/science/article/pii/037026937990830X.

[6] C. Berger *et al.*, "Evidence for gluon bremsstrahlung in e+e- annihilations at high energies", *Physics Letters B*, vol. 86, no. 3, pp. 418–425, 1979, ISSN: 0370-2693. DOI: https://doi.org/10.1016/0370-2693(79)90869-4. [Online]. Available: https://www.sciencedirect.com/science/article/pii/0370269379908694.

[7] L. Lindemann, "Proton structure functions and gluon density at hera", *Nuclear Physics B - Proceedings Supplements*, vol. 64, no. 1, pp. 179–183, 1998, Proceedings of the QCD 97 Euroconference 25th Anniversary of QCD, ISSN: 0920-5632. DOI: https://doi.org/10.1016/S0920-5632(97)01057-8. [Online]. Available: https://www.sciencedirect.com/science/article/pii/S0920563297010578.

[8] Y. Aoki, Z. Fodor, S. D. Katz, and K. K. Szabo, "The Equation of state in lattice QCD: With physical quark masses towards the continuum limit", *JHEP*, vol. 01, p. 089, 2006. DOI: 10.1088/1126-6708/2006/01/089. arXiv: hep-lat/0510084.

[9] S. Borsanyi *et al.*, "The QCD equation of state with dynamical quarks", *JHEP*, vol. 11, p. 077, 2010. DOI: 10.1007/JHEP11(2010)077. arXiv: 1007.2580 [hep-lat].

[10] A. Bazavov and P. Petreczky, "Taste symmetry and QCD thermodynamics with improved staggered fermions", *PoS*, vol. LATTICE2010, G. Rossi, Ed., p. 169, 2010. DOI: 10.22323/1.105.0169. arXiv: 1012.1257 [hep-lat].

78

[11] A. Bazavov *et al.*, "Equation of state in (2+1)-flavor QCD", *Phys. Rev. D*, vol. 90, p. 094 503, 2014. DOI: 10.1103/PhysRevD.90.094503. arXiv: 1407.6387 `[hep-lat]`.

[12] S. A. Voloshin, "Anisotropic flow", *Nucl. Phys. A*, vol. 715, H. Gutbrod, J. Aichelin, and K. Werner, Eds., pp. 379–388, 2003. DOI: 10.1016/S0375-9474(02)01450-1. arXiv: nucl-ex/0210014.

[13] K. Adcox *et al.*, "Formation of dense partonic matter in relativistic nucleus-nucleus collisions at RHIC: Experimental evaluation by the PHENIX collaboration", *Nucl. Phys. A*, vol. 757, pp. 184–283, 2005. DOI: 10.1016/j.nuclphysa.2005.03.086. arXiv: nucl-ex/0410003.

[14] I. Arsene *et al.*, "Quark gluon plasma and color glass condensate at RHIC? The Perspective from the BRAHMS experiment", *Nucl. Phys. A*, vol. 757, pp. 1–27, 2005. DOI: 10.1016/j.nuclphysa.2005.02.130. arXiv: nucl-ex/0410020.

[15] B. B. Back *et al.*, "Elliptic flow in Au + Au collisions at RHIC", *J. Phys. G*, vol. 31, F. Antinori, S. A. Bass, R. Bellwied, T. Ullrich, J. Velkovska, and U. Wiedemann, Eds., S41–S48, 2005. DOI: 10.1088/0954-3899/31/4/006. arXiv: nucl-ex/0410008.

[16] J. Adams *et al.*, "Experimental and theoretical challenges in the search for the quark gluon plasma: The STAR Collaboration's critical assessment of the evidence from RHIC collisions", *Nucl. Phys. A*, vol. 757, pp. 102–183, 2005. DOI: 10.1016/j.nuclphysa.2005.03.085. arXiv: nucl-ex/0501009.

[17] D. Teaney, J. Lauret, and E. V. Shuryak, "A Hydrodynamic Description of Heavy Ion Collisions at the SPS and RHIC", Oct. 2001. arXiv: nucl-th/0110037.

[18] P. Huovinen, "Hydrodynamical description of collective flow. Chapter 1.", R. C. Hwa and X.-N. Wang, Eds., pp. 600–633, May 2003. DOI: 10.1142/9789812795533_0009. arXiv: nucl-th/0305064.

[19] P. Romatschke and U. Romatschke, "Viscosity Information from Relativistic Nuclear Collisions: How Perfect is the Fluid Observed at RHIC?", *Phys. Rev. Lett.*, vol. 99, p. 172 301, 2007. DOI: 10.1103/PhysRevLett.99.172301. arXiv: 0706.1522 `[nucl-th]`.

[20] H. Niemi, K. J. Eskola, and P. V. Ruuskanen, "Elliptic flow in nuclear collisions at the Large Hadron Collider", *Phys. Rev. C*, vol. 79, p. 024 903, 2009. DOI: 10.1103/PhysRevC.79.024903. arXiv: 0806.1116 `[hep-ph]`.

[21] M. Luzum and P. Romatschke, "Conformal Relativistic Viscous Hydrodynamics: Applications to RHIC results at s(NN)**(1/2) = 200-GeV", *Phys. Rev. C*, vol. 78, p. 034 915, 2008, [Erratum: Phys.Rev.C 79, 039903 (2009)]. DOI: 10.1103/PhysRevC.78.034915. arXiv: 0804.4015 `[nucl-th]`.

[22] K Aamodt *et al.*, "Elliptic flow of charged particles in Pb-Pb collisions at 2.76 TeV", *Phys. Rev. Lett.*, vol. 105, p. 252 302, 2010. DOI: 10.1103/PhysRevLett.105.252302. arXiv: 1011.3914 `[nucl-ex]`.

[23] G. Aad *et al.*, "Measurement of the pseudorapidity and transverse momentum dependence of the elliptic flow of charged particles in lead-lead collisions at $\sqrt{s_{NN}}$ = 2.76 TeV with the ATLAS detector", *Phys. Lett. B*, vol. 707, pp. 330–348, 2012. DOI: 10.1016/j.physletb.2011.12.056. arXiv: 1108.6018 [hep-ex].

[24] S. Chatrchyan *et al.*, "Measurement of the Elliptic Anisotropy of Charged Particles Produced in PbPb Collisions at $\sqrt{s_{NN}}$=2.76 TeV", *Phys. Rev. C*, vol. 87, no. 1, p. 014 902, 2013. DOI: 10.1103/PhysRevC.87.014902. arXiv: 1204.1409 [nucl-ex].

[25] H. Song, S. A. Bass, and U. Heinz, "Elliptic flow in 200 A GeV Au+Au collisions and 2.76 A TeV Pb+Pb collisions: insights from viscous hydrodynamics + hadron cascade hybrid model", *Phys. Rev. C*, vol. 83, p. 054 912, 2011, [Erratum: Phys.Rev.C 87, 019902 (2013)]. DOI: 10.1103/PhysRevC.83.054912. arXiv: 1103.2380 [nucl-th].

[26] C. Gale, S. Jeon, B. Schenke, P. Tribedy, and R. Venugopalan, "Event-by-event anisotropic flow in heavy-ion collisions from combined Yang-Mills and viscous fluid dynamics", *Phys. Rev. Lett.*, vol. 110, no. 1, p. 012 302, 2013. DOI: 10.1103/PhysRevLett.110.012302. arXiv: 1209.6330 [nucl-th].

[27] H. Niemi, K. J. Eskola, and R. Paatelainen, "Event-by-event fluctuations in a perturbative QCD + saturation + hydrodynamics model: Determining QCD matter shear viscosity in ultrarelativistic heavy-ion collisions", *Phys. Rev. C*, vol. 93, no. 2, p. 024 907, 2016. DOI: 10.1103/PhysRevC.93.024907. arXiv: 1505.02677 [hep-ph].

[28] J. E. Bernhard, J. S. Moreland, S. A. Bass, J. Liu, and U. Heinz, "Applying Bayesian parameter estimation to relativistic heavy-ion collisions: simultaneous characterization of the initial state and quark-gluon plasma medium", *Phys. Rev. C*, vol. 94, no. 2, p. 024 907, 2016. DOI: 10.1103/PhysRevC.94.024907. arXiv: 1605.03954 [nucl-th].

[29] S. A. Bass, J. E. Bernhard, and J. S. Moreland, "Determination of Quark-Gluon-Plasma Parameters from a Global Bayesian Analysis", *Nucl. Phys. A*, vol. 967, U. Heinz, O. Evdokimov, and P. Jacobs, Eds., pp. 67–73, 2017. DOI: 10.1016/j.nuclphysa.2017.05.052. arXiv: 1704.07671 [nucl-th].

[30] J. E. Bernhard, J. S. Moreland, and S. A. Bass, "Bayesian estimation of the specific shear and bulk viscosity of quark–gluon plasma", *Nature Phys.*, vol. 15, no. 11, pp. 1113–1117, 2019. DOI: 10.1038/s41567-019-0611-8.

[31] D. Everett *et al.*, "Multisystem Bayesian constraints on the transport coefficients of QCD matter", *Phys. Rev. C*, vol. 103, no. 5, p. 054 904, 2021. DOI: 10.1103/PhysRevC.103.054904. arXiv: 2011.01430 [hep-ph].

[32] G. Nijs, W. van der Schee, U. Gürsoy, and R. Snellings, "Bayesian analysis of heavy ion collisions with the heavy ion computational framework Trajectum", *Phys. Rev. C*, vol. 103, no. 5, p. 054 909, 2021. DOI: 10.1103/PhysRevC.103.054909. arXiv: 2010.15134 [nucl-th].

[33] J. Auvinen, K. J. Eskola, P. Huovinen, H. Niemi, R. Paatelainen, and P. Petreczky, "Temperature dependence of η/s of strongly interacting matter: Effects of the equation of state and the parametric form of $(\eta/s)(T)$", *Phys. Rev. C*, vol. 102, no. 4, p. 044 911, 2020. DOI: 10.1103/PhysRevC.102.044911. arXiv: 2006.12499 [nucl-th].

[34] J. E. Parkkila, A. Onnerstad, and D. J. Kim, "Bayesian estimation of the specific shear and bulk viscosity of the quark-gluon plasma with additional flow harmonic observables", *Phys. Rev. C*, vol. 104, no. 5, p. 054 904, 2021. DOI: 10.1103/PhysRevC.104.054904. arXiv: 2106.05019 [hep-ph].

[35] J. E. Parkkila *et al.*, "New constraints for QCD matter from improved Bayesian parameter estimation in heavy-ion collisions at LHC", *Phys. Lett. B*, vol. 835, p. 137 485, 2022. DOI: 10.1016/j.physletb.2022.137485. arXiv: 2111.08145 [hep-ph].

[36] D. Liyanage, O. Sürer, M. Plumlee, S. M. Wild, and U. Heinz, "Bayesian calibration of viscous anisotropic hydrodynamic simulations of heavy-ion collisions", *Phys. Rev. C*, vol. 108, no. 5, p. 054 905, 2023. DOI: 10.1103/PhysRevC.108.054905. arXiv: 2302.14184 [nucl-th].

[37] M. R. Heffernan, C. Gale, S. Jeon, and J.-F. Paquet, "Bayesian quantification of strongly-interacting matter with color glass condensate initial conditions", Feb. 2023. arXiv: 2302.09478 [nucl-th].

[38] S. A. Bass *et al.*, "Microscopic models for ultrarelativistic heavy ion collisions", *Prog. Part. Nucl. Phys.*, vol. 41, pp. 255–369, 1998. DOI: 10.1016/S0146-6410(98)00058-1. arXiv: nucl-th/9803035.

[39] H. Petersen, D. Oliinychenko, M. Mayer, J. Staudenmaier, and S. Ryu, "SMASH – A new hadronic transport approach", *Nucl. Phys. A*, vol. 982, F. Antinori, A. Dainese, P. Giubellino, V. Greco, M. P. Lombardo, and E. Scomparin, Eds., pp. 399–402, 2019. DOI: 10.1016/j.nuclphysa.2018.08.008. arXiv: 1808.06832 [nucl-th].

[40] Y. Nara and A. Ohnishi, "Mean-field update in the JAM microscopic transport model: Mean-field effects on collective flow in high-energy heavy-ion collisions at sNN=2–20 GeV energies", *Phys. Rev. C*, vol. 105, no. 1, p. 014 911, 2022. DOI: 10.1103/PhysRevC.105.014911. arXiv: 2109.07594 [nucl-th].

[41] S. A. Bass and A. Dumitru, "Dynamics of hot bulk QCD matter: From the quark gluon plasma to hadronic freezeout", *Phys. Rev. C*, vol. 61, p. 064 909, 2000. DOI: 10.1103/PhysRevC.61.064909. arXiv: nucl-th/0001033.

[42] H. Petersen, J. Steinheimer, G. Burau, M. Bleicher, and H. Stöcker, "A Fully Integrated Transport Approach to Heavy Ion Reactions with an Intermediate Hydrodynamic Stage", *Phys. Rev. C*, vol. 78, p. 044 901, 2008. DOI: 10.1103/PhysRevC.78.044901. arXiv: 0806.1695 [nucl-th].

[43]   H. Song, S. A. Bass, and U. Heinz, "Viscous QCD matter in a hybrid hy-drodynamic+Boltzmann approach", *Phys. Rev. C*, vol. 83, p. 024 912, 2011. DOI: 10.1103/PhysRevC.83.024912. arXiv: 1012.0555 [nucl-th].

[44]   C. Shen, Z. Qiu, H. Song, J. Bernhard, S. Bass, and U. Heinz, "The iEBE-VISHNU code package for relativistic heavy-ion collisions", *Comput. Phys. Commun.*, vol. 199, pp. 61–85, 2016. DOI: 10.1016/j.cpc.2015.08.039. arXiv: 1409.8164 [nucl-th].

[45]   D. Oliinychenko, L.-G. Pang, H. Elfner, and V. Koch, "Microscopic study of deuteron production in PbPb collisions at $\sqrt{s} = 2.76 TeV$ via hydro-dynamics and a hadronic afterburner", *Phys. Rev. C*, vol. 99, no. 4, p. 044 907, 2019. DOI: 10.1103/PhysRevC.99.044907. arXiv: 1809.03071 [hep-ph].

[46]   ALICE Collaboration, "The ALICE experiment – A journey through QCD", Nov. 2022. arXiv: 2211.04384 [nucl-ex].

[47]   B. Abelev *et al.*, "Centrality determination of Pb-Pb collisions at $\sqrt{s_{NN}} = $ 2.76 TeV with ALICE", *Phys. Rev. C*, vol. 88, no. 4, p. 044 909, 2013. DOI: 10.1103/PhysRevC.88.044909. arXiv: 1301.4361 [nucl-ex].

[48]   ALICE Collaboration, "Centrality determination in heavy ion collisions", *ALICE-PUBLIC-2018-011*, 2018. [Online]. Available: https://cds.cern.ch/record/2636623.

[49]   N. Borghini, P. M. Dinh, and J.-Y. Ollitrault, "Flow analysis from multipar-ticle azimuthal correlations", *Phys. Rev. C*, vol. 64, p. 054 901, 2001. DOI: 10.1103/PhysRevC.64.054901. arXiv: nucl-th/0105040.

[50]   M. Luzum and J.-Y. Ollitrault, "Eliminating experimental bias in anisotropic-flow measurements of high-energy nuclear collisions", *Phys. Rev. C*, vol. 87, no. 4, p. 044 907, 2013. DOI: 10.1103/PhysRevC.87.044907. arXiv: 1209.2323 [nucl-ex].

[51]   M. Luzum and H. Petersen, "Initial State Fluctuations and Final State Correlations in Relativistic Heavy-Ion Collisions", *J. Phys. G*, vol. 41, p. 063 102, 2014. DOI: 10.1088/0954-3899/41/6/063102. arXiv: 1312.5503 [nucl-th].

[52]   A. Bilandzic, C. H. Christensen, K. Gulbrandsen, A. Hansen, and Y. Zhou, "Generic framework for anisotropic flow analyses with multiparticle az-imuthal correlations", *Phys. Rev. C*, vol. 89, no. 6, p. 064 904, 2014. DOI: 10.1103/PhysRevC.89.064904. arXiv: 1312.3572 [nucl-ex].

[53]   S. Acharya *et al.*, "Measurements of mixed harmonic cumulants in Pb–Pb collisions at $\sqrt{s_{NN}} = $ 5.02 TeV", *Phys. Lett. B*, vol. 818, p. 136 354, 2021. DOI: 10.1016/j.physletb.2021.136354. arXiv: 2102.12180 [nucl-ex].

[54]   S. Acharya *et al.*, "Higher-order correlations between different moments of two flow amplitudes in Pb-Pb collisions at sNN=5.02 TeV", *Phys. Rev. C*, vol. 108, no. 5, p. 055 203, 2023. DOI: 10.1103/PhysRevC.108.055203. arXiv: 2303.13414 [nucl-ex].

[55] Z. Moravcova, K. Gulbrandsen, and Y. Zhou, "Generic algorithm for multiparticle cumulants of azimuthal correlations in high energy nucleus collisions", *Phys. Rev. C*, vol. 103, no. 2, p. 024 913, 2021. DOI: 10.1103/PhysRevC.103.024913. arXiv: 2005.07974 `[nucl-th]`.

[56] G. Giacalone, B. Schenke, and C. Shen, "Observable signatures of initial state momentum anisotropies in nuclear collisions", *Phys. Rev. Lett.*, vol. 125, no. 19, p. 192 301, 2020. DOI: 10.1103/PhysRevLett.125.192301. arXiv: 2006.15721 `[nucl-th]`.

[57] P. Bozek, "Transverse-momentum–flow correlations in relativistic heavy-ion collisions", *Phys. Rev. C*, vol. 93, no. 4, p. 044 908, 2016. DOI: 10.1103/PhysRevC.93.044908. arXiv: 1601.04513 `[nucl-th]`.

[58] B. Schenke, C. Shen, and D. Teaney, "Transverse momentum fluctuations and their correlation with elliptic flow in nuclear collision", *Phys. Rev. C*, vol. 102, no. 3, p. 034 905, 2020. DOI: 10.1103/PhysRevC.102.034905. arXiv: 2004.00690 `[nucl-th]`.

[59] J. D. Bjorken, "Highly relativistic nucleus-nucleus collisions: The central rapidity region", *Phys. Rev. D*, vol. 27, pp. 140–151, 1 Jan. 1983. DOI: 10.1103/PhysRevD.27.140. [Online]. Available: https://link.aps.org/doi/10.1103/PhysRevD.27.140.

[60] L. D. Landau, "On the multiparticle production in high-energy collisions", *Izv. Akad. Nauk Ser. Fiz.*, vol. 17, pp. 51–64, 1953.

[61] P. B. Arnold, G. D. Moore, and L. G. Yaffe, "Effective kinetic theory for high temperature gauge theories", *JHEP*, vol. 01, p. 030, 2003. DOI: 10.1088/1126-6708/2003/01/030. arXiv: hep-ph/0209353.

[62] Z. Xu and C. Greiner, "Transport rates and momentum isotropization of gluon matter in ultrarelativistic heavy-ion collisions", *Phys. Rev. C*, vol. 76, p. 024 911, 2007. DOI: 10.1103/PhysRevC.76.024911. arXiv: hep-ph/0703233.

[63] A. Kurkela, A. Mazeliauskas, J.-F. Paquet, S. Schlichting, and D. Teaney, "Matching the Nonequilibrium Initial Stage of Heavy Ion Collisions to Hydrodynamics with QCD Kinetic Theory", *Phys. Rev. Lett.*, vol. 122, no. 12, p. 122 302, 2019. DOI: 10.1103/PhysRevLett.122.122302. arXiv: 1805.01604 `[hep-ph]`.

[64] J. Berges, M. P. Heller, A. Mazeliauskas, and R. Venugopalan, "QCD thermalization: Ab initio approaches and interdisciplinary connections", *Rev. Mod. Phys.*, vol. 93, no. 3, p. 035 003, 2021. DOI: 10.1103/RevModPhys.93.035003. arXiv: 2005.12299 `[hep-th]`.

[65] A. Kurkela, R. Törnkvist, and K. Zapp, "AMY Lorentz invariant parton cascade – the thermal equilibrium case", *Eur. Phys. J. C*, vol. 84, no. 1, p. 74, 2024. DOI: 10.1140/epjc/s10052-024-12424-2. arXiv: 2211.15454 `[hep-ph]`.

[66] S. Schlichting and P. Tribedy, "Collectivity in Small Collision Systems: An Initial-State Perspective", *Adv. High Energy Phys.*, vol. 2016, p. 8 460 349, 2016. DOI: 10.1155/2016/8460349. arXiv: 1611.00329 `[hep-ph]`.

[67] C. Shen, J.-F. Paquet, G. S. Denicol, S. Jeon, and C. Gale, "Collectivity and electromagnetic radiation in small systems", *Phys. Rev. C*, vol. 95, no. 1, p. 014 906, 2017. DOI: 10.1103 / PhysRevC.95.014906. arXiv: 1609.02590 `[nucl-th]`.

[68] J. Jia, M. Zhou, and A. Trzupek, "Revealing long-range multiparticle collectivity in small collision systems via subevent cumulants", *Phys. Rev. C*, vol. 96, no. 3, p. 034 906, 2017. DOI: 10.1103/PhysRevC.96.034906. arXiv: 1701.03830 `[nucl-th]`.

[69] J. L. Nagle and W. A. Zajc, "Small System Collectivity in Relativistic Hadronic and Nuclear Collisions", *Ann. Rev. Nucl. Part. Sci.*, vol. 68, pp. 211–235, 2018. DOI: 10.1146 / annurev - nucl - 101916 - 123209. arXiv: 1801.03477 `[nucl-ex]`.

[70] C. Eckart, "The thermodynamics of irreversible processes. iii. relativistic theory of the simple fluid", *Phys. Rev.*, vol. 58, pp. 919–924, 10 Nov. 1940. DOI: 10.1103/PhysRev.58.919. [Online]. Available: https://link.aps.org/doi/10.1103/PhysRev.58.919.

[71] L. D. Landau and E. M. Lifshitz, *Fluid Mechanics*, Second Edition. Pergamon, 1987, vol. 6.

[72] W. A. Hiscock and L. Lindblom, "Generic instabilities in first-order dissipative relativistic fluid theories", *Phys. Rev. D*, vol. 31, pp. 725–733, 4 Feb. 1985. DOI: 10.1103 / PhysRevD.31.725. [Online]. Available: https://link.aps.org/doi/10.1103/PhysRevD.31.725.

[73] F. S. Bemfica, M. M. Disconzi, and J. Noronha, "First-Order General-Relativistic Viscous Fluid Dynamics", *Phys. Rev. X*, vol. 12, no. 2, p. 021 044, 2022. DOI: 10.1103 / PhysRevX.12.021044. arXiv: 2009.11388 `[gr-qc]`.

[74] W. Israel, "Nonstationary irreversible thermodynamics: A Causal relativistic theory", *Annals Phys.*, vol. 100, pp. 310–331, 1976. DOI: 10.1016/0003-4916(76)90064-6.

[75] W. Israel and J. M. Stewart, "Thermodynamics of nonstationary and transient effects in a relativistic gas", *Phys. Lett. A*, vol. 58, no. 4, pp. 213–215, 1976. DOI: 10.1016/0375-9601(76)90075-X.

[76] W. Israel, J. M. Stewart, and S. W. Hawking, "On transient relativistic thermodynamics and kinetic theory. il", *Proceedings of the Royal Society of London. A. Mathematical and Physical Sciences*, vol. 365, no. 1720, pp. 43–52, 1979. DOI: 10.1098 / rspa.1979.0005. eprint: https://royalsocietypublishing.org/doi/pdf/10.1098/rspa.1979.0005. [Online]. Available: https://royalsocietypublishing.org/doi/abs/10.1098/rspa.1979.0005.

[77] J. M. Stewart and S. W. Hawking, "On transient relativistic thermodynamics and kinetic theory", *Proceedings of the Royal Society of London. A. Mathematical and Physical Sciences*, vol. 357, no. 1688, pp. 59–75, 1977. DOI: 10.1098/rspa.1977.0155. eprint: https://royalsocietypublishing.org/doi/pdf/10.1098/rspa.1977.0155. [Online]. Available: https://royalsocietypublishing.org/doi/abs/10.1098/rspa.1977.0155.

[78] W. Israel and J. M. Stewart, "Transient relativistic thermodynamics and kinetic theory", *Annals Phys.*, vol. 118, pp. 341–372, 1979. DOI: 10.1016/0003-4916(79)90130-1.

[79] D. Molnar and P. Huovinen, "Dissipation and elliptic flow at RHIC", *Phys. Rev. Lett.*, vol. 94, p. 012302, 2005. DOI: 10.1103/PhysRevLett.94.012302. arXiv: nucl-th/0404065.

[80] P. Huovinen and D. Molnar, "The Applicability of causal dissipative hydrodynamics to relativistic heavy ion collisions", *Phys. Rev. C*, vol. 79, p. 014906, 2009. DOI: 10.1103/PhysRevC.79.014906. arXiv: 0808.0953 [nucl-th].

[81] A. Kurkela and Y. Zhu, "Isotropization and hydrodynamization in weakly coupled heavy-ion collisions", *Phys. Rev. Lett.*, vol. 115, no. 18, p. 182301, 2015. DOI: 10.1103/PhysRevLett.115.182301. arXiv: 1506.06647 [hep-ph].

[82] K. Gallmeister, H. Niemi, C. Greiner, and D. H. Rischke, "Exploring the applicability of dissipative fluid dynamics to small systems by comparison to the Boltzmann equation", *Phys. Rev. C*, vol. 98, no. 2, p. 024912, 2018. DOI: 10.1103/PhysRevC.98.024912. arXiv: 1804.09512 [nucl-th].

[83] I. Bouras *et al.*, "Investigation of shock waves in the relativistic Riemann problem: A Comparison of viscous fluid dynamics to kinetic theory", *Phys. Rev. C*, vol. 82, p. 024910, 2010. DOI: 10.1103/PhysRevC.82.024910. arXiv: 1006.0387 [hep-ph].

[84] G. S. Denicol, T. Koide, and D. H. Rischke, "Dissipative relativistic fluid dynamics: a new way to derive the equations of motion from kinetic theory", *Phys. Rev. Lett.*, vol. 105, p. 162501, 2010. DOI: 10.1103/PhysRevLett.105.162501. arXiv: 1004.5013 [nucl-th].

[85] G. S. Denicol, H. Niemi, E. Molnar, and D. H. Rischke, "Derivation of transient relativistic fluid dynamics from the Boltzmann equation", *Phys. Rev. D*, vol. 85, p. 114047, 2012, [Erratum: Phys.Rev.D 91, 039902 (2015)]. DOI: 10.1103/PhysRevD.85.114047. arXiv: 1202.4551 [nucl-th].

[86] G. S. Denicol, E. Molnár, H. Niemi, and D. H. Rischke, "Derivation of fluid dynamics from kinetic theory with the 14-moment approximation", *Eur. Phys. J. A*, vol. 48, p. 170, 2012. DOI: 10.1140/epja/i2012-12170-x. arXiv: 1206.1554 [nucl-th].

[87] E. Molnár, H. Niemi, G. S. Denicol, and D. H. Rischke, "Relative importance of second-order terms in relativistic dissipative fluid dynamics", *Phys. Rev. D*, vol. 89, no. 7, p. 074 010, 2014. DOI: 10.1103/PhysRevD.89.074010. arXiv: 1308.0785 `[nucl-th]`.

[88] G. S. Denicol and H. Niemi, "Derivation of transient relativistic fluid dynamics from the Boltzmann equation for a multi-component system", *Nucl. Phys. A*, vol. 904-905, T. Ullrich, B. Wyslouch, and J. W. Harris, Eds., pp. 369c–372c, 2013. DOI: 10.1016/j.nuclphysa.2013.02.026. arXiv: 1212.1473 `[nucl-th]`.

[89] J. A. Fotakis, E. Molnár, H. Niemi, C. Greiner, and D. H. Rischke, "Multicomponent relativistic dissipative fluid dynamics from the Boltzmann equation", *Phys. Rev. D*, vol. 106, no. 3, p. 036 009, 2022. DOI: 10.1103/PhysRevD.106.036009. arXiv: 2203.11549 `[nucl-th]`.

[90] G. S. Denicol, J. Noronha, H. Niemi, and D. H. Rischke, "Origin of the Relaxation Time in Dissipative Fluid Dynamics", *Phys. Rev. D*, vol. 83, p. 074 019, 2011. DOI: 10.1103/PhysRevD.83.074019. arXiv: 1102.4780 `[hep-th]`.

[91] S. R. De Groot, *Relativistic Kinetic Theory. Principles and Applications*, W. A. Van Leeuwen and C. G. Van Weert, Eds. 1980.

[92] W. A. Hiscock and L. Lindblom, "Stability and causality in dissipative relativistic fluids", *Annals Phys.*, vol. 151, pp. 466–496, 1983. DOI: 10.1016/0003-4916(83)90288-9.

[93] W. A. Hiscock and L. Lindblom, "Generic instabilities in first-order dissipative relativistic fluid theories", *Phys. Rev. D*, vol. 31, pp. 725–733, 1985. DOI: 10.1103/PhysRevD.31.725.

[94] W. A. Hiscock and L. Lindblom, "Linear plane waves in dissipative relativistic fluids", *Phys. Rev. D*, vol. 35, pp. 3723–3732, 1987. DOI: 10.1103/PhysRevD.35.3723.

[95] G. S. Denicol *et al.*, "Solving the heat-flow problem with transient relativistic fluid dynamics", *Phys. Rev. D*, vol. 89, no. 7, p. 074 005, 2014. DOI: 10.1103/PhysRevD.89.074005. arXiv: 1207.6811 `[nucl-th]`.

[96] G. S. Denicol, S. Jeon, and C. Gale, "Transport Coefficients of Bulk Viscous Pressure in the 14-moment approximation", *Phys. Rev. C*, vol. 90, no. 2, p. 024 912, 2014. DOI: 10.1103/PhysRevC.90.024912. arXiv: 1403.0962 `[nucl-th]`.

[97] G. S. Rocha and G. S. Denicol, "Transport coefficients of transient hydrodynamics for the hadron-resonance gas and thermal-mass quasiparticle models", *Phys. Rev. D*, vol. 109, no. 9, p. 096 011, 2024. DOI: 10.1103/PhysRevD.109.096011. arXiv: 2402.06996 `[nucl-th]`.

[98] G. Nijs and W. van der Schee, "A generalized hydrodynamizing initial stage for Heavy Ion Collisions", Apr. 2023. arXiv: 2304.06191 `[nucl-th]`.

86

[99] J. Engels, J. Fingberg, F. Karsch, D. Miller, and M. Weber, "Nonperturbative thermodynamics of SU(N) gauge theories", *Phys. Lett. B*, vol. 252, pp. 625–630, 1990. DOI: 10.1016/0370-2693(90)90496-S.

[100] G. Boyd *et al.*, "Equation of state for the SU(3) gauge theory", *Phys. Rev. Lett.*, vol. 75, pp. 4169–4172, 1995. DOI: 10.1103/PhysRevLett.75.4169. arXiv: hep-lat/9506025.

[101] G. Boyd *et al.*, "Thermodynamics of SU(3) lattice gauge theory", *Nucl. Phys. B*, vol. 469, pp. 419–444, 1996. DOI: 10.1016/0550-3213(96)00170-8. arXiv: hep-lat/9602007.

[102] G. Pan and Z. Y. Meng, "Sign Problem in Quantum Monte Carlo Simulation", Apr. 2022. DOI: 10.1016/B978-0-323-90800-9.00095-0. arXiv: 2204.08777 [cond-mat.str-el].

[103] C. R. Allton *et al.*, "Thermodynamics of two flavor QCD to sixth order in quark chemical potential", *Phys. Rev. D*, vol. 71, p. 054508, 2005. DOI: 10.1103/PhysRevD.71.054508. arXiv: hep-lat/0501030.

[104] R. V. Gavai and S. Gupta, "QCD at finite chemical potential with six time slices", *Phys. Rev. D*, vol. 78, p. 114503, 2008. DOI: 10.1103/PhysRevD.78.114503. arXiv: 0806.2233 [hep-lat].

[105] P. de Forcrand and O. Philipsen, "The QCD phase diagram for small densities from imaginary chemical potential", *Nucl. Phys. B*, vol. 642, pp. 290–306, 2002. DOI: 10.1016/S0550-3213(02)00626-0. arXiv: hep-lat/0205016.

[106] M. D'Elia and M.-P. Lombardo, "Finite density QCD via imaginary chemical potential", *Phys. Rev. D*, vol. 67, p. 014505, 2003. DOI: 10.1103/PhysRevD.67.014505. arXiv: hep-lat/0209146.

[107] P. Huovinen and P. Petreczky, "QCD Equation of State and Hadron Resonance Gas", *Nucl. Phys. A*, vol. 837, pp. 26–53, 2010. DOI: 10.1016/j.nuclphysa.2010.02.015. arXiv: 0912.2541 [hep-ph].

[108] P. Kovtun, D. T. Son, and A. O. Starinets, "Viscosity in strongly interacting quantum field theories from black hole physics", *Phys. Rev. Lett.*, vol. 94, p. 111601, 2005. DOI: 10.1103/PhysRevLett.94.111601. arXiv: hep-th/0405231.

[109] M. Prakash, M. Prakash, R. Venugopalan, and G. Welke, "Nonequilibrium properties of hadronic mixtures", *Phys. Rept.*, vol. 227, pp. 321–366, 1993. DOI: 10.1016/0370-1573(93)90092-R.

[110] L. P. Csernai, J. I. Kapusta, and L. D. McLerran, "On the Strongly-Interacting Low-Viscosity Matter Created in Relativistic Nuclear Collisions", *Phys. Rev. Lett.*, vol. 97, p. 152303, 2006. DOI: 10.1103/PhysRevLett.97.152303. arXiv: nucl-th/0604032.

[111] J. B. Rose, J. M. Torres-Rincon, A. Schäfer, D. R. Oliinychenko, and H. Petersen, "Shear viscosity of a hadron gas and influence of resonance lifetimes on relaxation time", *Phys. Rev. C*, vol. 97, no. 5, p. 055204, 2018. DOI: 10.1103/PhysRevC.97.055204. arXiv: 1709.03826 [nucl-th].

[112] M. Byres, S. H. Lim, C. McGinn, J. Ouellette, and J. L. Nagle, "Bulk viscosity and cavitation in heavy ion collisions", *Phys. Rev. C*, vol. 101, no. 4, p. 044 902, 2020. DOI: 10.1103 / PhysRevC.101.044902. arXiv: 1910.12930 `[nucl-th]`.

[113] R. Krupczak *et al.*, "Causality violations in simulations of large and small heavy-ion collisions", *Phys. Rev. C*, vol. 109, no. 3, p. 034 908, 2024. DOI: 10.1103/PhysRevC.109.034908. arXiv: 2311.02210 `[nucl-th]`.

[114] J. S. Moreland, J. E. Bernhard, and S. A. Bass, "Alternative ansatz to wounded nucleon and binary collision scaling in high-energy nuclear collisions", *Phys. Rev. C*, vol. 92, no. 1, p. 011 901, 2015. DOI: 10.1103/PhysRevC.92.011901. arXiv: 1412.4708 `[nucl-th]`.

[115] B. Schenke, S. Jeon, and C. Gale, "(3+1)D hydrodynamic simulation of relativistic heavy-ion collisions", *Phys. Rev. C*, vol. 82, p. 014 903, 2010. DOI: 10.1103/PhysRevC.82.014903. arXiv: 1004.1408 `[hep-ph]`.

[116] B. Schenke, P. Tribedy, and R. Venugopalan, "Fluctuating Glasma initial conditions and flow in heavy ion collisions", *Phys. Rev. Lett.*, vol. 108, p. 252 301, 2012. DOI: 10.1103/PhysRevLett.108.252301. arXiv: 1202.6646 `[nucl-th]`.

[117] K. J. Eskola, K. Kajantie, P. V. Ruuskanen, and K. Tuominen, "Scaling of transverse energies and multiplicities with atomic number and energy in ultrarelativistic nuclear collisions", *Nucl. Phys. B*, vol. 570, pp. 379–389, 2000. DOI: 10.1016/S0550-3213(99)00720-8. arXiv: hep-ph/9909456.

[118] R. Paatelainen, K. J. Eskola, H. Holopainen, and K. Tuominen, "Multiplicities and p_T spectra in ultrarelativistic heavy ion collisions from a next-to-leading order improved perturbative QCD + saturation + hydrodynamics model", *Phys. Rev. C*, vol. 87, no. 4, p. 044 904, 2013. DOI: 10.1103 / PhysRevC.87.044904. arXiv: 1211.0461 `[hep-ph]`.

[119] R. Paatelainen, K. J. Eskola, H. Niemi, and K. Tuominen, "Fluid dynamics with saturated minijet initial conditions in ultrarelativistic heavy-ion collisions", *Phys. Lett. B*, vol. 731, pp. 126–130, 2014. DOI: 10.1016/j.physletb.2014.02.018. arXiv: 1310.3105 `[hep-ph]`.

[120] T. Pierog and K. Werner, "EPOS Model and Ultra High Energy Cosmic Rays", *Nucl. Phys. B Proc. Suppl.*, vol. 196, J.-N. Capdevielle, R. Engel, and B. Pattison, Eds., pp. 102–105, 2009. DOI: 10.1016/j.nuclphysbps.2009.09.017. arXiv: 0905.1198 `[hep-ph]`.

[121] K. Werner, "Revealing a deep connection between factorization and saturation: New insight into modeling high-energy proton-proton and nucleus-nucleus scattering in the EPOS4 framework", *Phys. Rev. C*, vol. 108, no. 6, p. 064 903, 2023. DOI: 10.1103/PhysRevC.108.064903. arXiv: 2301.12517 `[hep-ph]`.

88

[122] L.-G. Pang, G.-Y. Qin, V. Roy, X.-N. Wang, and G.-L. Ma, "Longitudinal decorrelation of anisotropic flows in heavy-ion collisions at the CERN Large Hadron Collider", *Phys. Rev. C*, vol. 91, no. 4, p. 044 904, 2015. DOI: 10.1103/PhysRevC.91.044904. arXiv: 1410.8690 [nucl-th].

[123] L.-G. Pang, H. Petersen, G.-Y. Qin, V. Roy, and X.-N. Wang, "Decorrelation of anisotropic flow along the longitudinal direction", *Eur. Phys. J. A*, vol. 52, no. 4, p. 97, 2016. DOI: 10.1140/epja/i2016-16097-x. arXiv: 1511.04131 [nucl-th].

[124] Y. Kanakubo, Y. Tachibana, and T. Hirano, "Unified description of hadron yield ratios from dynamical core-corona initialization", *Phys. Rev. C*, vol. 101, no. 2, p. 024 912, 2020. DOI: 10.1103/PhysRevC.101.024912. arXiv: 1910.10556 [nucl-th].

[125] Y. Kanakubo, Y. Tachibana, and T. Hirano, "Interplay between core and corona components in high-energy nuclear collisions", *Phys. Rev. C*, vol. 105, no. 2, p. 024 905, 2022. DOI: 10.1103/PhysRevC.105.024905. arXiv: 2108.07943 [nucl-th].

[126] P. Möller, A. J. Sierk, T. Ichikawa, and H. Sagawa, "Nuclear ground-state masses and deformations: FRDM(2012)", *Atom. Data Nucl. Data Tabl.*, vol. 109-110, pp. 1–204, 2016. DOI: 10.1016/j.adt.2015.10.002. arXiv: 1508.06294 [nucl-th].

[127] K. J. Eskola, C. A. Flett, V. Guzey, T. Löytäinen, and H. Paukkunen, "Exclusive J/ψ photoproduction in ultraperipheral Pb+Pb collisions at the CERN Large Hadron Collider calculated at next-to-leading order perturbative QCD", *Phys. Rev. C*, vol. 106, no. 3, p. 035 202, 2022. DOI: 10.1103/PhysRevC.106.035202. arXiv: 2203.11613 [hep-ph].

[128] S. Chekanov *et al.*, "Exclusive electroproduction of J/psi mesons at HERA", *Nucl. Phys. B*, vol. 695, pp. 3–37, 2004. DOI: 10.1016/j.nuclphysb.2004.06.034. arXiv: hep-ex/0404008.

[129] C. A. Flett, "Exclusive Observables to NLO and Low x PDF Phenomenology at the LHC", Ph.D. dissertation, U. Liverpool (main), U. Liverpool (main), 2021.

[130] A. Aktas *et al.*, "Elastic J/psi production at HERA", *Eur. Phys. J. C*, vol. 46, pp. 585–603, 2006. DOI: 10.1140/epjc/s2006-02519-5. arXiv: hep-ex/0510016.

[131] H. Mäntysaari and B. Schenke, "Evidence of strong proton shape fluctuations from incoherent diffraction", *Phys. Rev. Lett.*, vol. 117, no. 5, p. 052 301, 2016. DOI: 10.1103/PhysRevLett.117.052301. arXiv: 1603.04349 [hep-ph].

[132] J. R. Cudell *et al.*, "Benchmarks for the forward observables at RHIC, the Tevatron Run II and the LHC", *Phys. Rev. Lett.*, vol. 89, p. 201 801, 2002. DOI: 10.1103/PhysRevLett.89.201801. arXiv: hep-ph/0206172.

[133] G. Antchev *et al.*, "First measurement of elastic, inelastic and total cross-section at $\sqrt{s}$ = 13 TeV by TOTEM and overview of cross-section data at LHC energies", *Eur. Phys. J. C*, vol. 79, no. 2, p. 103, 2019. DOI: 10.1140/epjc/s10052-019-6567-0. arXiv: 1712.06153 [hep-ex].

[134] B. Abelev *et al.*, "Measurement of the Cross Section for Electromagnetic Dissociation with Neutron Emission in Pb-Pb Collisions at $\sqrt{s_{NN}}$ = 2.76 TeV", *Phys. Rev. Lett.*, vol. 109, p. 252 302, 2012. DOI: 10.1103/PhysRevLett.109.252302. arXiv: 1203.2436 [nucl-ex].

[135] S. Acharya *et al.*, "ALICE luminosity determination for Pb−Pb collisions at $\sqrt{s_{NN}}$ = 5.02 TeV", *JINST*, vol. 19, no. 02, P02039, 2024. DOI: 10.1088/1748-0221/19/02/P02039. arXiv: 2204.10148 [nucl-ex].

[136] K. J. Eskola and K. Tuominen, "Production of transverse energy from minijets in next-to-leading order perturbative QCD", *Phys. Lett. B*, vol. 489, pp. 329–336, 2000. DOI: 10.1016/S0370-2693(00)00946-1. arXiv: hep-ph/0002008.

[137] K. J. Eskola and K. Tuominen, "Transverse energy from minijets in ultra-relativistic nuclear collisions: A Next-to-leading order analysis", *Phys. Rev. D*, vol. 63, p. 114 006, 2001. DOI: 10.1103/PhysRevD.63.114006. arXiv: hep-ph/0010319.

[138] B. I. Abelev *et al.*, "Systematic Measurements of Identified Particle Spectra in pp, d^+ Au and Au+Au Collisions from STAR", *Phys. Rev. C*, vol. 79, p. 034 909, 2009. DOI: 10.1103/PhysRevC.79.034909. arXiv: 0808.2041 [nucl-ex].

[139] S. S. Adler *et al.*, "Systematic studies of the centrality and s(NN)**(1/2) dependence of the d E(T) / d eta and d (N(ch) / d eta in heavy ion collisions at mid-rapidity", *Phys. Rev. C*, vol. 71, p. 034 908, 2005, [Erratum: Phys.Rev.C 71, 049901 (2005)]. DOI: 10.1103/PhysRevC.71.034908. arXiv: nucl-ex/0409015.

[140] K. Aamodt *et al.*, "Centrality dependence of the charged-particle multiplicity density at mid-rapidity in Pb-Pb collisions at $\sqrt{s_{NN}}$ = 2.76 TeV", *Phys. Rev. Lett.*, vol. 106, p. 032 301, 2011. DOI: 10.1103/PhysRevLett.106.032301. arXiv: 1012.1657 [nucl-ex].

[141] J. Adam *et al.*, "Centrality Dependence of the Charged-Particle Multiplicity Density at Midrapidity in Pb-Pb Collisions at $\sqrt{s_{NN}}$ = 5.02 TeV", *Phys. Rev. Lett.*, vol. 116, no. 22, p. 222 302, 2016. DOI: 10.1103/PhysRevLett.116.222302. arXiv: 1512.06104 [nucl-ex].

[142] S. Acharya *et al.*, "Centrality and pseudorapidity dependence of the charged-particle multiplicity density in Xe–Xe collisions at $\sqrt{s_{NN}}$ =5.44TeV", *Phys. Lett. B*, vol. 790, pp. 35–48, 2019. DOI: 10.1016/j.physletb.2018.12.048. arXiv: 1805.04432 [nucl-ex].

[143] I. Helenius, K. J. Eskola, H. Honkanen, and C. A. Salgado, "Impact-Parameter Dependent Nuclear Parton Distribution Functions: EPS09s and EKS98s and Their Applications in Nuclear Hard Processes", *JHEP*, vol. 07, p. 073, 2012. DOI: 10.1007/JHEP07(2012)073. arXiv: 1205.5359 `[hep-ph]`.

[144] F. Debbasch and W. van Leeuwen, "General relativistic boltzmann equation, i: Covariant treatment", *Physica A: Statistical Mechanics and its Applications*, vol. 388, no. 7, pp. 1079–1104, 2009, ISSN: 0378-4371. DOI: https://doi.org/10.1016/j.physa.2008.12.023. [Online]. Available: https://www.sciencedirect.com/science/article/pii/S037843710801042X.

[145] B. B. Back *et al.*, "The Significance of the fragmentation region in ultrarelativistic heavy ion collisions", *Phys. Rev. Lett.*, vol. 91, p. 052 303, 2003. DOI: 10.1103/PhysRevLett.91.052303. arXiv: nucl-ex/0210015.

[146] E. Abbas *et al.*, "Centrality dependence of the pseudorapidity density distribution for charged particles in Pb-Pb collisions at $\sqrt{s_{\mathrm{NN}}}$ = 2.76 TeV", *Phys. Lett. B*, vol. 726, pp. 610–622, 2013. DOI: 10.1016/j.physletb.2013.09.022. arXiv: 1304.0347 `[nucl-ex]`.

[147] J. Adam *et al.*, "Centrality dependence of the pseudorapidity density distribution for charged particles in Pb-Pb collisions at $\sqrt{s_{\mathrm{NN}}}$ = 5.02 TeV", *Phys. Lett. B*, vol. 772, pp. 567–577, 2017. DOI: 10.1016/j.physletb.2017.07.017. arXiv: 1612.08966 `[nucl-ex]`.

[148] H. Bebie, P. Gerber, J. L. Goity, and H. Leutwyler, "The Role of the entropy in an expanding hadronic gas", *Nucl. Phys. B*, vol. 378, pp. 95–128, 1992. DOI: 10.1016/0550-3213(92)90005-V.

[149] T. Hirano and K. Tsuda, "Collective flow and two pion correlations from a relativistic hydrodynamic model with early chemical freezeout", *Phys. Rev. C*, vol. 66, p. 054 905, 2002. DOI: 10.1103/PhysRevC.66.054905. arXiv: nucl-th/0205043.

[150] P. Huovinen, "Chemical freeze-out temperature in hydrodynamical description of Au+Au collisions at s(NN)**(1/2) = 200-GeV", *Eur. Phys. J. A*, vol. 37, pp. 121–128, 2008. DOI: 10.1140/epja/i2007-10611-3. arXiv: 0710.4379 `[nucl-th]`.

[151] B. Abelev *et al.*, "Centrality dependence of π, K, p production in Pb-Pb collisions at $\sqrt{s_{NN}}$ = 2.76 TeV", *Phys. Rev. C*, vol. 88, p. 044 910, 2013. DOI: 10.1103/PhysRevC.88.044910. arXiv: 1303.0737 `[hep-ex]`.

[152] S. S. Adler *et al.*, "Identified charged particle spectra and yields in Au+Au collisions at S(NN)**1/2 = 200-GeV", *Phys. Rev. C*, vol. 69, p. 034 909, 2004. DOI: 10.1103/PhysRevC.69.034909. arXiv: nucl-ex/0307022.

[153] A. Wiranata, M. Prakash, P. Huovinen, V. Koch, and X. N. Wang, "The η/s of hadrons out of chemical equilibrium", *J. Phys. Conf. Ser.*, vol. 535, p. 012 017, 2014. DOI: 10.1088/1742-6596/535/1/012017.

[154] P. Huovinen and H. Petersen, "Particlization in hybrid models", *Eur. Phys. J. A*, vol. 48, p. 171, 2012. DOI: 10.1140/epja/i2012-12171-9. arXiv: 1206.3371 [nucl-th].

[155] F. Cooper and G. Frye, "Comment on the Single Particle Distribution in the Hydrodynamic and Statistical Thermodynamic Models of Multiparticle Production", *Phys. Rev. D*, vol. 10, p. 186, 1974. DOI: 10.1103/PhysRevD.10.186.

[156] A. Monnai and T. Hirano, "Effects of Bulk Viscosity at Freezeout", *Phys. Rev. C*, vol. 80, p. 054906, 2009. DOI: 10.1103/PhysRevC.80.054906. arXiv: 0903.4436 [nucl-th].

[157] D. Molnar and Z. Wolff, "Self-consistent conversion of a viscous fluid to particles", *Phys. Rev. C*, vol. 95, no. 2, p. 024903, 2017. DOI: 10.1103/PhysRevC.95.024903. arXiv: 1404.7850 [nucl-th].

[158] A. Jaiswal, R. Ryblewski, and M. Strickland, "Transport coefficients for bulk viscous evolution in the relaxation time approximation", *Phys. Rev. C*, vol. 90, no. 4, p. 044908, 2014. DOI: 10.1103/PhysRevC.90.044908. arXiv: 1407.7231 [hep-ph].

[159] M. McNelis and U. Heinz, "Modified equilibrium distributions for Cooper–Frye particlization", *Phys. Rev. C*, vol. 103, no. 6, p. 064903, 2021. DOI: 10.1103/PhysRevC.103.064903. arXiv: 2103.03401 [nucl-th].

[160] P. Bozek, "Bulk and shear viscosities of matter created in relativistic heavy-ion collisions", *Phys. Rev. C*, vol. 81, p. 034909, 2010. DOI: 10.1103/PhysRevC.81.034909. arXiv: 0911.2397 [nucl-th].

[161] K. Dusling, G. D. Moore, and D. Teaney, "Radiative energy loss and v(2) spectra for viscous hydrodynamics", *Phys. Rev. C*, vol. 81, p. 034907, 2010. DOI: 10.1103/PhysRevC.81.034907. arXiv: 0909.0754 [nucl-th].

[162] J. Sollfrank, P. Koch, and U. W. Heinz, "Is there a low p(T) 'anomaly' in the pion momentum spectra from relativistic nuclear collisions?", *Z. Phys. C*, vol. 52, pp. 593–610, 1991. DOI: 10.1007/BF01562334.

[163] H. Holopainen and P. Huovinen, "Dynamical Freeze-out in Event-by-Event Hydrodynamics", *J. Phys. Conf. Ser.*, vol. 389, R. Bellwied and C. A. Pruneau, Eds., p. 012018, 2012. DOI: 10.1088/1742-6596/389/1/012018. arXiv: 1207.7331 [hep-ph].

[164] E. Molnar, H. Holopainen, P. Huovinen, and H. Niemi, "Influence of temperature-dependent shear viscosity on elliptic flow at backward and forward rapidities in ultrarelativistic heavy-ion collisions", *Phys. Rev. C*, vol. 90, no. 4, p. 044904, 2014. DOI: 10.1103/PhysRevC.90.044904. arXiv: 1407.8152 [nucl-th].

[165] C. M. Hung and E. V. Shuryak, "Equation of state, radial flow and freeze-out in high-energy heavy ion collisions", *Phys. Rev. C*, vol. 57, pp. 1891–1906, 1998. DOI: 10.1103/PhysRevC.57.1891. arXiv: hep-ph/9709264.

[166] U. Heinz and G. Kestin, "Universal chemical freeze-out as a phase transition signature", *PoS*, vol. CPOD2006, F. Becattini, Ed., p. 038, 2006. DOI: 10.22323/1.029.0038. arXiv: nucl-th/0612105.

[167] K. J. Eskola, H. Niemi, and P. V. Ruuskanen, "Dynamical freeze-out condition in ultrarelativistic heavy ion collisions", *Phys. Rev. C*, vol. 77, p. 044 907, 2008. DOI: 10.1103/PhysRevC.77.044907. arXiv: 0710.4476 `[hep-ph]`.

[168] L. Adamczyk *et al.*, "Beam Energy Dependence of the Third Harmonic of Azimuthal Correlations in Au+Au Collisions at RHIC", *Phys. Rev. Lett.*, vol. 116, no. 11, p. 112 302, 2016. DOI: 10.1103/PhysRevLett.116.112302. arXiv: 1601.01999 `[nucl-ex]`.

[169] L. Adamczyk *et al.*, "Harmonic decomposition of three-particle azimuthal correlations at energies available at the BNL Relativistic Heavy Ion Collider", *Phys. Rev. C*, vol. 98, no. 3, p. 034 918, 2018. DOI: 10.1103/PhysRevC.98.034918. arXiv: 1701.06496 `[nucl-ex]`.

[170] S. Acharya *et al.*, "Energy dependence and fluctuations of anisotropic flow in Pb-Pb collisions at $\sqrt{s_{\mathrm{NN}}} = 5.02$ and 2.76 TeV", *JHEP*, vol. 07, p. 103, 2018. DOI: 10.1007/JHEP07(2018)103. arXiv: 1804.02944 `[nucl-ex]`.

[171] S. Acharya *et al.*, "Anisotropic flow in Xe-Xe collisions at $\sqrt{\mathbf{s}_{\mathrm{NN}}} = \mathbf{5.44}$ TeV", *Phys. Lett. B*, vol. 784, pp. 82–95, 2018. DOI: 10.1016/j.physletb.2018.06.059. arXiv: 1805.01832 `[nucl-ex]`.

[172] S. A. Bass *et al.*, "Neural networks for impact parameter determination", *J. Phys. G*, vol. 20, pp. L21–L26, 1994. DOI: 10.1088/0954-3899/20/1/004.

[173] C. David, M. Freslier, and J. Aichelin, "Impact parameter determination for heavy-ion collisions by use of a neural network", *Phys. Rev. C*, vol. 51, pp. 1453–1459, 1995. DOI: 10.1103/PhysRevC.51.1453.

[174] S. A. Bass, A. Bischoff, J. A. Maruhn, H. Stoecker, and W. Greiner, "Neural networks for impact parameter determination", *Phys. Rev. C*, vol. 53, pp. 2358–2363, 1996. DOI: 10.1103/PhysRevC.53.2358. arXiv: nucl-th/9601024.

[175] A. Andreassen, P. T. Komiske, E. M. Metodiev, B. Nachman, and J. Thaler, "OmniFold: A Method to Simultaneously Unfold All Observables", *Phys. Rev. Lett.*, vol. 124, no. 18, p. 182 001, 2020. DOI: 10.1103/PhysRevLett.124.182001. arXiv: 1911.09107 `[hep-ph]`.

[176] G. Aad *et al.*, "ATLAS b-jet identification performance and efficiency measurement with $t\bar{t}$ events in pp collisions at $\sqrt{s} = 13$ TeV", *Eur. Phys. J. C*, vol. 79, no. 11, p. 970, 2019. DOI: 10.1140/epjc/s10052-019-7450-8. arXiv: 1907.05120 `[hep-ex]`.

[177] A. M. Sirunyan *et al.*, "Identification of heavy, energetic, hadronically decaying particles using machine-learning techniques", *JINST*, vol. 15, no. 06, P06005, 2020. DOI: 10.1088/1748-0221/15/06/P06005. arXiv: 2004.08262 `[hep-ex]`.

[178] L. K. Graczykowski, M. Jakubowska, K. R. Deja, and M. Kabus, "Using machine learning for particle identification in ALICE", *JINST*, vol. 17, no. 07, p. C07016, 2022. DOI: 10.1088/1748-0221/17/07/C07016. arXiv: 2204.06900 [nucl-ex].

[179] D. J. C. MacKay, *Information Theory, Inference, and Learning Algorithms*. Copyright Cambridge University Press, 2003.

[180] J. E. Bernhard, "Bayesian parameter estimation for relativistic heavy-ion collisions", Ph.D. dissertation, Duke U., Apr. 2018. arXiv: 1804.06469 [nucl-th].

[181] D. Liyanage *et al.*, "Efficient emulation of relativistic heavy ion collisions with transfer learning", *Phys. Rev. C*, vol. 105, no. 3, p. 034 910, 2022. DOI: 10.1103/PhysRevC.105.034910. arXiv: 2201.07302 [nucl-th].

[182] Y.-L. Cheng, S. Shi, Y.-G. Ma, H. Stöcker, and K. Zhou, "Examination of nucleon distribution with Bayesian imaging for isobar collisions", *Phys. Rev. C*, vol. 107, no. 6, p. 064 909, 2023. DOI: 10.1103/PhysRevC.107.064909. arXiv: 2301.03910 [nucl-th].

[183] S. Ioffe and C. Szegedy, "Batch normalization: Accelerating deep network training by reducing internal covariate shift", 2015. arXiv: 1502.03167 [cs.LG].

[184] D. P. Kingma and J. Ba, "Adam: A Method for Stochastic Optimization", Dec. 2014. arXiv: 1412.6980 [cs.LG].

[185] X. Ying, "An overview of overfitting and its solutions", *Journal of Physics: Conference Series*, vol. 1168, p. 022 022, Feb. 2019. DOI: 10.1088/1742-6596/1168/2/022022.

[186] M. Ganaie, M. Hu, A. Malik, M. Tanveer, and P. Suganthan, "Ensemble deep learning: A review", *Engineering Applications of Artificial Intelligence*, vol. 115, p. 105 151, Oct. 2022, ISSN: 0952-1976. DOI: 10.1016/j.engappai.2022.105151. [Online]. Available: http://dx.doi.org/10.1016/j.engappai.2022.105151.

[187] G. Huang, Z. Liu, L. van der Maaten, and K. Q. Weinberger, *Densely connected convolutional networks*, 2018. arXiv: 1608.06993 [cs.CV].

[188] G. Aad *et al.*, "Measurement of flow harmonics correlations with mean transverse momentum in lead-lead and proton-lead collisions at $\sqrt{s_{NN}} = 5.02$ TeV with the ATLAS detector", *Eur. Phys. J. C*, vol. 79, no. 12, p. 985, 2019. DOI: 10.1140/epjc/s10052-019-7489-6. arXiv: 1907.05176 [nucl-ex].

[189] E. Retinskaya, M. Luzum, and J.-Y. Ollitrault, "Constraining models of initial conditions with elliptic and triangular flow data", *Phys. Rev. C*, vol. 89, no. 1, p. 014 902, 2014. DOI: 10.1103/PhysRevC.89.014902. arXiv: 1311.5339 [nucl-th].

ORIGINAL PAPERS

PI

FLOW CORRELATIONS FROM A HYDRODYNAMICS MODEL WITH DYNAMICAL FREEZE-OUT AND INITIAL CONDITIONS BASED ON PERTURBATIVE QCD AND SATURATION

by

Henry Hirvonen, Kari J. Eskola and Harri Niemi.

Flow correlations from a hydrodynamics model with dynamical freeze-out and initial conditions based on perturbative QCD and saturation

H. Hirvonen ●, K. J. Eskola ●, and H. Niemi ●

University of Jyväskylä, Department of Physics, P.O. Box 35, FI-40014 University of Jyväskylä, Finland
and Helsinki Institute of Physics, P.O. Box 64, FI-00014 University of Helsinki, Finland

We extend the applicability of the hydrodynamics, perturbative QCD and saturation -based EKRT (Eskola-Kajantie-Ruuskanen-Tuominen) framework for ultrarelativistic heavy-ion collisions to peripheral collisions by introducing dynamical freeze-out conditions. As a new ingredient compared to the previous EKRT computations we also introduce a nonzero bulk viscosity. We compute various hadronic observables and flow correlations, including normalized symmetric cumulants, mixed harmonic cumulants, and flow–transverse-momentum correlations, and compare them against measurements from the BNL Relativistic Heavy Ion Collider (RHIC) and the CERN Large Hadron Collider (LHC) . We demonstrate that the inclusion of the dynamical freeze-out and bulk viscosity allows a better description of the measured flow coefficients in peripheral collisions and enables the use of an extended centrality range when constraining the properties of QCD matter in the future.

I. INTRODUCTION

Heavy-ion collisions at ultrarelativistic energies provide the means to produce and investigate experimentally quark-gluon plasma (QGP), a strongly interacting fluid of quarks and gluons. In recent years the two main collider experiments that have investigated QGP properties are the Relativistic Heavy Ion Collider (RHIC) at Brookhaven National Laboratory (BNL), and Large Hadron Collider (LHC) at CERN. In these experiments a small, short-lived, fluid-like behaving droplet of strongly interacting matter is created at nearly zero net-baryon density. The matter properties of QGP such as its equation of state (EoS) and transport coefficients are reflected in the detailed behavior of various experimental observables; see, e.g., Refs. [1–7].

The equation of state of strongly interacting matter at zero net-baryon density is currently well known from lattice-QCD computations, and the expected transition temperature $T_c \approx$ 150–160 MeV [8–11] from hadronic matter to QGP is well within the reach of the LHC and RHIC experiments. Currently there are some experimental constraints on the equation of state [12–14], but even the lattice-QCD data allows some freedom in the EoS parametrizations [15]. The best knowledge about the transport properties of QCD matter is coming from the global fits of fluid dynamical computations to the available low-p_T data from RHIC and LHC [15–22]. Currently, at least

within the given models, the shear viscosity at temperatures near the QCD transition temperature is quite well constrained. However, the same cannot be said about the bulk viscosity. Even if the different analyses are based on very similar underlying models, the final constraints on the bulk viscosity can differ quite significantly depending on the details of the selected data and fine details of the models.

The experimental information about the collective dynamics and the spatial structure of the initial conditions is primarily encoded in the flow measurements. The most basic quantities are the Fourier components of the azimuthal hadron spectra, usually called the flow coefficients v_n. The measured flow coefficients reflect the collective fluid dynamical behavior of the system, as they are generated during the evolution of the system when the initial spatial inhomogeneities are converted into momentum-space anisotropies. In the fluid dynamical limit the driving force for this conversion is the inhomogeneous pressure gradients, and the effectiveness of the conversion is dictated by the EoS and the transport properties of QCD matter.

In the actual collisions the flow coefficients fluctuate strongly from event to event, and the fluctuations need to be explicitly considered when modeling the collisions. The presence of the flow fluctuations complicates the modeling, but at the same time they offer also a possibility to probe the initial conditions and the spacetime evolution in much greater detail. For example, the relative fluctuation spectra of the elliptic flow coefficient v_2 are practically independent of the QCD matter properties, and reflect mainly the initial density fluctuations, giving thus a way to directly constrain the initial particle production [23], at least at the LHC energies; see the discussion in Ref. [24]. Moreover, the various observables measuring the correlations between the flow coefficients react to the matter properties and initial conditions in a nontrivial

way, and offer further constraints on both of them. In particular, the correlations cannot be trivially reproduced just by reproducing the flow coefficients themselves [25].

The aim of this paper is to calculate various measurable flow-correlators by using relativistic second-order fluid dynamics with QCD-based initial conditions. The main ingredients that go into the computation are the matter properties, equation of state and transport coefficients, initial conditions for the fluid dynamical evolution given by the primary production of particles, and finally the conditions when the fluid dynamical evolution ceases and the fluid decouples into free hadrons.

The initial conditions are computed by using the perturbative QCD based EKRT (Eskola-Kajantie-Ruuskanen-Tuominen) saturation model [25,26], where the primary quantity is the minijet transverse energy computed in next-to-leading order perturbative QCD. The low-p_T production of the particles is then controlled by a saturation conjecture, detailed in Sec. II. The EKRT saturation model is the main feature that gives a predictive power to our computation. Once the framework is fixed at some collision system, e.g., in central Pb + Pb collisions at the LHC, the collision energy, centrality, and nuclear mass number dependence of hadronic observables are predictions of the model [25,27–29]

Once the initial conditions are given, the remaining inputs to the fluid dynamical computation are the matter properties. The EoS is provided by the s95p parametrization of lattice-QCD results [30], and the specific shear viscosity η/s, is parametrized such that it has a minimum around the QCD transition temperature. As a new ingredient compared to the previous EKRT computations we introduce nonzero bulk viscosity, parametrized such that it is peaked close to T_c. The main impact of bulk viscosity is to reduce the average p_T of hadrons [6]. This allows us to relax our earlier [25,27–29] rather high chemical freeze-out temperature $T_{\text{chem}} = 175$ MeV, in order to better reproduce the measured identified hadron abundances, while still reproducing the measured average transverse momentum of hadrons.

Another new feature in the computation is the dynamical condition to decouple the system into free hadrons. The earlier EKRT results were computed using a constant-temperature decoupling at $T_{\text{dec}} = 100$ MeV. It can be argued that the system decouples when the mean free path of hadrons is larger than the size of the system. The mean free path is a function of temperature, and if the system size is fixed the condition gives a constant temperature. However, the system size actually changes as function of time when the system expands, and moreover the system size varies from collision to collision: Central nuclear collisions produce a much larger system than peripheral ones. In order to account for the differences in the size of the systems, we introduce two conditions for decoupling. The global condition compares the overall size of the system to the mean free path, or here rather to the relaxation time in the second-order fluid dynamics, and the local condition that requires that the Knudsen number Kn, the ratio of microscopic and macroscopic length or time scales, is sufficiently small for the fluid dynamics to be applicable [31,32]. We note that this approach, in particular the global condition, is slightly different from

the earlier works where dynamical decoupling was developed [33,34].

The main advantage of using dynamical decoupling, besides that it is physically better motivated than the constant-temperature decoupling, is that it allows one to extend the agreement between the fluid computation and the measured flow coefficients towards peripheral nuclear collisions. In particular, the success of fluid dynamics in reproducing the flow coefficients in high-multiplicity proton-nucleus collisions [35–42] suggests that fluid dynamical models should then also describe peripheral nuclear collisions with similar hadron multiplicities.

This paper is organized in the following way: In Sec. II we shortly review the EKRT saturation model. In Sec. III we introduce the second-order fluid dynamics, and give the parametrizations of shear and bulk viscosities, and the corresponding corrections to the hadron momentum distributions. In Sec. IV we detail the dynamical freeze-out conditions, and in Sec. V we introduce the definitions of the experimental observables. The results from the computations are given in Sec. VI, where we show the new results with bulk viscosity and dynamical decoupling and compare those to the earlier predictions of the EKRT model. Finally the summary and conclusions are given in Sec. VII.

II. INITIAL CONDITIONS

The initial energy density profile is computed by using the EKRT saturation model [25,26,43,44]. It is based on the next-to-leading-order perturbative QCD (pQCD) computation of transverse energy (E_T) production, controlled by the low-p_T cutoff scale p_0 determined from the local saturation condition [44],

$$\frac{dE_T}{d^2\mathbf{r}}(T_A T_A(\mathbf{r}), p_0, \sqrt{s_{NN}}, A, \Delta y, \mathbf{b}, \beta) = \left(\frac{K_{\text{sat}}}{\pi}\right)p_0^3 \Delta y, \quad (1)$$

where Δy is the rapidity interval, $\mathbf{b}$ is the impact parameter, K_{sat} quantifies the uncertainty in the onset of saturation, and β quantifies the freedom in the NLO E_T definition with low-p_T cutoff. The solution $p_0 = p_{\text{sat}}$ of the saturation condition then inherits the $\sqrt{s_{NN}}$ and A dependence from the NLO pQCD computation of E_T, and the nuclear geometry enters through the product $T_A T_A$ of the nuclear thickness functions,

$$p_{\text{sat}} = p_{\text{sat}}(T_A T_A(\mathbf{r}), \sqrt{s_{NN}}, A, \Delta y, \mathbf{b}, K_{\text{sat}}, \beta). \quad (2)$$

The local energy density at the formation time $\tau_s = 1/p_{\text{sat}}$ can then be written using p_{sat} as

$$e(\mathbf{r}, \tau_s(\mathbf{r})) = \frac{dE_T(p_{\text{sat}})}{d^2\mathbf{r}} \frac{1}{\tau_s(\mathbf{r})\Delta y} = \frac{K_{\text{sat}}}{\pi}[p_{\text{sat}}(\mathbf{r})]^4. \quad (3)$$

At each point in the transverse plane the energy density is further evolved into a common initialization time $\tau_0 = 1/p_{\text{sat,min}} \approx 0.2$ fm by using $(0 + 1)$-dimensional Bjorken expansion, where the minimum saturation scale $p_{\text{sat,min}} = 1 \, \text{GeV}$. Below this scale the computed energy density profile is connected smoothly to the $e \propto T_A T_A$ profile. As in the earlier works, we take $\beta = 0.8$, and K_{sat} is fixed from the charged particle multiplicity measured in central

$\sqrt{s_{NN}} = 2.76$ TeV Pb + Pb collisions. For further details and explicit parametrizations of p_{sat}, see Refs. [25,27,28].

The nuclear thickness functions are computed by first randomly sampling the nucleon positions from the Woods-Saxon nucleon density profiles. The Au and Pb nuclei are taken as spherical with a radius $R = 6.38(6.7)$ fm for Au (Pb), and a thickness parameter $d = 0.55$ fm. As in Ref. [45], in the case of Xe we take into account the deformation by introducing the parameters $\beta_2 = 0.162$ and $\beta_4 = -0.003$ [46]. The Xe radius is $R = 5.49$ fm and the thickness parameter $d = 0.54$ fm.

The nuclear thickness functions are then computed by summing up the individual nucleon thickness functions,

$$T_A(\mathbf{r}) = \sum_i T_{n,i}(\mathbf{r}_i - \mathbf{r}), \qquad (4)$$

where T_n is a Gaussian with a width $\sigma = 0.43$ fm. The event-by-event fluctuations emerge from the random positions of the nuclei, and impact parameter: The fluctuating $T_A T_A$ profile leads to a fluctuating energy density profile through the $T_A T_A$ dependence of the saturation scale in Eq. (3).

A randomly sampled collision event, i.e., the nucleon positions in the nuclei and the impact parameter between the two nuclei, is accepted using a geometric criterion: We require that there is at least one pair of colliding nucleons with a transverse distance less than $\sqrt{\sigma_{NN}/\pi}$, where σ_{NN} is the inelastic nucleon-nucleon cross section. Here we take $\sigma_{NN} = 42$ mb in $\sqrt{s_{NN}} = 200$ GeV Au + Au, $\sigma_{NN} = 64$ mb in $\sqrt{s_{NN}} = 2.76$ TeV Pb + Pb, $\sigma_{NN} = 70$ mb in $\sqrt{s_{NN}} = 5.023$ TeV Pb + Pb, and $\sigma_{NN} = 72$ mb in $\sqrt{s_{NN}} = 5.44$ TeV Xe + Xe collisions. We emphasize that this criterion is only used as a condition that nuclear collision happens at all; it is not needed in the computation of the initial profile.

III. FLUID DYNAMICAL EVOLUTION AND PARTICLE SPECTRA

After the hot strongly interacting system is produced at $\tau_0 \sim 1/p_{\text{sat}}$, the subsequent spacetime evolution is computed using relativistic dissipative fluid dynamics. The basic equations of fluid dynamics are the local conservation laws of energy, momentum, and conserved charges like net-baryon number. These can be expressed in terms of the energy-momentum tensor and charge four-currents as $\partial_\mu T^{\mu\nu} = 0$ and $\partial_\mu N_i^\mu = 0$. In what follows we shall neglect the conserved charges so that it is sufficient to consider only the energy-momentum tensor. It can be decomposed with respect to the fluid four-velocity u^μ as

$$T^{\mu\nu} = e u^\mu u^\nu - P \Delta^{\mu\nu} + \pi^{\mu\nu}, \qquad (5)$$

where the fluid velocity is defined in the Landau picture, i.e., as a timelike, normalized eigenvector of the energy momentum tensor, $T_\nu^\mu u^\nu = e u^\mu$. Here $e = T^{\mu\nu} u_\mu u_\nu$ is the local energy density, $P = -\frac{1}{3} \Delta_{\mu\nu} T^{\mu\nu}$ is the isotropic pressure, and $\pi^{\mu\nu} = T^{\langle \mu\nu \rangle}$ is the shear-stress tensor. The angular brackets denote the projection operator that takes the symmetric and traceless part of the tensor that is orthogonal to the fluid velocity, i.e., $A^{\langle \mu \rangle} = \Delta^{\mu\nu} A_\nu$ and

$$A^{\langle \mu\nu \rangle} = \frac{1}{2} \left[\Delta_\alpha^\mu \Delta_\beta^\nu + \Delta_\beta^\mu \Delta_\alpha^\nu - \frac{2}{3} \Delta^{\mu\nu} \Delta_{\alpha\beta} \right] A^{\alpha\beta}, \qquad (6)$$

where $\Delta^{\mu\nu} = g^{\mu\nu} - u^\mu u^\nu$, and $g^{\mu\nu}$ is the metric tensor for which we use the $g^{\mu\nu} = \text{diag}(+, -, -, -)$ convention. The bulk viscous pressure is defined as $\Pi = P - P_0$, where P is the total isotropic pressure and P_0 is the equilibrium pressure.

The conservation laws are exact, but they do not give sufficient constraints to solve the evolution. The simplest fluid dynamical theory follows by neglecting the dissipative effects completely. In that case the system is always in a strict thermal equilibrium, entropy is conserved, and the equation of state in the form $P_0 = P_0(e)$ closes the system. The dissipation plays, however, a significant role in the evolution of the system in heavy-ion collisions, and it cannot be readily neglected. The dissipative effects are contained in the shear-stress tensor and in the bulk viscous pressure. Therefore the remaining task is to write evolution equations for them. In the formalism of Israel and Stewart [47] the equations take the form

$$\tau_\Pi \frac{d}{d\tau} \Pi + \Pi = -\zeta \theta - \delta_{\Pi\Pi} \Pi \theta + \lambda_{\Pi\pi} \pi^{\mu\nu} \sigma_{\mu\nu}, \quad (7)$$

$$\tau_\pi \frac{d}{d\tau} \pi^{\langle \mu\nu \rangle} + \pi^{\mu\nu} = 2\eta \sigma^{\mu\nu} + 2\tau_\pi \pi_\alpha^{\langle \mu} \omega^{\nu \rangle \alpha}$$
$$- \delta_{\pi\pi} \pi^{\mu\nu} \theta - \tau_{\pi\pi} \pi_\alpha^{\langle \mu} \sigma^{\nu \rangle \alpha}$$
$$+ \varphi_7 \pi_\alpha^{\langle \mu} \pi^{\nu \rangle \alpha} + \lambda_{\pi\Pi} \Pi \sigma^{\mu\nu}, \qquad (8)$$

where $\sigma^{\mu\nu} = \nabla^{\langle \mu} u^{\nu \rangle}$ is the strain-rate tensor, $\omega^{\mu\nu} = \frac{1}{2}(\nabla^\mu u^\nu - \nabla^\nu u^\mu)$ is the vorticity tensor, and $\theta = \nabla_\mu u^\mu$ is the expansion rate. The shear and bulk relaxation times are denoted by τ_π and τ_Π respectively, while first-order transport coefficients are the shear viscosity η and the bulk viscosity ζ. The coefficients of the nonlinear terms $\delta_{\Pi\Pi}, \lambda_{\Pi\pi}, \delta_{\pi\pi}, \tau_{\pi\pi}, \varphi_7, \lambda_{\pi\Pi}$ are second-order transport coefficients. Formally these equations can be derived from kinetic theory [47–54], by expanding around equilibrium and keeping terms up to the first order in gradients (or Knudsen number, a ratio of microscopic and macroscopic time/length scales, such as $\text{Kn} \sim \tau_\pi \nabla_\mu u^\mu$, [55]), second order in inverse Reynolds number $\sim \pi^{\mu\nu}/P_0$, and product of Knudsen number and inverse Reynolds number.

In this work the fluid dynamical setup is the same as in our previous works [4,5,25,27,28], i.e., we assume boost-invariant longitudinal expansion, so that it is enough to solve the equations of motion numerically in $(2 + 1)$ dimensions [56]. The second-order transport coefficients in the Israel-Stewart equations are taken from the 14-moment approximation to massless gas [48,49,51] and bulk-related coefficients are from Ref. [57], i.e.,

$$\delta_{\Pi\Pi} = \frac{2}{3} \tau_\Pi, \quad \lambda_{\Pi\pi} = \frac{8}{5} \left(\frac{1}{3} - c_s^2 \right) \tau_\Pi, \quad \delta_{\pi\pi} = \frac{4}{3} \tau_\pi$$

$$\tau_{\pi\pi} = \frac{10}{7} \tau_\pi, \quad \varphi_7 = \frac{9}{70 P_0}, \quad \lambda_{\pi\Pi} = \frac{6}{5} \tau_\pi, \qquad (9)$$

where c_s^2 is the speed of sound. The shear and bulk relaxation times are given by

$$\tau_\pi = \frac{5\eta}{e + P_0}, \quad \tau_\Pi = \left(15 \left(\frac{1}{3} - c_s^2 \right)^2 (e + P_0) \right)^{-1} \zeta. \quad (10)$$
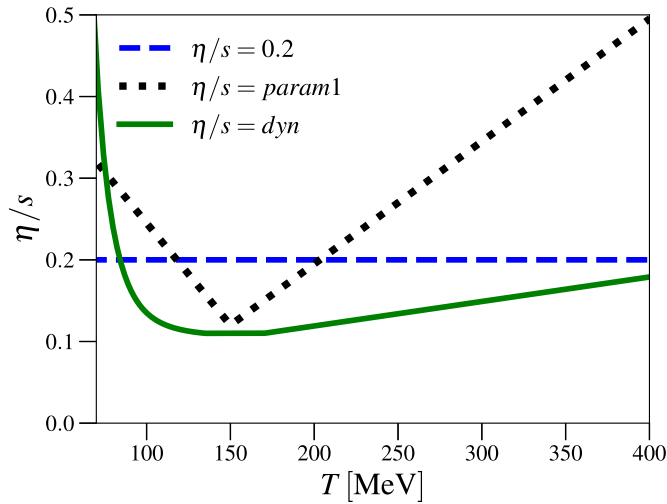
FIG. 1. Shear viscosity to entropy density ratio as a function of temperature.

FIG. 2. Bulk viscosity to entropy density ratio as a function of temperature.

The remaining input to the equations of motion are the equation of state and the temperature dependence of the shear and bulk viscosities.

The parametrizations of the shear viscosity to entropy density ratio are shown in Fig. 1, where $\eta/s = 0.20$ and $\eta/s = $ param1 are the same as implemented in earlier works [25,27,28]. The new parametrization $\eta/s = $ dyn has a similar linear QGP part as the previous parametrizations while the hadronic part follows a power law, with power P_H, reaching its minimum $(\eta/s)_{\min}$ at temperature T_H followed by a constant part with width $W_{\min}$, i.e.,

$$\eta/s(T) = \begin{cases} (\eta/s)_{\min} + S_H T\left(\left(\frac{T}{T_H}\right)^{-P_H} - 1\right), & T < T_H \\ (\eta/s)_{\min}, & T_H \leqslant T \leqslant T_Q \\ (\eta/s)_{\min} + S_Q(T - T_Q), & T > T_Q, \end{cases}$$
(11)

where S_H and S_Q are the slope parameters below T_H and above $T_Q = T_H + W_{\min}$, respectively. The bulk viscosity is included together with the new $\eta/s = $ dyn parametrization and its ratio to entropy density is plotted as a function of temperature in Fig. 2. Formally our paramaterization is written in the form

$$\zeta/s(T) = \frac{(\zeta/s)_{\max}}{1 + \left(\frac{T - T_{\max}^{\zeta/s}}{w(T)}\right)^2},$$
(12)

$$w(T) = \frac{2(\zeta/s)_{\text{width}}}{1 + \exp\left(\frac{a_{\zeta/s}(T - T_{\max}^{\zeta/s})}{(\zeta/s)_{\text{width}}}\right)},$$
(13)

where $(\zeta/s)_{\max}$, $T_{\max}^{\zeta/s}$, $(\zeta/s)_{\text{width}}$, and $a_{\zeta/s}$ are free parameters. The asymmetry parameter $a_{\zeta/s}$ describes the asymmetry of the bulk viscosity peak in such a way that $a_{\zeta/s} = 0$ gives a completely symmetric peak. For the EoS we use the s95p parametrization [30] of the lattice QCD results that includes the chemical freeze-out, implemented as effective chemical potentials in the hadronic part of the EoS [58–60]. The earlier $\eta/s = 0.20$ and $\eta/s = $ param1 parametrizations use chemical

freeze-out temperature $T_{\text{chem}} = 175$ MeV while the $\eta/s = $ dyn parametrization uses $T_{\text{chem}} = 155$ MeV.

The transverse momentum spectra of hadrons are obtained by computing the Cooper-Frye freeze-out integrals on the kinetic decoupling surface for the hadrons included in the hadronic part of the EoS. The two- and three-body decays of unstable hadrons are accounted for. For the earlier parametrizations $\eta/s = 0.20$ and $\eta/s = $ param1 the kinetic decoupling surface is set to a constant $T_{\text{dec}} = 100$ MeV temperature hypersurface while the $\eta/s = $ dyn parametrization uses dynamical criteria (see Sec. IV for details) to determine the decoupling surface. The Cornelius algorithm [61] is employed to find the decoupling surface. The viscous correction δf_i to each single-particle equilibrium momentum distribution, needed in the Cooper-Frye integrals, is implemented as in Refs. [2,62–64],

$$\delta f_i = -f_{0i}\tilde{f}_{0i}\frac{C_{\text{bulk}}}{T}\left[\frac{m^2}{3E_k} - \left(\frac{1}{3} - c_s^2\right)E_k\right]\Pi$$
$$+ \frac{f_{0i}\tilde{f}_{0i}}{2T^2(e + P_0)}\pi^{\mu\nu}k_\mu k_\nu,$$
(14)

where k^μ is the four-momentum of a given hadron, $E_k = u^\mu k_\mu$ is the energy of the hadron in the local rest frame, f_{0i} is its equilibrium distribution, and $\tilde{f}_{0i} = 1 \pm f_{0i}$, with $+ (-)$ for bosons (fermions). The coefficient C_{bulk} is determined from

$$\frac{1}{C_{\text{bulk}}} = \sum_i \frac{g_i m_i^2}{3T} \int \frac{d^3\mathbf{k}}{(2\pi)^3 k^0} f_{0i}\tilde{f}_{0i}\left[\frac{m_i^2}{3E_k} - \left(\frac{1}{3} - c_s^2\right)E_k\right].$$
(15)

Here g_i is the degeneracy factor of a given hadron species i, and the sum includes all the species in the EoS.

The fluid dynamical evolution and the transverse momentum spectra are computed for each collision event. The events are then grouped to the centrality classes according to the final charged particle multiplicities. However, if the experiments report the centrality of the collision by using the number of wounded nucleons, we can compute it by

TABLE I. Numerical values of the fit parameters used in the current study.

Initial state	
K_{sat}	0.67
Shear viscosity	
$(\eta/s)_{\text{min}}$	0.11
T_H (MeV)	135
S_H (GeV^{-1})	0.025
S_Q (GeV^{-1})	0.3
W_{min} (MeV)	35
P_{HG}	8.0
Bulk viscosity	
$(\zeta/s)_{\text{max}}$	0.09
$(\zeta/s)_{\text{width}}$ (MeV)	60
$T_{\text{max}}^{\zeta/s}$ (MeV)	240
$a_{\zeta/s}$	-0.5
Dynamical freeze-out	
C_{Kn}	0.8
C_R	0.15

using the geometric collision criterion detailed at the end of Sec. II.

Numerical values of the parameters used here for the $\eta/s =$ dyn parametrization are shown in Table I. The initial state parameter K_{sat} is tuned to produce the same charged particle multiplicity in 2.76 TeV Pb + Pb collisions as obtained in the ALICE measurements. Parameters of the shear viscosity and the dynamical freeze-out are iteratively adjusted to obtain results that match with ALICE measurements of $v_n\{2\}$ in 2.76 TeV Pb + Pb collisions. Further tuning of the hadronic part of the η/s parametrization is done to also match STAR measurements of $v_n\{2\}$ in central to mid-central 200 GeV Au + Au collisions. The chemical freeze-out temperature is adjusted together with the parameters of bulk viscosity to achieve a good simultaneous agreement of the pion average p_T and the proton multiplicity.

We note that the idea here is that bulk viscosity in hadronic evolution is mainly described by chemical freeze-out [65–67]. In chemical freeze-out the corresponding bulk relaxation time is formally infinite, or at least much longer than the evolution time of the system, and the dynamics of the bulk pressure related to the nonequilibrium chemistry in this case cannot be readily computed using Israel-Stewart type of theory that assumes that the relaxation times are smaller than the evolution timescale. Instead, the bulk viscosity that is parametrized here should be thought as the residual bulk viscosity that is not included in the partial chemical freeze-out formalism [60]. In practice, the condition that low-temperature bulk viscosity is described mainly by chemical freeze-out is set by adjusting the asymmetry parameter $a_{\zeta/s}$ in the parametrization such that bulk viscosity over entropy density becomes very small near and below the chemical freeze-out temperature.

We want to emphasize here that this is only one example parametrization which seems to give a good agreement

with the LHC and RHIC measurements. To get more detailed estimates of the parameters and their errors and correlations, a global analysis of heavy-ion observables and the parameter space is needed.

IV. DYNAMICAL FREEZE-OUT

When modeling heavy-ion collisions using hydrodynamics the kinetic freeze-out is usually set to take place at a constant-temperature hypersurface. The basic argument is that the fluid decouples into free particles when the temperature dependent mean free path of the particles becomes of the same order as the size of the system R, i.e., $\lambda_{\text{mfp}}(T) \sim R$. If the system size was a constant, this condition would give a constant freeze-out temperature. However, in reality the system size changes as a function of time, and moreover it can differ significantly from collision to collision. In particular, the systems created in central collisions are much larger than the ones created in peripheral collisions.

A typical way to solve this issue is to connect fluid dynamics to a microscopic hadronic afterburner that automatically takes care of the freeze-out. However, a drawback in this approach is that it can easily lead to unphysical discontinuities in the transport coefficients, as at typical temperatures at the switching between fluid dynamics and hadron cascade the η/s values in the fluid evolution are $\mathcal{O}(0.1)$, whereas on the hadron cascade side they are $\mathcal{O}(1)$ [68–70]. Instead of a coupling to hadron cascade, in this work we treat the whole evolution, including the hadronic phase, using fluid dynamics. This has the specific advantage that it allows us to keep all the transport coefficients continuous throughout the whole temperature range realized in the evolution.

In order to account for the nontrivial system size dependence of the freeze-out, we determine the decoupling surface dynamically [33,34] using two different conditions. The applicability of fluid dynamics requires that the local Knudsen number is sufficiently small, and fluid evolution becomes effectively free streaming when Kn $\gg$ 1. In comparisons between kinetic theory and fluid dynamics it was shown that a constant Knudsen number freeze-out in fluid dynamics catches very well the freeze-out dynamics of the kinetic evolution [32]. On the other hand, even if the local condition gives that fluid dynamics is applicable, the overall size of the system can still be small compared to the mean free path of the particles. In order to account for this kind of nonlocal freeze-out, we impose a second condition that the fluid element decouples when the mean free path is of the same order as the system size. Hence, our dynamical freeze-out setup is determined by the following two conditions:

$$\text{Kn} = \tau_\pi \theta = C_{\text{Kn}}, \tag{16}$$

$$\frac{\gamma \tau_\pi}{R} = C_R, \tag{17}$$

where $C_{\text{Kn}}, C_R = \mathcal{O}(1)$ are some proportionality constants and R is the size of the system. Here we have assumed that the mean free path is proportional to the relaxation time. The additional gamma factor in the second equation takes into account that the size of the system is calculated in the center-of-

momentum frame of the nuclear collision, while the relaxation time is calculated in the fluid rest frame. To make sure that we are not in the QGP phase when freeze-out happens, we also require that at the freeze-out surface $T < 150$ MeV. In order to use latter condition (17) we need to have some kind of estimate for the system size which, however, is not uniquely determined. In this work we define the size of the system as

$$R = \sqrt{\frac{A}{\pi}}, \tag{18}$$

where A is the area in the x, y plane in which $\mathrm{Kn} < C_{\mathrm{Kn}}$. Additionally we take into account the possibility that the system may consist of multiple separate areas of a fluid and calculate the system size for each of these regions separately. We note that our approximation of the system size is close to the maximum length that a particle must travel from the center to the edge of the system. In practice, however, most of the matter is distributed closer to the edges of the system and most of the particles are moving with the fluid also towards the edge. For this reason the actual size of the system that the particles see can be significantly smaller than R, and as a result the proportionality constant C_R can also be significantly smaller than 1.

In summary, here we have on the one hand reduced a possibly complicated nonequilibrium dynamics of the hadronic evolution in the dynamical treatment of kinetic freeze-out, and on the other hand we treat the nontrivial chemistry in the hadronic evolution as a constant-temperature chemical freeze-out. While such an approach may not catch the full microscopic details of the freeze-out dynamics, the purpose is that it would still capture its essential features. A clear advantage is, as mentioned above, that it allows us to keep the transport coefficients of the matter continuous throughout the evolution, and at the same time it also allows us to get constraints for the hadronic part of the transport coefficients. As we can see, the physical picture of the evolution is somewhat different from the typical hybrid hydro+cascade models, where the low viscosity QGP evolution is immediately followed by high-viscosity hadronic evolution. In our picture the peripheral collisions decouple practically immediately after the hadronization, but in the central collisions there can still be quite long low-viscosity evolution in the hadronic phase. This is demonstrated in Fig. 3 where the entropy-flux-weighted average freeze-out temperature is plotted as a function of centrality for the $\eta/s = \mathrm{dyn}$ parametrization introduced in Sec. III. We can also notice that the average freeze-out temperature is sensitive to the collision energy and size of the colliding nuclei.

V. FLOW COEFFICIENTS AND CORRELATORS

The fluid dynamical computation gives a single-particle transverse momentum spectrum of hadrons for each event, and its azimuthal modulation can be expressed by its p_T dependent Fourier components $v_n(p_T)$ and the phases or event-plane
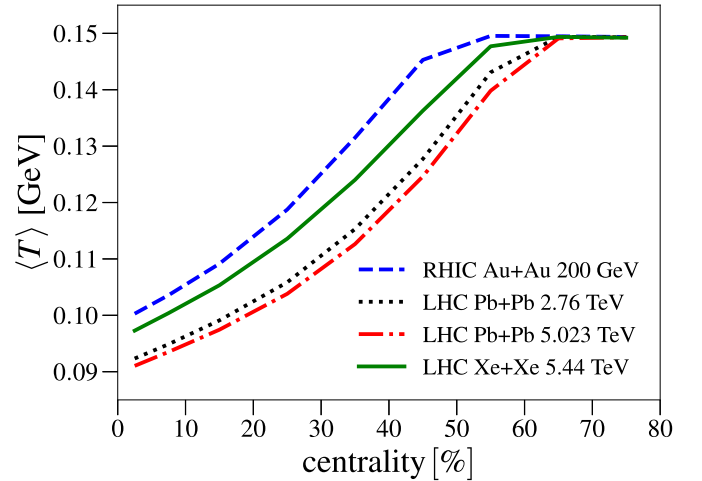
FIG. 3. Average freeze-out temperature for $\eta/s = \mathrm{dyn}$ parametrization in 200 GeV Au + Au, 2.76 TeV Pb + Pb, 5.023 TeV Pb + Pb, and 5.44 TeV Xe + Xe collisions.

angles $\Psi_n(p_T)$,

$$\frac{dN}{dy\,dp_T^2\,d\phi}$$
$$= \frac{1}{2\pi}\frac{dN}{dy\,dp_T^2}\left(1 + \sum_{n=1}^{\infty} v_n(p_T)\cos\{n[\phi - \Psi_n(p_T)]\}\right). \tag{19}$$

The flow coefficients can be expressed in a convenient way by a complex flow vector V_n as

$$V_n(p_T) = v_n(p_T)e^{in\Psi_n(p_T)} = \langle e^{in\phi}\rangle_\phi, \tag{20}$$

where the angular brackets denote an average:

$$\langle\cdots\rangle_\phi = \left(\frac{dN}{dy\,dp_T^2}\right)^{-1}\int_0^{2\pi} d\phi\,\frac{dN}{dy\,dp_T^2\,d\phi}(\cdots). \tag{21}$$

Similarly, the p_T-integrated flow coefficients can be defined as

$$V_n = v_n e^{in\Psi_n} = \langle e^{in\phi}\rangle_{\phi,p_T}, \tag{22}$$

where the average is defined as

$$\langle\cdots\rangle_{\phi,p_T} = \left(\frac{dN}{dy}\right)^{-1}\int_0^{2\pi} d\phi\int_{p_T,\min}^{p_T,\max} dp_T^2\,w\,\frac{dN}{dy\,dp_T^2\,d\phi}(\cdots), \tag{23}$$

and the p_T-integrated multiplicity $\frac{dN}{dy}$ is defined with the same p_T integration limits $p_{T,\min}$ and $p_{T,\max}$ as above. In addition it is possible to use a p_T or an energy dependent weight w in the p_T integration.

In the following we will write down the expressions of various measurable p_T-integrated quantities, but suppress the rapidity, weight, and p_T integration limits from the notation. The p_T limits will be denoted explicitly when we show our results. Unless otherwise stated, the weight function $w = 1$.

In the fluid dynamical simulations of heavy-ion collisions we are working directly with continuous particle distributions. In the experiments this is not the case, but each event is

measured as a finite number of particles. Therefore, the definitions above are not directly applicable, but the flow coefficients are rather defined through particle correlations. As an example of a two-particle correlation and its continuum limit we can write

$$\frac{1}{N_e(N_e - 1)} \sum_{\text{pairs } i \neq j} e^{in\phi_1} e^{-in\phi_2}$$

$$\longrightarrow \frac{1}{N_2} \int d\phi_1 d\phi_2 \frac{dN_2}{d\phi_1 d\phi_2} e^{in\phi_1} e^{-in\phi_2}, \quad (24)$$

where N_e is the number of hadrons in the event, and $dN_2/d\phi_1 d\phi_2$ is a two-particle distribution function that can be written as a sum of the product of the single-particle distribution functions and a direct correlation

$$\frac{dN_2}{d\phi_1 d\phi_2} = \frac{dN}{d\phi_1} \frac{dN}{d\phi_2} + \delta_2(\phi_1, \phi_2), \quad (25)$$

where the direct part emerges, e.g., due to hadron decays. It is a genuine two-particle correlation that is absent if all the correlations between the hadrons are due to the underlying collective flow. If the direct component can be neglected, the two-particle correlation above can be written in the continuum limit as

$$\frac{1}{N_2} \int d\phi_1 d\phi_2 \frac{dN}{d\phi_1} \frac{dN}{d\phi_2} e^{in\phi_1} e^{-in\phi_2} = v_n e^{in\Psi_n} v_n e^{-in\Psi_n} = v_n^2. \quad (26)$$

In this limit the two-particle correlator can be written in terms of the flow coefficient. This particular correlator is referred to as the two-particle cumulant, and its average over events gives the two-particle cumulant $v_n\{2\}$,

$$v_n\{2\} = \sqrt{\langle v_n^2 \rangle_{\text{ev}}}, \quad (27)$$

where $\langle \cdots \rangle_{\text{ev}}$ denotes the average over the events. A similar reasoning leads to a multitude of flow observables. Here we write down only the continuum limit in the absence of direct or nonflow correlations. It should be noted, however, that although the experimental procedures try to suppress the nonflow part by, e.g., requiring a rapidity gap between each pair of hadrons, it is still possible that some of the observables are still plagued by the nonflow. With the current setup we cannot address the nonflow part theoretically, but will assume that the experimental techniques remove them completely.

In a naive picture one may think that the flow coefficients are generated independently as a fluid dynamical response to the corresponding eccentricities of the initial conditions, $v_n \propto \varepsilon_n$. In practice, however, this picture holds only for the elliptic flow coefficient v_2 and to a lesser degree for v_3 [23,71], and even then the relation between v_2 and ε_2 ceases to be linear when ε_2 becomes large in noncentral collisions [25]. In general, the flow coefficients are not independent of each other, but both the correlations between the eccentricities in the initial conditions and the nonlinear fluid dynamical evolution generate correlations between them. The degree of the correlation can be measured through various observables that correlate both the magnitudes of the flow, v_n, and the event-plane angles Ψ_n [71].

A measurable way to quantify the degree of correlation between the flow coefficients is the so called symmetric cumulant [72], defined as

$$\text{SC}(n, m) = \langle v_n^2 v_m^2 \rangle_{\text{ev}, N^4} - \langle v_n^2 \rangle_{\text{ev}, N^2} \langle v_m^2 \rangle_{\text{ev}, N^2}, \quad (28)$$

where it is important to notice that the event-average is performed with powers of multiplicity as a weight, as denoted in the above equation. An advantage of this definition is that at the particle correlation level the latter term in the definition removes the direct two-particle correlations from the first term, which in turn is a four-particle correlator at the particle level. Thus the direct two-particle nonflow does not affect the symmetric cumulant. The symmetric cumulant is not a correlator in a sense that it depends not only on the degree of correlation between v_n and v_m, but also on their absolute magnitudes. On the other hand, the normalized symmetric cumulant, defined as

$$\text{NSC}(n, m) = \frac{\text{SC}(n, m)}{\langle v_n^2 \rangle_{\text{ev}, N^2} \langle v_m^2 \rangle_{\text{ev}, N^2}}, \quad (29)$$

is a measure of only the correlation. The downside of the normalized version is that the normalization can be affected by the direct two-particle nonflow contributions.

The symmetric cumulants measure only correlations involving two second-order flow coefficients. The more general mixed harmonic cumulants (MHC) were introduced in Ref. [73] to give observables that can quantify the correlations between between more than two flow coefficients with higher-order moments of v_n's. Like symmetric cumulants, mixed harmonic cumulants are also constructed in such a way that lower order correlations are removed from multiparticle correlations and the definition of MHC containing two second order flow coefficients is identical to the symmetric cumulants, i.e., $\text{MHC}(v_m^2, v_n^2) = \text{SC}(v_m^2, v_n^2)$. Mixed harmonic cumulants for six-particle correlations involving moments of v_2 and v_3 can be defined as

$$\text{MHC}(v_2^4, v_3^2) = \langle v_2^4 v_3^2 \rangle_6 - 4\langle v_2^2 v_3^2 \rangle_4 \langle v_2^2 \rangle_2$$
$$- \langle v_2^4 \rangle_4 \langle v_3^2 \rangle_2 + 4\langle v_2^2 \rangle_2^2 \langle v_3^2 \rangle_2,$$

$$\text{MHC}(v_2^2, v_3^4) = \langle v_2^2 v_3^4 \rangle_6 - 4\langle v_2^2 v_3^2 \rangle_4 \langle v_3^2 \rangle_2$$
$$- \langle v_2^2 \rangle_2 \langle v_3^4 \rangle_4 + 4\langle v_2^2 \rangle_2 \langle v_3^2 \rangle_2^2, \quad (30)$$

where $\langle \cdots \rangle_i = \langle \cdots \rangle_{\text{ev}, N^i}$. Similarly one can define mixed harmonic cumulants for eight-particle correlations between v_2 and v_3 as

$$\text{MHC}(v_2^6, v_3^2) = \langle v_2^6 v_3^2 \rangle_8 - 9\langle v_2^4 v_3^2 \rangle_6 \langle v_2^2 \rangle_2$$
$$- \langle v_2^6 \rangle_6 \langle v_3^2 \rangle_2 - 9\langle v_2^4 \rangle_4 \langle v_2^2 v_3^2 \rangle_4$$
$$- 36\langle v_2^2 \rangle_2^3 \langle v_3^2 \rangle_2 + 18\langle v_2^2 \rangle_2 \langle v_3^2 \rangle_2 \langle v_2^4 \rangle_4,$$
$$+ 36\langle v_2^2 \rangle_2^2 \langle v_2^2 v_3^2 \rangle_4,$$

$$\text{MHC}(v_2^2, v_3^6) = \langle v_2^2 v_3^6 \rangle_8 - 9\langle v_2^2 v_3^4 \rangle_6 \langle v_3^2 \rangle_2$$
$$- \langle v_2^2 \rangle_2 \langle v_3^6 \rangle_6 - 9\langle v_3^4 \rangle_4 \langle v_2^2 v_3^2 \rangle_4$$
$$- 36\langle v_2^2 \rangle_2 \langle v_3^2 \rangle_2^3 + 18\langle v_2^2 \rangle_2 \langle v_3^2 \rangle_2 \langle v_3^4 \rangle_4$$
$$+ 36\langle v_3^2 \rangle_2^2 \langle v_2^2 v_3^2 \rangle_4,$$

$$
\begin{aligned}
\mathrm{MHC}(v_2^4, v_3^4) = &\langle v_2^4 v_3^4 \rangle_8 - 4\langle v_2^4 v_3^2 \rangle_6 \langle v_3^2 \rangle_2 \\
&- 4\langle v_2^2 v_3^4 \rangle_6 \langle v_2^2 \rangle_2 - \langle v_2^4 \rangle_4 \langle v_3^4 \rangle_4 \\
&- 8\langle v_2^2 v_3^2 \rangle_4^2 - 24\langle v_2^2 \rangle_2^2 \langle v_3^2 \rangle_2^2 \\
&+ 4\langle v_2^2 \rangle_2^2 \langle v_3^4 \rangle_4 + 4\langle v_2^4 \rangle_4 \langle v_3^2 \rangle_2^2 \\
&+ 32\langle v_2^2 \rangle_2 \langle v_3^2 \rangle_2 \langle v_2^2 v_3^2 \rangle_4,
\end{aligned} \tag{31}
$$

and for six-particle correlations between v_2, v_3, and v_4 as

$$
\begin{aligned}
\mathrm{MHC}(v_2^2, v_3^2, v_4^2) = &\langle v_2^2 v_3^2 v_4^2 \rangle_6 - \langle v_2^2 v_3^2 \rangle_4 \langle v_4^2 \rangle_2 \\
&- \langle v_2^2 v_4^2 \rangle_4 \langle v_3^2 \rangle_2 - \langle v_3^2 v_4^2 \rangle_4 \langle v_2^2 \rangle_2 \\
&+ 2\langle v_2^2 \rangle_2 \langle v_3^2 \rangle_2 \langle v_4^2 \rangle_2.
\end{aligned} \tag{32}
$$

Analogously to normalized symmetric cumulants one defines normalized mixed harmonic cumulants as

$$
\mathrm{nMHC}(v_n^k, v_m^l) = \frac{\mathrm{MHC}(v_n^k, v_m^l)}{\langle v_n^k \rangle_k \langle v_m^l \rangle_l}, \tag{33}
$$

$$
\mathrm{nMHC}(v_n^k, v_m^l, v_p^q) = \frac{\mathrm{MHC}(v_n^k, v_m^l, v_p^q)}{\langle v_n^k \rangle_k \langle v_m^l \rangle_l \langle v_p^q \rangle_q}. \tag{34}
$$

A complementary observable to the symmetric cumulants, usually referred to as the event-plane correlator, is defined as [74]

$$
\begin{aligned}
&\langle \cos(k_1 \Psi_1 + \cdots + n k_n \Psi_n) \rangle_{\mathrm{SP}} \\
&= \frac{\langle v_1^{|k_1|} \cdots v_n^{|k_n|} \cos(k_1 \Psi_1 + \cdots + n k_n \Psi_n) \rangle_{\mathrm{ev}}}{\sqrt{\langle v_1^{2|k_1|} \rangle_{\mathrm{ev}} \cdots \langle v_n^{2|k_n|} \rangle_{\mathrm{ev}}}}, \quad (35)
\end{aligned}
$$

where the k_n's are integers with the property $\sum_n n k_n = 0$ so that the correlator is independent of the azimuthal orientation. Despite its name it actually measures a correlation between both the magnitudes of the flow and event-plane angle, and in this sense provides complementary information to the symmetric cumulants above.

These correlations as such provide information that is independent from the flow magnitudes themselves, and give further independent constraints to the initial conditions and transport coefficients. However, it is interesting that the event-plane correlations are closely related to the magnitude of nonlinear response to the initial conditions [75]. The basic idea in quantifying the nonlinear response is that the complex flow vector V_n is divided into a linear part $V_{n\mathrm{L}}$ that is assumed to correlate only with the corresponding initial state eccentricity ε_n, and into a nonlinear part that is independent of ε_n [71]. If we consider the simplest possible nonlinear contributions, we can write

$$
V_4 = V_{4\mathrm{L}} + \chi_{4,22}(V_2)^2, \tag{36}
$$

$$
V_5 = V_{5\mathrm{L}} + \chi_{5,23} V_2 V_3, \tag{37}
$$

$$
V_6 = V_{6\mathrm{L}} + \chi_{6,222} V_2^3 + \chi_{6,33} V_3^2 \tag{38}
$$

where χ's are the nonlinear response coefficients. Note that the nonlinear parts include only the largest flow vectors V_2 and V_3 that can also, to a reasonable approximation as discussed above, assumed to have only the linear part $V_2 = V_{2\mathrm{L}}$ and $V_3 =$

$V_{3\mathrm{L}}$. If we further assume that the linear and nonlinear parts are uncorrelated, we may express the response coefficients as

$$
\chi_{4,22} = \frac{\mathrm{Re}\langle V_4 (V_2^*)^2 \rangle_{\mathrm{ev}}}{\langle |V_2|^4 \rangle_{\mathrm{ev}}} \tag{39}
$$

$$
\chi_{5,23} = \frac{\mathrm{Re}\langle V_5 V_2^* V_3^* \rangle_{\mathrm{ev}}}{\langle |V_2|^2 |V_3|^2 \rangle_{\mathrm{ev}}} \tag{40}
$$

$$
\chi_{6,222} = \frac{\mathrm{Re}\langle V_6 (V_2^*)^3 \rangle_{\mathrm{ev}}}{\langle |V_2|^6 \rangle_{\mathrm{ev}}} \tag{41}
$$

$$
\chi_{6,33} = \frac{\mathrm{Re}\langle V_6 (V_3^*)^2 \rangle_{\mathrm{ev}}}{\langle |V_3|^4 \rangle_{\mathrm{ev}}}, \tag{42}
$$

and the linear parts of V_4 and V_5 can be written as

$$
\sqrt{\langle |V_{4\mathrm{L}}|\rangle_{\mathrm{ev}}^2} = \sqrt{(v_4\{2\})^2 - \chi_{4,22}^2 \langle |V_2|^4 \rangle_{\mathrm{ev}}}, \tag{43}
$$

$$
\sqrt{\langle |V_{5\mathrm{L}}|\rangle_{\mathrm{ev}}^2} = \sqrt{(v_5\{2\})^2 - \chi_{5,23}^2 \langle |V_2|^2 |V_3|^2 \rangle_{\mathrm{ev}}}. \tag{44}
$$

The connection between the event-plane correlators and the nonlinear response coefficients can be seen by observing, e.g., that

$$
\chi_{4,22} = \langle \cos(4[\Psi_4 - \Psi_2]) \rangle_{\mathrm{SP}} \sqrt{\frac{\langle v_4^2 \rangle_{\mathrm{ev}}}{\langle v_2^4 \rangle_{\mathrm{ev}}}}, \tag{45}
$$

so that the two measures differ by a normalization factor that depends on the magnitude of the flow, but not on correlators. A similar connection can also be made between the other χ's. A more complete list of relations can be found from Refs. [75,76].

Even though the nonlinear response coefficients and the correlations between the flow harmonics give information about the initial state eccentricities and their conversion to momentum space anisotropies, they do not directly probe the size of the initial nuclear overlap region, which is more sensitive to the average p_T fluctuations. Thus, the correlation between the flow coefficients and the average p_T is a good probe of the initial state structure [77]. This flow–transverse-momentum correlation is defined by a modified Pearson correlation coefficient [78]

$$
\rho(v_n^2, [p_T]) = \frac{\langle \hat{\delta} v_n^2 \hat{\delta}[p_T] \rangle_{\mathrm{ev}}}{\sqrt{\langle (\hat{\delta} v_n^2)^2 \rangle_{\mathrm{ev}} \langle (\hat{\delta}[p_T])^2 \rangle_{\mathrm{ev}}}}, \tag{46}
$$

where the event-by-event variance at a fixed multiplicity for some observable O is defined by

$$
\hat{\delta} O = \delta O - \frac{\langle \delta O \, \delta N \rangle_{\mathrm{ev}}}{\sigma_N} \delta N, \tag{47}
$$

$$
\delta O = O - \langle O \rangle_{\mathrm{ev}}, \quad \sigma_O^2 = \langle (\delta O)^2 \rangle_{\mathrm{ev}}. \tag{48}
$$

VI. RESULTS

In this section we present the results for hadron multiplicities, average p_T, flow coefficients, and correlations calculated from the EKRT pQCD + hydrodynamics framework with the bulk viscosity and the dynamical freeze-out, and compare these against the results from our earlier works [25,27–29] with the constant-temperature freeze-out and without the bulk
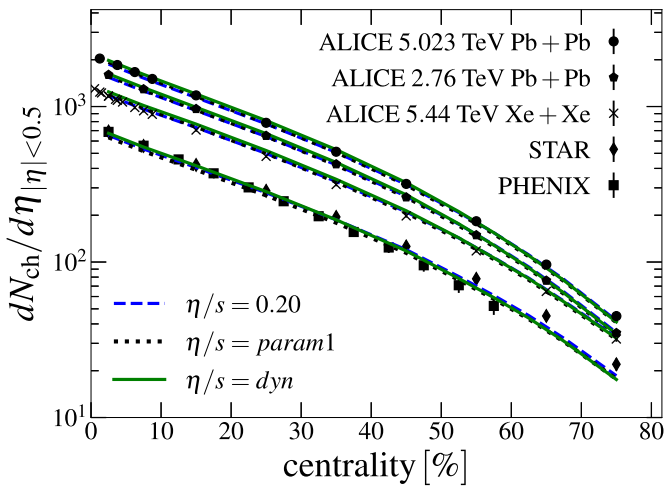
FIG. 4. Charged hadron multiplicity in 200 GeV Au + Au, 2.76 TeV Pb + Pb, 5.023 TeV Pb + Pb, and 5.44 TeV Xe + Xe collisions. The experimental data are from the ALICE [79–81], STAR [82], and PHENIX [83] Collaborations.

viscosity. The systems we show here are 200 GeV Au + Au, 2.76 TeV Pb + Pb, 5.023 TeV Pb + Pb, and 5.44 TeV Xe + Xe collisions. As explained in Sec. III, the initial conditions, the transport coefficients, and the freeze-out parameters are fixed on the basis of 200 GeV Au + Au and 2.76 TeV data from RHIC and LHC. For both Pb + Pb collision systems we run 40 000 event simulations to get better statistics for the symmetric cumulants while for other collision systems we did 20 000 event simulations. The statistical errors for different quantities are estimated, as in Ref. [76], via jackknife resampling.

A. Multiplicity, average p_T, and flow

In Fig. 4 we show the centrality dependence of charged hadron multiplicities for all the above systems compared to the STAR [82], PHENIX [83], and ALICE [79–81] data. The essential parameter that controls the multiplicity is K_{sat} in the local saturation criterion. This coefficient is fixed from the multiplicity in 0–5% 2.76 TeV Pb + Pb collisions. The centrality, $\sqrt{s_{NN}}$, and nuclear mass number dependence are predictions of the model. The value of K_{sat} depends on the chosen $\eta/s(T)$ and $\zeta/s(T)$ parametrizations due to the different entropy production with different shear and bulk viscosities. However, the final results for the multiplicities are in practice the same for all parametrizations and they agree excellently with the experimental data across all centrality classes and collision energies.

The centrality dependences of identified particle multiplicities for 200 GeV Au + Au, 2.76 TeV Pb + Pb, and 5.023 TeV Pb + Pb collisions are shown in Fig. 5 (left). All of the parametrizations manage to produce the same pion multiplicities as the ALICE and PHENIX measurements while the kaon multiplicities differ significantly from the experimental data. The ratio between the proton and pion multiplicities is mostly controlled by the chemical freeze-out temperature. Parametrizations $\eta/s = 0.2$ and $\eta/s = \text{param}1$ use $T_{chem} =$

175 MeV in order to obtain the same average p_T for pions in 2.76 TeV Pb + Pb collisions as the ALICE measurements. However this comes with the drawback that the proton multiplicities differ from the experimental data by a factor of $\sim$2. The addition of the bulk viscosity in the $\eta/s =$ dyn parametrization enables the possibility to use $T_{chem} =$ 155 MeV, which clearly improves the proton multiplicities. However, there is still some discrepancy left that is most visible in the most central collisions at the LHC.

In Fig. 5 (right) we show the average p_T of identified particles as a function of centrality for 200 GeV Au + Au, 2.76 TeV Pb + Pb, and 5.023 TeV Pb + Pb collisions. Compared to the earlier results, the $\eta/s =$ dyn parametrization improves the agreement with the experimental data across both collision systems, except for kaons at the LHC energies. In particular, the relative change of the proton $\langle p_T \rangle$ as a function of centrality is reproduced better. This improvement is not only due to the addition of the bulk viscosity but also the dynamical freeze-out plays a major part by affecting the lifetime of the fluid. The centrality dependencies of the p_T-integrated flow coefficients $v_2\{2\}$, $v_3\{2\}$, and $v_4\{2\}$ in all studied systems are shown in Fig. 6. The shear viscosity and the dynamical freeze-out parameters of the $\eta/s =$ dyn parametrization were tuned to approximately reproduce $v_2\{2\}$ in 2.76 TeV Pb + Pb collisions while also reproducing $v_2\{2\}$ in central to mid-central 200 GeV Au + Au collisions. The most essential feature of the dynamical freeze-out is that the smaller collision systems freeze out earlier in the hadronic phase. This means that there is less time for the initial state eccentricities to convert to the momentum space anisotropies in peripheral collisions. Indeed, as seen in Fig. 6, all p_T-integrated flow coefficients for the $\eta/s =$ dyn parametrization are significantly smaller in peripheral collisions than the results of the η/s parametrizations from the earlier works that used a constant-temperature decoupling surface. As can be seen from the comparison to measurements, the $\eta/s =$ dyn parametrization reproduces well the centrality dependence of all flow coefficients in all LHC collision systems and clearly improves the results from the earlier ones in peripheral collisions. The biggest discrepancy with the data and the model calculation is the 40–80% centrality range in 200 GeV Au + Au collisions. In this region especially the predictions for the flow coefficients $v_3\{2\}$ and $v_4\{2\}$ are well outside of the error bars of the measurements. There are multiple possible reasons for this. First of all, due to the lower multiplicity in the 200 GeV Au + Au collisions it is reasonable to expect significantly larger nonflow effects compared to the LHC systems. Additionally, the δf corrections to the particle spectra are much larger at RHIC than at LHC, which adds additional uncertainty to the RHIC results. Lastly, we do not include any nucleon substructure [91], initial flow, or nonzero $\pi^{\mu\nu}$ to our initial state model, and effects of these modifications are still under investigation. We note that other groups report very similar flow coefficients in peripheral RHIC collisions; see, e.g., Refs. [19,92].

The change in the magnitude of the flow coefficients is quite modest from 2.76 to 5.023 TeV Pb + Pb collisions, and a better way to quantify the change is to plot the ratio of the coefficients between the two collision energies. The ratio is also a more robust prediction from fluid dynamics and
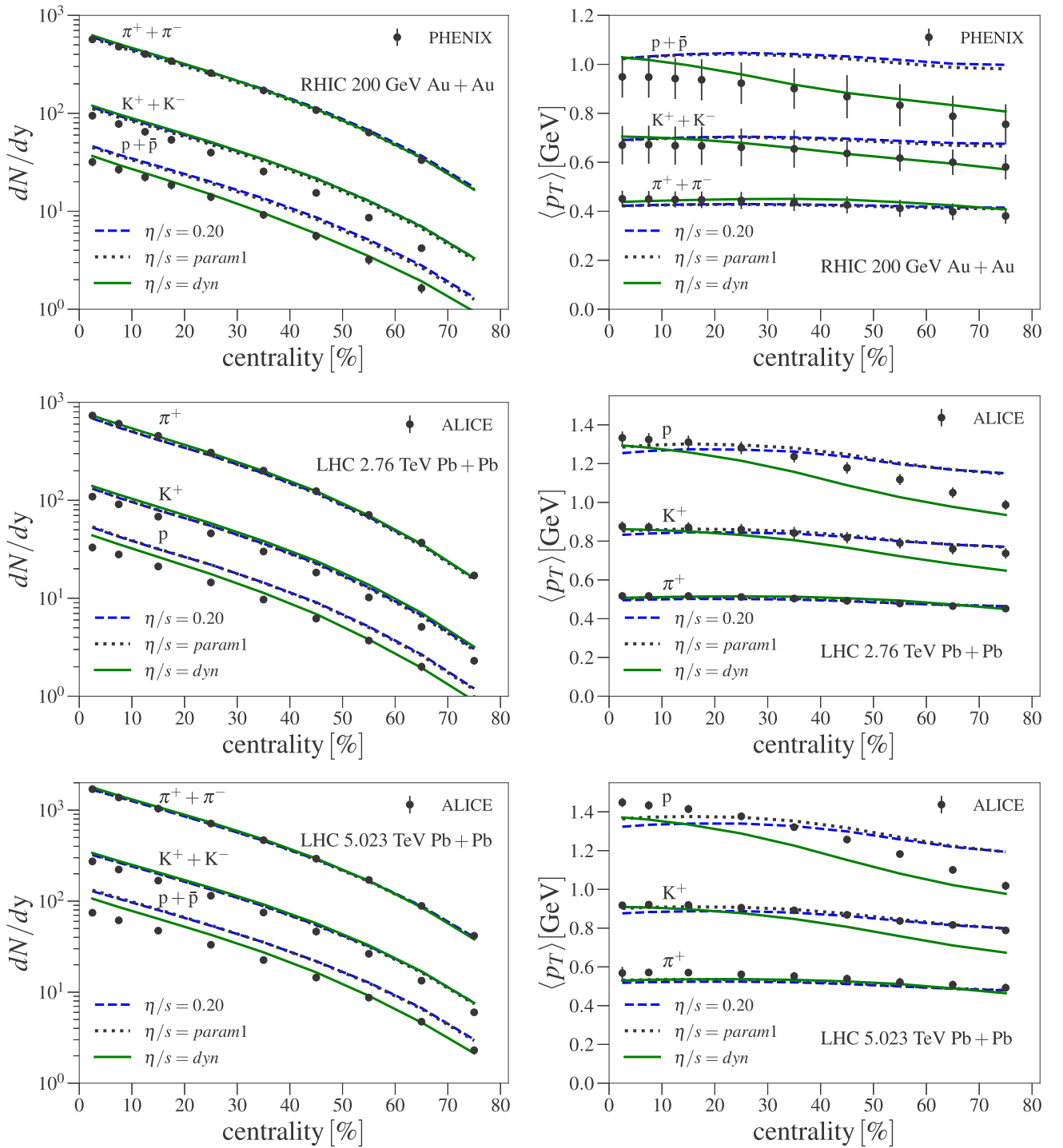
FIG. 5. Identified particle multiplicities (left) and average transverse momenta (right) for pions, kaons, and protons in 200 GeV Au + Au, 2.76 TeV Pb + Pb, and 5.023 TeV Pb + Pb collisions. The experimental data are from the PHENIX [84] and ALICE [85,86] Collaborations.

less sensitive to fine tuning of $\eta/s(T)$; for a discussion see Ref. [93]. The predictions for the ratios of $v_n\{2\}$ in Pb + Pb collisions at 2.76 to 5.023 TeV are shown in the upper panel of Fig. 7. The predicted increase ranges from up to 8% for v_2 to up to 25% for v_4. The predictions match well with the ALICE measurements for central to mid-central collisions, only in the most peripheral collisions the $\eta/s = $ dyn parametrization overestimates the data slightly, especially in the case of v_4, but there the experimental errors of the ratios are also quite large.

The situation is quite different in the case of Xe + Xe collisions. The ratio of the flow coefficients between the 5.44 TeV Xe + Xe and 5.023 TeV Pb + Pb collisions is shown in the lower panel of Fig. 7. The change in the flow coefficients is significantly larger than in the previous case, even if the collision energy is almost the same in Xe + Xe as in Pb + Pb collisions. The reason is that the system size is quite different when the nuclear mass number changes from $A = 208$ to $A = 129$. The most striking feature is the strong increase of v_2
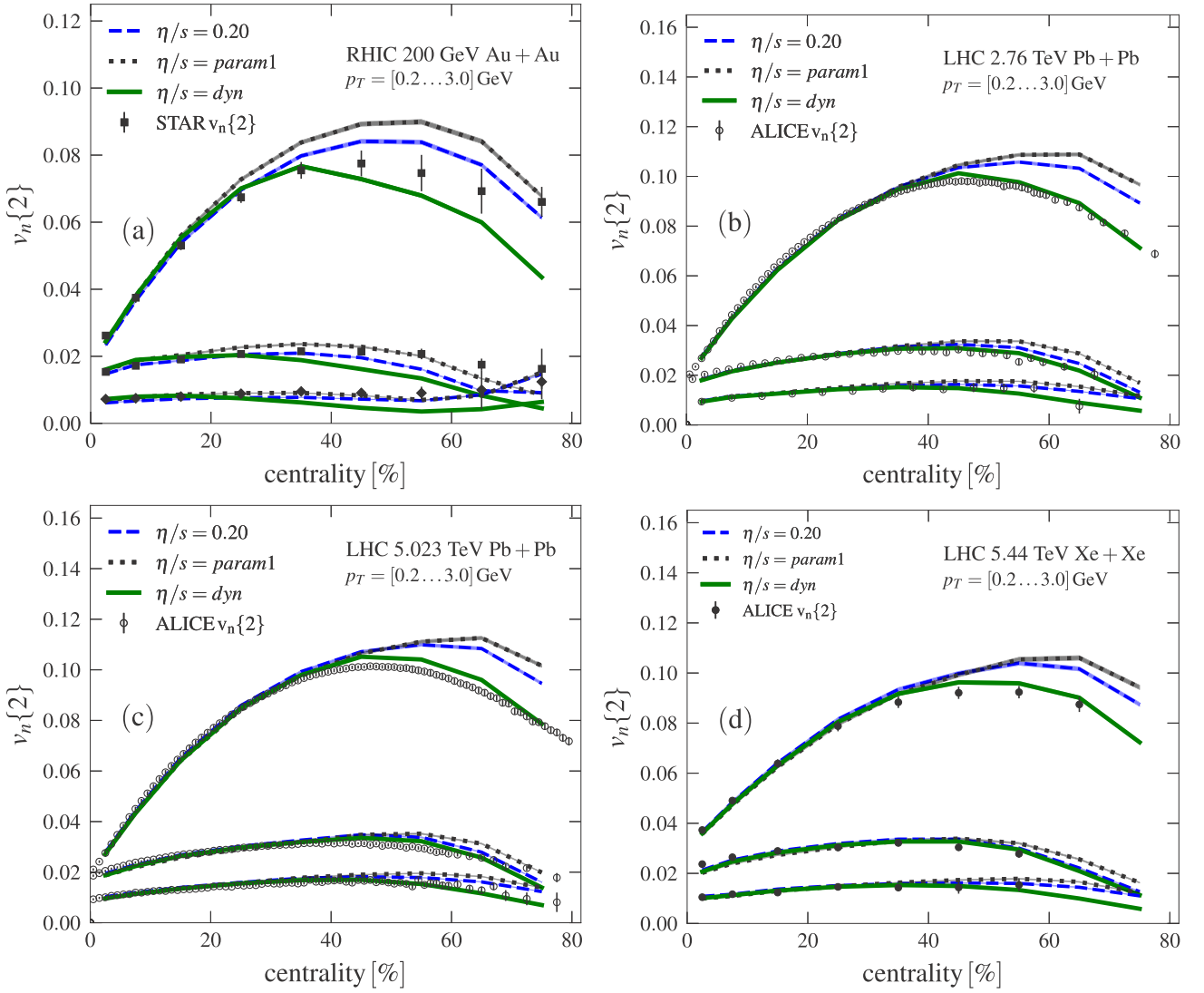
FIG. 6. Flow coefficients in 200 GeV Au + Au (a), 2.76 TeV Pb + Pb (b), 5.023 TeV Pb + Pb (c), and 5.44 TeV Xe + Xe (d) collisions. The experimental data are from the STAR [87,88] and ALICE Collaborations [89,90].

B. Event-plane correlations, cumulants, and flow–transverse-momentum correlations

in central Xe + Xe collisions compared to Pb + Pb collisions. A significant factor in the increase is the shape deformation of Xe nuclei. The deformation enhances the initial elliptic eccentricity fluctuations compared to the spherical double magic Pb nuclei. As a result the elliptic flow is 30% higher in the Xe case. The fact that we correctly predict this increase by taking into account the nuclear deformation is further evidence that the azimuthal asymmetries in the p_T spectra are resulting from a fluid dynamical response to the initial geometry.

The event-plane correlations, defined in Eq. (35), quantify the correlation between the event-plane angles Ψ_n, and also between the flow magnitudes v_n. The computed event-plane correlations in 2.76 TeV Pb + Pb are shown in Fig. 8. Only a slight separation between the dynamical freeze-out and earlier $\eta/s(T)$ parametrizations can be seen and all parametrizations

are able to describe the data. The most notable exceptions are the correlations involving the event-plane angle Ψ_6, which are very sensitive to δf corrections. In these, the $\eta/s =$ dyn parametrization slightly improves the agreement with the data from the earlier works. This is mostly due the fact that the $\eta/s =$ dyn parametrization has lower shear viscosity and thus smaller δf corrections. The event-plane correlations have only been measured for 2.76 TeV Pb + Pb collisions which is why we do not show results for other collision systems.

The symmetric cumulants, defined through Eq. (28), are complementary to the event-plane correlators in the sense that they depend on the correlation between the flow magnitudes v_n like the event-plane correlators, but are independent of the event-plane angles. The symmetric cumulants themselves are not a measure of correlation, but depend explicitly on the magnitude of v_n, and not only on the degree of correlation. The corresponding correlation measure is defined through the normalized symmetric cumulants, Eq. (29).
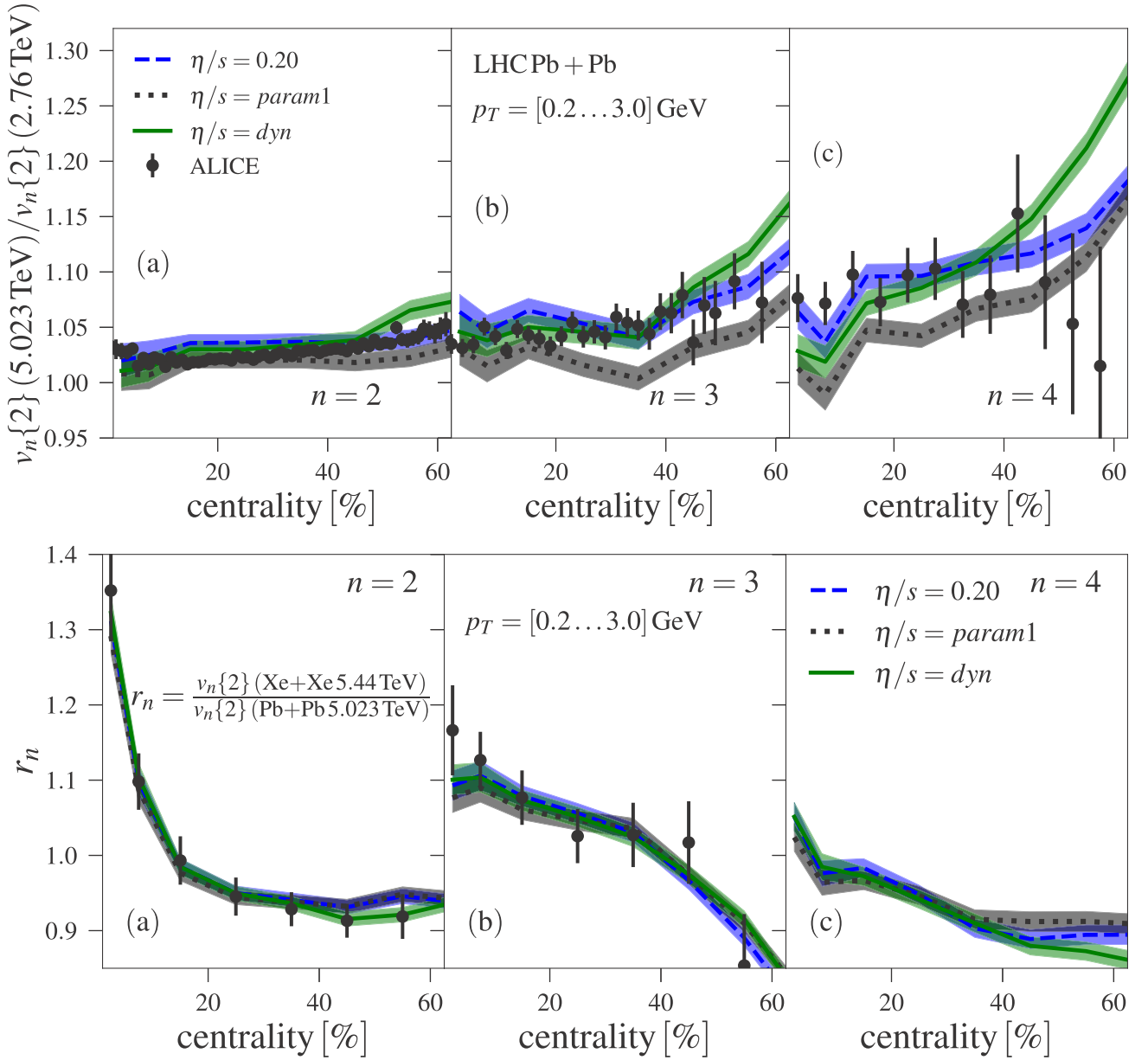
FIG. 7. The ratio of flow coefficients v_n between 5.023 and 2.76 TeV Pb + Pb collisions, and the ratio of v_n between 5.44 TeV Xe + Xe and 5.023 TeV Pb + Pb collisions. The experimental data are from the ALICE Collaboration [89,90].

The normalized symmetric cumulants in 2.76 TeV Pb + Pb collisions are shown in Fig. 9 compared to the ALICE data [95]. As in the case of event-plane correlations, there are only small differences between the three η/s parametrizations. The overall agreement between the data and the computations is good, but with a notable exception that in peripheral collisions we underpredict the NSC(2, 4) correlation. The collision energy dependence of the normalized symmetric cumulants is weak, as can be seen in Fig. 10 where we show them in 5.023 TeV Pb + Pb collisions.

In Fig. 11 we show the normalized symmetric cumulants in 200 GeV Au + Au collisions. Note that here the centrality of the collisions is given by the number of participants, as reported by the STAR Collaboration [96]. Compared to Pb + Pb collisions we see much more separation between the

dynamical freeze-out and earlier parametrizations for the NSC(3, 4), NSC(3, 5) and NSC(4, 6) correlations. The predictions for the NSC(2, 3) correlation are in line with the measurements while for NSC(2, 4) all the parametrizations clearly underestimate the data in peripheral collisions.

The correlations between higher order moments of two or three flow coefficients can be studied using the mixed harmonic cumulants which provide information that is independent of the normalized symmetric cumulants. The EKRT model predictions for nMHC(v_2^2, v_3^2, v_4^2) and nMHC(v_2^k, v_3^l) are compared against the ALICE measurements for 5.023 TeV Pb + Pb collisions in Fig. 12. As can be seen there are only modest differences between the parametrizations and the statistical errors in our simulations are already quite large, especially with nMHC(v_2^4, v_3^4). This is expected, since the
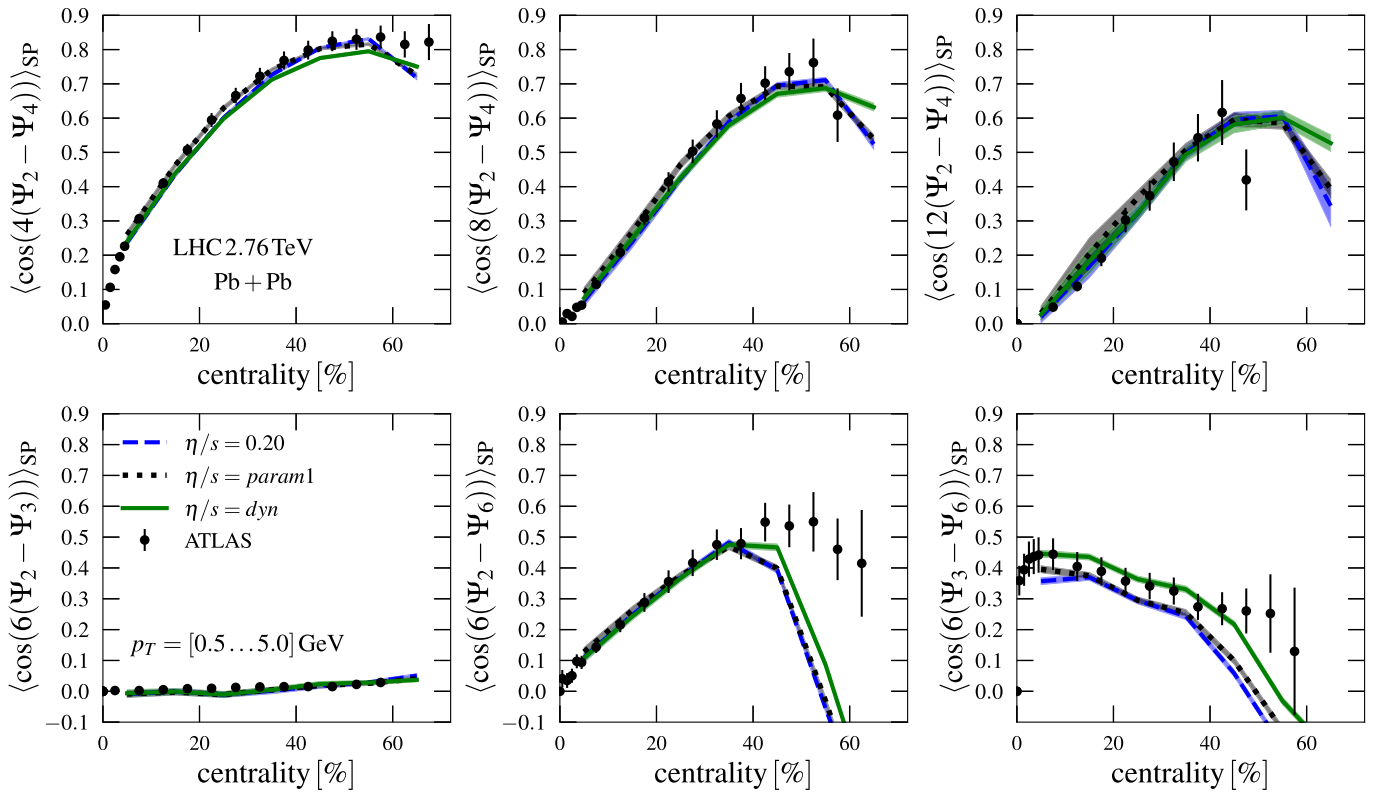
FIG. 8. Event-plane correlations in 2.76 TeV Pb + Pb collisions. The data are from the ATLAS Collaboration [94].

correlations between v_2 and v_3 are thought to be more sensitive to the initial state rather than to the dynamics of the system. Our predictions seem to agree quite well with the data except for nMHC(v_2^4, v_3^4), for which we predict a stronger correlation in peripheral collisions than what is measured.

Finally in Fig. 13 we show our predictions for the recently measured flow–transverse-momentum correlations $\rho(v_n^2, [p_T])$ as a function of the number of participant nucleons in 5.023 TeV Pb + Pb collisions. These correlators describe the correlation between the average transverse
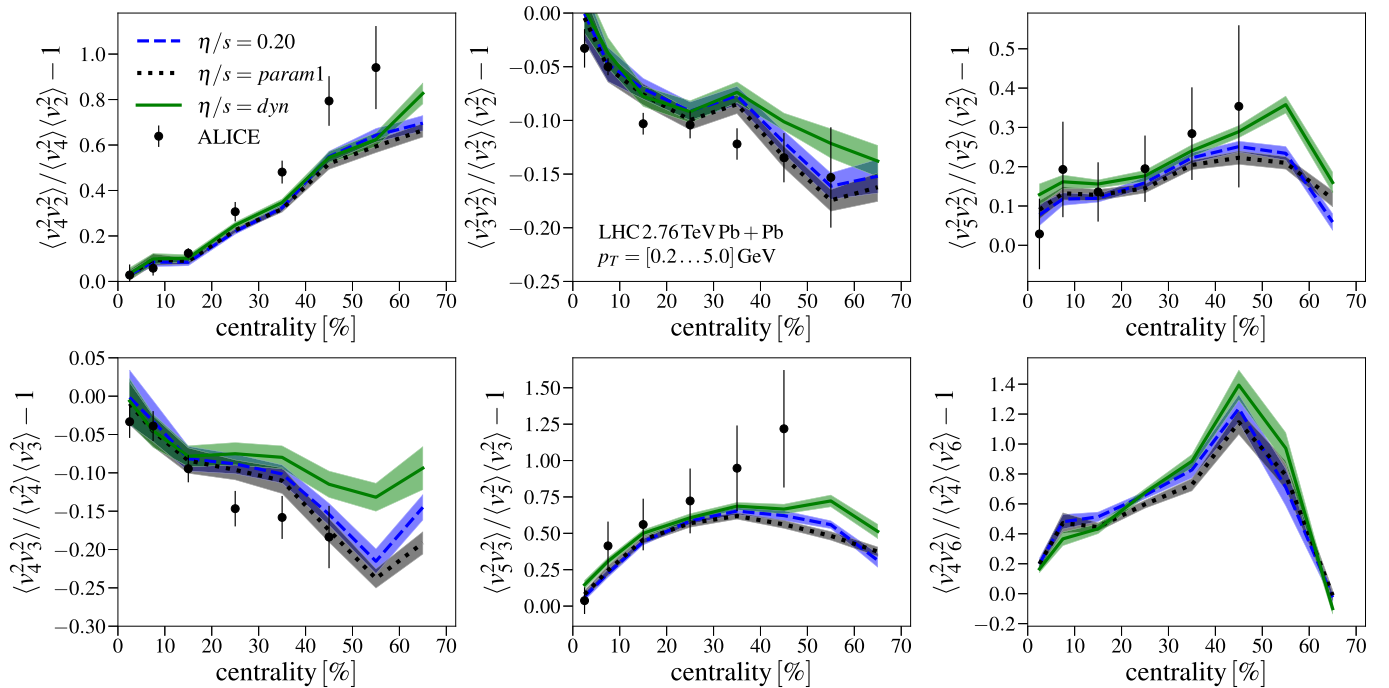
FIG. 9. Normalized symmetric cumulants $NSC(n, m)$ in 2.76 TeV Pb + Pb collisions. The data are from the ALICE Collaboration [95].
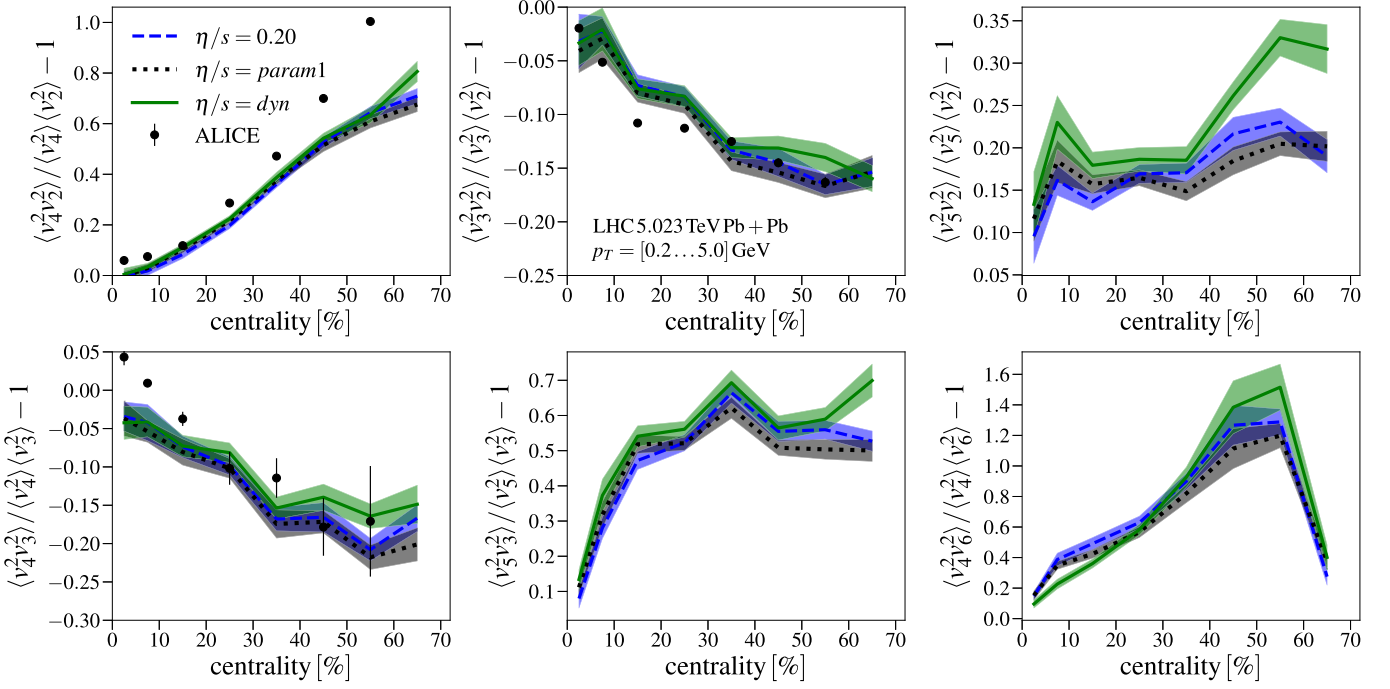
FIG. 10. Normalized symmetric cumulants $NSC(n, m)$ in 5.023 TeV Pb + Pb collisions. The data are from the ALICE Collaboration [97].

momentum and the flow coefficients and thus one would expect it to be somewhat sensitive to the bulk viscosity and freeze-out criterion. The EKRT model calculations confirm this by showing an increase in all $\rho(v_n^2, [p_T])$ correlations, especially in the peripheral region. This also improves the agreement with the ATLAS measurements in peripheral collisions, even though the agreement with the data is still only qualitative. Most notably the $\eta/s = dyn$ parametrization gives

the same sign as the measurements for $\rho(v_4^2, [p_T])$ in peripheral collisions.

C. Higher-order flow and response coefficients

In Fig. 14 we show the higher-order flow coefficients v_4, v_5, and v_6 compared to the ALICE data [99] in 2.76 TeV Pb + Pb collisions. As can be seen in the figure, the
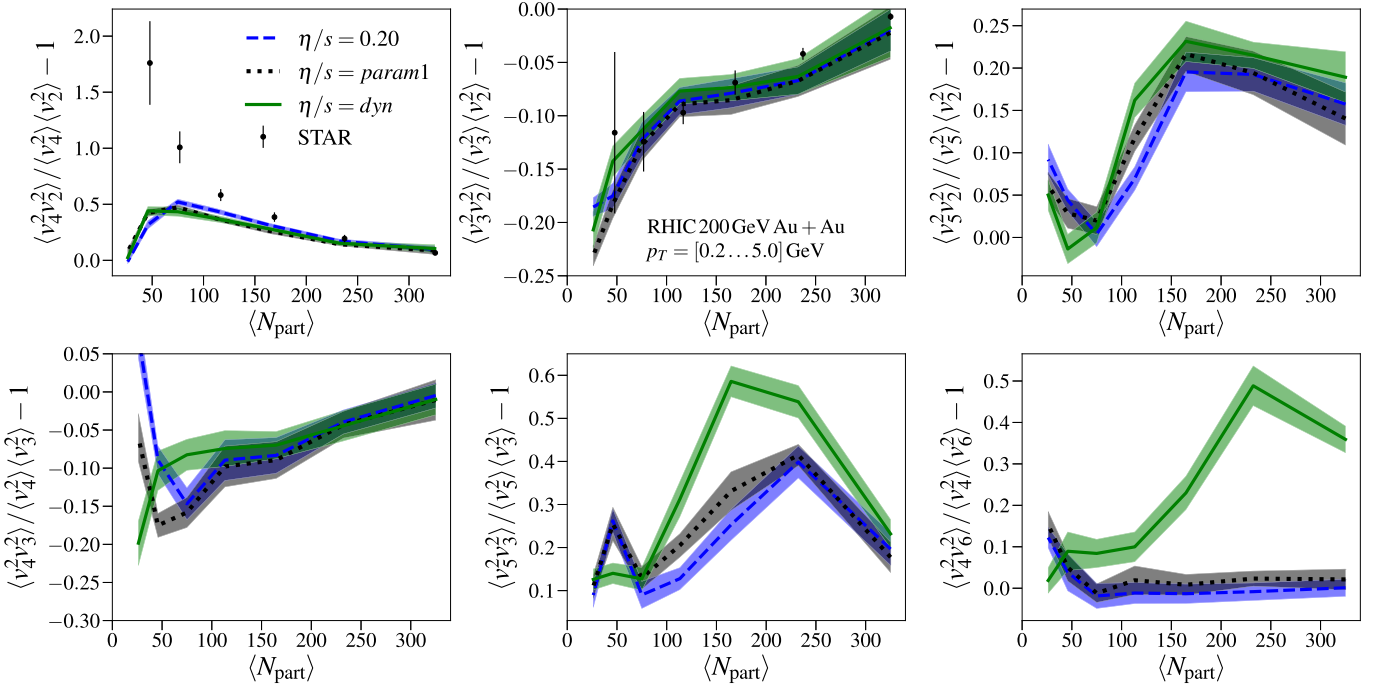
FIG. 11. Normalized symmetric cumulants $NSC(n, m)$ in 200 GeV Au + Au collisions. The data are from the STAR Collaboration [96].
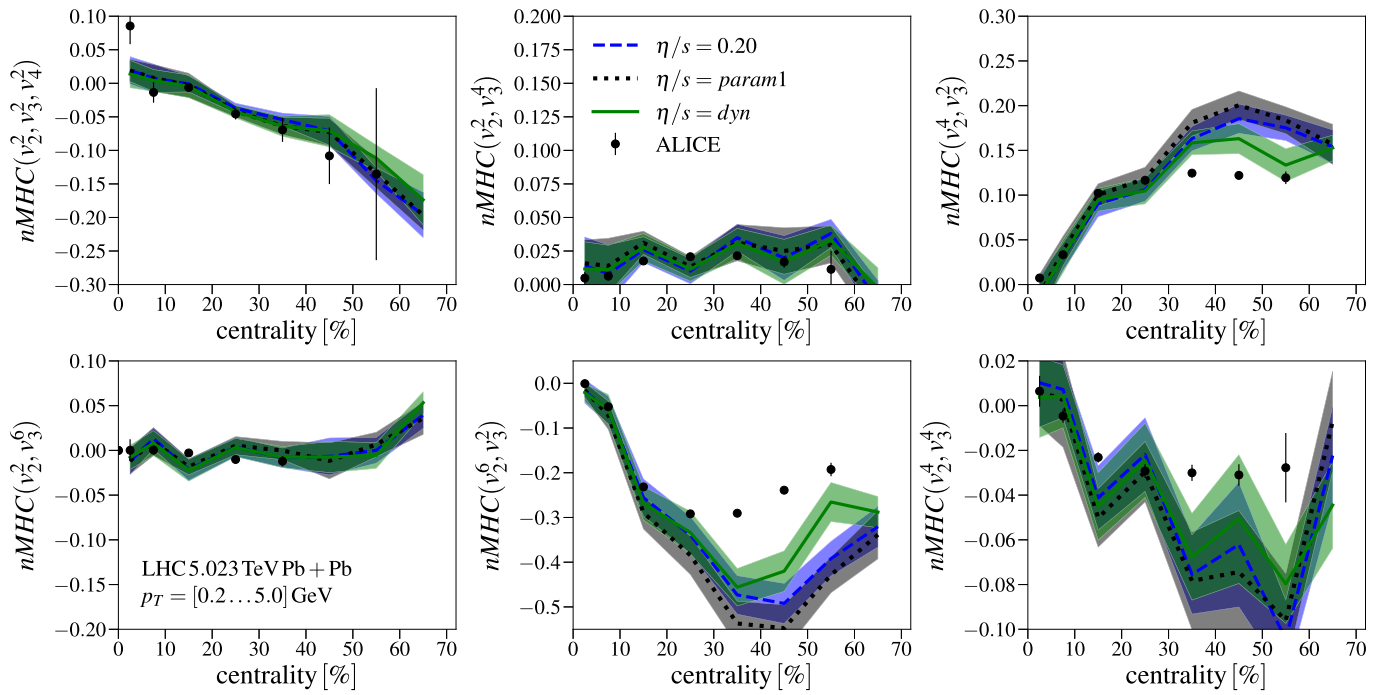
FIG. 12. Normalized mixed harmonic cumulants $nMHC$ in 5.023 TeV Pb + Pb collisions. The data are from the ALICE Collaboration [97].
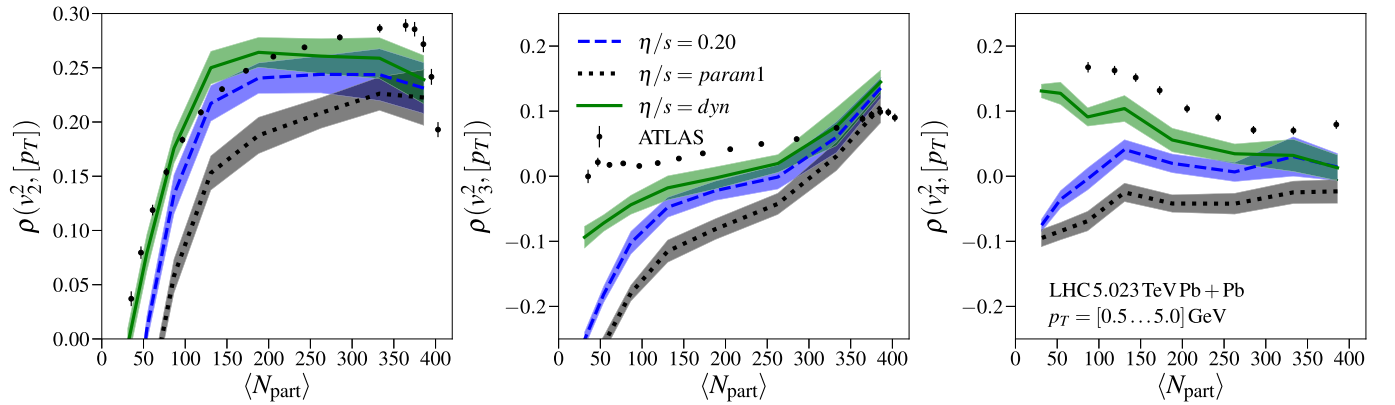
FIG. 13. The flow–transverse-momentum correlation coefficient $\rho(v_n\{2\}, [p_T])$ in 5.023 TeV Pb + Pb collisions. The data are from the ATLAS Collaboration [98].
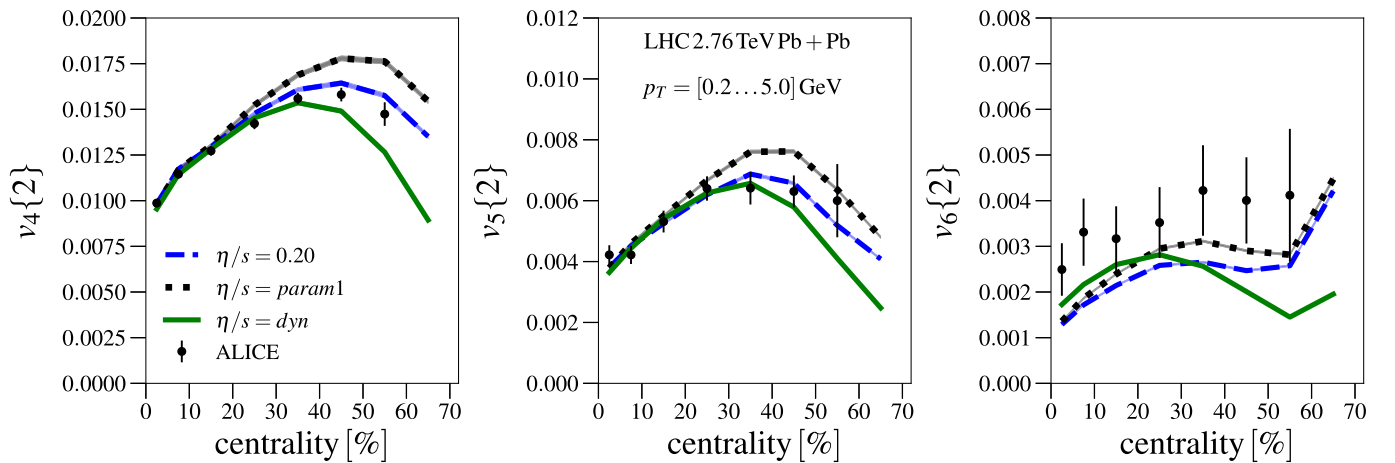
FIG. 14. Higher-order flow coefficients in 2.76 TeV Pb + Pb collisions. The data are from the ALICE Collaboration [99].
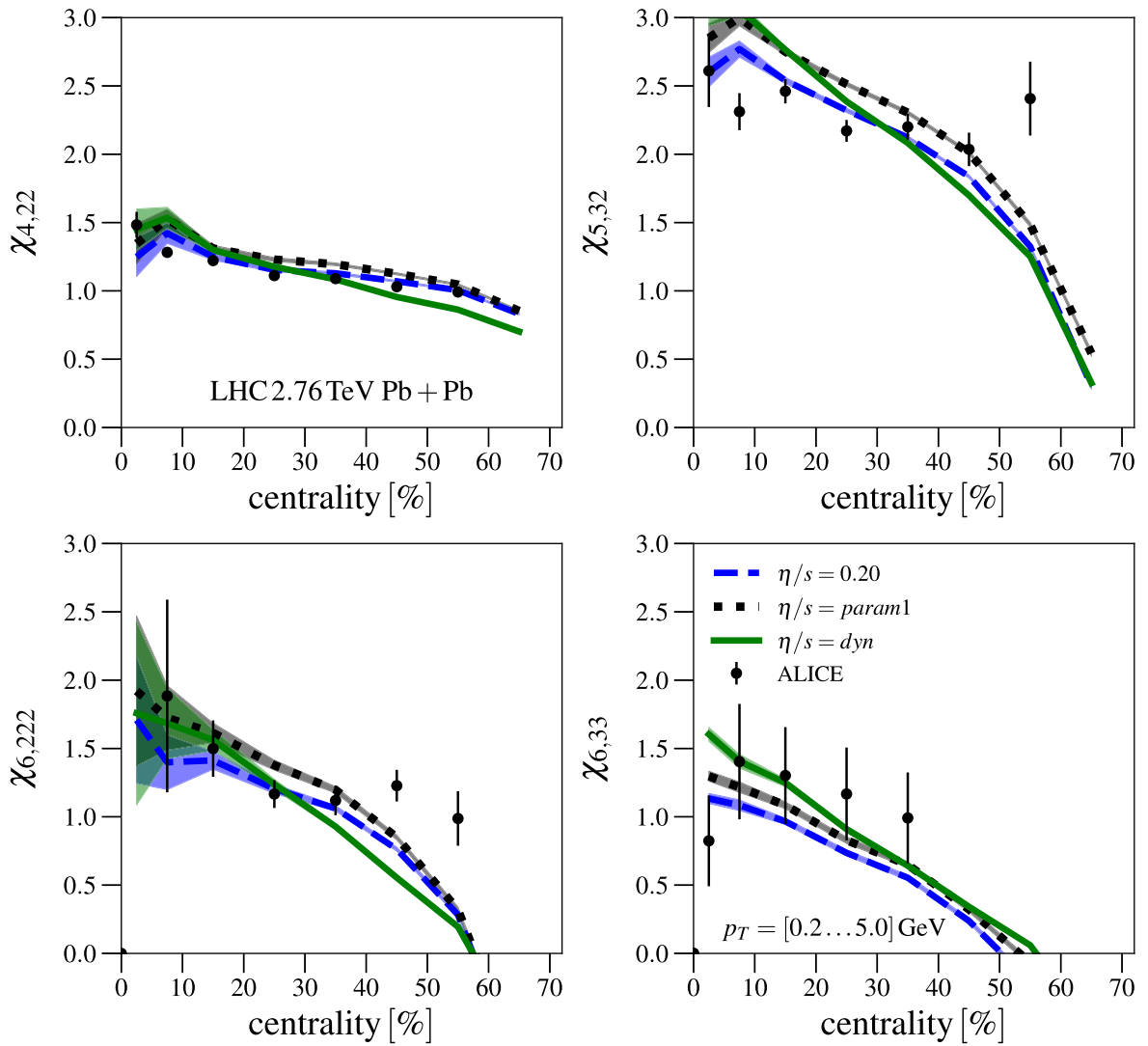
FIG. 15. Non-linear flow response coefficients in 2.76 TeV Pb + Pb collisions. The data are from the ALICE Collaboration [99].

η/s = dyn parametrization seems to slightly underpredict the higher order flow coefficients in peripheral collisions, while the $\eta/s = 0.2$ parametrization manages to reproduce the data quite well. For v_6 we point out that the measured flow is larger in 2.76 TeV than in 5.023 TeV collisions, as can be seen by comparing measurements with Fig. 16, which is in conflict with the behavior of the other flow coefficients. We also note that the difference between the earlier parametrizations $\eta/s = 0.2$ and $\eta/s = $ param1 is more visible here than in the case of lower-order flow coefficients.

The corresponding nonlinear response coefficients are shown in Fig. 15. As explained in Sec. V they are closely related to the event-plane correlations, and the good agreement of the calculated response coefficients with the ALICE data is consistent with the good agreement between the calculated and the measured ATLAS event-plane correlations in Fig. 8.

The same flow and response coefficients as above, but for 5.023 TeV Pb + Pb collisions, are shown in Figs. 16 and 17, respectively. Together with other higher order flow harmonics we also show v_7, v_8, and v_9, which are only

measured for the 5.023 TeV energy. Here we see that the parametrization that uses dynamical freeze-out predicts the higher order flow coefficients quite well while the parametrizations from earlier works are slightly above the measurements.

The response coefficients are not directly proportional to the magnitude of the flow coefficients, or the proportionality is partly canceled by the normalization. That is to say that the agreement in the response coefficients with the ALICE data is similar as at the lower collision energy even though we cannot exactly reproduce the higher order v_n's for both collision energies simultaneously.

The overall agreement with the higher-order flow coefficients with the data is quite similar for both the earlier and current EKRT setup. The improvements due to the dynamical decoupling are not as clear as for v_2. However, the differences between the parametrizations are also larger, highlighting the fact that higher-order coefficients, and their $\sqrt{s_{NN}}$ dependence give important constraints on the determination of shear viscosity.
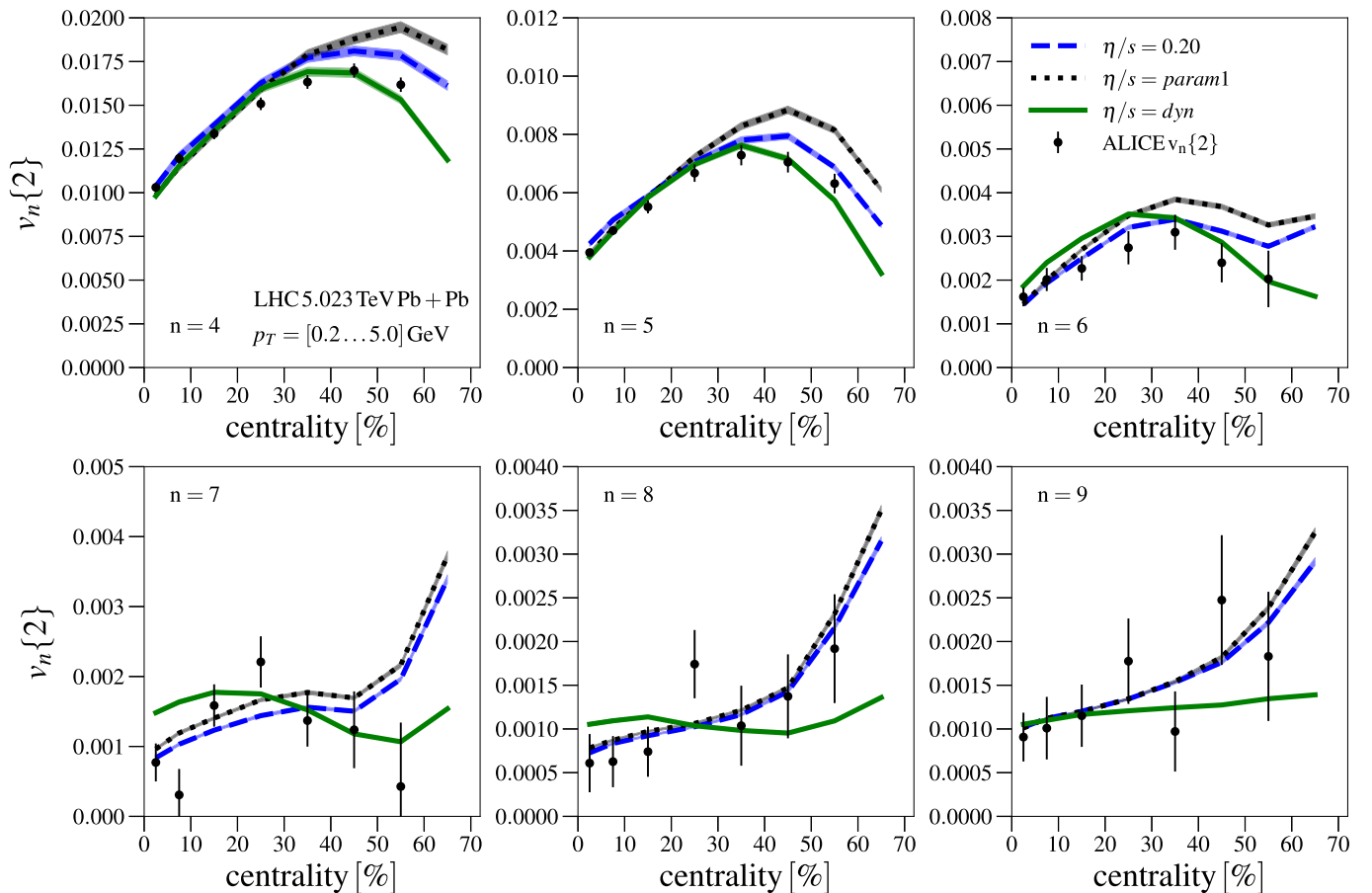
FIG. 16. Higher-order flow coefficients in 5.023 TeV Pb + Pb collisions. The data are from the ALICE Collaboration [100].

VII. SUMMARY AND CONCLUSIONS

We have presented the results for the low-p_T observables in Pb + Pb, Au + Au, and Xe + Xe collisions at RHIC and LHC energies from the fluid dynamical computations using the NLO pQCD based EKRT model for the initial conditions. Compared to the previous EKRT works in Refs. [25,27,28] we have now added the bulk viscosity together with the dynamical decoupling conditions to improve the validity of our model in peripheral collisions.

The overall agreement of the computed results with the data is very good in particular for the $\sqrt{s_{NN}}$, A, and centrality dependence of the charged hadron multiplicity. This is mainly a feature of the EKRT initial conditions. The main uncertainty in the EKRT model is the K_{sat} parameter in the saturation condition, but this can be essentially fixed from one measurement of charged hadron multiplicity. Even if the value of K_{sat} depends on the η/s parametrization through the entropy production during the fluid dynamical evolution, the final results for the $\sqrt{s_{NN}}$, A, and centrality dependence are practically independent of the K_{sat} value, making them very robust predictions of the EKRT model.

The most significant effect of the dynamical freeze-out can be seen in the absolute magnitude of the flow coefficients v_n. We have demonstrated that we can reproduce the experimental data for v_2 and v_3 across the centrality range 0–80% in all the collision systems with the exception of

peripheral RHIC collisions. This is a significant improvement from the constant-temperature freeze-out which only manages to describe the data up to the 30–40% centrality class. The higher harmonics v_4, v_5, and v_6 are quite similarly described by both the earlier computations and the current setup, but the differences between the η/s parametrizations are also more pronounced. On the other hand, the relative increase of the flow coefficients from 2.76 TeV Pb + Pb to 5.023 TeV Pb + Pb and 5.44 TeV Xe + Xe collisions is well described in all the centrality classes shown here. The addition of the dynamical freeze-out together with the bulk viscosity has also made it possible to improve the simultaneous agreement of the identified particle multiplicities and the mean transverse momenta with the measurements.

We have also shown the EKRT model predictions for the most recent correlation measurements. Our results for the symmetric cumulants, the mixed harmonic cumulants, the response coefficients, and closely related event-plane correlators are very similar to the earlier EKRT results and the agreement with the data remains reasonably good. The most notable differences are in NSC(2, 4) correlators in peripheral collisions, where the predictions are visibly below the experimental data. The effect of the dynamical freeze-out and the bulk viscosity can be seen in the flow–transverse-momentum correlators $\rho(v_n^2, [p_T])$, where we demonstrated a better quantitative agreement with the experimental measurements in
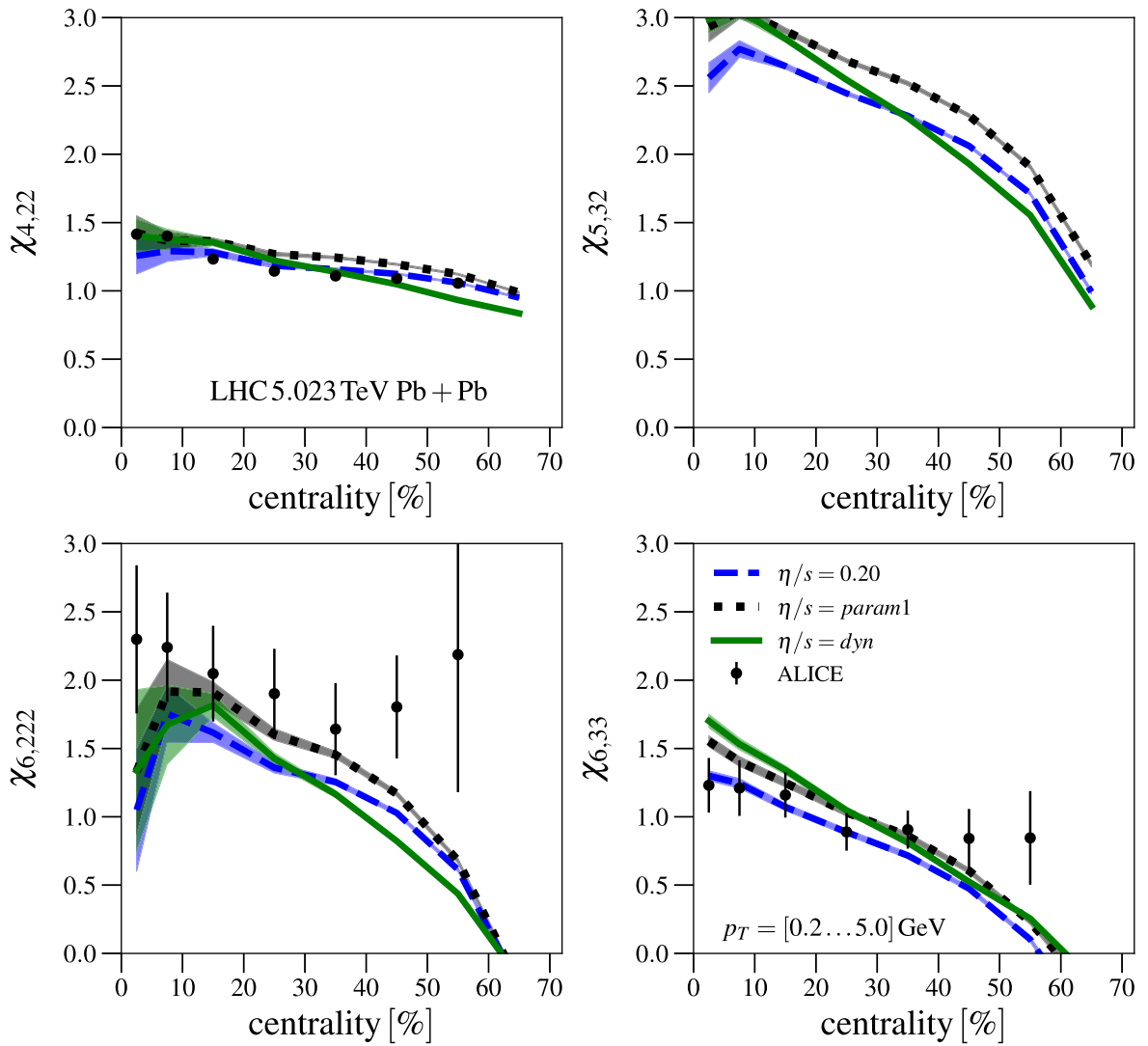
FIG. 17. Non-linear flow response coefficients in 5.023 TeV Pb + Pb collisions. The data are from the ALICE Collaboration [100].

peripheral collisions than given by the previous EKRT computations. Especially, we obtained the correct sign in $\rho(v_4^2, [p_T])$ correlation in peripheral collisions.

In conclusion, we have introduced dynamical freeze-out conditions to model the decoupling of the fluid to free hadrons. In particular, the aim was to capture the essential features of the decoupling that take into account the system size variations at different collision energies and centralities. The clear benefit here is that it allows us to keep the transport coefficients continuous throughout the whole temperature range, without unphysical discontinuities that can appear at a switching between fluid dynamics and hadron cascade. At the same time it is then possible to use the measured data to constrain the QCD matter transport properties also in the hadronic phase.

We emphasize that in spite of the extensive iteration work done, the parametrizations shown here do not necessarily represent the absolute best fit to the data. For that we would need to do a full statistical global Bayesian analysis of the parameter space. This we have left as a future work. However, we have demonstrated that we can reproduce the measured

LHC and RHIC low-p_T observables reasonably well, and the dynamical decoupling leads to quite a different spacetime picture compared to many hydro+cascade models. Instead of a very viscous hadronic evolution directly after the low-viscosity QGP evolution, in the picture presented here the low-viscosity evolution can extend to quite low temperatures on the hadronic side.

[1] M. Luzum and P. Romatschke, Phys. Rev. C **78**, 034915 (2008); **79**, 039903 (2009).
[2] P. Bożek, Phys. Rev. C **81**, 034909 (2010).
[3] H. Song, S. A. Bass, and U. Heinz, Phys. Rev. C **83**, 054912 (2011); **87**, 019902 (2013).
[4] H. Niemi, G. S. Denicol, P. Huovinen, E. Molnar, and D. H. Rischke, Phys. Rev. Lett. **106**, 212302 (2011).
[5] H. Niemi, G. S. Denicol, P. Huovinen, E. Molnar, and D. H. Rischke, Phys. Rev. C **86**, 014909 (2012).
[6] S. Ryu, J. F. Paquet, C. Shen, G. S. Denicol, B. Schenke, S. Jeon, and C. Gale, Phys. Rev. Lett. **115**, 132301 (2015).
[7] I. A. Karpenko, P. Huovinen, H. Petersen, and M. Bleicher, Phys. Rev. C **91**, 064901 (2015).
[8] A. Bazavov *et al.* (HotQCD Collaboration), Phys. Rev. D **90**, 094503 (2014).
[9] A. Bazavov, P. Petreczky, and J. H. Weber, Phys. Rev. D **97**, 014510 (2018).
[10] S. Borsanyi, Z. Fodor, C. Hoelbling, S. D. Katz, S. Krieg, and K. K. Szabo, Phys. Lett. B **730**, 99 (2014).
[11] S. Borsanyi, G. Endrodi, Z. Fodor, A. Jakovac, S. D. Katz, S. Krieg, C. Ratti, and K. K. Szabo, J. High Energy Phys. 11 (2010) 077.
[12] S. Pratt, E. Sangaline, P. Sorensen, and H. Wang, Phys. Rev. Lett. **114**, 202301 (2015).
[13] J. S. Moreland and R. A. Soltz, Phys. Rev. C **93**, 044913 (2016).
[14] P. Alba, V. Mantovani Sarti, J. Noronha, J. Noronha-Hostler, P. Parotto, I. Portillo Vazquez, and C. Ratti, Phys. Rev. C **98**, 034909 (2018).
[15] J. Auvinen, K. J. Eskola, P. Huovinen, H. Niemi, R. Paatelainen, and P. Petreczky, Phys. Rev. C **102**, 044911 (2020).
[16] J. E. Bernhard, J. S. Moreland, S. A. Bass, J. Liu, and U. Heinz, Phys. Rev. C **94**, 024907 (2016).
[17] S. A. Bass, J. E. Bernhard, and J. S. Moreland, Nucl. Phys. A **967**, 67 (2017).
[18] J. E. Bernhard, J. S. Moreland, and S. A. Bass, Nat. Phys. **15**, 1113 (2019).
[19] D. Everett *et al.* (JETSCAPE Collaboration), Phys. Rev. C **103**, 054904 (2021).
[20] G. Nijs, W. van der Schee, U. Gürsoy, and R. Snellings, Phys. Rev. C **103**, 054909 (2021).
[21] J. E. Parkkila, A. Onnerstad, and D. J. Kim, Phys. Rev. C **104**, 054904 (2021).
[22] J. E. Parkkila, A. Onnerstad, F. Taghavi, C. Mordasini, A. Bilandzic, and D. J. Kim, Phys. Lett. B **835**, 137485 (2022).
[23] H. Niemi, G. S. Denicol, H. Holopainen, and P. Huovinen, Phys. Rev. C **87**, 054901 (2013).
[24] L. Barbosa, F. G. Gardim, F. Grassi, P. Ishida, M. Luzum, M. V. Machado, and J. Noronha-Hostler, arXiv:2105.12792.
[25] H. Niemi, K. J. Eskola, and R. Paatelainen, Phys. Rev. C **93**, 024907 (2016).
[26] R. Paatelainen, K. J. Eskola, H. Niemi, and K. Tuominen, Phys. Lett. B **731**, 126 (2014).
[27] H. Niemi, K. J. Eskola, R. Paatelainen, and K. Tuominen, Phys. Rev. C **93**, 014912 (2016).
[28] K. J. Eskola, H. Niemi, R. Paatelainen, and K. Tuominen, Phys. Rev. C **97**, 034911 (2018).
[29] K. J. Eskola, H. Niemi, R. Paatelainen, and K. Tuominen, Nucl. Phys. A **967**, 313 (2017).
[30] P. Huovinen and P. Petreczky, Nucl. Phys. A **837**, 26 (2010).
[31] P. Huovinen and D. Molnar, Phys. Rev. C **79**, 014906 (2009).
[32] K. Gallmeister, H. Niemi, C. Greiner, and D. H. Rischke, Phys. Rev. C **98**, 024912 (2018).
[33] K. J. Eskola, H. Niemi, and P. V. Ruuskanen, Phys. Rev. C **77**, 044907 (2008).
[34] S. Ahmad, H. Holopainen, and P. Huovinen, Phys. Rev. C **95**, 054911 (2017).
[35] P. Bożek and W. Broniowski, Phys. Lett. B **718**, 1557 (2013).
[36] P. Bożek and W. Broniowski, Phys. Rev. C **88**, 014903 (2013).
[37] P. Bożek, W. Broniowski, and G. Torrieri, Phys. Rev. Lett. **111**, 172303 (2013).
[38] G. Y. Qin and B. Müller, Phys. Rev. C **89**, 044902 (2014).
[39] K. Werner, M. Bleicher, B. Guiot, I. Karpenko, and T. Pierog, Phys. Rev. Lett. **112**, 232301 (2014).
[40] I. Kozlov, M. Luzum, G. Denicol, S. Jeon, and C. Gale, arXiv:1405.3976.
[41] P. Romatschke, Eur. Phys. J. C **75**, 305 (2015).
[42] C. Shen, J. F. Paquet, G. S. Denicol, S. Jeon, and C. Gale, Phys. Rev. C **95**, 014906 (2017).
[43] K. J. Eskola, K. Kajantie, P. V. Ruuskanen, and K. Tuominen, Nucl. Phys. B **570**, 379 (2000).
[44] R. Paatelainen, K. J. Eskola, H. Holopainen, and K. Tuominen, Phys. Rev. C **87**, 044904 (2013).
[45] G. Giacalone, J. Noronha-Hostler, M. Luzum, and J. Y. Ollitrault, Phys. Rev. C **97**, 034904 (2018).
[46] P. Möller, A. J. Sierk, T. Ichikawa, and H. Sagawa, At. Data Nucl. Data Tables **109-110**, 1 (2016).
[47] W. Israel and J. M. Stewart, Ann. Phys. (NY) **118**, 341 (1979).
[48] G. S. Denicol, T. Koide, and D. H. Rischke, Phys. Rev. Lett. **105**, 162501 (2010).
[49] G. S. Denicol, H. Niemi, E. Molnar, and D. H. Rischke, Phys. Rev. D **85**, 114047 (2012); **91**, 039902 (2015).
[50] G. S. Denicol, E. Molnár, H. Niemi, and D. H. Rischke, Eur. Phys. J. A **48**, 170 (2012).
[51] E. Molnár, H. Niemi, G. S. Denicol, and D. H. Rischke, Phys. Rev. D **89**, 074010 (2014).
[52] B. Betz, D. Henkel, and D. H. Rischke, Prog. Part. Nucl. Phys. **62**, 556 (2009).
[53] B. Betz, G. S. Denicol, T. Koide, E. Molnar, H. Niemi, and D. H. Rischke, EPJ Web Conf. **13**, 07005 (2011).
[54] G. S. Denicol, J. Noronha, H. Niemi, and D. H. Rischke, Phys. Rev. D **83**, 074019 (2011).
[55] H. Niemi and G. S. Denicol, arXiv:1404.7327.
[56] E. Molnar, H. Niemi, and D. H. Rischke, Eur. Phys. J. C **65**, 615 (2010).
[57] G. S. Denicol, S. Jeon, and C. Gale, Phys. Rev. C **90**, 024912 (2014).
[58] H. Bebie, P. Gerber, J. L. Goity, and H. Leutwyler, Nucl. Phys. B **378**, 95 (1992).
[59] T. Hirano and K. Tsuda, Phys. Rev. C **66**, 054905 (2002).
[60] P. Huovinen, Eur. Phys. J. A **37**, 121 (2008).
[61] P. Huovinen and H. Petersen, Eur. Phys. J. A **48**, 171 (2012).
[62] A. Hosoya and K. Kajantie, Nucl. Phys. B **250**, 666 (1985).
[63] S. Gavin, Nucl. Phys. A **435**, 826 (1985).
[64] C. Sasaki and K. Redlich, Phys. Rev. C **79**, 055207 (2009).
[65] K. Paech and S. Pratt, Phys. Rev. C **74**, 014901 (2006); **93**, 059902 (2016).
[66] K. Dusling and T. Schäfer, Phys. Rev. C **85**, 044909 (2012).
[67] J. B. Rose, J. M. Torres-Rincon, and H. Elfner, J. Phys. G: Nucl. Part. Phys. **48**, 015005 (2021).

[68] J. B. Rose, J. M. Torres-Rincon, A. Schäfer, D. R. Oliinychenko, and H. Petersen, Phys. Rev. C **97**, 055204 (2018).

[69] M. Prakash, M. Prakash, R. Venugopalan, and G. Welke, Phys. Rep. **227**, 321 (1993).

[70] L. P. Csernai, J. I. Kapusta, and L. D. McLerran, Phys. Rev. Lett. **97**, 152303 (2006).

[71] F. G. Gardim, F. Grassi, M. Luzum, and J. Y. Ollitrault, Phys. Rev. C **85**, 024908 (2012).

[72] J. Adam *et al.* (ALICE Collaboration), Phys. Rev. Lett. **117**, 182301 (2016).

[73] Z. Moravcova, K. Gulbrandsen, and Y. Zhou, Phys. Rev. C **103**, 024913 (2021).

[74] M. Luzum and J. Y. Ollitrault, Phys. Rev. C **87**, 044907 (2013).

[75] L. Yan and J. Y. Ollitrault, Phys. Lett. B **744**, 82 (2015).

[76] G. Giacalone, L. Yan, J. Noronha-Hostler, and J. Y. Ollitrault, Phys. Rev. C **94**, 014906 (2016).

[77] G. Giacalone, B. Schenke, and C. Shen, Phys. Rev. Lett. **125**, 192301 (2020).

[78] B. Schenke, C. Shen, and D. Teaney, Phys. Rev. C **102**, 034905 (2020).

[79] K. Aamodt *et al.* (ALICE Collaboration), Phys. Rev. Lett. **106**, 032301 (2011).

[80] J. Adam *et al.* (ALICE Collaboration), Phys. Rev. Lett. **116**, 222302 (2016).

[81] S. Acharya *et al.* (ALICE Collaboration), Phys. Lett. B **790**, 35 (2019).

[82] B. I. Abelev *et al.* (STAR Collaboration), Phys. Rev. C **79**, 034909 (2009).

[83] S. S. Adler *et al.* (PHENIX Collaboration), Phys. Rev. C **71**, 034908 (2005); **71**, 049901 (2005).

[84] S. S. Adler *et al.* (PHENIX Collaboration), Phys. Rev. C **69**, 034909 (2004).

[85] B. Abelev *et al.* (ALICE Collaboration), Phys. Rev. C **88**, 044910 (2013).

[86] S. Acharya *et al.* (ALICE Collaboration), Phys. Rev. C **101**, 044907 (2020).

[87] L. Adamczyk *et al.* (STAR Collaboration), Phys. Rev. Lett. **116**, 112302 (2016).

[88] L. Adamczyk *et al.* (STAR Collaboration), Phys. Rev. C **98**, 034918 (2018).

[89] S. Acharya *et al.* (ALICE Collaboration), J. High Energy Phys. 07 (2018) 103.

[90] S. Acharya *et al.* (ALICE Collaboration), Phys. Lett. B **784**, 82 (2018).

[91] H. Mäntysaari and B. Schenke, Phys. Rev. Lett. **117**, 052301 (2016).

[92] C. Gale, J. F. Paquet, B. Schenke, and C. Shen, Phys. Rev. C **105**, 014909 (2022).

[93] J. Noronha-Hostler, M. Luzum, and J. Y. Ollitrault, Phys. Rev. C **93**, 034912 (2016).

[94] G. Aad *et al.* (ATLAS Collaboration), Phys. Rev. C **90**, 024905 (2014).

[95] S. Acharya *et al.* (ALICE Collaboration), Phys. Rev. C **97**, 024906 (2018).

[96] J. Adam *et al.* (STAR Collaboration), Phys. Lett. B **783**, 459 (2018).

[97] S. Acharya *et al.* (ALICE Collaboration), Phys. Lett. B **818**, 136354 (2021).

[98] G. Aad *et al.* (ATLAS Collaboration), Eur. Phys. J. C **79**, 985 (2019).

[99] S. Acharya *et al.* (ALICE Collaboration), Phys. Lett. B **773**, 68 (2017).

[100] S. Acharya *et al.* (ALICE Collaboration), J. High Energy Phys. 05 (2020) 085.

PII

DEEP LEARNING FOR FLOW OBSERVABLES IN ULTRARELATIVISTIC HEAVY-ION COLLISIONS

by

Henry Hirvonen, Kari J. Eskola and Harri Niemi.

Deep learning for flow observables in ultrarelativistic heavy-ion collisions

H. Hirvonen ⬤, K. J. Eskola ⬤, and H. Niemi ⬤

University of Jyväskylä, Department of Physics, P.O. Box 35, FI-40014 University of Jyväskylä, Finland
and Helsinki Institute of Physics, P.O. Box 64, FI-00014 University of Helsinki, Finland

We train a deep convolutional neural network to predict hydrodynamic results for flow coefficients, average transverse momenta, and charged particle multiplicities in ultrarelativistic heavy-ion collisions from the initial energy density profiles. We show that the neural network can be trained accurately enough so that it can reliably predict the hydrodynamic results for the flow coefficients and, remarkably, also their correlations like normalized symmetric cumulants, mixed harmonic cumulants, and flow-transverse-momentum correlations. At the same time the required computational time decreases by several orders of magnitude. To demonstrate the advantage of the significantly reduced computation time, we generate 10^7 initial energy density profiles from which we predict the flow observables using the neural network, which is trained using 5×10^3, and validated using 9×10^4 events per collision energy. We then show that increasing the number of collision events from 9×10^4 to 10^7 can have significant effects on certain statistics-expensive flow correlations, which should be taken into account when using these correlators as constraints in the determination of the quantum chromodynamics matter properties.

I. INTRODUCTION

Probing the properties of the strongly interacting matter close to a zero net-baryon density is the primary goal of the highest-energy ultrarelativistic heavy-ion collision experiments. One of the most important tools in interpreting the experimental data is relativistic hydrodynamics. In the hydrodynamic limit the matter behavior is controlled by the matter properties like equation of state and transport coefficients, such as shear and bulk viscosity. It has been well established that in heavy-ion collisions flow-like signatures are seen in azimuthal angle spectra of produced particles. This indicates that a small droplet of deconfined phase of quantum chromodynamics (QCD) matter called quark-gluon plasma (QGP) is created in these collisions, and that it exhibits a fluid-like behavior [1–4].

Comparing the measurements with the predictions of hydrodynamic computations gives then a possibility to determine the QCD matter properties. A reliable estimate of the QCD matter properties with well-defined error bars demands a global analysis of as many experimental observables and collision systems as possible. In the recent years, such global analyses have given constraints on the QCD transport properties [5–14]. In particular, the shear viscosity near the QCD transition temperature $T \approx 155$ MeV is rather well constrained. For the full temperature dependence of shear viscosity, and especially bulk viscosity, the uncertainties are significantly larger.

A way to improve the analysis is to consider more observables. One challenge here is that in practice it is necessary to compute the hydrodynamic evolution event by event, i.e., for each collision event separately, so that the computed observables are obtained as averages over a large number of collisions to closely match with the actual measurements. The nontrivial dependence of the final observables on the equation of state, transport coefficients, initial conditions, and the details of the conversion of the fluid to particles together with numerically demanding hydrodynamic simulations makes the global analysis a very CPU intensive task. In particular, this is the case when the global analysis takes into account observables that require high statistics obtained by accumulating a large number of computed collision events.

The most basic experimental observables quantifying the magnitude and details of the flow-like behavior are the Fourier coefficients of an azimuthal hadron spectrum, which are usually referred to as flow coefficients v_n. They are measured as multiparticle correlations. The increased luminosity in recent measurements, especially at the CERN Large Hadron Collider (LHC), has enabled precision measurements of multiparticle correlations between flow coefficients all the way up to the eight-particle level. Obtaining reliable estimates of these correlations from the fluid dynamical simulation can require gathering statistics from about 10^6 collision events. Obtaining such high statistics is computationally very expensive and performing computations gets even more expensive when sampling the $\mathcal{O}(15)$-dimensional parameter space of a global analysis, where statistics should be obtained for around 300 different parametrizations. Typically one event needs about 30 min computing time from a CPU and thus the total

time it would take to perform high statistic global analysis is around $0.5 \times 10^6 \times 300 \approx 10^8$ CPU hours.

One way to decrease the computation time would be to convert the codes to GPU and use a modern GPU based supercomputer to do the computing. Even though this would significantly speed up the simulations, the task would still require a significant amount of computing time. Another possibility is to simplify the complicated fluid dynamical computations and construct fast estimators that can give good estimates of the final state observables from the initial state alone. The simple version of such an estimator for flow coefficients could be constructed, for example, by assuming a linear relation between initial state eccentricities and corresponding flow coefficients. As shown in Refs. [6,15,16] this kind of linear relation works reasonably well for v_2 in central collisions, but nonlinear effects start to get noticeable in more peripheral collisions and even more so in the case of higher-order flow coefficients for which this kind of estimator would not work well even to begin with.

In this article we present a way to estimate p_T-integrated flow observables and correlators directly from the initial energy density profile based on deep convolutional neural networks (CNN). The convolutional neural networks have been proven to be very efficient and accurate tools when it comes to image classification and computer vision tasks. During the past decade, network architectures have evolved towards deeper and deeper networks, i.e., a typical network contains more layers than before. A modern CNN architecture can contain hundreds of layers and tens of millions trainable parameters. Neural networks and deep learning have been utilized before in the context of heavy-ion collisions for various different applications, such as impact parameter estimation, identifying quenched jets, or determination of the QCD matter phase transition [17–21]. In Ref. [22] it was shown that the neural network can also model full hydrodynamic evolution on short time periods, $\Delta \tau \approx 2$ fm, but this kind of method has not yet been applicable for modeling a complete space-time evolution of QGP. The deep neural network was also applied to estimating v_2 from the kinematic information of particles in the context of the AMPT model [23]. However, until the current study, neural networks have not been successfully trained to predict flow observables and correlators from the initial state energy density.

The basic setup here is the perturbative QCD based EKRT (Eskola-Kajantie-Ruuskanen-Tuominen) gluon saturation model [24,25] for the computation of initial conditions that, when supplemented by relativistic hydrodynamic evolution [6,26], gives a good overall description of the available flow data from heavy-ion collisions at the BNL Relativistic Heavy Ion Collider (RHIC) and LHC [27–29]. The neural network constructed here is, however, not restricted to this particular model, but can in principle be applied to any similar framework.

This paper is organized in the following way. In Sec. II we briefly go through the structure of the used neural network and give details about how it is implemented in practice. In Sec. III we validate the accuracy of the neural network by showing that the results obtained by the network match well with the hydrodynamic simulations. The main results are then

TABLE I. The structure of the used DenseNet network.

Block	Output size	Layers
Convolution	$134 \times 134 \times 64$	7×7 conv, stride 2
Pooling	$67 \times 67 \times 64$	3×3 max pool, stride 2
Dense block	$67 \times 67 \times 256$	$\begin{bmatrix} 1 \times 1 \text{ conv} \\ 3 \times 3 \text{ conv} \end{bmatrix} \times 6$
Transition layer	$67 \times 67 \times 128$ $33 \times 33 \times 128$	1×1 conv 2×2 average pooling, stride 2
Dense block	$33 \times 33 \times 512$	$\begin{bmatrix} 1 \times 1 \text{ conv} \\ 3 \times 3 \text{ conv} \end{bmatrix} \times 12$
Transition layer	$33 \times 33 \times 256$ $16 \times 16 \times 256$	1×1 conv 2×2 average pooling, stride 2
Dense block	$16 \times 16 \times 896$	$\begin{bmatrix} 1 \times 1 \text{ conv} \\ 3 \times 3 \text{ conv} \end{bmatrix} \times 20$
Transition layer	$16 \times 16 \times 448$ $8 \times 8 \times 448$	1×1 conv 2×2 average pooling, stride 2
Dense block	$8 \times 8 \times 1216$	$\begin{bmatrix} 1 \times 1 \text{ conv} \\ 3 \times 3 \text{ conv} \end{bmatrix} \times 24$
Output layer	$1 \times 1 \times 1216$	8×8 global average pooling
	N_{out}	Fully connected layer with ReLU activation

shown in Sec. IV, where we present the neural network predictions for various different correlators with 10^7 generated collision events. The summary and conclusions are then given in Sec. V.

II. MODEL SETUP

A. DenseNet

The evolution of CNN architectures towards deeper networks has caused challenges to their design [30]. Very deep networks can easily lose some information about the input. Additionally, when propagating the gradient information from the output back to the input, the gradients can start to approach zero. Therefore, the optimizer leaves the network weights close to the input nearly unchanged so that the loss function won't converge to the global minima. This makes the training of a model slow and inaccurate. To solve the vanishing gradient and feature loss problem a dense convolutional network or DenseNet was introduced [31]. The DenseNet consists of two major building blocks: dense blocks and transition layers. The dense block solves the vanishing gradient and feature loss problems by reusing features from the previous layers via concatenation, so that all the proceeding layers in the dense block use feature maps from the previous layers as inputs. This makes it possible to maintain low complexity features while also taking advantage of the deep network's ability to probe very complex features of the training data. Such a property makes the DenseNet a great choice when the data
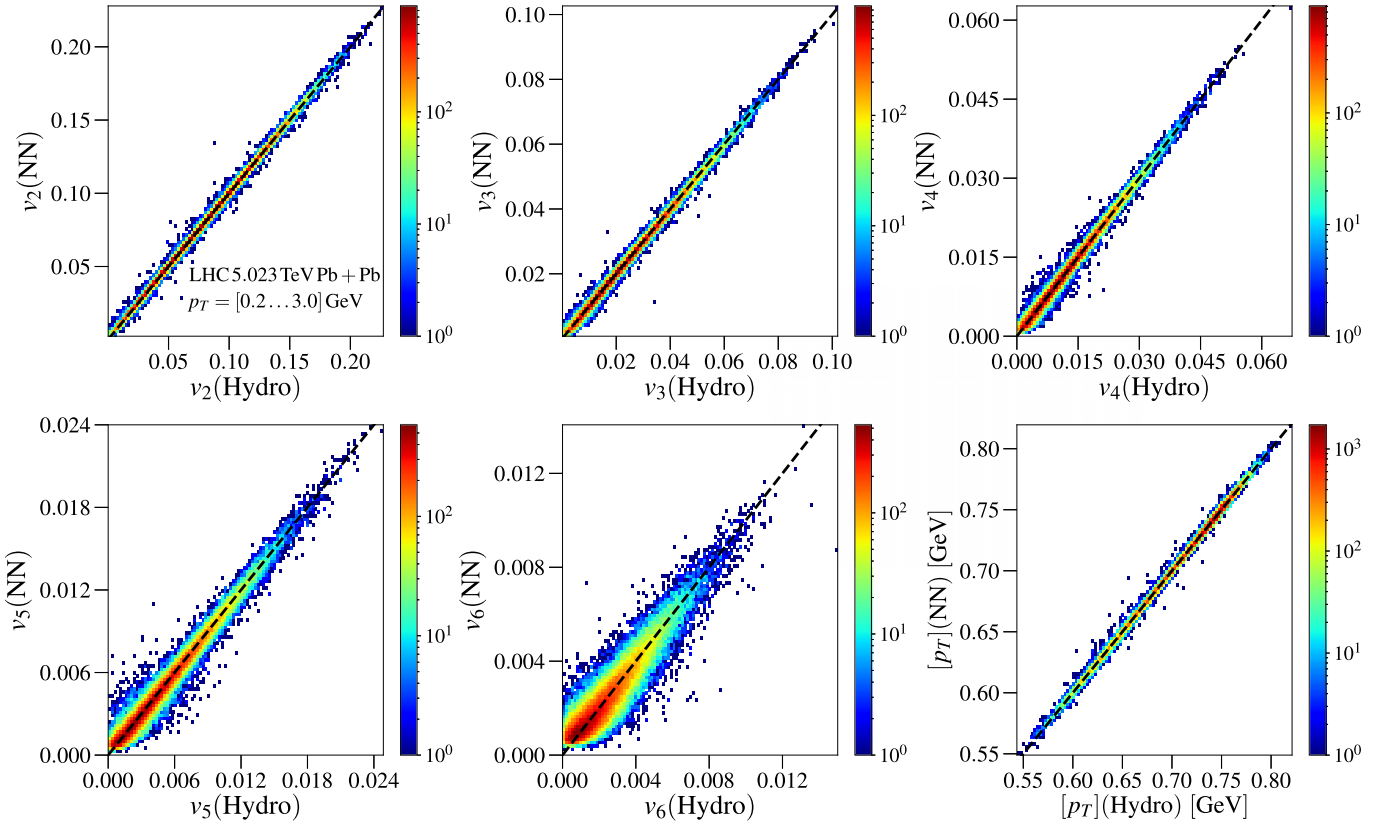
FIG. 1. The event-by-event neural network (NN) predictions versus the results from the hydrodynamic simulations for the validation events in the 0–80% centrality range.

set is somewhat limited and overfitting becomes an issue. The transition layers are then used to reduce the input size. It uses a 1×1 convolutional layer followed by a 2×2 average pooling layer.

In this study we use the DenseNet-BC variant which applies a 1×1 convolutional bottleneck layer before each 3×3 convolution layer in the dense blocks and compression to the transition layer with compression parameter $\theta = 0.5$, which reduces the number of feature-maps by a factor of 2. The growth rate is set to $k = 32$. The DenseNet is originally designed for computer vision tasks and to adapt it to a regression task we change the softmax activation function of the output layer to a linear activation function. The exact structure of the model is shown in Table I, where each convolutional layer contains convolutional layer + batch normalization + ReLU activation. Compared to the original DenseNet model we have changed 3×3 and 7×7 convolution layers with depthwise separable convolution layers, which seems to improve the stability and slightly decrease the validation loss of the model.

B. Implementation

The DenseNet model is trained using midrapidity observables obtained from the hydrodynamic simulations of heavy-ion collisions computed in Ref. [29]. The initial energy density profiles for the hydrodynamic evolution are calculated from the EKRT model [6,26], where the event-by-event fluctuations emerge from the random positions of nucleons inside

the colliding nuclei. The computation of the initial profiles is very fast and takes a negligible amount of CPU time compared to the computation of the hydrodynamic evolution and the corresponding physical observables for each event. It is quite easy to generate millions of initial conditions corresponding to different collision events.

As an input, the DenseNet model uses discretized initial energy density in the transverse-coordinate (x, y) plane calculated from the EKRT-model with a grid size 269×269 and a resolution of 0.07 fm. The DenseNet model is trained to reproduce a set of final state p_T integrated observables v_n, average transverse momentum $[p_T]$, and charged particle multiplicity $dN_{ch}/d\eta$ for each event. The input energy density is normalized in such a way that the training data set has a mean of zero and a standard deviation of one.

The DenseNet model gives then a full event-by-event distribution of these observables, and it allows us to build a set of measurable quantities, such as event-averaged N-particle flow coefficients $v_n\{N\}$, normalized symmetric cumulants $NSC(m, n)$, normalized mixed harmonic cumulants $nMHC(n, m)$, and flow-transverse-momentum correlations $\rho(v_n^2, [p_T])$. Note that these observables are different moments of the full $\mathcal{P}(v_n, [p_T], dN_{ch}/d\eta)$ distribution, e.g., two-particle flow coefficient $v_n\{2\}$ is a root-mean-square event average of v_n. It is nontrivial that the network can be trained to a sufficient accuracy to reproduce these observables, the correlators in particular. The definitions of all these
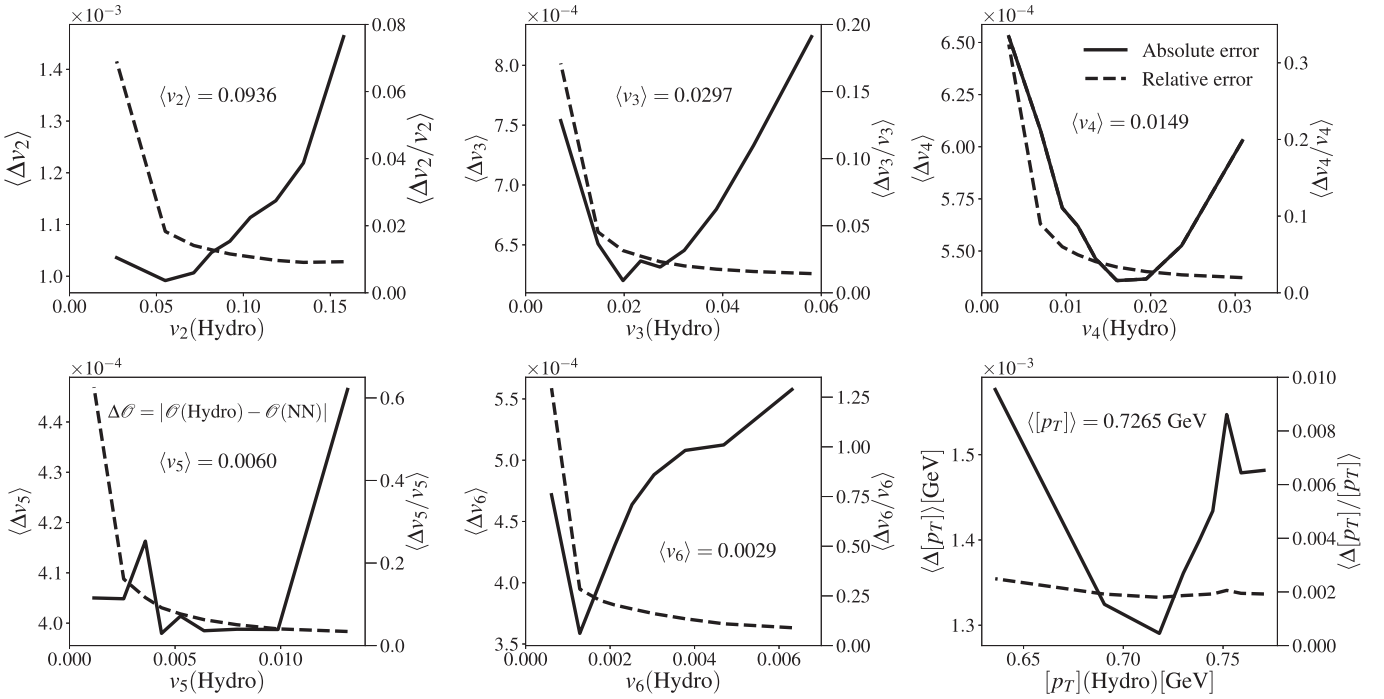
FIG. 2. The mean absolute and relative errors between the neural network predictions and the results from the hydrodynamic simulations for the validation events in the 0–80% centrality range.

observables and the details of the EKRT-model and hydrodynamic computations can be found from Refs. [6,29].

We note that here all the events in a training data set use the same parameters for hydrodynamic evolution, meaning that, currently, the trained neural network cannot predict results from hydrodynamic simulations that use for example different viscosity parametrizations.

We train a separate neural network for each of the flow coefficient v_2, v_3, v_4, v_5, v_6, for the average transverse momentum $[p_T]$, and multiplicity $dN_{ch}/d\eta$ outputs using in total of 2×10^4 hydrodynamic events in the training. However, one network can give multiple outputs (N_{out} in Table I) of the same observable with different p_T integration ranges. This is necessary since different measurements use different p_T ranges when measuring the observables.

The training events are distributed evenly (5000 events each) between 200 GeV Au + Au, 2.76 TeV Pb + Pb, 5.023 TeV Pb + Pb, and 5.44 TeV Xe + Xe collision systems. The outputs of different neural networks are normalized with a constant such that the typical value of a given output observable is O(1). This makes possible to set the same learning rate for different observables without affecting the quality of the training too much. The exception to this is the charged particle multiplicity network for which the output is not normalized because it uses a different loss function than the other networks. The training data are heavily augmented by applying random rotations (rotation angle from 0 to 2π), flips and translations (shifts from -0.92 fm to 0.92 fm in both x and y directions) to the input during the training.

All the network models above are trained using the Adam optimizer [32] for 120 epochs with a batch size of 64. Using larger batch sizes made the training phase faster, but at the same time significantly decreased the accuracy of the networks. The learning rate is initially set to 0.001, except in the case of the charged particle multiplicity where the initial learning rate is 0.01, and it is divided by a factor of 10 at epochs 75 and 110. Even though the use of a decaying learning rate is not completely necessary because of the adaptive nature of the Adam optimizer, we noticed that adding a learning rate decay made the training faster without sacrificing accuracy. Additionally, the batch normalization momentum is set to 0.1. As a regularization method we tried both the dropout and L2 regularization, but they did not give any improvements for the validation accuracy or made it worse. This is most likely due to a heavy data augmentation which in itself acts as an efficient regularization method.

For all observables except charged particle multiplicity, we use a mean squared error (MSE) loss function which is defined as

$$\text{Loss(MSE)} = \frac{1}{N} \sum_i (y_{i,\text{true}} - y_{i,\text{pred}})^2, \quad (1)$$

where the sum is over all events in the training batch, N is the number of events in a training batch, and $y_{i,\text{true}}$ and $y_{i,\text{pred}}$ are the true and predicted values of an observable, respectively. For the charged particle multiplicity we use a mean squared logarithmic error (MSLE) loss function,

$$\text{Loss(MSLE)} = \frac{1}{N} \sum_i \left(\ln(y_{i,\text{true}} + 1) - \ln(y_{i,\text{pred}} + 1) \right)^2. \quad (2)$$

The training is done using the Nvidia Tesla V100 GPU, which has 32 GB of VRAM and 640 tensor cores. The training time for one network is ca. 80 min. The neural network code
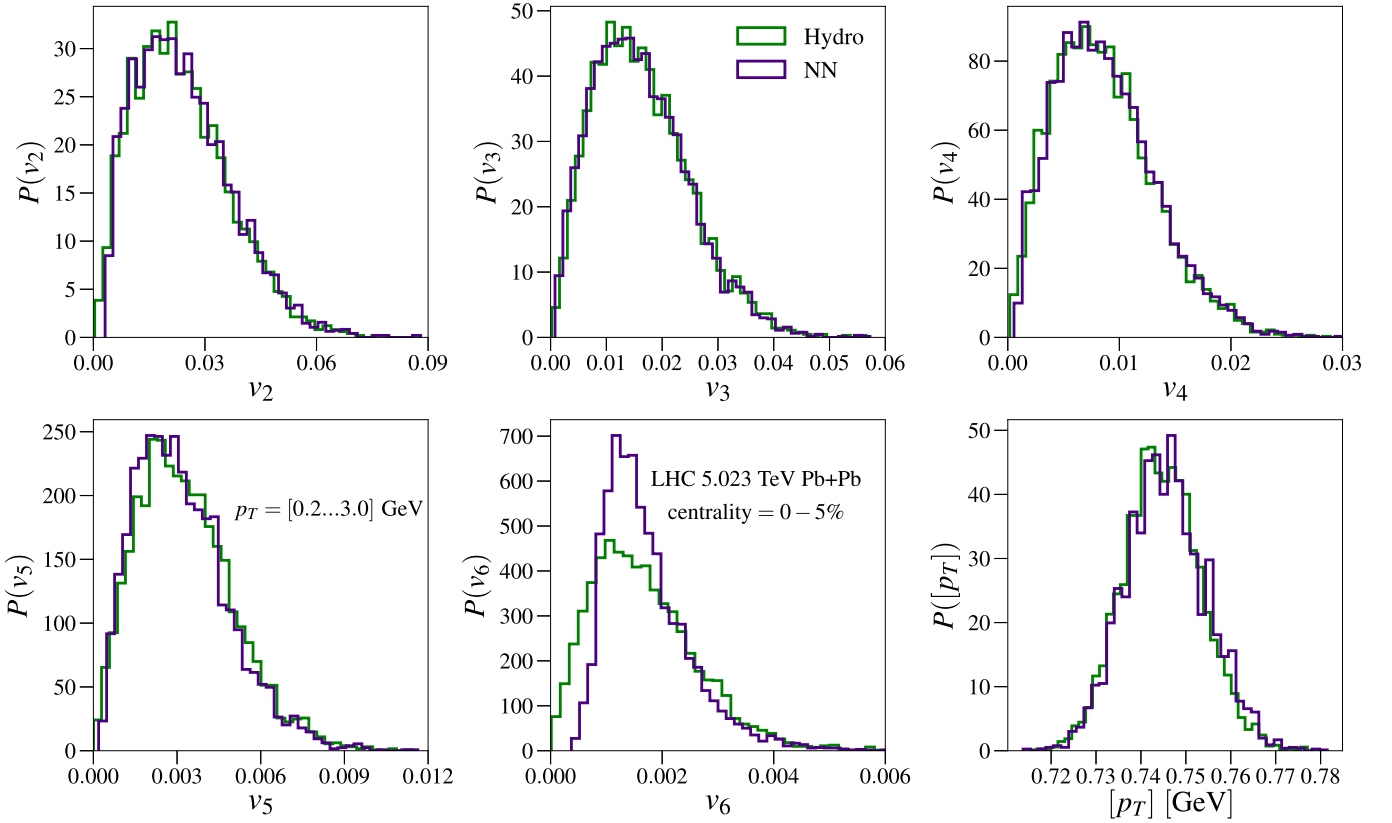
FIG. 3. The distributions of flow observables from the neural network predictions and hydrodynamic simulations for the validation events in the 0–5% centrality range.

is written in PYTHON and it is implemented using the Keras Deep Learning API v2.10.0 [33] together with the Tensorflow v2.10.0 library [34]. The pretrained networks and the code that can be used to generate EbyE flow observables from EKRT-model initial energy density are available as the Supplemental Material [35].

III. VALIDATION

After the training, the accuracy of the neural network needs to be tested with an independent validation data set. Here, we only focus on results for a 5.023 TeV Pb + Pb collision system, but the performance of the neural network is similar for other systems as well. The testing is done by generating 9×10^7 initial energy density profiles and comparing neural network predictions for different observables against those obtained from hydrodynamic simulations. We remind that only 5000 5.023 TeV events were used in the training of the network.

In Fig. 1, we show a two-dimensional (2D) histogram comparing the neural network predictions against hydrodynamic computations event by event for the flow coefficients v_n ($n = 2, 3, 4, 5, 6$) and average transverse momenta $[p_T]$. The color bar indicates the number of events in each histogram bin and the dashed black line indicates where hydrodynamic computations and neural network predictions match exactly. Because the observables we are interested in are inside the 0–80% centrality range, we only show events from this centrality range in the histogram.

For v_2 we see an excellent agreement between the neural network and hydrodynamic results. The accuracy of the network starts to slowly decrease when moving towards higher-order flow coefficients and in the cases of v_5 and v_6 we already start to see clear deviations from the hydrodynamic results. This behavior is expected since the lower-order flow coefficients and initial-state eccentricities have quite linear dependence and they are not as sensitive to nonlinear effects arising from hydrodynamic evolution as higher-order flow coefficients. For the average transverse momentum the neural network seems to predict the hydrodynamic results very accurately. However, one needs to note that event-by-event fluctuations of $[p_T]$ are very small compared to the absolute value of $[p_T]$. This means that relatively small errors are not necessarily a guarantee of that the network can correctly predict correlations involving $[p_T]$.

To complement the information in Fig. 1 and to give more quantitative estimates of errors, we show the mean absolute and the relative errors for different observables in Fig. 2. Here, we can confirm that the relative error is indeed increasing when increasing the order of the flow coefficients. The errors are not very sensitive to the value of an observable but typically the absolute errors are smallest close to the average value of the observable. We can also notice that the relative error is the largest when the value of an observable is small. The small values of flow coefficients
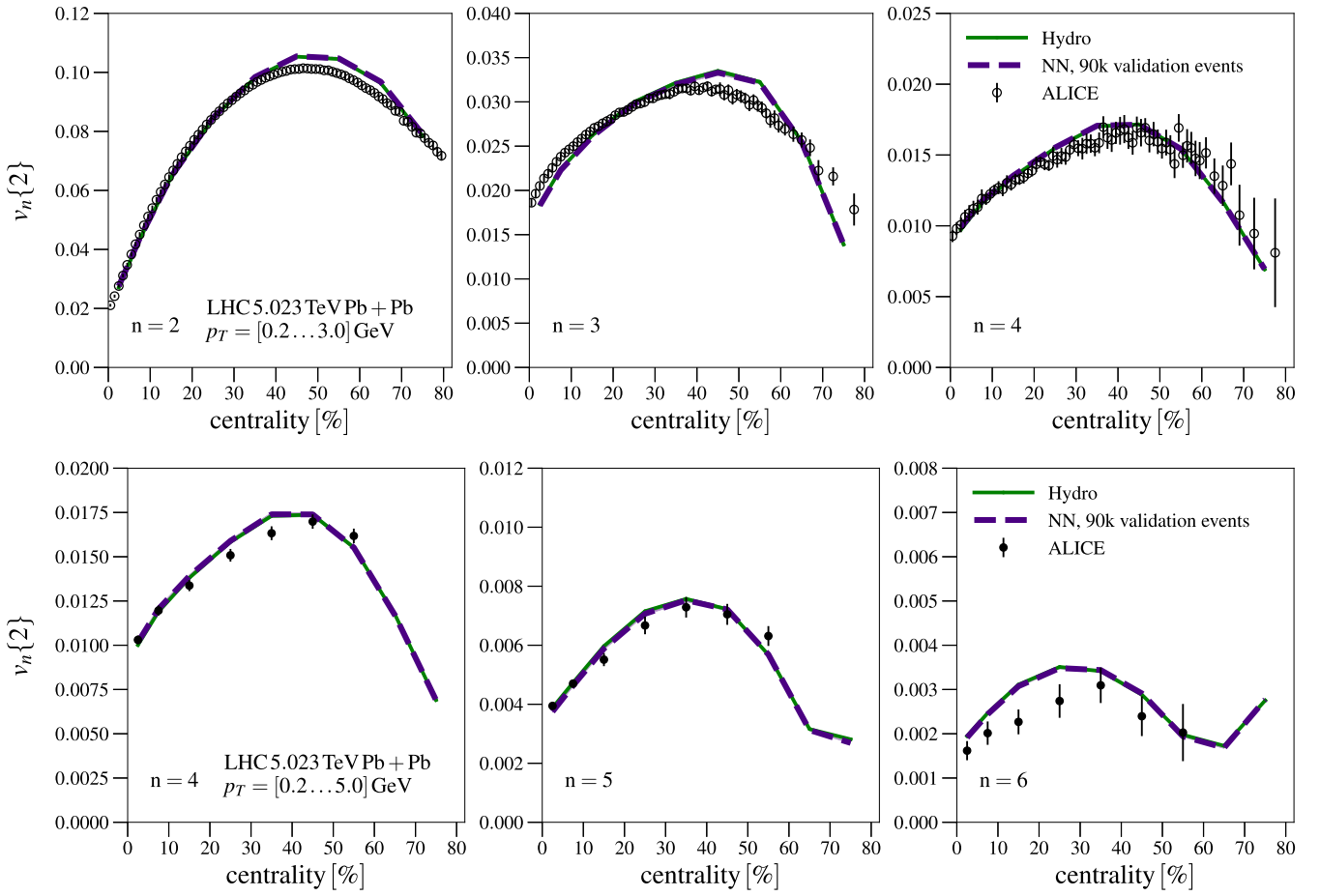
FIG. 4. The comparison of the flow coefficients $v_n\{2\}$ between the neural network predictions and hydrodynamic computations. The experimental data are from the ALICE Collaboration [36,37].

usually correspond to the most central or the most peripheral collisions.

To see where the growing relative errors at the smallest values of v_n start to play a role, we compare distributions of flow observables between the neural network predictions and hydrodynamic computations in the most central collisions. The results are shown in Fig. 3, where we

can see that the distributions are nearly identical except for the flow coefficient v_6. In this case the distribution given by the neural network prediction is narrower than the one obtained from the hydrodynamic computation while the location of the peak value is very similar in both cases. This indicates that the neural network might be able to reproduce the average values of v_6 quite well but it
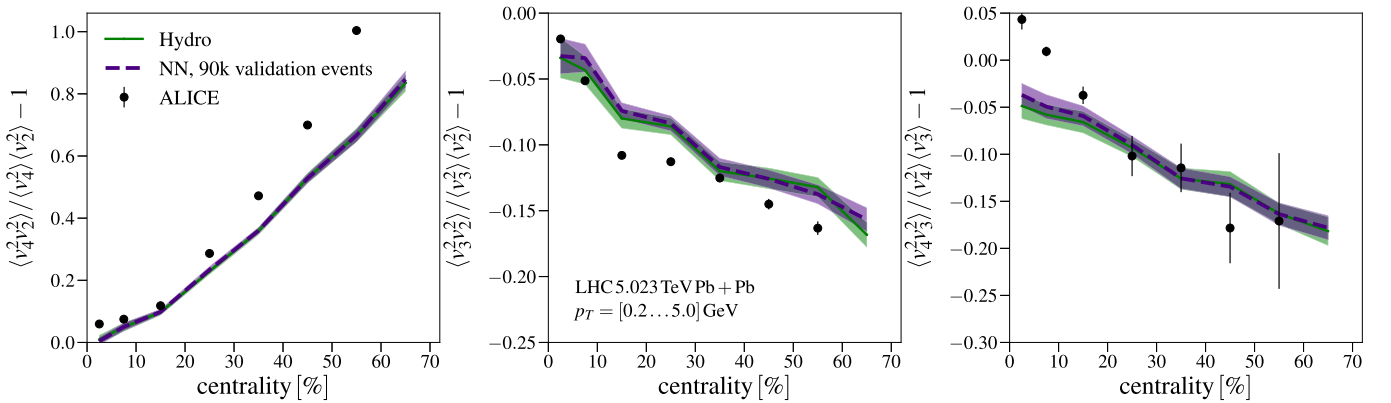
FIG. 5. The comparison of normalized symmetric cumulants between the neural network predictions and hydrodynamic computations. The experimental data are from the ALICE Collaboration [38].
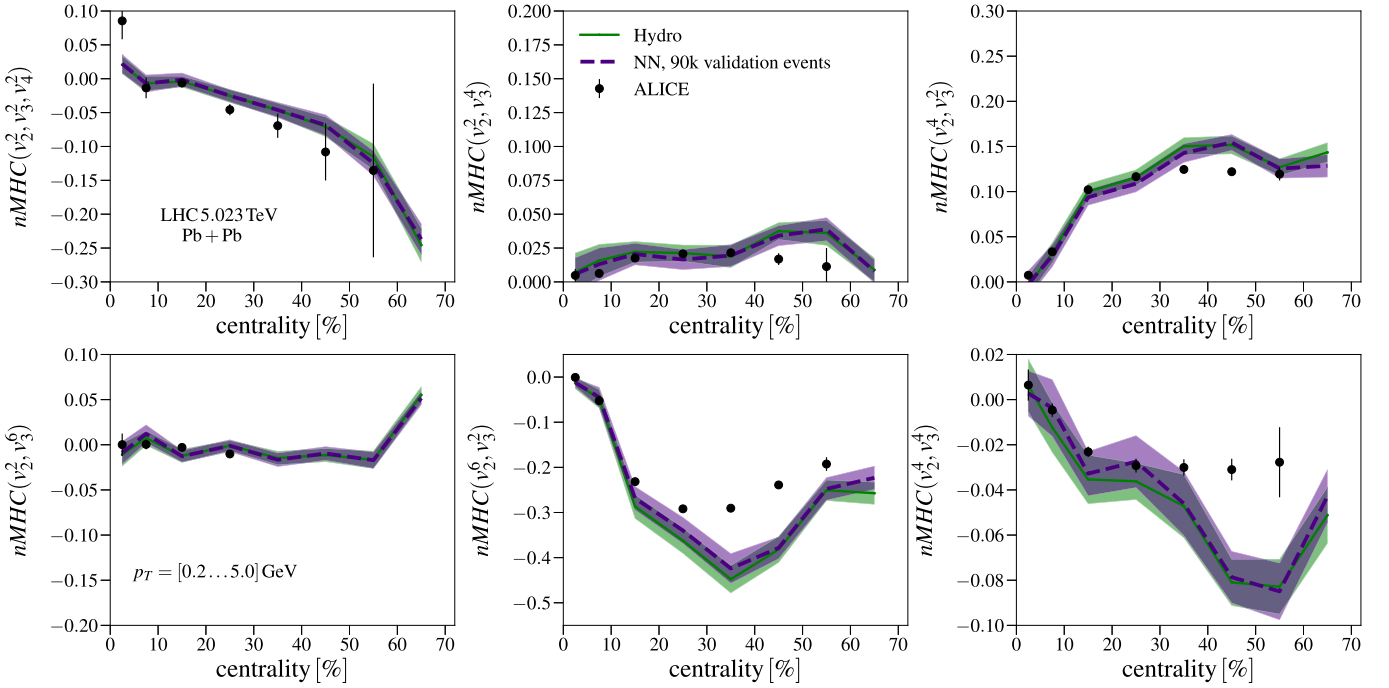
FIG. 6. The comparison of normalized mixed harmonic cumulants between the neural network predictions and hydrodynamic computations. The experimental data are from the ALICE Collaboration [38].

cannot be guaranteed to reliably predict the correlations involving v_6.

Comparing the neural network and hydrodynamic results event by event gives information about the accuracy of the network, but the measurements average over a large number of events in centrality bins. Consequently, it is crucial to test the performance of the network in these cases as well. To get a comprehensive view of the network's ability we check its performance for two-particle flow coefficients $v_n\{2\}$, normalized symmetric cumulants $NSC(m, n)$, normalized mixed harmonic cumulants $nMHC(n, m)$, and flow-transverse-momentum correlations $\rho(v_n^2, [p_T])$.

The flow coefficients $v_n\{2\}$ are shown in Fig. 4 as a function of centrality. We can see that the neural network results seem to match the hydrodynamic results nearly exactly. This is true even in the cases of v_5 and v_6 where the event-by-event accuracy of networks was not as good.

Much more challenging quantities to predict are the different correlations between the flow coefficients. In Fig. 5 we show the centrality dependence of the normalized symmetric cumulants $NSC(m, n)$. The statistical errors are estimated via jackknife resampling as in Ref. [29]. The normalized symmetric cumulants are four-particle correlations between two flow harmonics and thus are more sensitive to event-by-event fluctuations than the flow coefficients $v_n\{2\}$. This makes it more challenging to predict them using the neural network. Nevertheless, in the case of $NSC(4, 2)$ we get an almost exact agreement between the neural network and the hydrodynamic results. For $NSC(3, 2)$ and $NSC(4, 3)$ there are some visible differences between the two, but deviations are still quite small compared to the statistical errors.

The normalized mixed harmonic cumulants $nMHC(n, m)$, which are six- or eight-particle correlations, are shown in

Fig. 6. The agreement between the neural network predictions and the hydrodynamic computation is again good, even in the cases where the correlation is very weak. Finally, in Fig. 7, we show the flow-transverse-momentum correlations $\rho(v_n^2, [p_T])$ as a function of the number of participant nucleons. In this observable the biggest challenge for the neural network is not the accuracy of the flow coefficients as one might naively expect, but instead the accuracy of the mean transverse momentum. This is due to the fact that the correlation is very sensitive to the mean transverse momentum fluctuations and, as discussed earlier, catching these fluctuations requires a very good precision from the neural network. Nevertheless, as can be seen from Fig. 7, the neural network predictions agree well with the hydrodynamic results.

IV. HIGH-STATISTICS PREDICTIONS

Now that the accuracy of the neural network has been established, we can use it to estimate what happens to the above correlations at a high-statistics limit. To do so we generate 10^7 events using the neural network, which takes around 20 h with the GPU. This is a very substantial difference compared to doing full hydrodynamic simulations using CPU, which would take about 5×10^6 CPU hours.

The effect of increased statistics for the normalized symmetric cumulants can be seen in Fig. 8. In the case of $NSC(4, 2)$ we see slight deviations in the most central and peripheral collisions, but the centrality dependence is very similar to the lower statistics hydrodynamic results. This is not surprising since the statistical errors are already relatively small with 9×10^4 events. The situation is quite different for $NSC(3, 2)$ where the statistical errors are of considerable size with 9×10^4 events. Here, we see that
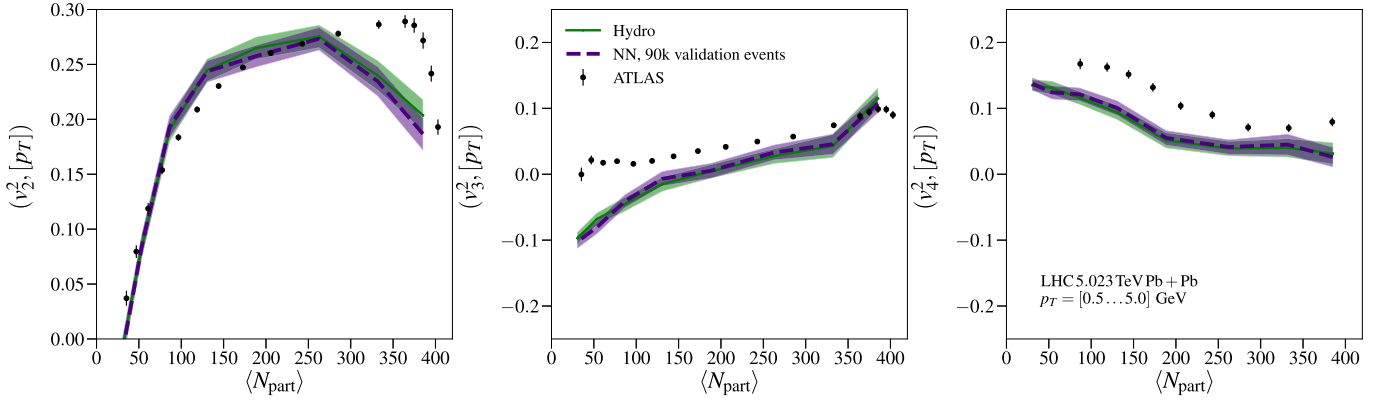
FIG. 7. The comparison of flow-transverse-momentum correlations between the neural network predictions and hydrodynamic computations. The experimental data are from the ATLAS Collaboration [39].

with 10^7 events the statistical fluctuations are negligible, revealing the true centrality dependence from the model, and it now gives a very similar shape as the ALICE measurements, even though the neural network prediction (i.e., the underlying hydrodynamic simulation with which the network was trained) underestimates the amount of anticorrelation. For $NSC(4, 3)$ we also see some deviations from the lower-statistics hydrodynamic result in the most central and peripheral collisions. We note that in the most central collisions we see a somewhat similar difference between the neural network and the hydrodynamic result also in the validation data set, which might indicate that this difference can be a systematic error caused by the inaccuracy of the neural network.

In principle, the normalized mixed harmonic cumulants in Fig. 9 should be even more sensitive to the increased event number, since correlations are usually weaker than in the case of the normalized symmetric cumulants. For $nMHC(v_2^2, v_3^4)$ the neural network prediction with 10^7 events is inside the statistical errors of the hydrodynamic results, but in the central collisions the increased number of events reveals a very different kind of centrality dependence which seems to agree well with the ALICE measurements. In the cases of $nMHC(v_2^4, v_3^2)$ and

$nMHC(v_2^6, v_3^2)$ we see statistically significant differences between the hydrodynamic results and 10^7 event predictions, which signals that the jackknife resampling can sometimes significantly underestimate the statistical errors. For $nMHC(v_2^2, v_3^6)$ we see that increasing the number of events from 9×10^4 to 10^7 removes the sharp changes between the correlation and anticorrelation and the high statistic result is nearly zero except in the most peripheral collisions. This is again in line with the ALICE measurements.

The flow-transverse-momentum correlations for the 10^7 neural network prediction are shown in Fig. 10. The increased statistics makes it now possible to use exactly the same centrality bins as the ATLAS measurements without completely ruining the accuracy. For $\rho(v_2^2, [p_T])$ the 10^7 event result differs substantially from the 9×10^4 event hydrodynamic result only in the most central collisions. This effect is mostly a combination of different centrality binning and the fact that correlation decreases very quickly when moving from 375 to 400 participants. The effect of statistics can be better seen in the case of $\rho(v_3^2, [p_T])$, where in the central collisions the 10^7 event result has different dependence on participant number than the 9×10^4 event hydrodynamic result. In this region the 10^7 event neural network result also agrees better with the ALICE measurements.
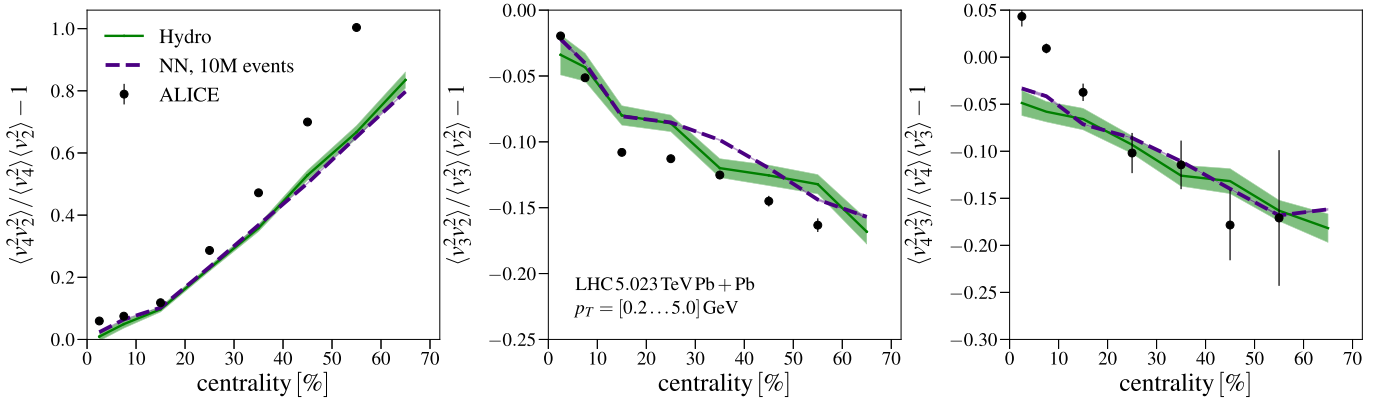

FIG. 8. The neural network prediction of normalized symmetric cumulants with 10^7 collision events compared with the hydrodynamic results from 9×10^4 collision events. The experimental data are from the ALICE Collaboration [38].
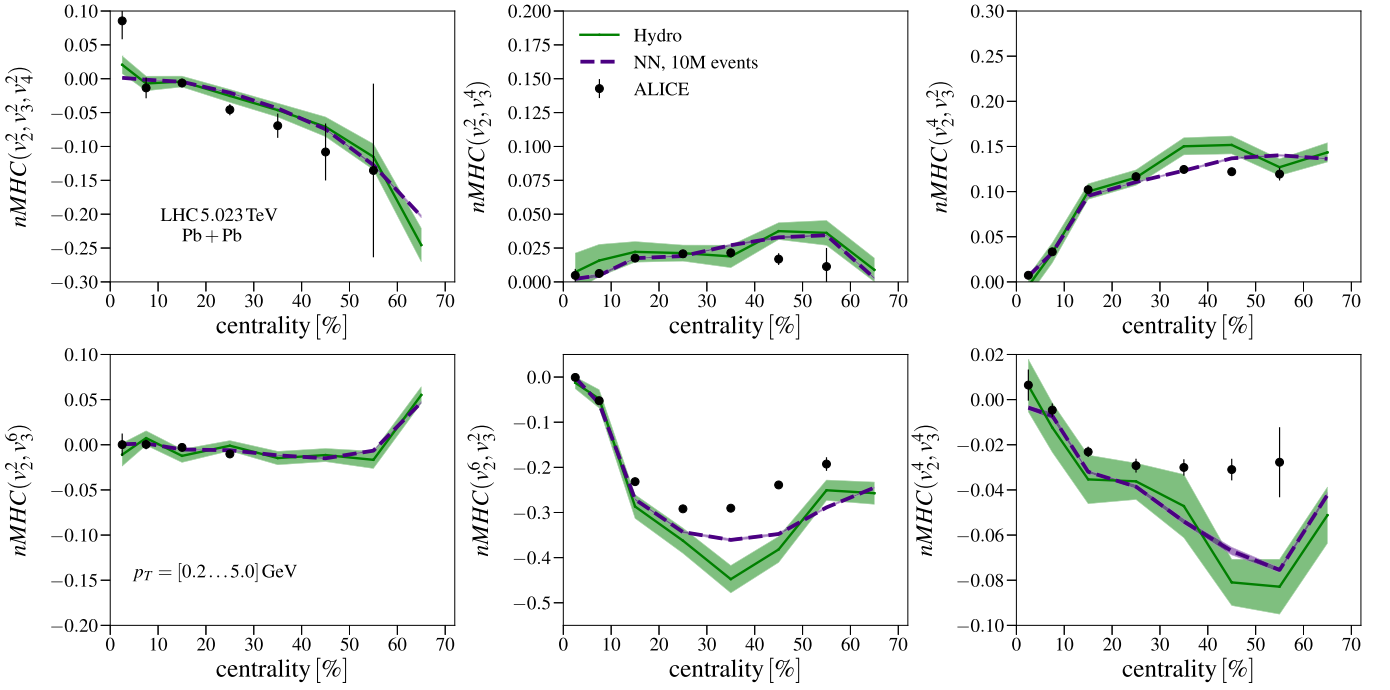
FIG. 9. The neural network prediction of normalized mixed harmonic cumulants with 10^7 collision events compared with the hydrodynamic results from 9×10^4 collision events. The experimental data are from the ALICE Collaboration [38].

V. CONCLUSIONS AND SUMMARY

We have trained a deep convolutional neural network to predict a variety of flow observables from the initial state energy density profiles. The training was done using 2×10^4 training events from 200 GeV Au + Au, 2.76 TeV Pb + Pb, 5.023 TeV Pb + Pb, and 5.44 TeV Xe + Xe collision systems, with 5000 events for each collision system. The training data were computed using viscous relativistic hydrodynamics with initial conditions from the EKRT model, and using the model and viscosity parameters from Ref. [29].

The accuracy of the network was tested against the results from hydrodynamic simulations for two-particle flow coefficients $v_n\{2\}$, normalized symmetric cumulants $NSC(m, n)$, normalized mixed harmonic cumulants $nMHC$, and flow-transverse-momentum correlations $\rho(v_n^2, [p_T])$. We

emphasize that this is a nontrivial test for the accuracy of the network, especially with the correlators. The validation tests used in total of 9×10^4 events for each collision system, independent of the training data, and in all of the cases the neural network was able to predict hydrodynamic results quite reliably. This is already a significant improvement in terms of computational time, as only 5000 events were used per collision system to train the network.

The neural network was then used to predict the same flow observables but this time with 10^7 generated events. This took around 20 GPU hours of computing time which is many orders of magnitude faster than doing the same number of hydrodynamic simulations using CPU. The increased number of events made statistical errors negligibly small and allowed us to estimate the observables with a higher precision. In many
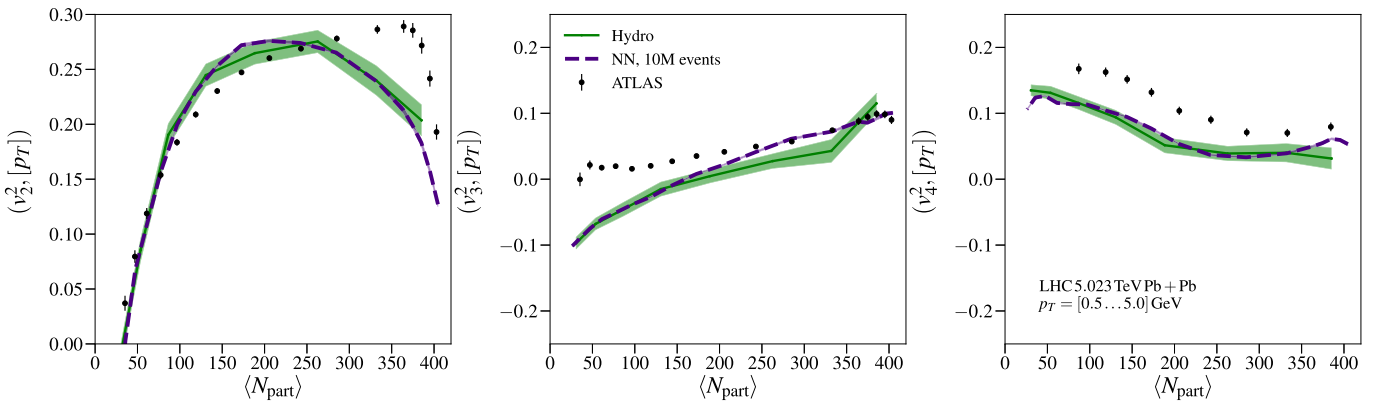

FIG. 10. The neural network prediction of flow-transverse-momentum correlations with 10^7 collision events compared with the hydrodynamic results from 9×10^4 collision events. The experimental data are from the ATLAS Collaboration [39].

cases the 10^7 event neural network prediction differed from the 9×10^4 event hydrodynamic computations by a quite large margin emphasizing the importance of a large event statistics when comparing simulations with the measurements.

As there are still considerable uncertainties in determining QCD matter properties from the experimental data, it is important to be able to use as many measurements as possible to constrain the properties. In particular, the current measurements at the LHC give a wealth of different flow correlations with tight error bars that provide independent information about the matter properties. Many of the measured correlators are rather weak, and can require millions of computed hydrodynamic events in order to get similar statistical errors as in the experiments. To use these quantities as a constraint to the QCD properties, it is then necessary to have a computationally efficient way to generate such a large set of events, and this is exactly what the neural network presented here can do.

Currently the neural network can predict flow observables for different initial energy density profiles, but the predictions always describe a hydrodynamic evolution that is identical to the one used in the training data set, i.e., it is not possible to change the viscosity parametrization after the network has been trained. The network should next be constructed to be more versatile and take viscosity parameters as additional inputs, making the neural network an even more efficient tool in global analysis. This is left as future work.

[1] U. Heinz and R. Snellings, Annu. Rev. Nucl. Part. Sci. **63**, 123 (2013).

[2] C. Gale, S. Jeon, and B. Schenke, Int. J. Mod. Phys. A **28**, 1340011 (2013).

[3] P. Huovinen, Int. J. Mod. Phys. E **22**, 1330029 (2013).

[4] C. Shen, Nucl. Phys. A **1005**, 121788 (2021).

[5] C. Gale, S. Jeon, B. Schenke, P. Tribedy, and R. Venugopalan, Phys. Rev. Lett. **110**, 012302 (2013).

[6] H. Niemi, K. J. Eskola, and R. Paatelainen, Phys. Rev. C **93**, 024907 (2016).

[7] J. E. Bernhard, J. S. Moreland, S. A. Bass, J. Liu, and U. Heinz, Phys. Rev. C **94**, 024907 (2016).

[8] S. A. Bass, J. E. Bernhard, and J. S. Moreland, Nucl. Phys. A **967**, 67 (2017).

[9] J. E. Bernhard, J. S. Moreland, and S. A. Bass, Nat. Phys. **15**, 1113 (2019).

[10] D. Everett *et al.* (JETSCAPE Collaboration), Phys. Rev. C **103**, 054904 (2021).

[11] G. Nijs, W. van der Schee, U. Gürsoy, and R. Snellings, Phys. Rev. C **103**, 054909 (2021).

[12] J. Auvinen, K. J. Eskola, P. Huovinen, H. Niemi, R. Paatelainen, and P. Petreczky, Phys. Rev. C **102**, 044911 (2020).

[13] J. E. Parkkila, A. Onnerstad, and D. J. Kim, Phys. Rev. C **104**, 054904 (2021).

[14] J. E. Parkkila, A. Onnerstad, S. F. Taghavi, C. Mordasini, A. Bilandzic, M. Virta, and D. J. Kim, Phys. Lett. B **835**, 137485 (2022).

[15] F. G. Gardim, F. Grassi, M. Luzum, and J. Y. Ollitrault, Phys. Rev. C **85**, 024908 (2012).

[16] H. Niemi, G. S. Denicol, H. Holopainen, and P. Huovinen, Phys. Rev. C **87**, 054901 (2013).

[17] C. David, M. Freslier, and J. Aichelin, Phys. Rev. C **51**, 1453 (1995).

[18] S. A. Bass, A. Bischoff, J. A. Maruhn, H. Stöcker, and W. Greiner, Phys. Rev. C **53**, 2358 (1996).

[19] P. Xiang, Y. S. Zhao, and X. G. Huang, Chin. Phys. C **46**, 074110 (2022).

[20] L. Liu, J. Velkovska, and M. Verweij, J. High Energy Phys. 04 (2023) 140.

[21] L. G. Pang, K. Zhou, N. Su, H. Petersen, H. Stöcker, and X. N. Wang, Nat. Commun. **9**, 210 (2018).

[22] H. Huang, B. Xiao, Z. Liu, Z. Wu, Y. Mu, and H. Song, Phys. Rev. Res. **3**, 023256 (2021).

[23] N. Mallick, S. Prasad, A. N. Mishra, R. Sahoo, and G. G. Barnaföldi, Phys. Rev. D **105**, 114022 (2022).

[24] K. J. Eskola, K. Kajantie, P. V. Ruuskanen, and K. Tuominen, Nucl. Phys. B **570**, 379 (2000).

[25] R. Paatelainen, K. J. Eskola, H. Holopainen, and K. Tuominen, Phys. Rev. C **87**, 044904 (2013).

[26] R. Paatelainen, K. J. Eskola, H. Niemi, and K. Tuominen, Phys. Lett. B **731**, 126 (2014).

[27] H. Niemi, K. J. Eskola, R. Paatelainen, and K. Tuominen, Phys. Rev. C **93**, 014912 (2016).

[28] K. J. Eskola, H. Niemi, R. Paatelainen, and K. Tuominen, Phys. Rev. C **97**, 034911 (2018).

[29] H. Hirvonen, K. J. Eskola, and H. Niemi, Phys. Rev. C **106**, 044913 (2022).

[30] L. Alzubaidi, J. Zhang, A. J. Humaidi, A. Al-Dujaili, Y. Duan, O. Al-Shamma, J. Santamaría, M. A. Fadhel, M. Al-Amidie, and L. Farhan, J. Big Data **8**, 53 (2021).

[31] G. Huang, Z. Liu, L. van der Maaten, and K. Q. Weinberger, arXiv:1608.06993.

[32] D. P. Kingma and J. Ba, arXiv:1412.6980.

[33] F. Chollet *et al.*, https://keras.io/.

[34] M. Abadi *et al.*, arXiv:1603.04467, https://www.tensorflow.org/.

[35] See Supplemental Material at http://link.aps.org/supplemental/10.1103/PhysRevC.108.034905 for the pretrained neural networks and the event generation code.

[36] S. Acharya *et al.* (ALICE Collaboration), J. High Energy Phys. 07 (2018) 103.

[37] S. Acharya *et al.* (ALICE Collaboration), J. High Energy Phys. 05 (2020) 085.

[38] S. Acharya *et al.* (ALICE Collaboration), Phys. Lett. B **818**, 136354 (2021).

[39] G. Aad *et al.* (ATLAS Collaboration), Eur. Phys. J. C **79**, 985 (2019).

PIII

DEEP LEARNING FOR FLOW OBSERVABLES IN HIGH ENERGY HEAVY-ION COLLISIONS

by

Henry Hirvonen, Kari J. Eskola and Harri Niemi.

Deep learning for flow observables in high energy heavy-ion collisions

Henry Hirvonen[1,2,*], *Kari* J. Eskola[1,2,**], and *Harri* Niemi[1,2,***]

[1]University of Jyväskylä, Department of Physics, P.O.B. 35, FI-40014 University of Jyväskylä, Finland
[2]Helsinki Institute of Physics, P.O.B. 64, FI-00014 University of Helsinki, Finland

Abstract. We demonstrate how deep convolutional neural networks can be trained to predict 2+1 D hydrodynamic simulation results for flow coefficients, mean-p_T and charged particle multiplicity from the initial energy density profile. We show that this method provides results that are accurate enough, so that one can use neural networks to reliably estimate multi-particle flow correlators. Additionally, we train networks that can take any model parameter as an additional input and demonstrate with a few examples that the accuracy remains good. The usage of neural networks can reduce the computation time needed in performing Bayesian analyses with multi-particle flow correlators by many orders of magnitude.

1 Introduction

Neural networks have proven to be an effective tool for a variety of applications in heavy-ion physics. These range from performing pre-processing or selection of large data flows in experiments to emulating computationally expensive simulations [1–4]. The rising popularity of neural networks is driven by their accuracy and fast inference speed when dealing with complex multi-dimensional data. These aspects can be crucial when performing real-time data selection or heavy numerical simulations that need to be repeated a large number of times.

The reduced computation time is especially needed when trying to extract the matter properties of the quark-gluon plasma (QGP) from the experimental data through hydrodynamic simulations using a Bayesian analysis. This is due to the fact that one Bayesian analysis will need $\sim 10^6 - 10^9$ simulated collision events depending on which measured observables one includes in the analysis. Performing this many hydrodynamic simulations will take $\sim 10^5 - 10^8$ CPU hours, which makes the inclusion of some multi-particle correlations impractical, even though they could provide additional information to constrain the QCD matter properties.

In principle, all the final state information in hydrodynamic simulation is encoded into the initial state and the matter properties of QGP. However, extracting the final state information directly from the initial state is a highly nontrivial task since relativistic hydrodynamics is a nonlinear theory. The convolutional networks are particularly good at detecting patterns in structured 2-dimensional data, like images, which is why they are excellent tools when trying to estimate the final state observables from an initial state event by event.

---

*Speaker, e-mail: hevivahi@jyu.fi
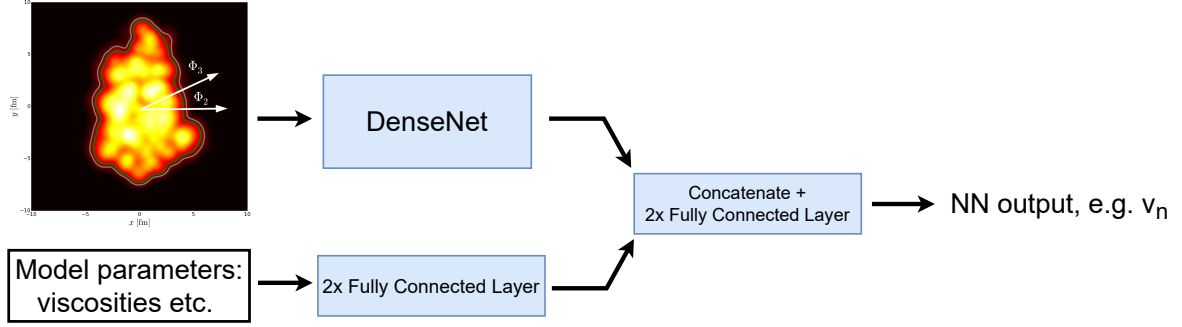**e-mail: kari.eskola@jyu.fi
***e-mail: harri.m.niemi@jyu.fi

Figure 1. Schematic presentation of neural network structure with multiple inputs.

2 Neural network

The convolutional neural networks, one for each observable, are trained to produce p_T-integrated flow coefficients v_n, mean transverse momentum $[p_T]$ and charged particle multiplicities $dN_{ch}/d\eta$. This was originally done in Ref. [4], from where one can find a detailed description of the setup. Here we just go through the main points.

As the training data, we used 20 k EKRT (Eskola-Kajantie-Ruuskanen-Tuominen) model [5–8] initial energy density profiles in the transverse plane and the corresponding final state observables in these events at midrapidity. The final state observables are obtained from the 2+1 D hydrodynamic simulations done in Ref. [9]. The training events are distributed evenly between four different collision systems: 200 GeV Au+Au, 2.76 TeV Pb+Pb, 5.023 TeV Pb+Pb, and 5.44 TeV Xe+Xe. Even though we use one specific setup of an initial state model combined with a hydrodynamics code to produce the training data, the methods introduced here are expected to be applicable also with training data obtained from any other setup of a similar type.

The neural network architecture is the DenseNet architecture [10] with slight modifications that will make it suitable for regression tasks. For a more complete description of the architecture, see Ref. [4]. It took ~ 1 hour to train a network that can produce one observable. With a set of trained networks, one can generate 1 M events in ~ 20 hours.

2.1 Model parameters as an input

A neural network that can predict a final state observable from an initial state is already a lot faster than doing full hydrodynamic simulations, but it has a drawback: every time one wants to change QCD matter properties or model parameters that affect time evolution of the system, one would need to generate a new set of training data and retrain the networks. This issue can be solved by adding all the parameters of interest as additional input to the neural networks. Here we refer to this type of network with additional input parameters as NN_p. The architecture of NN_p is demonstrated in Fig. 1. The energy density input is treated the same way as without additional inputs and all the additional inputs are put through two fully connected layers and then combined with the output of the DenseNet layer structure. After this, we have included two fully connected layers from which we then obtain the final output. The training of NN_p was done using in total of 160 k training events distributed evenly between 4 collision systems and 2 k parameter points sampled from a Latin hypercube. This makes only 80 events of training data for one parameter point, which is 250 times more efficient than the training in the previous case.
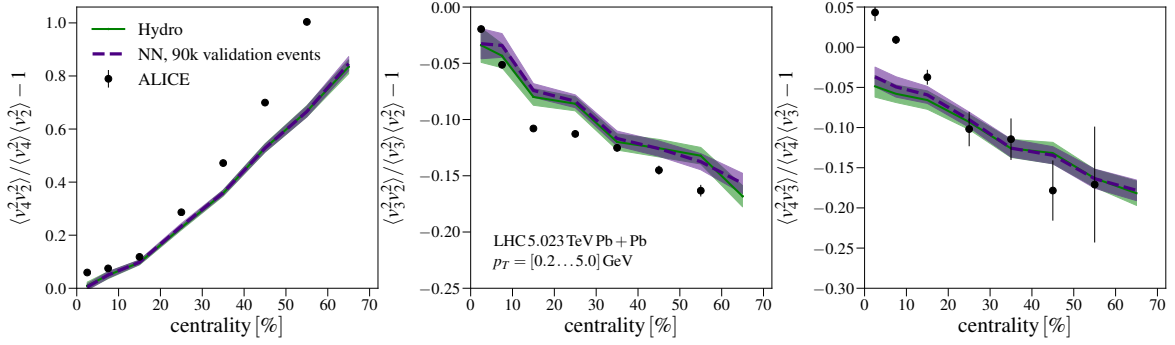
Figure 2. Validation test of the neural networks for $NSC(m, n)$ with 90 k validation events. The experimental data are from the ALICE Collaboration [11]. Figure from Ref. [4].
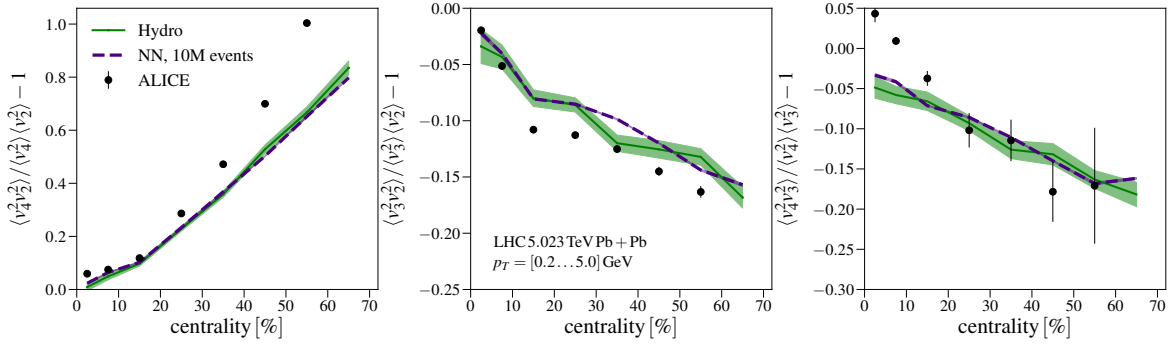

Figure 3. Neural network prediction for $NSC(m, n)$ with 10 M events. The experimental data are from the ALICE Collaboration [11]. Figure from Ref. [4].

3 Results and conclusions

To test the accuracy of the neural networks that were trained with one set of model parameters, we generated 90 k independent EKRT initial energy density profiles and compared the results of hydrodynamic simulations against the neural network predictions. In Fig. 2 we show a comparison of these two for normalized symmetric cumulants $NSC(m, n)$ as a function of centrality. We can see that the neural network can reproduce the cumulants well, even though the size of the training data for one collision system was only 5 k events. In Fig. 3, we demonstrate how one can then generate 10 M events with the neural networks to see how these cumulants would look when statistical errors became insignificant. Here we can see quite noticeable deviations from the result that used 90 k events, especially for $NSC(2, 3)$, for which the centrality dependence clearly changes, matching the shape of the ALICE measurements better. This illustrates the importance of the number of events used when trying to constrain the QCD matter properties with multi-particle flow correlations.

In the case of NN_p networks, we are mostly interested in the network accuracy for generating new events with the same parameter values as in the training data. This is because the most efficient way to do Bayesian analysis is to first generate a high number of events using neural networks in a set of parameter points, compute all of the observables in these parameter points, and then train Gaussian process emulators for these observables. Here the accuracy of NN_p networks was tested by taking two sets of model parameter points from the training data which correspond to drastically different values of viscosities, and then generating 20 k new independent initial state profiles for both points and doing a similar validation comparison between NN_p and hydrodynamic simulations as before. The results are shown in
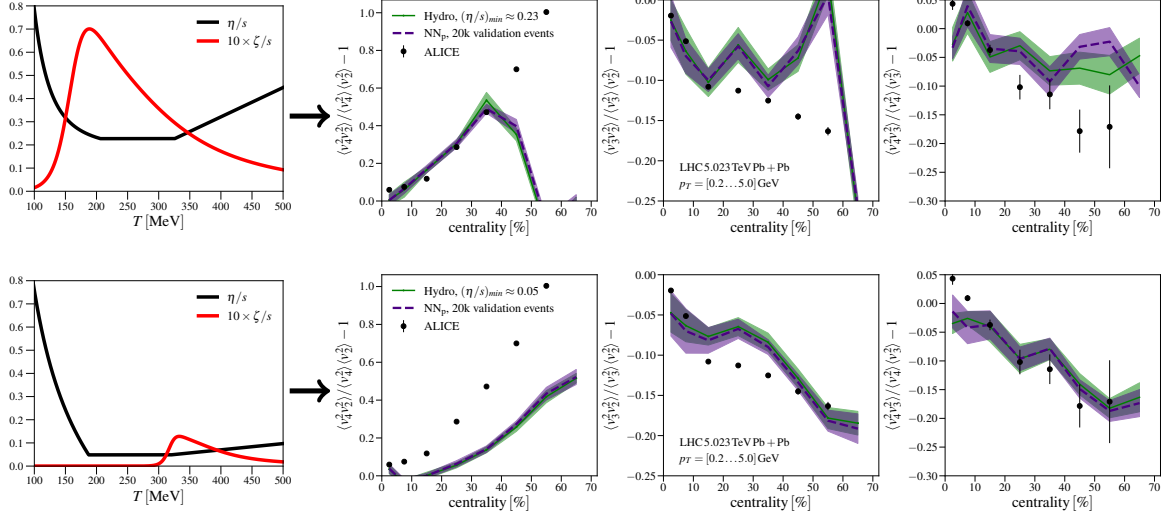
Figure 4. Validation tests of NN_p networks for $NSC(m, n)$ with 20 k validation events in each case. The upper (lower) panels show result with high (low) values of specific viscosities. The experimental data are from the ALICE Collaboration [11].

Fig. 4, from where one can see that NN_p can still very accurately reproduce the results from hydrodynamic simulations. The only exception is the peripheral region of $NSC(3, 4)$ in the extremely high viscosity case, where the numerical errors of hydrodynamical simulations of themselves might be very significant.

The goal of introducing neural networks in this work was to replace the slow hydrodynamic simulations and make it possible to add multi-particle flow correlators to Bayesian analysis. We have demonstrated that this is indeed possible and has the potential to cut the computational time needed for these analyses by many orders of magnitude.

References

[1] G. Aad *et al.* [ATLAS], Eur. Phys. J. C **79**, no.11, 970 (2019)

[2] L. Liu, J. Velkovska, Y. Wu and M. Verweij, JHEP **04**, 140 (2023)

[3] H. S. Wang, S. Guo, K. Zhou and G. L. Ma, [arXiv:2305.09937 [nucl-th]]

[4] H. Hirvonen, K. J. Eskola and H. Niemi, Phys. Rev. C **108**, no.3, 034905 (2023)

[5] K.J. Eskola, K. Kajantie, P.V. Ruuskanen, K. Tuominen, Nucl. Phys. B **570**, 379 (2000)

[6] R. Paatelainen *et al.*, Phys. Rev. C **87**, no.4, 044904 (2013)

[7] R. Paatelainen, K.J. Eskola, H. Niemi, K. Tuominen, Phys. Lett. B **731**, 126 (2014)

[8] H. Niemi, K. J. Eskola and R. Paatelainen, Phys. Rev. C **93**, no.2, 024907 (2016)

[9] H. Hirvonen, K. J. Eskola and H. Niemi, Phys. Rev. C **106**, no.4, 044913 (2022)

[10] G. Huang, Z. Liu, L. van der Maaten, K. Q. Weinberger, CVPR, 4700-4708 (2017)

[11] S. Acharya *et al.* [ALICE], Phys. Lett. B **818**, 136354 (2021)

PIV

MC-EKRT: MONTE CARLO EVENT GENERATOR WITH SATURATED MINIJET PRODUCTION FOR INITIALIZING 3+1 D FLUID DYNAMICS IN HIGH ENERGY NUCLEAR COLLISIONS

by

Mikko Kuha, Jussi Auvinen, Kari J. Eskola, Henry Hirvonen, Yuuka Kanakubo and Harri Niemi.

MC-EKRT: Monte Carlo event generator with saturated minijet production for initializing 3+1 D fluid dynamics in high energy nuclear collisions

Mikko Kuha, Jussi Auvinen, Kari J. Eskola, Henry Hirvonen, Yuuka Kanakubo, Harri Niemi

University of Jyväskylä, Department of Physics, P.O. Box 35, FI-40014 University of Jyväskylä, Finland, and
Helsinki Institute of Physics, P.O.Box 64, FI-00014 University of Helsinki, Finland

We present a novel Monte-Carlo implementation of the EKRT model, MC-EKRT, for computing partonic initial states in high-energy nuclear collisions. Our new MC-EKRT event generator is based on collinearly factorized, dynamically fluctuating pQCD minijet production, supplemented with a saturation conjecture that controls the low-p_T particle production. Previously, the EKRT model has been very successful in describing low-p_T observables at mid-rapidity in heavy-ion collisions at the LHC and RHIC energies. As novel features, our new MC implementation gives a full 3-dimensional initial state event-by-event, includes dynamical minijet-multiplicity fluctuations in the saturation and particle production, introduces a new type of spatially dependent nuclear parton distribution functions, and accounts for the conservation of energy/momentum and valence-quark number. In this proof-of-principle study, we average a large set of event-by-event MC-EKRT initial conditions and compute the rapidity and centrality dependence of the charged hadron multiplicities and elliptic flow for the LHC Pb+Pb and RHIC Au+Au collisions using 3+1 D viscous fluid-dynamical evolution. Also event-by-event fluctuations and decorrelations of initial eccentricities are studied. The good agreement with the rapidity-dependent data suggests that the same saturation mechanism that has been very successful in explaining the mid-rapidity observables, works well also at larger rapidities.

I. INTRODUCTION

The theory of the strong interaction, Quantum Chromodynamics (QCD), predicts that at very high energy densities, at temperatures $T \gtrsim 150 - 160$ MeV and at a vanishing baryochemical potential, strongly interacting matter is in the form of a quark-gluon plasma (QGP) [1–4]. Such extreme conditions can be momentarily created and the properties of the QGP experimentally studied in laboratory by colliding heavy ions at ultrarelativistic energies at the CERN Large Hadron Collider (LHC) and the Brookhaven National Laboratory (BNL) Relativistic Heavy Ion Collider (RHIC). In these collisions, the "heating" of the matter necessary for the QGP formation is obtained from the kinetic energy of the colliding nuclei, through copious primary production of QCD quanta, quarks and gluons [5].

The QCD system formed in ultrarelativistic heavy-ion collisions is expected to experience various spacetime evolution stages: initial formation of a nearly-thermalized QGP, expansion and cooling of the QGP, transition of the QGP into a hadron resonance gas (HRG), expansion and cooling of the HRG, and finally decoupling of the HRG into non-interacting hadrons, out of which the resonances still decay before they can be detected. The dynamical expansion stages of QCD matter can be described with relativistic dissipative fluid dynamics [6–21] which nowadays is a cornerstone in the event-by-event analysis of heavy-ion observables.

The heavy-ion programs at the LHC and RHIC aim especially at the determination of the QCD matter properties, such as the temperature dependencies of the specific shear and bulk viscosities and other transport coefficients, from the experimental data. In practice, this can be achieved only by performing a fluid-dynamics based "global analysis", a simultaneous study of various different (low-transverse-momentum) observables from as many types of collision systems as possible. These analyses have evolved from pioneering works [12, 14, 17] (see also [22]) to those with a proper Bayesian statistical analysis and well defined uncertainty estimates [21, 23–31]. So far, the analyses have mainly focused on studies at mid-rapidity, where one assumes a longitudinally boost symmetric (but 3-dimensionally expanding) system described by the 2+1 D fluid dynamical equations of motion. The studies of rapidity-dependent observables requires a full 3+1 D implementation of viscous fluid dynamics [9–11, 32–38]. Recently, global analyses have been also extended into this direction [39–41]. Moreover, neural networks have been developed for studying rare observables [42, 43].

In such global analyses, the results obtained for the QCD matter properties are strongly correlated with the the assumed fluid-dynamical initial conditions. Then, if the initial states are obtained from an ad hoc parametrization that is blind to QCD dynamics – as is typically the case, see e.g. [21, 24–27, 29–31] – it is not at all clear whether the initial densities such as the ones extracted from the global analysis could actually be realized in the studied nuclear collisions. It is therefore of paramount importance to try to study and model the QCD collision dynamics responsible for the QCD matter initial conditions. Works into this direction include the developments of the IP-Sat+MUSIC (Impact parameter dependent saturation + MUScl for Ion Collisions) model [10, 14, 44], the EKRT (Eskola-Kajantie-Ruuskanen-Tuominen) model [17, 45–47], the EPOS (Energy conservation + Parallel scattering + factOrization + Saturation) model [48–53], the AMPT (A Multi-Phase Transport) model [38, 54], and the Dynamical Core-Corona Initialization model [55, 56] with initial state generated by Pythia Angantyr [57], as well as initial

state models such as in Refs. [58, 59].

In this work, we adopt, and significantly further develop, the pQCD and saturation -based EKRT model for computing event-by-event initial conditions of the QCD matter produced in nucleus-nucleus collisions at the LHC and at the highest RHIC energies. The leading idea in the EKRT model [17, 45–47] is that at sufficiently high collision energies the nucleus-nucleus collisions can be described as collisions of parton clouds rather than a collection of Glauber-model like nucleon-nucleon collisions. Then, gluons and quarks that are produced with transverse momenta (p_T) of the order of a few GeV, minijets, become so copiously produced [60, 61] that their production processes start to overlap in the transverse coordinate space [62], which dynamically generates a saturation scale (p_{sat}) that suppresses softer particle production [47].

The original versions of the EKRT model [45, 46], combined with longitudinally boost invariant 1+1 D ideal fluid dynamics, predicted successfully the LHC and RHIC hadron multiplicities and p_T distributions at mid-rapidity in central collisions [45, 63], and, with 2+1 D fluid dynamics, also the centrality dependence of these and of the elliptic flow coefficients (v_2) of the azimuth-angle asymmetries [64, 65]. Based on a well-defined (collinear- and infrared-safe) pQCD calculation of minijet transverse energy production [47, 66, 67], the model was extended to next-to-leading order (NLO) in Ref. [47]. Combined then with shear-viscous fluid dynamics, the NLO-improved EKRT model described well the centrality dependent hadron multiplicities, p_T distributions and v_2 at mid-rapidity both at RHIC and LHC, systematically indicating a relatively low value for the QCD matter shear-viscosity-to-entropy (η/s) ratio [47].

An event-by-event version of the EKRT model (EbyE-EKRT) was developed in Ref. [17]. The pioneering global analysis of a multitude of LHC and RHIC bulk (low-p_T) observables presented in Ref. [17] demonstrated a very good overall agreement with the measurements, and resulted in improved constraints for the temperature dependence of η/s. Very interestingly (but not unexpectedly), also the Bayesian global analysis of LHC bulk observables of Ref. [26], which used QCD-blind parametrized initial states, confirmed that the initial density profiles predicted by the EbyE-EKRT [17] and the IP-Sat models [44] gave the best match with those obtained from the Bayesian inference.

The first attempt to perform a Bayesian global analysis of LHC and RHIC bulk observables using directly the EKRT initial states as input for the fluid-dynamics, for studying the effects of the EoS and for obtaining statistically controlled uncertainty estimates on the temperature dependence of η/s, can be found in Ref. [28]. The latest developments in the EKRT-initiated 2+1 D fluid-dynamics framework are a dynamically determined decoupling, which improves the description of peripheral collisions, and the inclusion of bulk viscosity. These developments are presented in Ref. [22] together with a demonstration of a very good simultaneous global fit to bulk observables from various collision systems at the LHC and RHIC, and the corresponding extracted specific shear and bulk viscosities of QCD matter. Finally, the first study of how deep convolutional neural networks can be trained to predict hydrodynamical bulk observables from the EbyE-EKRT-generated energy density profiles, and how they can significantly speed up the statistics-expensive EbyE analysis of rare flow correlators especially, can be found in Ref. [42].

The predictive power of the EbyE-EKRT model originates from the underlying collinearly factorized NLO pQCD calculation. The model has been remarkably successful, especially in genuinely predicting bulk observables at mid-rapidity also for higher LHC energies, 5.02 TeV Pb+Pb collisions [68], as well as for collisions of deformed nuclei, 5.44 TeV Xe+Xe collisions at [69] – see the data comparisons e.g. Refs. [22, 70]. However, there still is a number of shortcomings with the EKRT-model that need to be addressed.

First, for addressing also rapidity-dependent observables, the EbyE-EKRT initial state model should be extended to off-central rapidities and then coupled to 3+1 D viscous fluid dynamics.

Second, the average number of (or the average E_T from) the parton-parton collisions is thus far in the EKRT saturation model computed as a product of a nuclear overlap function and (p_T weighted) collinearly factorized integrated minijet cross section. This assumes essentially independent partonic collisions, and as discussed in Ref. [62], especially towards larger rapidities at the LHC one easily violates the conservation of energy and baryon number. This problem clearly needs to be addressed together with the rapidity dependence.

Third, thus far in the EbyE-EKRT [17], the local fluctuations of the saturation scale, and thus of the computed energy densities, in the transverse coordinate plane are only of a geometrical origin, i.e. they follow only from the sampled fluctuating positions of the nucleons inside the colliding nuclei. Dynamical, local EbyE fluctuations in the minijet multiplicity, inducing then further local EbyE fluctuations to the saturation scale and hence to the energy densities, should clearly be accounted for. Only by including these fluctuations can the EKRT model be relevantly applied to the studies of smaller collision systems, i.e. proton-nucleus and perhaps even proton-proton collisions.

Fourth, in an EbyE analysis the factorized minijet cross sections must be computed using nuclear parton distribution functions (nPDFs) that depend on the transverse position ($\bar{s}$) in each of the colliding nuclei. The spatial dependence can be modeled in terms of a power series of the nuclear thickness function, $T_A(\bar{s})$, as was done e.g. in EPS09s nPDFs [71] that are used in EbyE-EKRT. The EbyE fluctuating T_A's, however, often reach so large values (up to more than 3 times the largest average $T_A(0)$) that the T_A-applicability range of EPS09s is significantly exceeded. In EbyE-EKRT this problem was solved by an

ad-hoc extrapolation of the saturation scale towards the larger values of T_A. Clearly, this problem is not EKRT-specific but should be addressed for the benefit of any factorized EbyE study of centrality dependence of hard processes, where spatial dependence of nPDFs is needed.

In this paper, we address these shortcomings and the arising uncertainties in solving them, for the first time in the EKRT-model framework. In particular, we introduce a completely new Monte Carlo EKRT event-generator, which we name *MC-EKRT* [72], for computing EbyE fluctuating initial states for fluid dynamics in nuclear collisions. We couple the MC-EKRT minijets to 3+1 D shear-viscous fluid dynamics [73], and discuss the various uncertainties in doing this. In this proof-of-principle paper we do not, however, aim at a full EbyE global analysis, yet, but instead study the model systematics by computing averaged initial conditions for each centrality class by summing over a large set of event-by-event MC-EKRT initial states. Running then 3+1 D shear-viscous fluid dynamics with these, we can meaningfully compare the MC-EKRT results against the measured pseudorapidity distributions of charged hadrons in different centrality classes, and also elliptic flow coefficients in semicentral collisions in Pb+Pb collisions at the LHC and Au+Au collisions at RHIC. We also study the decorrelation of eccentricities in spacetime rapidity, which was to our knowledge discussed first in [36, 54].

The paper is organized as follows: In Sec. II we define the MC-EKRT model framework and discuss how the previous shortcomings are solved. Section III discusses our fluid-dynamics setup, and how the 3+1 D fluid dynamics is initialized with the computed MC-EKRT minijet states. Comparisons against LHC and RHIC data, and the results for the decorrelation of eccentricities, are shown in Sec. IV. Finally, conclusions and outlook are given in Sec. V.

II.   MONTE CARLO EKRT MODEL SETUP

Let us first see how the geometric saturation criterion that we will employ in the MC-EKRT set-up below, arises using collinearly factorized lowest-order pQCD $2 \to 2$ gluonic processes as the basis and imagining the colliding nuclei as parton (gluon) clouds [45, 74]. In an inelastic nucleus-nucleus collision at an impact parameter $\bar{b}_{AA}$, the average transverse density of the number of gluon-gluon collisions that are producing minijets with p_T above a cut-off p_0 and at rapidities $y_{1,2}$, is

$$\frac{dN_{AA}^{2\to2}(\bar{b}_{AA})}{d^2\bar{s}} = T_A(\bar{s}_1)T_A(\bar{s}_2)\frac{1}{2}\int_{p_0}dp_T^2dy_1dy_2$$
$$\times \ x_1g(x_1,Q^2)x_2g(x_2,Q^2)\times\frac{d\hat{\sigma}^{2\to2}}{d\hat{t}} \quad (1)$$

where $T_A(\bar{s})$ is the standard nuclear thickness function obtained as an integral of the nuclear density over the longitudinal coordinate, $\bar{s}_{1,2} = \bar{s} \pm \bar{b}_{AA}/2$ are the transverse

coordinates, $g(x,Q^2)$ are the gluon PDFs, $x_{1,2} \sim p_T/\sqrt{s}$ are the longitudinal momentum fractions of the colliding gluons and $Q \sim p_T$ is the factorization/renormalization scale, $\hat{t}$ is a Mandelstam variable for the partonic scattering and $d\hat{\sigma}^{2\to2}/d\hat{t} \sim \alpha_s^2/p_T^4$ is the $2 \to 2$ LO pQCD gluonic cross section.

On dimensional grounds, and ignoring the rapidity dependence, we may write for a symmetric system in central collisions [17]

$$\frac{dN_{AA}^{2\to2}(0)}{d^2\bar{s}} \sim (T_Axg) \times (T_Axg) \times \left(\frac{\alpha_s^2}{p_0^2}\right), \quad (2)$$

where $x \sim p_0/\sqrt{s}$. Correspondingly, for $3 \to 2$ processes, which can be expected to become important at small x, where the initial gluon densities become large, we would on dimensional grounds write, assuming here the double-PDFs from the nucleus 1 (and similarly for the other nucleus),

$$\frac{dN_{AA}^{3\to2}(0)}{d^2\mathbf{s}} \sim (T_Axg)^2 \times T_Axg \times \frac{\alpha_s}{p_0^2}\left(\frac{\alpha_s^2}{p_0^2}\right), \quad (3)$$

where we have accounted for the extra power of α_s in the numerator, and for the p_0^2 in the denominator canceling the dimension of the extra T_A there in the double-PDF. Saturation effects are expected to become dominant, and softer parton production suppressed, when $dN_{AA}^{3\to2} \sim dN_{AA}^{2\to2}$, i.e. when

$$T_Axg \sim \frac{p_0^2}{\alpha_s}. \quad (4)$$

Substituting this back to Eq. (2), and integrating over an effective nuclear transverse area πR_A^2 (R_A being the nuclear radius), gives the geometrical EKRT scaling law, introduced in Ref. [45]

$$N_{AA}^{2\to2}(0)\frac{\pi}{p_0^2} \sim \pi R_A^2, \quad (5)$$

where π/p_0^2 can be interpreted as a transverse formation-area for a produced dijet [45, 62]. Thus, the minijet production saturates when the minijet production processes fill the available transverse area in the nuclear collision.

In the MC-EKRT set-up introduced below, we will take the above geometric interpretation of saturation as our starting point, when deciding on an event-by-event and on a parton-by-parton basis, whether the produced minijet system becomes locally saturated. With the above discussion, we would also like to emphasize that saturation in the EKRT model is *not* fusion of produced final-state gluons, but saturation of the minijet production processes themselves.

Our MC-EKRT simulation of a nucleus-nucleus $(A+B)$ collision proceeds through the following steps, each of which will be discussed in more detail in this and the following sections.
1. Sample the positions of the nucleons in $a \in A$ and $b \in B$ from the Woods-Saxon distribution, keeping track of the proton/neutron identity of each nucleon (Sec. II A).

2. Sample the impact parameter for the $A+B$ collision similarly as in the MC Glauber model (Sec. II B), and check whether the chosen trigger condition for the $A+B$ collision is fulfilled. If it is not, start again from item 1 (Sec. II C).

3. If the $A+B$ collision is triggered, find all the binary ab pairs of nucleons, $a \in A$ and $b \in B$. Then go through the generated list of the ab pairs and regard each ab pair as a possible independent source of multiple minijet production. Sample the number of produced minijet pairs, dijets, for each ab pair from a Poissonian probability distribution (Sec. II D 1).

4. For each produced dijet, sample the parton flavors and momenta from collinearly factorized LO pQCD cross sections (Sec. II D 2), using nuclear PDFs that depend on the transverse positions of $a \in A$ and $b \in B$ (Sec. II D 3). For quark-initiated processes, decide (sampling the LO pQCD cross sections) whether the colliding quarks are valence quarks or sea quarks (Sec. II D 2). Sample also the transverse production point for each dijet from a Gaussian overlap function for each nucleon pair ab (Sec. II D 1).

5. Consider all the generated dijets as candidates for the final minijet-state of this $A+B$ event. For filtering away the excess (unphysical) dijets, order the dijet candidates according to the transverse momentum p_T of the minijets forming the dijet (Sec. II E).

6. Filter the excess dijets in the order of decreasing p_T, by imposing a local geometric EKRT saturation criterion (cf. Eq. (5)). If a dijet gets filtered, both final-state partons are removed (Sec. II E).

7. Filter the surviving dijets further by imposing conservation of energy and valence quark number for each nucleon, doing the filtering again in the order of decreasing p_T. Optionally, this filtering step can be ignored, or chosen to be done simultaneously with the dijet filtering in step 6 (Sec. II E).

8. Collect the MC-EKRT minijet output data for the surviving dijets: the $\mathbf{p_T}$ vector, the rapidity, and the flavour of each minijet, along with the transverse location of each dijet's formation point, to be used in Sec. III B. Order the $A+B$ events according to the total minijet E_T (a scalar sum of minijet p_T's) for the centrality selection (Sec. II F).

A separate interface is then developed to initialize fluid dynamics, with the following steps:

9. Propagate the surviving minijets as free particles to the proper time surface $\tau_0 = 1/p_0$, assuming that minijets with momentum rapidity y move along the corresponding spacetime rapidity $\eta_s = y$. The parameter p_0 here is the smallest partonic p_T allowed in the pQCD cross sections for the dijet candidates (Sec. III B 1).

10. Feed the minijets into 3+1 D fluid dynamics as initial conditions at τ_0: At each η_s and transverse-coordinate grid cell, using a Gaussian smearing, convert the minijet transverse energy E_T into a local energy density (Sec. III B 2).

11. Run 3+1 D viscous fluid dynamics with these mini-jet initial conditions, in principle event by event. Note, however, that in the present exploratory study we are testing the model setup using averaged initial states for each centrality class (Sec. III B 3). We do not couple the fluid dynamics with a hadron cascade afterburner but run fluid dynamics until the freeze-out of the system. Resonance decays are accounted for, as usual (Sec. III A).

12. Form the observables for which statistics is collected (Sec. IV).

Next, we look at the above steps in more detail, and also specify the few parameters that the MC-EKRT minijet event generator has.

A. Nucleon configurations of A and B

First, we construct the nucleon structure of the colliding nuclei. Here, we essentially follow the procedure nowadays standard in the Monte Carlo Glauber approach [75]. The distributions of the positions of the nucleons are taken to follow the nuclear charge densities extracted from low energy electron scattering experiments [76, 77]. The lead nucleus, Pb^{208} (used at the LHC) is assumed perfectly spherical, and as the gold nucleus Au^{197} (used at RHIC) is also nearly spherical, the current version of the MC-EKRT assumes spherically symmetric nuclei A and B. Thus, the azimuthal angle $\phi \in [0, 2\pi]$ and the cosine of the polar angle $\cos\theta \in [-1, 1]$ are sampled from a uniform distribution, while the radial coordinate r is sampled from the two-parameter Fermi (2pF) distribution, the Woods-Saxon distribution [78],

$$\rho_{\mathrm{WS}}(r) = \frac{\rho_0}{1 + \exp\left(\frac{r - R_A}{d}\right)}, \qquad (6)$$

where R_A is the nuclear radius and d is the diffusion parameter. For the lead and gold nuclei we study here, $(R_A, d) = (6.624, 0.550)\,\mathrm{fm}$ and $(6.380, 0.535)\,\mathrm{fm}$, correspondingly [76]. The normalization constant ρ_0 is fixed by requiring the volume integral of $\rho_{\mathrm{WS}}(r)$ to give A, but in the simulation here ρ_0 has no effect. The nuclei which have nucleons with positions closer to each other than $d_{\min} = 0.4$ fm, are discarded and sampled again. The introduction of an exclusion radius $d_{\min}$ is known to slightly deform the radial density profile [75, 79], but we neglect this small effect here.

B. Impact parameter sampling

Next, the squared impact parameter, $\bar{b}_{AB}^2$, for the $A+B$ collision is sampled from a uniform distribution. As long as the colliding nuclei are spherically symmetric on the average, we do not need to randomly rotate the nuclei. We can fix the impact parameter vector, as a vector in the transverse (x, y) plane, to be on the x-axis, pointing from the nucleus A to the nucleus B – see Fig. 1.

Once the positions of the nucleons in each nucleus – $\{\bar{s}_a\}$ in A and $\{\bar{s}_b\}$ in B – have been determined,
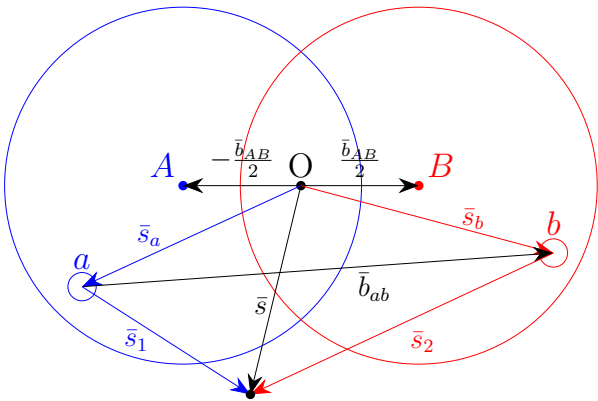
FIG. 1: Projection of the $A+B$ collision system into the transverse plane. The impact parameter vector $\bar{b}_{AB}$, extending from the center-of-mass of the nucleus A to the center-of-mass of the nucleus B, is along the x-axis (axes are not shown), with the origin O in the middle. The location vectors of the nucleons $a \in A$ and $b \in B$ are $\bar{s}_a$ and $\bar{s}_b$, respectively. The impact parameter between the nucleons a and b is $\bar{b}_{ab}$.

the center of the mass of the projectile nucleus A is shifted to $(-b_{AB}/2, 0)$ and that of the target nucleus B to $(b_{AB}/2, 0)$, thus fixing the origin O of the collision frame. Finally, Z_A (Z_B) of the nucleons in A (B) are randomly labeled as protons and the rest as neutrons, i.e. we neglect possible effects arising from the differences of proton and neutron density distributions (such as a neutron skin), in this study.

C. Trigger condition for the $A+B$ collision

Next, our simulation checks whether an inelastic collision between the generated nucleon configurations A and B takes place. We devise the trigger condition for the $A+B$ collision as follows: Assuming a hard-sphere scattering of two nucleons, $a \in A$ and $b \in B$, with a cross section $\sigma_{\mathrm{trig}}^{ab}(s_{NN})$ at a nucleon-nucleon center-of-momentum system (CMS) energy $\sqrt{s_{NN}}$, an $A+B$ collision takes place if for at least one of the ab pairs the squared transverse distance between a and b does not exceed $\sigma_{\mathrm{trig}}^{ab}(s_{NN})/\pi$. In terms of the transverse-coordinate vectors introduced in Fig. 1, with nucleons $a \in A$ and $b \in B$, their transverse positions at $\bar{s}_a$ and $\bar{s}_b$, and impact parameters $\bar{b}_{ab}$, the triggering condition for the $A+B$ collision is fulfilled if at least for one ab pair

$$|\bar{b}_{ab}| = |\bar{s}_b - \bar{s}_a| \leq \sqrt{\sigma_{\mathrm{trig}}^{ab}(s_{NN})/\pi}. \qquad (7)$$

If the above condition is not met, new nucleon configurations A and B, and a new impact parameter b_{AB}^2 are generated. For the triggering cross section $\sigma_{\mathrm{trig}}^{ab}(s_{NN})$ we use the inelastic nucleon-nucleon cross section $\sigma_{\mathrm{inel}}^{NN}(s_{NN})$, calculated as

$$\sigma_{\mathrm{inel}}^{NN}(s_{NN}) = \sigma_{\mathrm{tot}}^{NN}(s_{NN}) - \sigma_{\mathrm{el}}^{NN}(s_{NN}), \qquad (8)$$

where the total cross section $\sigma_{\mathrm{tot}}^{NN}$ is obtained from a fit by COMPETE [80],

$$\sigma_{\mathrm{tot}}^{NN}(s_{NN})/\mathrm{mb} = 42.6 s^{-0.46} - 33.4 s^{-0.545}$$
$$+ 0.307 \log^2(s/29.1) + 35.5, \qquad (9)$$

and the elastic cross section from a fit by TOTEM [81],

$$\sigma_{\mathrm{el}}^{NN}(s_{NN})/\mathrm{mb} = -1.617 \log(s) + 0.1359 \log(s)^2 + 11.84, \qquad (10)$$

with $s = s_{NN}/\mathrm{GeV}^2$. For the CMS energies $\sqrt{s_{NN}} = 5020, 2700, 200$ GeV, which we study here, this gives $\sigma_{\mathrm{inel}}^{NN}(s_{NN}) = 69.14, 62.96, 41.78$ mb, correspondingly.

We emphasize that $\sigma_{\mathrm{inel}}^{NN}$ is here used only for the triggering of the nuclear collision, i.e. for determining the inelastic $A+B$ cross-section. It does not play any other role in what follows.

D. Multiple dijet production

1. Probability distribution and nucleon thickness function

If the trigger condition is fulfilled, the collision between A and B takes place. The $A+B$ collision here is assumed to be a very high-energy one, and furthermore a collision of two large parton clouds, which are originating from the sampled nucleons and extending around the Lorentz contracted nuclei. In this case, the multiple minijets originating from each ab pair are produced practically instantaneously around $z \sim 0$, and simultaneously everywhere in the transverse plane.

At this stage of our setup, all the ab pairs can be considered to be fully independent from each other, they just divide the interaction of the two large nuclear parton-clouds into ab contributions. Saturation and energy conservation, which will here be imposed in the order of decreasing minijet p_T, do not depend on the ordering of the ab pairs, either. Thus, in our setup the ordering of the ab pairs becomes irrelevant [1].

Next, all the ab nucleon pairs will be considered as potential sources for multiple minijet (dijet) production. In each ab contribution, the candidate dijets are supposed to be produced independently from each other, hence Poissonian statistics is used in sampling the number of produced dijets. Then, the probability of producing $n \geq 0$ independent dijets from the pair ab, where the locations of a and b, in the fixed nucleon configurations of this event, are $\bar{s}_a$ and $\bar{s}_b$, correspondingly, and whose impact parameter thus is $\bar{b}_{ab} = \bar{s}_b - \bar{s}_a$, is

$$P_n(\{\bar{s}_a\}, \{\bar{s}_b\}, p_0, \sqrt{s_{NN}}) = \frac{\left(\bar{N}_{\mathrm{jets}}^{ab}\right)^n}{n!} e^{-\bar{N}_{\mathrm{jets}}^{ab}}, \qquad (11)$$

---

[1] Note, however, that if one models nuclear collisions as subsequent energy-conserving NN subcollisions (like e.g. in HIJING [82]), then the ordering (randomization) of the ab pairs would be important.

where the average number of dijets produced from the pair ab is

$$\bar{N}_{\text{jets}}^{ab} \equiv \bar{N}_{\text{jets}}^{ab}(p_0, \sqrt{s_{NN}}, \{\bar{s}_a\}, \{\bar{s}_b\}) \quad (12)$$

$$= T_{NN}(\bar{b}_{ab})\, \sigma_{\text{jet}}^{ab}(p_0, \sqrt{s_{NN}}, \{\bar{s}_a\}, \{\bar{s}_b\}) \quad (13)$$

where σ_{jet}^{ab} is an integrated inclusive pQCD cross section for producing a pair of minijets with transverse momenta $p_T \geq p_0$ and any rapidities (details of obtaining σ_{jet}^{ab} will be explained in Sec. II D 2), and with the notation $\{\bar{s}_a\}$ ($\{\bar{s}_b\}$) we underline that the computed pQCD cross section here depends both on the location $\bar{s}_a$ ($\bar{s}_b$) of the nucleon $a \in A$ ($b \in B$) and on the positions of all other nucleons in the nucleon configuration forming the nucleus A (B) in each event. Above, T_{NN} is the nucleon-nucleon overlap function,

$$T_{NN}(\bar{b}_{ab}) = \int d^2s\, T_N(\bar{s} - \bar{s}_a)T_N(\bar{s} - \bar{s}_b) \quad (14)$$

$$= \int d^2s_1\, T_N(\bar{s}_1)T_N(\bar{s}_1 - \bar{b}_{ab}) \quad (15)$$

where the transverse vectors $\bar{s} - \bar{s}_a \equiv \bar{s}_1$ and $\bar{s} - \bar{s}_b = \bar{s}_1 - \bar{b}_{ab} \equiv \bar{s}_2$ measure the transverse distance from the centers of the nucleons $a \in A$ and $b \in B$, correspondingly, see Fig. 1. Here, T_N is the nucleon thickness function, which is obtained from the spatial density distribution ρ_N as

$$T_N(\bar{s}) = \int_{-\infty}^{\infty} dz \rho_N(\mathbf{x}), \quad (16)$$

where $\mathbf{x} = (\bar{s}, z)$. Both T_N and T_{NN} are normalized to one through the transverse integrals,

$$\int d^2s\, T_N(\bar{s}) = \int d^3x\, \rho_N(\mathbf{x}) = 1, \quad (17)$$

$$\int d^2s\, T_{NN}(\bar{s}) = 1. \quad (18)$$

It should also be emphasized that in writing Eq. (12) into the form of Eq. (13), we are assuming that the PDFs carry spatial dependence in that they do (quite strongly) depend on the locations $\bar{s}_a$ of $a \in A$ and $\bar{s}_b$ of $b \in B$, as well as on the positions of all the other nucleons in A and B (which all are fixed for one $A+B$ collision event), but that for each nucleon $a \in A$ and $b \in B$ we have fixed PDFs that do not depend on the variable $\bar{s}$ appearing in Eq. (14). This allows us to factorize the nucleon-nucleon overlap function T_{NN} from the minijet cross section σ_{jet}^{ab} in Eq. (13).

Following Ref. [17], we extract ρ_N, and thereby T_N, from exclusive J/ψ photo-production cross sections that have been measured in $\gamma + p \rightarrow J/\psi + p$ collisions at HERA [83]. As discussed e.g. in Ref. [84], the amplitude of this process is proportional to generalized parton distribution functions (GPDs) and a two-parton form factor $F_N(t)$ that depends on the Mandelstam variable t and is

linked to ρ_N via a 3D Fourier transform,

$$F_N(t) = \int d^3x\, e^{i\mathbf{q}\cdot\mathbf{x}}\rho_N(\mathbf{x}), \quad (19)$$

where $|\mathbf{q}|^2 = |t|$, and $F_N(0) = 1$. As the GPDs become ordinary PDFs at the forward limit, and as the J/Ψ mass scale is of the same order of magnitude as the dominant minijet p_T scale, the above ρ_N should to a good approximation describe also the corresponding partonic spatial density related to the PDFs we use here. The measured HERA cross sections show a behavior $d\sigma/dt \propto e^{-b|t|}$, with a slope parameter b that depends on the photon-proton system c.m.s. energy W as

$$b/\text{GeV}^{-2} = b_0 + 4\alpha_P' \log\left(\frac{W}{W_0}\right), \quad (20)$$

where b_0, α_P' and W_0 are constants. Here, identifying $W = \sqrt{s_{NN}}$, our default choice is the parametrization from Ref. [85] (also used in [84]), with $b_0 = 4.9$, $\alpha_P' = 0.06$ and $W_0 = 90$ GeV. Then, an inverse Fourier transform of $F_N(t) = \exp(-b|t|/2) = \exp(-b|\mathbf{q}|^2/2)$ results in a 3D Gaussian density,

$$\rho_N(\mathbf{x}) = \int \frac{d^3q}{(2\pi)^3} e^{-i\mathbf{q}\cdot\mathbf{x}} F_N(t) \quad (21)$$

$$= \left(\frac{1}{2\pi\sigma_N^2}\right)^{3/2} \exp\left(-\frac{|\mathbf{x}|^2}{2\sigma_N^2}\right), \quad (22)$$

and a 2D Gaussian thickness function,

$$T_N(\bar{s}) = \frac{1}{2\pi\sigma_N^2} \exp\left(-\frac{|\bar{s}|^2}{2\sigma_N^2}\right), \quad (23)$$

with a width parameter $\sigma_N^2 \equiv b$. With the parametrization (20), we have $\sigma_N = 0.478\,(0.472)$ fm, at $\sqrt{s_{NN}} = 5.02\,(2.76)$ TeV at the LHC, and $\sigma_N = 0.445$ fm for $\sqrt{s_{NN}} = 200$ GeV at RHIC.

Then, with the Gaussian forms for T_N, also the nucleon-nucleon overlap function in Eq. (15) can be expressed in a closed form, which also becomes a Gaussian,

$$T_{NN}(\bar{b}_{ab}) = \frac{1}{4\pi\sigma_N^2} \exp\left(-\frac{|\bar{b}_{ab}|^2}{4\sigma_N^2}\right). \quad (24)$$

Once the number of the independent dijet candidates has been sampled, each dijet candidate is assigned a spatial production point $\bar{s}$ that is sampled from the product distribution $T_N(\bar{s} - \bar{s}_a)T_N(\bar{s} - \bar{s}_b)$.

The modeling here is inspired by the eikonal minijet models [86, 87] which are high-energy limits of potential scattering, but we emphasize the different roles of the parameter p_0 in these models. In MC-EKRT, the impact parameter integral of the eikonal $1 - P_0 = 1 - \exp(-T_{NN}(b)\sigma_{\text{jet}}(p_0))$ is *not* normalized to an inelastic NN cross section $\sigma_{\text{inel}}^{NN}(s_{NN})$ but is allowed to obtain larger values. Instead, the parameter p_0 needs to be chosen so small, of the order 1 GeV, that minijets are

produced so abundantly that they overfill the coordinate space, so that saturation can become effective in regulating the smallest-p_T minijet production. For this reason, our results are also fairly *insensitive* to the value of p_0, unlike typically in the eikonal minijet models. Notice also that as we extend the value of p_0 to unphysically low values (but still keeping it in the pQCD region, $p_0 \gg \Lambda_{\rm QCD}$), and since we are considering the earliest moments in the collision, $\tau \lesssim 1/p_0$, we do not include any soft particle production component, but consider only the (semi)hard (mini)jet production in what follows.

2. Dijet kinematics and parton chemistry

A key element in our MC-EKRT framework is the differential LO pQCD cross section of hard parton production [88, 89]

$$\frac{\mathrm{d}\sigma_{\rm jet}^{ab}(\{\bar{s}_a\}, \{\bar{s}_b\})}{\mathrm{d}p_T^2 \mathrm{d}y_1 \mathrm{d}y_2} = K \sum_{ij\langle kl\rangle} x_1 f_i^{a/A}(\{\bar{s}_a\}, x_1, Q^2) \, x_2 f_j^{b/B}(\{\bar{s}_b\}, x_2, Q^2) \frac{\mathrm{d}\hat{\sigma}^{ij\to kl}}{\mathrm{d}\hat{t}}(\hat{s}, \hat{t}, \hat{u}), \tag{25}$$

where y_1 and y_2 are the rapidities of the two final-state partons, p_T is the transverse momentum of each of them, $f_i^{a/A}(\{\bar{s}_a\})$ $(f_i^{b/B}(\{\bar{s}_b\}))$ is the nucleon-configuration-specific PDF of a parton flavor i (j) of the bound nucleon $a \in A$ $(b \in B)$ which is centered at $\bar{s}_a$ $(\bar{s}_b)$ in the nucleon configuration of each event, and x_1 (x_2) is the parton's longitudinal momentum fraction, Q^2 is the factorization/renormalization scale which we set equal to p_T, and $\frac{\mathrm{d}\hat{\sigma}^{ij\to kl}}{\mathrm{d}\hat{t}}$ are the differential LO pQCD cross sections, which depend on the parton-level Mandelstam variables $\hat{s}$, $\hat{t}$, and $\hat{u}$. The notation $\langle kl\rangle$ indicates a sum over pairs of final-state partons, so that, say, $u_1 g_2 \to ug$ and $u_1 g_2 \to gu$ are the same process and hence are not to be counted as two separate ones, whereas $u_1 g_2 \to ug$ and $g_1 u_2 \to ug$ naturally are two different processes as the initial-state partons originate from different nucleons. Notice also that since we aim to follow the partons' identities as well, we do not introduce any t, u-symmetrized cross sections which are often used when observable jet cross sections are studied. In the present exploratory study, in the interest of the simulation speed and as there anyways are various other uncertainties and scale dependence present, we do not (yet) attempt to perform an NLO calculation similar to that in [66, 67] but account

for the missing higher order terms simply by a K-factor that is a constant for a fixed $\sqrt{s_{NN}}$ and that will be fitted to the $A{+}A$ data separately at the LHC and at RHIC. Then, in LO, the momentum fractions can be expressed in terms of the transverse momentum p_T and rapidities of each minijet as

$$x_{1,2} = \frac{p_T}{\sqrt{s_{NN}}} \left(\mathrm{e}^{\pm y_1} + \mathrm{e}^{\pm y_2}\right), \tag{26}$$

and the Mandelstam variables become

$$\hat{s} = 2p_T^2 \left(1 + \cosh(y_1 - y_2)\right), \tag{27}$$

$$\hat{t} = -p_T^2 \left(1 + \mathrm{e}^{-(y_1 - y_2)}\right), \tag{28}$$

$$\hat{u} = -p_T^2 \left(1 + \mathrm{e}^{+(y_1 - y_2)}\right). \tag{29}$$

Once the spatially dependent nuclear PDFs (PDFs of nucleons a and b) have been devised (see discussion below), Eq. (25) can be integrated over the momentum phase space, to give the minijet cross section $\sigma_{\rm jet}^{ab}(p_0, \sqrt{s_{NN}}, \{\bar{s}_a\}, \{\bar{s}_b\})$ which is employed in Eq. (11). Explicitly, accounting for the symmetry factors for the identical final-state partons, we have

$$\sigma_{\rm jet}^{ab}(p_0, \sqrt{s_{NN}}, \{\bar{s}_a\}, \{\bar{s}_b\}) = K \int dp_T^2 dy_1 dy_2 \sum_{ij\langle kl\rangle} \frac{1}{1 + \delta_{kl}} x_1 f_i^{a/A}(\{\bar{s}_a\}, x_1, Q^2) \, x_2 f_j^{b/B}(\{\bar{s}_b\}, x_2, Q^2) \frac{\mathrm{d}\hat{\sigma}^{ij\to kl}}{\mathrm{d}\hat{t}}(\hat{s}, \hat{t}, \hat{u}), \tag{30}$$

where, assuming a fixed lower limit $p_0 = 1$ GeV for p_T, the integration limits become

$$p_0 \leq p_T \leq \sqrt{s_{NN}}/2, \quad |y_1| \leq \mathrm{arcosh}(1/x_T), \tag{31}$$

$$-\log(2/x_T - \mathrm{e}^{-y_1}) \leq y_2 \leq \log(2/x_T - \mathrm{e}^{y_1}), \tag{32}$$

with $x_T = 2p_T/\sqrt{s_{NN}}$.

With these elements, the dijet kinematics and parton chemistry can be straightforwardly generated. Once the number of independent dijets from an interaction of nucleons $a \in A$ and $b \in B$ has been determined using the

Poissonian probabilities of Eq. (11), the transverse momentum p_T and rapidities y_1, y_2 of each (mini)jet in the dijet are obtained with rejection sampling from the differential minijet cross section (integrand) of Eq. (30). With the fixed kinematic variables, we then sample Eq. (30) again for the parton process type that fixes the flavors of the participating partons. If the parton process involves a quark from either a or b, we also identify each participating quark as a sea quark or as a valence quark again on the basis of Eq. (30) (i.e. the PDFs, in this case, $(f_q^{a/A} - f_{\bar{q}}^{a/A})/f_q^{a/A}$ being the probability for obtaining a valence quark). Finally, one minijet in each dijet is assigned an azimuth angle ϕ from a flat distribution and its partner is then an angle π apart in the $2 \to 2$ kinematics assumed here.

3. EbyE fluctuating spatial nuclear PDFs

Systematic global analyses of collinearly factorized nuclear PDFs (nPDFs) indicate that bound-nucleon PDFs clearly differ from the free-proton PDFs, see e.g. Refs. [90–95]. The resulting nuclear modifications in the bound-proton PDFs $f_i^{p/A}$ can be quantified with

$$f_i^{p/A}(x,Q^2) = R_i^{p/A}(x,Q^2)f_i^p(x,Q^2), \qquad (33)$$

where i denotes the parton flavor, f_i^p is the free-proton PDF and $R_i^{p/A}$ is the nuclear modification. The corresponding neutron PDFs are obtained using isospin symmetry. The above PDFs and their modifications are, however, *spatial averages* of the nPDFs, they do not account for the dependence of the nuclear density and especially not its fluctuations, i.e. for the fact that in the lowest-density regions the nuclear effects should vanish whereas in the high-density regions they should be larger than in the average $R_i^{p/A}$. These spatial effects can become significant especially in the small-x region relevant for lowest-p_T minijet production of interest here, hence they are an important contributing factor in computing hydrodynamic initial density profiles that directly influence the centrality dependence of observables like multiplicities and flow coefficients. Therefore, in an EbyE simulation such as MC-EKRT here, we cannot use the spatially averaged nPDFs but need to introduce *EbyE-fluctuating* spatially dependent nPDFs (snPDFs), where the nuclear modifications are sensitive to the nucleon-density fluctuations from event to event. As we will discuss below, this turns out to be a non-trivial problem in an EbyE simulation where there are large density fluctuations present.

Originally, our idea was to directly utilize the available non-fluctuating snPDFs, such as EPS09s [71], where the nuclear modifications are encoded in as a power series of the average (optical Glauber) nuclear thickness function, $T_A^{WS}(\bar{s}) = \int dz \, \rho_{WS}(\mathbf{x})$, as follows:

$$f_i^{p/A}(\bar{s},x,Q^2) = f_i^p(x,Q^2)r_i^{p/A}(\bar{s},x,Q^2), \qquad (34)$$

where f_i^p again are the free-proton PDFs, and the nuclear modification part,

$$r_i^{p/A}(\bar{s},x,Q^2) = 1 + \sum_{n=1}^{4} c_n^i(x,Q^2)[T_A^{WS}(\bar{s})]^n, \qquad (35)$$

where the coefficients c_n^i are A-independent, is normalized to the known (EPS09 [90]) average nuclear modifications,

$$R_i^{p/A}(x,Q^2) = \frac{1}{A}\int d^2s \, T_A^{WS}(\bar{s})r_i^{p/A}(\bar{s},x,Q^2). \qquad (36)$$

Alternatively, as done e.g. in Refs. [96–98], one could in the interest of the simulation speed truncate the above power series at the second term, allow some residual A dependence in the remaining single coefficient, and obtain

$$f_i^{p/A}(\bar{s},x,Q^2) = f_i^p(x,Q^2)\left[1 + c_A^i(x,Q^2)T_A^{WS}(\bar{s})\right], \qquad (37)$$

where again the normalization to the average modifications $R_i^{p/A}(x,Q^2)$ would give

$$c_A^i(x,Q^2) = \frac{A}{T_{AA}(0)}\left(R_i^{p/A}(x,Q^2) - 1\right), \qquad (38)$$

with $T_{AA}(0) = \int d^2s \, [T_A^{WS}(\bar{s})]^2$. Then, with the nuclear density fluctuations present in an EbyE simulation, one could essentially just replace the average T_A^{WS} by the fluctuating $T_A(\bar{s}) = \sum_a T_N(\bar{s}-\bar{s}_a)$, where T_N is the Gaussian density from Eq. (23). This procedure does *not*, however, work, because in practice the maximal density at which the above approaches are applicable is the maximum of the average density [61], $T_A^{WS}(0) = 2\rho_0 d \log\left(1 + e^{R_A/d}\right)$, and now with fluctuations we encounter densities that easily exceed this (see Fig. 2 ahead), and can be even more than $3T_A^{WS}(0)$.

In particular with the latter approach above, in the small-x nuclear shadowing region, where $R_i^{p/A}(x,Q^2) < 1$ and thus $c_A^i(x,Q^2) < 0$, when a negative c_A^i is accompanied by a large enough $T_A(\bar{s})$, the spatial PDFs become negative, which cannot be allowed in LO. A possible cure for this could be to introduce an exponentiated ansatz for the above power series (motivated by Ref. [99]),

$$1 + c_A^i(x,Q^2)T_A(\bar{s}) \to \exp(c_A^i(x,Q^2)T_A(\bar{s})). \qquad (39)$$

However, with density fluctuations, in the region where $T_A(\bar{s}) \gg T_A^{WS}(0)$, also this form leads to too fast attenuating small-x parton densities in that the density function $T_A(\bar{s})\exp(c_A^i(x,Q^2)T_A(\bar{s}))$ (whose $\bar{s}$-integral is normalized to $R_i^{p/A}(x,Q^2)$), is not a monotonically rising function of $T_A(\bar{s})$ contrary to what it should be. This problem can be solved by using an another ansatz function, such as

$$1 + c_A^i(x,Q^2)T_A(\bar{s}) \to 1/(1 - c_A^i(x,Q^2)T_A(\bar{s})) \qquad (40)$$

instead, which, when multiplied by $T_A(\bar{s})$, conveniently gives a positive-definite function that is monotonously rising with $T_A(\bar{s})$. In the antishadowing region where $c_A^i(x, Q^2) > 0$, and where the A-dependence of the nuclear modification is modest in any case, such a function would at large T_A's lead to violation of the per-nucleon momentum sum rule that is assumed in the global PDF analyses. We have tested that this problem can be solved approximately (conserving momentum on a percent level) by choosing a more modestly increasing logarithmic function

$$1 + c_A^i(x, Q^2)T_A(\bar{s}) \rightarrow 1 + \log(1 + c_A^i(x, Q^2)T_A(\bar{s})). \quad (41)$$

Equations (40) and (41) above are therefore the functional choices we make in what follows.

Now, exploiting these preliminary observations, we can construct the needed snPDFs, $f_i^{a/A}(\{\bar{s}_a\}, x_1, Q^2)$, which are sensitive to the location $\bar{s}_a$ of the nucleon a in the nucleus A, and thereby also to the surrounding nucleon density in each event (indicated by $\{\bar{s}_a\}$), but which do *not* depend on the intra-nucleon density $T_N(\bar{s})$ of the nucleon a or its fluctuations. This is the approximation which we have used in writing Eq. (13) in its form, where the minijet cross section depends spatially only on the locations of the nucleons a and b but does not contain any transverse-coordinate integrals.

First, for each fixed nucleon configuration in the nucleus A (correspondingly for B), we define a nuclear thickness function T_A^a from where the contribution from the nucleon a, whose center is at $\bar{s}_a$, has been excluded,

$$T_A^a(\bar{s}) \equiv \sum_{a' \neq a}^{A} T_N^{a'}(\bar{s} - \bar{s}_{a'}). \quad (42)$$

Then the average nuclear thickness function experienced by the nucleon $a \in A$ can be defined as

$$\hat{T}_A^a(\{\bar{s}_a\}) \equiv \frac{\int d^2\bar{s}\, T_N(\bar{s} - \bar{s}_a)T_A^a(\bar{s})}{\int d^2\bar{s}\, T_N(\bar{s} - \bar{s}_a)} \quad (43)$$

$$= \sum_{a' \neq a}^{A} \int d^2\bar{s}\, T_N(\bar{s} - \bar{s}_a)T_N^{a'}(\bar{s} - \bar{s}_{a'}) \quad (44)$$

$$= \sum_{a' \neq a}^{A} T_{NN}^{aa'}(\bar{b}_{aa'}), \quad (45)$$

where we have used the normalization of T_N^a and Eqs. (42) and (15) with $\bar{b}_{aa'} = \bar{s}_{a'} - \bar{s}_a$, and where the overlap functions $T_{NN}^{aa'}(\bar{b}_{aa'})$ are of the same Gaussian form as that in Eq. (24). Two things are to be noted here: First, for a specific nucleon a in a nucleus A with a fixed (random) nucleon configuration, $\hat{T}_A^a(\{\bar{s}_a\})$ is a fixed number, whose value depends on the positions of the other nucleons (a') relative to the nucleon a. Second, the effect of the above self-exclusion is that in the region of very low nucleon density, which is the case in an event where a single nucleon a is far from other nucleons a', the density $T_N(\bar{s} - \bar{s}_{a'})$ vanishes, bringing thus also $\hat{T}_A^a$ appropriately to zero. The distribution of $\hat{T}_A^a$ for a lead nucleus is shown in Fig. 2.

Now, essentially using $\hat{T}_A^a$ in place of T_A^{WS}, we define the EbyE fluctuating snPDFs for a nucleon a analogously to the above discussion, as follows:

$$f_i^{a/A}(\{\bar{s}_a\}, x, Q^2) = f_i^a(x, Q^2)r_i^{a/A}(\{\bar{s}_a\}, x, Q^2), \quad (46)$$

where $\bar{s}_a$ is the location of the nucleon $a \in A$, which is fixed for each nucleon configuration (i.e., in each event), and the nuclear modification is
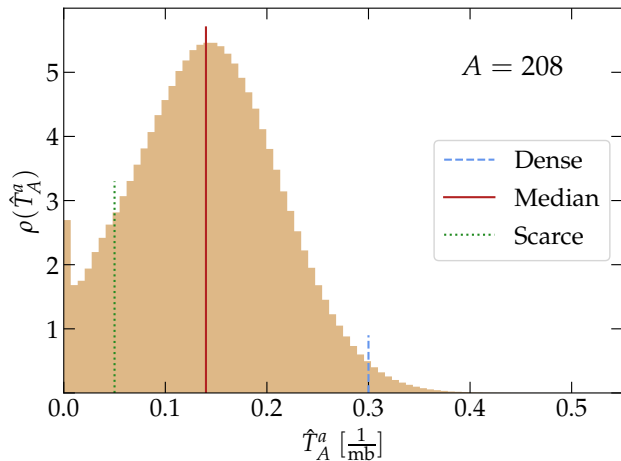

FIG. 2: Normalized distribution of the average nuclear thickness function $\hat{T}_A^a$ experienced by a nucleon $a \in A$, defined in Eq. (45), for the nucleus Pb^{208}, sampled from 10 000 nuclei. For comparison, optical Glauber $T_A^{\text{WS}}(0) \approx 0.212$/mb. The vertical lines indicate the example-density regions to which we refer as "dense" (dashed blue line), "median" (solid red line) and "scarce" (dotted green line). The peak at the smallest values of $\hat{T}_A^a$ arises at the edge of the nucleus where the internucleon distance becomes larger than the nucleonic width σ_N.

$$r_i^{a/A}(\{\bar{s}_a\}, x, Q^2) = \theta(c_A^i(x, Q^2)) \left[1 + \log(1 + c_A^i(x, Q^2)\hat{T}_A^a(\{\bar{s}_a\}))\right] + \frac{\theta(-c_A^i(x, Q^2))}{1 - c_A^i(x, Q^2)\hat{T}_A^a(\{\bar{s}_a\})}, \qquad (47)$$

where θ is the Heaviside step function. Because of the reasons discussed above, we have chosen the above functional forms for ensuring an appropriate behaviour of the modifications in $\hat{T}_A^a$, accurate enough momentum conservation, and a correct small-$\hat{T}_A^a$ limit. As explained above, at the limit of vanishing nucleon density, i.e. if a is an isolated single nucleon far away from other nucleons, $\hat{T}_A^a \to 0$ and thus also $r_i^{a/A}(\{\bar{s}_a\}, x, Q^2) \to 1$.

The coefficient function $c_A^i(x, Q^2)$ in Eq. (47) is determined for fixed x and Q^2 by requiring that the average modification, which is obtained by averaging first over all the nucleons a in each nucleus and then averaging over a large sample of nuclei A, becomes $R_i^{p/A}(x, Q^2)$ of Eq. (33),

$$R_i^{p/A}(x, Q^2) = \left\langle \frac{1}{A} \sum_a r_i^{a/A}(\{\bar{s}_a\}, x, Q^2) \right\rangle_{\{A\}} \qquad (48)$$

$$\equiv F\left(c_A^i(x, Q^2)\right), \qquad (49)$$

where $\langle \dots \rangle_{\{A\}}$ denotes the latter average. Note that here for each parton flavor i we are summing the modifications $r_i^{a/A}$ that are related to the bound proton's $R_i^{p/A}$ (e.g. related to $R_{u_V}^{p/A}$ we sum $r_{u_V}^{p/A}$ from Z protons and $r_{d_V}^{n/A} = r_{u_V}^{p/A}$ from $A - Z$ neutrons). Since we assume isospin symmetry and as the locations of the protons and neutrons are sampled from the same Woods-Saxon distribution, we do not need to keep track of the nucleon identity here but can take all nucleons to be just protons. The function $F(c_A^i)$ is a monotonous function of c_A^i, so it can be inverted to yield the normalization function

$$c_A^i(x, Q^2) = F^{-1}\left(R_i^{p/A}(x, Q^2)\right). \qquad (50)$$

The function F can be calculated numerically for any given c_A^i by sampling a large number of nuclei A. The inverse can then be approximated by creating an interpolation function for a list of numerically calculated values of $F\left(c_A^i(x, Q^2)\right)$, and then inverting that interpolation function. In what follows, in computing the nucleon-configuration-specific PDFs $f_i^{a/A}(\{\bar{s}_a\}, x, Q^2)$ in Eq. (46), we obtain the coefficients $c_A^i(x, Q^2)$ in Eq. (50) using the EPS09LO average modifications [90], and the free-proton PDFs correspondingly from the CT14LO set [100] using the LHAPDF library [101].

In Fig. 3 we compare the spatially dependent, nucleon-configuration-specific gluon modifications $r_g^{a/A}(\{\bar{s}_a\}, x, Q^2)$, computed from Eq. (47), with the average nuclear gluon modifications $R_g^A(x, Q^2)$, obtained from the EPS09LO nPDFs, for a lead nucleus at a

scale $Q^2 = 1.69\,\text{GeV}^2$. To illustrate how in the densest (scarcest) regions the nuclear effects become larger (smaller) than in the average modification $R_g^A(x, Q^2)$, we show the snPDF gluon modifications for three different fixed values of the average thickness function $\hat{T}_A^a(\bar{s}_a)$.
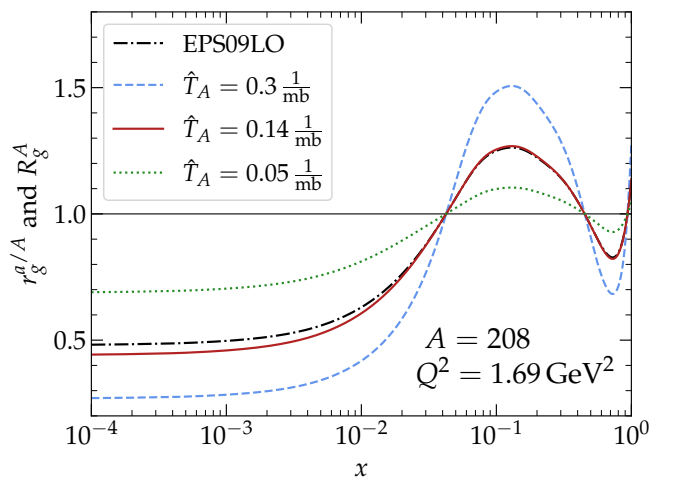

FIG. 3: Comparison of the snPDF gluon modification $r_g^{a/A}(\{\bar{s}_a\}, x, Q^2 = 1.69\,\text{GeV}^2)$ of Eq. (47) (dashed blue, solid red and dotted green curves) with the average EPS09LO [90] gluon modification $R_g^A(x, Q^2 = 1.69\,\text{GeV}^2)$ (dashed-dotted black curve) for the nucleus Pb^{208}. The fixed values $\hat{T}_A^a(\{\bar{s}_a\}) = 0.3, 0.14$, and 0.05 1/mb, chosen here as input for $r_g(\{\bar{s}_a\}, x, Q^2 = 1.69\,\text{GeV}^2)$, are representatives for a nucleon in the dense, median, and scarce density regions, correspondingly, see Fig. 2.

We have now discussed the elements necessary for obtaining the nucleon-nucleon overlap function $T_{NN}(\bar{b}_{ab})$ and the integrated minijet cross section $\sigma_{\text{jet}}^{ab}(\{\bar{s}_a\}, \{\bar{s}_b\}, p_0, \sqrt{s_{NN}})$ that go into the calculation of the probability distributions of multiple minijet production in nucleon-nucleon collisions in Eq. (11). Figure 4 shows examples of these distributions in Pb+Pb collisions at $\sqrt{s_{NN}} = 5.02$ TeV and $p_0 = 1$ GeV at three different nucleon-nucleon impact parameters $\bar{b}_{ab}$, and choosing both nucleons, $a \in A$ and $b \in B$, from the same densest, scarcest and median density regions of A and B as in Fig. 3, $\hat{T}_A^a(\bar{s}_a) = \hat{T}_B^b(\bar{s}_b) = 0.3, 0.05$, and 0.14 1/mb. The figure nicely illustrates the large fluctuations of the minijet multiplicity due to various sources. The minijet multiplicity is heavily sensitive not only to the nucleon-nucleon impact parameter $\bar{b}_{ab}$ (the larger $\bar{b}_{ab}$ the smaller $\bar{N}_{\text{jets}}^{ab}$) but also to the spatial dependence of the
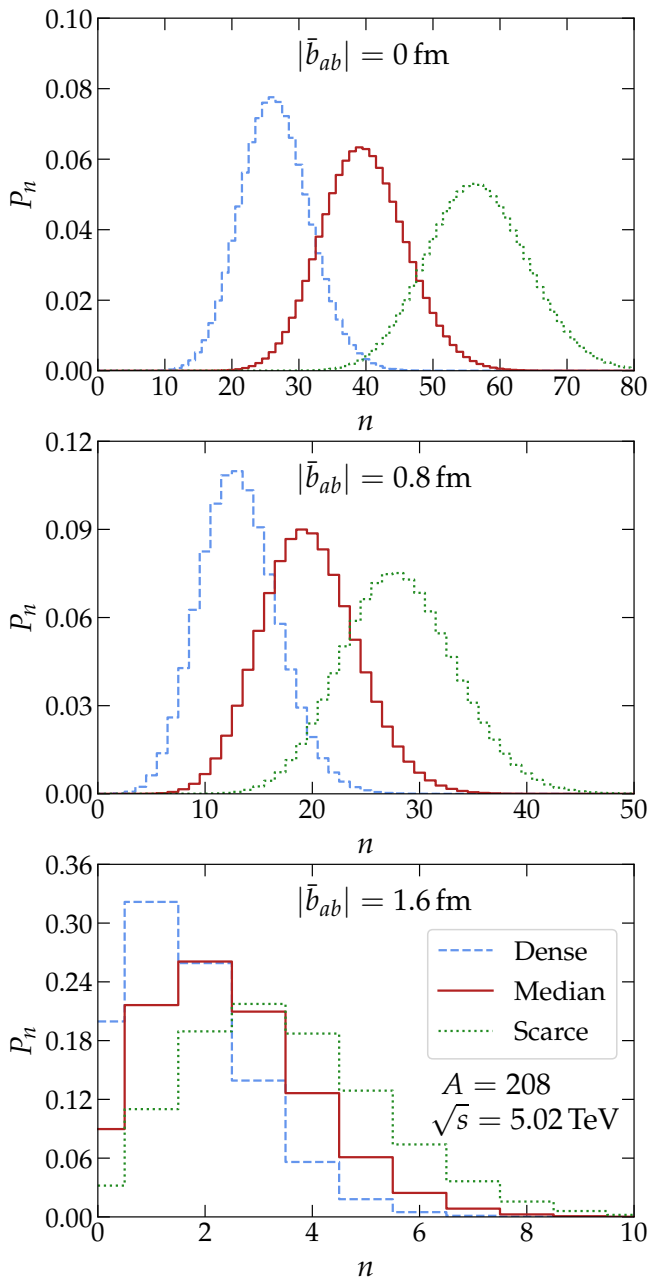
FIG. 5: Minijet transverse energy in the mid-rapidity unit as a function of the collision centrality in $\sqrt{s_{NN}} = 5.02\,\text{TeV}$ Pb+Pb collisions, as predicted from the MC-EKRT model using snPDFs (solid lines) and spatially averaged nPDFs (dashed lines). Here $K = 2$ and $\kappa_{\text{sat}} = 2$, see Sec. II E for the details of minijet filtering and Sec. II F for the details of the centrality selection.

nuclear density regions produce clearly less (more) dijet multiplicity than those who originate from the median-density regions.

In Fig. 5, we show the centrality dependence of the produced minijet transverse energy at mid-rapidity that is obtained from our MC-EKRT model with snPDFs and with average nPDFs. The figure very clearly demonstrates why it is important to account for the spatial dependence of the nPDFs (the details of the centrality selection and the imposed minijet filtering will be discussed below). As can be seen in the figure, in central collisions, where the minijet production on the average originates from the average nuclear-overlap regions (volume effect), the spatial nuclear effects due to the snPDFs average essentially to those obtained with spatially averaged nPDFs. Towards peripheral collisions, however, where scarcer regions of the nuclei are colliding and where the nuclear effects in the snPDFs become smaller, the difference to the average-nPDF results becomes increasingly larger. As the figure shows, we can expect easily over 20 % changes relative to the average-nPDF results, which is a significant effect when we compare the MC-EKRT results (after hydrodynamic evolution) with experimental data (Sec. IV ahead).

E. Minijet filtering by saturation and conservation of energy & valence quark number

After the dijet candidates have been generated from all the nucleon–nucleon pairs as described in Sec. II D, the next step in the MC-EKRT simulation is to filter away

FIG. 4: Examples of the Poissonian probability distributions P_n of Eq. (11) for multiple candidate-dijet production with partonic $p_T \geq 1\,\text{GeV}$ from a nucleon pair ab, $a \in A$ and $b \in B$, at some fixed nucleon-nucleon impact parameters $\bar{b}_{ab}$ in Pb+Pb collisions at $\sqrt{s_{NN}} = 5.02\,\text{TeV}$. The values used for σ_{jet}^{ab} (with $K = 2$) here are chosen so that they represent the cases where both of the nucleons originate from the same dense (dashed blue curves), median (solid red curves) and scarcest (dotted green curves) density regions as in Fig. 3.

nPDFs (large fluctuations at fixed $\bar{b}_{ab}$). We also see the role of shadowing and its spatial dependence, in that the colliding nucleons that come from the densest (scarcest)
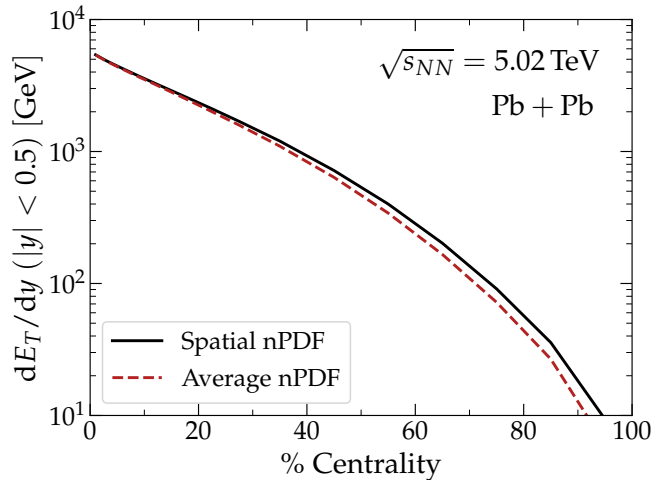
the excessive dijets on the basis of saturation, and conservation of energy/momentum and valence-quark numbers. Ideally of course the energy/momentum conservation should not be needed at all, as ideal multiparton distributions should conserve momentum, but as these are not available, and especially not to all orders as would be required here in the context of saturation, we have to impose energy/momentum conservation separately from the saturation. As we assume saturation to be the decisive dynamical mechanism that regulates minijet production at low transverse momenta, saturation-based filtering is done first, and conservation of momentum only after that. With such phenomenological details, experimental data is our guide as well: we have tested, averaging over the minijets falling into the mid-rapidity unit and feeding them into 2+1 D hydrodynamics event-by-event, that we reproduce systematically more correctly the measured ratio of the flow coefficients v_2 and v_3 [102] when the energy/momentum-conservation filtering is performed after the saturation-filtering and also when the latter filtering has as little effect as possible.

As is obvious, any kind of filtering breaks the factorization assumption of our pQCD calculation as the produced minijets are then not anymore independent of each other. The higher-twist effects (causing saturation here) die out in inverse powers of the virtuality Q^2, so that at the highest values of p_T, factorization is expected to hold. Also the global analysis of nPDFs [92, 94, 95] and jet production in minimum-bias proton-nucleus collisions [103] indicate this to be the case. Thus, to maintain factorization at the highest values of p_T, the list of all candidate dijets in an $A+B$ collision is next ordered in decreasing p_T. Both filterings are then done, separately, in this order, starting from the jets with highest values of p_T, and rejecting all those dijets that fulfill the filtering conditions.

Guided by the geometric EKRT saturation criterion, Eq. (5), each dijet is assumed to have a spatial uncertainty area of a radius $\propto 1/p_T$ in the transverse plane around the dijet production point. Consider a dijet candidate whose transverse momentum is p_T^{cand}, and transverse production point is $\bar{s}^{\mathrm{cand}}$. All of the previously accepted dijets with corresponding parameters $p_T \geq p_T^{\mathrm{cand}}$ and $\bar{s}$ are then inspected, and if for any of them

$$|\bar{s} - \bar{s}^{\mathrm{cand}}| < \frac{1}{\kappa_{\mathrm{sat}}} \left(\frac{1}{p_T} + \frac{1}{p_T^{\mathrm{cand}}} \right), \quad (51)$$

the dijet candidate is rejected. The parameter κ_{sat} introduced here is an external fit parameter, which acts as a "packing factor" in determining how close to each other the dijets can be produced. Notice that parametrically $\kappa_{\mathrm{sat}}^2 \propto K_{\mathrm{sat}}$ of Ref. [17], and that the smaller κ_{sat} the stronger the saturation, i.e. the more dijet candidates get rejected.

After the saturation filtering above, the remaining, still p_T-ordered, list of accepted dijets is then subjected to the filtering according to energy/momentum conservation. Again here it is not obvious, or even clear, whether the momentum should be conserved for each nucleon separately, or only for the whole nucleus as a parton cloud, or something in between. Here, to be consistent with what is typically done in the global analyses of the nPDFs, we require energy conservation at the nucleon level as a default. We do, however, test also the case where no separate energy/momentum conservation is required in addition to saturation.

To force the energy/momentum conservation (energy conservation, for short) per nucleon for a given dijet candidate with momentum fractions x_1^{cand} in a projectile nucleon $a \in A$ and x_2^{cand} in a target nucleon $b \in B$, we proceed as follows: Assume that we have a list of n already accepted dijets that involve the same projectile nucleon a, and m previously accepted dijets that involve the same target nucleon b. These dijets have momentum fractions $(x_1^{(1)}, \ldots, x_1^{(n)})_a$ and $(x_2^{(1)}, \ldots, x_2^{(m)})_b$ associated with a and b, respectively. Now, if either

$$x_1^{\mathrm{cand}} + \sum_{i=1}^n x_1^{(i)} > 1 \quad \text{or} \quad x_2^{\mathrm{cand}} + \sum_{j=1}^m x_2^{(j)} > 1, \quad (52)$$

the dijet candidate is rejected due to the breaking of the per-nucleon energy budget.

The third filtering, performed simultaneously with the above energy conservation, is the forcing of the valence quark number conservation. As explained earlier in Sec. II D 2, we can keep track of whether each candidate dijet involves valence quarks from the nucleons $a \in A$ and/or $b \in B$. If a candidate dijet involves a valence quark of a specific flavor either from a or from b, and if either a or b has already consumed all its valence quarks of that flavor in the prior parton scatterings at $p_T > p_T^{\mathrm{cand}}$, then the candidate dijet is rejected. For the multiplicities and elliptic flow that we will study later in this paper, this filtering causes a negligible effect but we nevertheless build it in for interesting further studies in the future.

As an illustration, in Fig. 6 we show the transverse-plane distribution of dijet production points before and after the filterings in a single central event. The radius of each disk surrounding the production points is $1/(\kappa_{\mathrm{sat}} p_T)$. As seen in the left panel, the candidate dijets overoccupy the transverse plane. As a result of applying the saturation condition of Eq. (51), none of the disks overlap in the right panel.

F. Centrality selection

To determine which centrality percentile each $A+B$ collision belongs to, one needs to classify the events according to, e.g., the produced minijet transverse energy E_T in a chosen rapidity window. Alternatively, when running hydrodynamics with the minijet initial conditions, converting E_T into initial state densities, one can use either initial state entropy or final state multiplicity as the criterion. In this work, in the interest of simulation speed, we do the centrality selection according to the
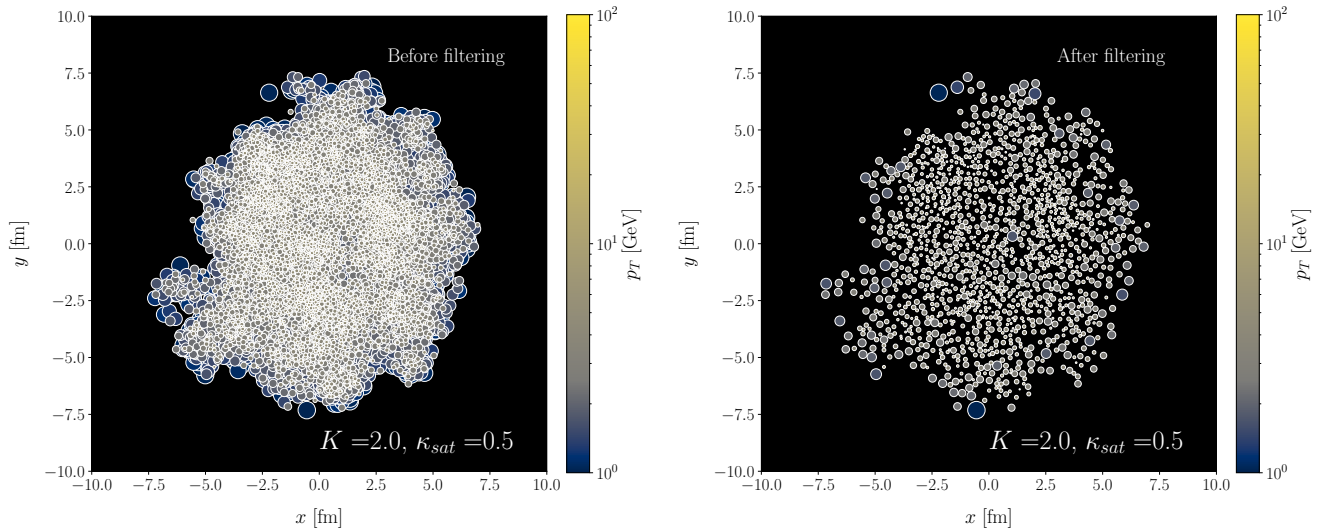
FIG. 6: Illustration of the effects of saturation and energy-conservation in the transverse distribution of produced dijets in one central event. Left panel shows the production points of all the candidate dijets, and the right panel the case after the filterings. The radius of the disk surrounding each dijet production point is $1/(\kappa_{\mathrm{sat}} p_T)$. Here for the illustration, we use $K = 2$, and $\kappa_{\mathrm{sat}} = 0.5$.
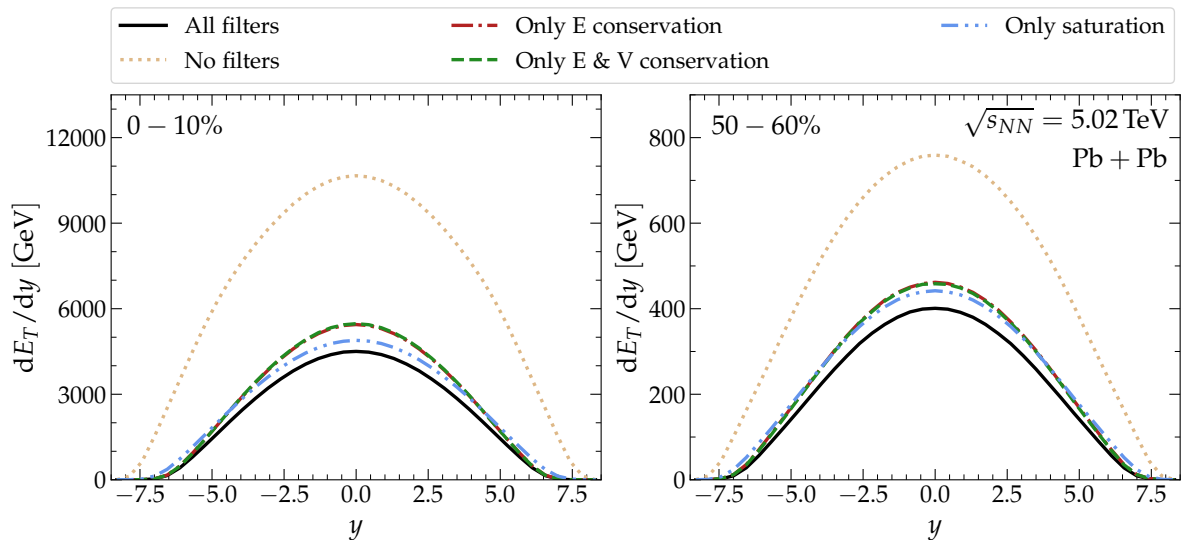

FIG. 7: The effects of the EKRT saturation, energy-conservation and valence-quark number conservation filters to the production of minijet transverse energy $\mathrm{d}E_T/\mathrm{d}y$, as a function of rapidity y, in central (left panel) and peripheral Pb+Pb collisions (right panel) at $\sqrt{s_{NN}} = 5.02\,\mathrm{TeV}$. Here $K = 2$ and $\kappa_{\mathrm{sat}} = 2$.

total minijet E_T produced (after the filterings) anywhere in rapidity. We have checked that the results would be very similar if e.g. a central rapidity unit would be used. Concretely then, for a simulation of, say, 10 000 $A+B$ collisions, the 0-5 % centrality class refers to the collection of 500 collisions with the highest total transverse energy.

G.   Systematics of minijet filtering

Figures 7 and 8 illustrate the effect of the three filters. Figure 7 shows the rapidity distribution of the transverse energy originating from the dijets, obtained as a scalar sum of minijet p_T's, plotted for 0-10 % central (left panel) and 50-60 % central (right panel) Pb+Pb collisions at $\sqrt{s_{NN}} = 5.02\,\mathrm{TeV}$, computed with $K = 2$, and $\kappa_{\mathrm{sat}} = 2$. The figure demonstrates first a considerable reduction of E_T when going from all the candidate

dijets (dotted brown curves) down to those who pass the saturation filter (dashed-double-dotted blue curves), and then a clearly smaller reduction down to those who pass also the energy-conservation and valence quark filters in addition (solid black curves). As expected, for this quantity the effect of the valence quark filtering is very small (see the overlapping dashed-dotted red and dashed green curves). Interestingly, however, we notice that imposing only the energy-conservation filter without saturation (dashed-dotted red curves) would lead to a similar result in E_T as the saturation filter alone, which essentially is a result of ordering the dijet candidates according to the minijet p_T. Here again, we note that although not visible in these plots, we have checked that the v_2/v_3 ratio prefers a strongest possible saturation [102], and also that imposing only the energy-conservation filter (when realized as in here) typically leads to too narrow rapidity distributions.

Figure 8 then, correspondingly, shows the p_T distribution of (mini)jets at all rapidities, originating from the dijets which have not been filtered at all (dotted brown curves), from those dijets that survived first the saturation filter (dashed-double-dotted blue curves) and then also the energy-conservation and valence-quark filters (black solid curves). In the left panel, we see – as is expected by construction – how factorization in central collisions (upper set of curves) remains unbroken at $p_T \gtrsim 5$ GeV, while both filters start to have an effect at $p_T \lesssim 5$ GeV. In peripheral collisions (lower set of curves), where the minijet multiplicities are smaller and therefore saturation becomes effective at smaller p_T, factorization remains unbroken until slightly smaller values of p_T than in central collisions. We again also see how saturation filter, the one imposed first, dominates here over that of energy conservation, and also that the saturation filter tends to remove dijets at slightly larger values of p_T than the energy-conservation filter (see dashed-double-dotted blue and the dotted-dashed red curves). Also here the valence quark conservation causes a negligible effect. The right panel of Fig. 8 is to demonstrate the difference of (mini)jet production in different spatial regions of central collisions: In the dilute overlap regions (upper set of curves) the factorization-breaking saturation and energy-conservation effects set in at clearly smaller values of p_T than in the regions of densest overlap (lower set of curves).

Figures 9 and 10 show the minijet transverse energy production in the central rapidity unit as a function of centrality in Pb+Pb collisions at $\sqrt{s_{NN}} = 5.02$ TeV, computed with various values of the fit parameters K and κ_{sat}, with all filters imposed in Fig. 9, and with only the saturation filter imposed Fig. 10. As can be seen from the right panels, where $\kappa_{\text{sat}} = 2$ is fixed, changing K changes mainly the overall normalization but essentially not the centrality slope of the produced E_T (and hence the final multiplicities as well). The energy-conservation filter weakens the K dependence, because with a larger K-factor the energy-conservation filter removes more can-

didate dijets. The left panels in turn show how, for a fixed value of $K = 2$, changing κ_{sat} changes both the normalization and especially the centrality slope. Here the energy-conservation filter in turn weakens the κ_{sat} dependence, as with a larger κ_{sat} there is less saturation and more minijet production and the energy conservation filter becomes more efficient in removing candidate dijets. In any case, as long as κ_{sat} does not become too large, and especially if only the saturation-filter is imposed, κ_{sat} serves as a centrality-slope parameter for the mid-rapidity multiplicities, whereas the K-factor controls mainly their normalization. This observation is exploited in what follows (Sec. IV), in finding the possible values for κ_{sat} and K with which we can reproduce the measured charged-hadron multiplicities.

III. FLUID DYNAMICAL EVOLUTION AND PARTICLE SPECTRA

The MC-EKRT computation gives the initially produced parton state. In order to compare with the measured data, we need to first propagate the partons to a proper time τ_0 for initializing the 3+1 D fluid dynamics, then compute the subsequent spacetime evolution of the matter, and eventually determine the experimentally measurable momentum spectra of hadrons.

A. Fluid dynamical framework

The spacetime evolution is computed using 3+1 D fluid dynamics, applying the code package developed in Ref. [73]. The fluid dynamical framework employed is the relativistic dissipative second-order transient fluid dynamics [104], originally formulated by Israel and Stewart [105].

The basic equations of motion governing the evolution of a fluid are the local conservation laws for energy, momentum and conserved charges, like the net-baryon number. In the following we, however, will neglect the conserved charges. In this case the state of the fluid is given by its energy-momentum tensor that can be decomposed with the help of the Landau-picture fluid 4-velocity u^μ as

$$T^{\mu\nu} = e u^\mu u^\nu - P\Delta^{\mu\nu} + \pi^{\mu\nu}, \tag{53}$$

where $\Delta^{\mu\nu} = g^{\mu\nu} - u^\mu u^\nu$ is a projection operator, $e = T^{\mu\nu}u_\mu u_\nu$ is the energy density in the local rest frame, $P = -\frac{1}{3}\Delta_{\mu\nu}T^{\mu\nu}$ is the isotropic pressure, and $\pi^{\mu\nu} = T^{\langle\mu\nu\rangle}$ is the shear-stress tensor. The angular brackets project the symmetric and traceless part of the energy-momentum tensor that is orthogonal to the fluid 4-velocity. We will also neglect the bulk viscous pressure, and the isotropic pressure is given by the equation of state (EoS) of the strongly interacting matter at zero net-baryon density, $P = P(e)$. In the Landau picture the
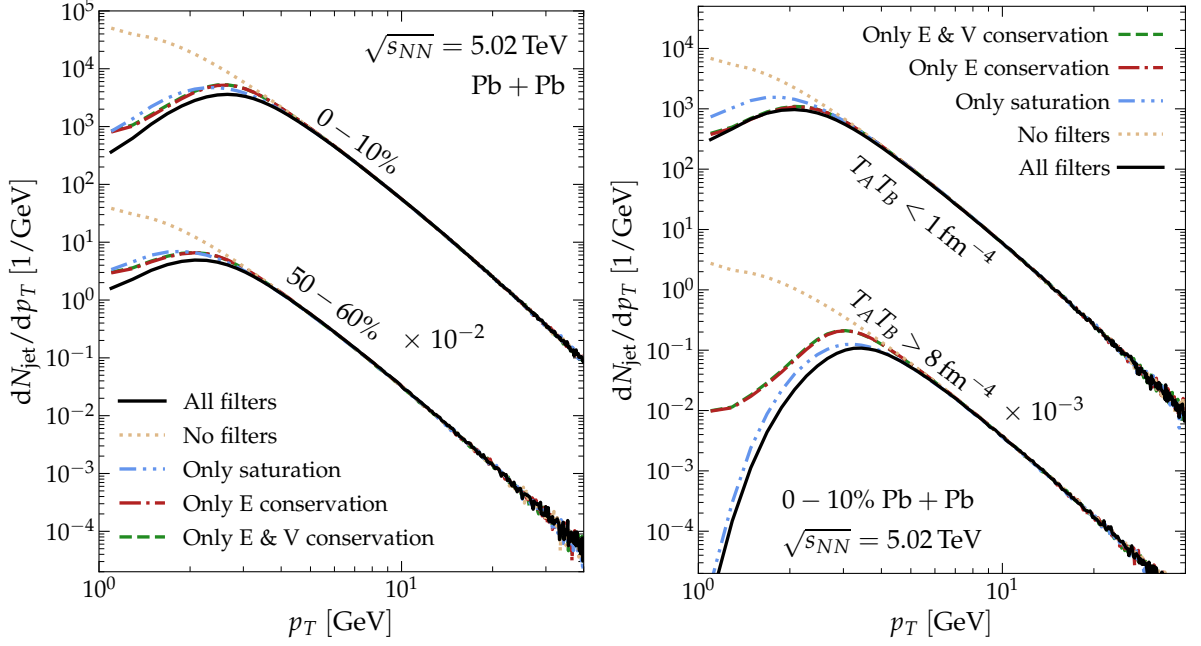
FIG. 8: The effects of the EKRT saturation and the energy- and valence-quark conservation filters to the transverse momentum distribution of produced (mini)jets in Pb+Pb collisions at $\sqrt{s_{NN}} = 5.02$ TeV, in 0-10% and 50-60% centrality classes (left panel) and in the different overlap-density regions in the 0-10% central collisions (right panel). Here $K = 2$ and $\kappa_{\mathrm{sat}} = 2$. For the lower set of curves in both panels, notice the downward scalings by the factors indicated in the panels.
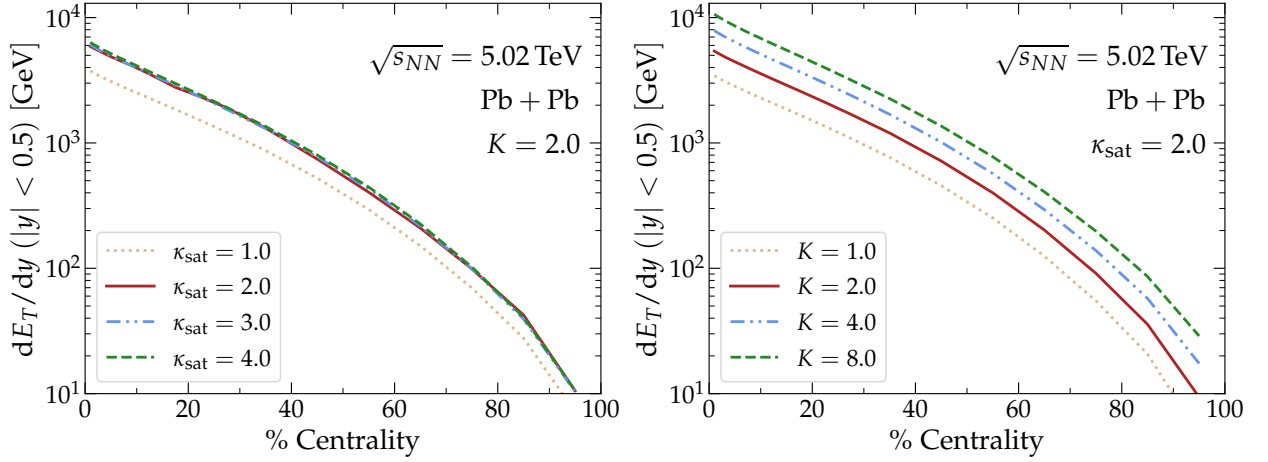

FIG. 9: Centrality dependence of minijet transverse energy in the mid-rapidity unit in Pb+Pb collisions at $\sqrt{s_{NN}} = 5.02$ TeV, corresponding to one fixed value of $K = 2$ and various values of κ_{sat} (left panel), and to one fixed value of $\kappa_{\mathrm{sat}} = 2$ and various values of K (right panel), with all filters imposed. The red solid curve is the same in both panels.

fluid 4-velocity is a time-like, normalized eigenvector of the energy-momentum tensor, defined by $T^{\mu}_{\nu} u^{\nu} = e u^{\mu}$. The energy diffusion current $W^{\mu} = \Delta^{\mu\alpha} T_{\alpha\beta} u^{\beta}$ is then zero and does not contribute to the energy-momentum tensor.

In the formalism by Israel and Stewart [105], the equations of motion for the remaining dissipative quantity,

shear-stress tensor, are given by [104, 106]

$$\tau_{\pi} \frac{d}{d\tau} \pi^{\langle\mu\nu\rangle} + \pi^{\mu\nu} = 2\eta\sigma^{\mu\nu} + 2\tau_{\pi}\pi_{\alpha}^{\langle\mu}\omega^{\nu\rangle\alpha}$$
$$- \delta_{\pi\pi}\pi^{\mu\nu}\theta - \tau_{\pi\pi}\pi_{\alpha}^{\langle\mu}\sigma^{\nu\rangle\alpha} + \varphi_7\pi_{\alpha}^{\langle\mu}\pi^{\nu\rangle\alpha}, \quad (54)$$

where $\sigma^{\mu\nu} = \nabla^{\langle\mu}u^{\nu\rangle}$ and $\omega^{\mu\nu} = \frac{1}{2}\left(\nabla^{\mu}u^{\nu} - \nabla^{\nu}u^{\mu}\right)$ are the strain-rate and vorticity tensors, respectively, $\theta = \nabla^{\mu}u_{\mu}$ is the volume expansion rate, and the gradient is
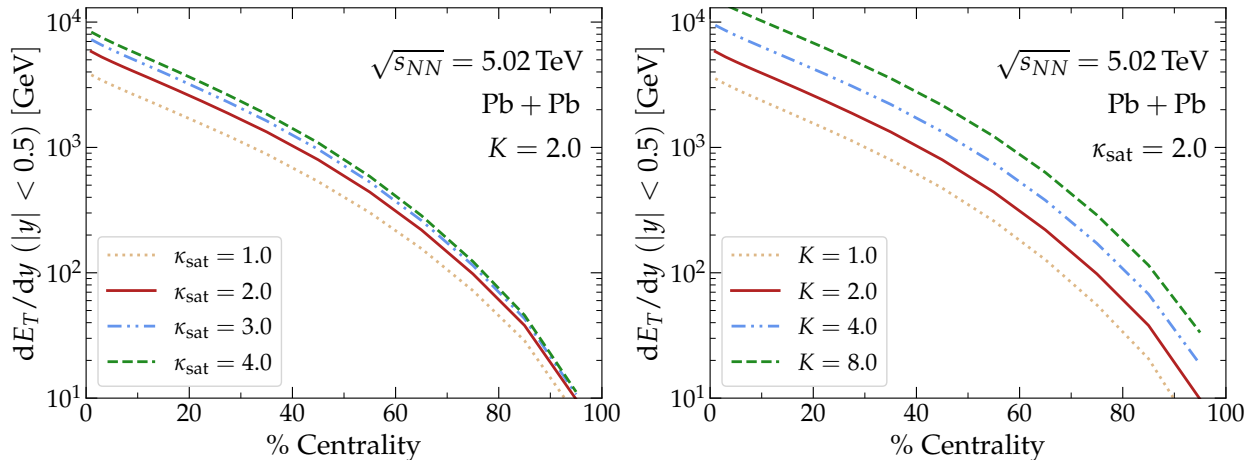
FIG. 10: The same as in Fig. 9 but with only the saturation filter imposed.

.

defined as $\nabla^\mu = \Delta^\mu_\alpha \partial^\alpha$. The coefficient η is the shear viscosity, $\tau_\pi = 5\eta/(e+P)$ is the shear relaxation time, and the remaining coefficients of the second-order terms are taken from the 14-moment approximation to massless gas [104, 106, 107], i.e. $\delta_{\pi\pi} = (4/3)\tau_\pi$, $\tau_{\pi\pi} = (10/7)\tau_\pi$, and $\varphi_7 = 9/(70P)$. The shear viscosity over entropy density η/s is chosen such that it roughly reproduces the elliptic flow in semi-central collisions. For the EoS of strongly interacting matter we use the $s95p$-v1 [108] parametrization, which interpolates between the lattice QCD at high temperatures and the hadron resonance gas model at low temperatures. The partial chemical freeze-out at $T = 150$ MeV is encoded into the hadronic part of the EoS as temperature-dependent chemical potentials for each hadron, $\mu_h = \mu_h(T)$ [109].

The Israel-Stewart equations together with the conservation laws are solved numerically in 3+1 dimensions [73] using the SHASTA algorithm [110] in (τ, x, y, η_s)– coordinates, where

$$\tau = \sqrt{t^2 - z^2} \tag{55}$$

is the longitudinal proper time, and

$$\eta_s = \frac{1}{2} \ln\left(\frac{t+z}{t-z}\right) \tag{56}$$

is the spacetime rapidity. The grid resolution is $\Delta\eta_s = 0.15$, $\Delta x = \Delta y = 0.15$ fm, and $\Delta\tau = 0.05$ fm. For further details of the algorithm, see Refs. [73, 111].

The final spectra of free hadrons are obtained by computing the Cooper-Frye integrals [112] on a constant-temperature decoupling surface, with $T_{\text{dec}} = 130$ MeV. The momentum distributions of hadrons on the decoupling surface are given by the 14-moment approximation, so that the single-particle momentum distribution function of a hadron h is

$$f_h(p^\mu, x) = f_{0h}\left(1 + (1 \pm f_{0h})\frac{p_\mu p_\nu \pi^{\mu\nu}}{2T^2(e+P)}\right), \tag{57}$$

where $+(-)$ is for bosons (fermions), p^μ is the 4-momentum of a hadron h, and $f_{0h} = f_{0h}(T, \mu_h)$ is the corresponding Bose-Einstein or Fermi-Dirac equilibrium distribution function. The Cooper-Frye integral is computed for all the hadrons included into the hadron resonance gas part of the EoS. As explained in Ref. [73], after computing the full spectra of hadrons, $dN_h/dydp_T^2 d\phi$, the spectra are interpreted as probability densities and they are randomly sampled to obtain a set of hadrons with 4-momenta p_i^μ. For the unstable hadrons the corresponding 2- and 3-particle strong and electromagnetic decays are then computed. The sampling procedure is then repeated several times in order to get smooth momentum distributions for the hadrons that are stable under strong decays.

B. Initialization

The equations of fluid dynamics take the energy-momentum tensor as an initial condition at a fixed initial proper time τ_0. However, an MC-EKRT event consists of a set of partons, and we need to convert this set to the corresponding $T^{\mu\nu}(\tau_0, x, y, \eta_s)$ using the momenta of the produced particles. There are two essential ingredients in this. First, we need to propagate the particles to a fixed proper time $\tau_0 = 1/p_0$, and for the determination of densities from a finite set of particles, we need to define an averaging volume where the components of the energy-momentum tensor are computed.

Naively, the grid size, e.g. Δx or $\Delta \eta_s$ in the numerical algorithm to solve the Israel-Stewart theory would provide such an averaging volume. However, the grid defines rather a discretization of the continuous fields in the hydrodynamic equations of motion, and in principle we should be able to take the limit to the continuum, i.e. $\Delta x, \Delta \eta_s \to 0$, and at this limit densities are no

longer well defined smooth functions. Thus, we should distinguish between the averaging volume and the numerical resolution. The procedure with which we define the averaging volume through Gaussian smearing and obtain the corresponding densities is described below. We note that here we will eventually only construct the local energy density from the MC-EKRT computation, and neglect the initial velocity and shear-stress components. Moreover, we do not take into account the event-by-event fluctuations in the hydrodynamical phase, but compute the initial conditions as averages over a large sample of MC-EKRT events. However, the procedure below can be extended to the computation of all the components of $T^{\mu\nu}$. We will leave the studies that take into account the event-by-event fluctuations as well as a complete $T^{\mu\nu}$ initialization as a future work.

1. Free streaming

Each parton i in an MC-EKRT event has the following information: transverse coordinate $\mathbf{x}_{\perp,0i}$ of the production point, transverse momentum $\mathbf{p}_{Ti}$, and rapidity y_i. All partons are massless in this work. We assume that each parton is produced at the location $\mathbf{x}_{\perp,0i}$ and $z_i = 0$ at time $t = 0$. The partons are assumed to travel as free particles along straight line trajectories. In this case, the spacetime rapidity $\eta_{s,i}$ of the parton i becomes equivalent to its momentum rapidity y_i, and longitudinal coordinate of the propagating parton is given by $z_i(t) = t \tanh \eta_{s,i}$. The transverse position of the parton at Cartesian coordinate time t is given by $\mathbf{x}_{\perp i}(t) = \mathbf{x}_{\perp,0i} + t\mathbf{p}_{Ti}/E_i$, where $E_i = p_{Ti} \cosh y_i$. However, we need to initialize fluid dynamics at a fixed proper time $\tau_0 = t/\cosh \eta_s$ in the τ-η_s coordinate system, in which case the parton's coordinates become $(\tau_0, \mathbf{x}_{\perp i}(\tau_0), \eta_{s,i})$, where $\mathbf{x}_{\perp i}(\tau_0) = \mathbf{x}_{\perp,0i} + \tau_0 \mathbf{p}_{Ti}/p_{Ti}$.

2. Smearing

In general, the four-momentum $p^\alpha = (p^\tau, \mathbf{p}_T, p^\eta)$ of a particle at a spacetime location $x^\alpha = (\tau, \mathbf{x}_\perp, \eta_s)$ in the τ-η_s coordinates is obtained as

$$p^\alpha = \frac{\partial x^\alpha}{\partial x'^\mu} p'^\mu = \begin{pmatrix} p_T \cosh(y - \eta_s) \\ \mathbf{p}_T \\ \tau^{-1} p_T \sinh(y - \eta_s) \end{pmatrix}, \quad (58)$$

where x'^μ and p'^μ are the corresponding spacetime point and four-momentum in the Cartesian coordinates.

The total number of partons N that flow through a surface, whose surface element 4-vector is $d\Sigma_\mu$, can be written as

$$N = \int d\Sigma_\alpha N^\alpha(\tau, \mathbf{x}_\perp, \eta_s), \quad (59)$$

where the particle 4-current N^α in the τ-η_s coordinates can be written using Eq. (58) as

$$N^\alpha(\tau, \mathbf{x}_\perp, \eta_s) = \int \frac{d^3 p}{p^\tau} \tau p^\alpha f(\tau, \mathbf{x}, \mathbf{p}), \quad (60)$$

where we defined $d^3p = d^2\mathbf{p}_T dp^\eta$, and f is a scalar momentum distribution function at a constant τ. For a constant-τ surface, the surface element 4-vector has only the τ component, $d\Sigma_\tau = d^2\mathbf{x}_\perp d\eta_s \tau$, and the total number of partons can be written as

$$N = \int d^2\mathbf{x}_\perp d\eta_s \tau \int d^2\mathbf{p}_T dp^\eta \tau f(\tau, \mathbf{x}, \mathbf{p}). \quad (61)$$

Now, following Ref. [113], the scalar momentum distribution function for a set of N partons can be written in terms of delta functions in coordinate and momentum space as

$$f(\tau, \mathbf{x}, \mathbf{p}) = \sum_{i=1}^{N} \delta^{(3)}(\mathbf{x} - \mathbf{x}_i) \delta^{(3)}(\mathbf{p} - \mathbf{p}_i)/|\det(g)|, \quad (62)$$

where $\mathbf{x}_i = (\mathbf{x}_{\perp i}, \eta_{s,i})$ is the three-location and $\mathbf{p}_i = (\mathbf{p}_{Ti}, p_i^\eta)$ is the three-momentum of the particle i at proper time τ, and $\det(g) = -\tau^2$ is the determinant of the metric tensor $g_{\mu\nu} = \text{diag}(1, -1, -1, -\tau^2)$. The summation is over all the particles. Substituting Eq. (62) into Eq. (61), it is easy to verify that we consistently arrive at the correct number of particles, i.e. in our case the number of partons from an MC-EKRT event. Similarly, the components of the energy-momentum tensor can be expressed as

$$T^{\alpha\beta}(\tau, \mathbf{x}_\perp, \eta_s) = \int \frac{d^2\mathbf{p}_T dp^\eta}{p^\tau} \tau p^\alpha p^\beta f(\tau, \mathbf{x}, \mathbf{p}). \quad (63)$$

In what follows, we will assume that $p_i^\eta = 0$, so that $y_i = \eta_{s,i}$. Changing the integration variable from p^η to rapidity y using Eq. (58), the integral can be then written as

$$T^{\alpha\beta} = \sum_i \int d^2\mathbf{p}_T dy \frac{p^\alpha p^\beta}{p^\tau} \frac{1}{\tau} \cosh(y - \eta_s) \quad (64)$$

$$\times \delta^{(2)}(\mathbf{x}_\perp - \mathbf{x}_{\perp i}) \delta(\eta_s - \eta_{s,i}) \delta^{(2)}(\mathbf{p}_T - \mathbf{p}_{Ti}) \delta(y - \eta_s).$$

The resulting $\delta(y - \eta_s)$ ensures that $y = \eta_s$, i.e. initial longitudinal scaling flow holds even after we replace the spatial delta functions by Gaussian smearing functions below.

To obtain a smooth density profile for relativistic hydrodynamics from the partons, we replace the spatial delta functions with Gaussian distributions,

$$\delta^{(2)}(\mathbf{x}_\perp - \mathbf{x}_{\perp i}) \delta(\eta_s - \eta_{s,i}) \to g_\perp(\mathbf{x}_\perp; \mathbf{x}_{\perp i}) g_\parallel(\eta_s; \eta_{s,i}), \quad (65)$$

with

$$g_\perp(\mathbf{x}_\perp; \mathbf{x}_{\perp i}) = \frac{C_\perp}{2\pi\sigma_\perp^2} \exp\left[-\frac{(\mathbf{x}_\perp - \mathbf{x}_{\perp i})^2}{2\sigma_\perp^2}\right], \quad (66)$$

$$g_\parallel(\eta_s; \eta_{s,i}) = \frac{C_\parallel}{\sqrt{2\pi\sigma_\parallel^2}} \exp\left[-\frac{(\eta_s - \eta_{s,i})^2}{2\sigma_\parallel^2}\right], \quad (67)$$

where $\sigma_\perp$ and $\sigma_\parallel$ are the widths of the distributions in the transverse and longitudinal directions, respectively. Both $\sigma_\perp$ and $\sigma_\parallel$ are considered to be free parameters of our model. Equations (66) and (67) are normalized as

$$\int d^2\mathbf{x}_\perp d\eta_s g_\perp(\mathbf{x}_\perp; \mathbf{x}_{\perp i}) g_\parallel(\eta_s; \eta_{s,i}) = 1. \qquad (68)$$

To reduce the computational costs, we impose a cut-off on the smearing range to $\pm 3\sigma$ in each direction from the centre of the Gaussian distribution. However, the cut-off on the integration range and the numerical error originating from the discretization of Gaussian functions violate the normalization condition in Eq. (68). Therefore, the constants $C_\perp$ and $C_\parallel$ in Eqs. (66) and (67) are adjusted in every $f_i(\tau, \mathbf{x}, \mathbf{p})$ so that the unit normalization is ensured. We checked, however, that $C_\perp$ and $C_\parallel$ are almost unity with the current parameters in the simulations.

With these choices, the initial value of the $T^{\tau\tau}(\tau_0, \mathbf{x}_\perp, \eta_s)$ component of the energy-momentum tensor in hydrodynamics is given as

$$T^{\tau\tau}(\tau_0, \mathbf{x}_\perp, \eta_s) = \qquad (69)$$
$$\frac{1}{\tau_0} \sum_i p_{Ti} g_\perp(\mathbf{x}_\perp; \mathbf{x}_{\perp i}) g_\parallel(\eta_s; \eta_{s,i}).$$

In this exploratory study, as we do not yet consider a more detailed spacetime picture of parton production [114], pQCD showering and secondary collisions of partons, and especially as we consider only averaged initial conditions, we follow Ref. [17] and compute only the above initial $T^{\tau\tau}(\tau_0)$ component, and ignore the initial bulk pressure and shear-stress tensor, as well as set $T^{\tau i}(\tau_0) = 0$, or equivalently set the spatial components of the four-velocity $u^\mu(\tau_0) = \gamma(1, \mathbf{v}_T(\tau_0), v^\eta(\tau_0))$ initially to zero. Here $v^\eta(\tau_0) = 0$ follows from the condition $y = \eta_s$ that corresponds to $v_z = z/t$ in the collision frame. The remaining diagonal components of the energy-momentum tensor are then given by the EoS as $T^{ij}(\tau_0) = P(e(\tau_0))\delta^{ij}$, where now in the absence of initial transverse flow, $e(\tau_0) = T^{\tau\tau}(\tau_0)$.

We note that this way of initializing does not explicitly conserve energy, but with $\sigma_\parallel = 0.15$ the total energy is increased only by $\sim 1\ \%$, while with e.g. $\sigma_\parallel = 0.5$ already by $\sim 13\ \%$. On the other hand, $dE/d\eta_s$ with a rapidity independent distribution of particles would be conserved in the smearing. The MC-EKRT distribution is not rapidity independent, but in practice $dE/d\eta_s$ is almost identical before and after the smearing of parton distribution in the mid-rapidity region. Only at larger rapidities, where experimental data are not available in any case, we start to see the the smeared case $dE/d\eta_s$ deviating from the unsmeared minijet $dE/d\eta_s$. This is shown in Fig. 11, where we compare event-averaged $dE/d\eta_s$ computed from the MC-EKRT partons to those obtained after smearing with different values of $\sigma_\parallel$.
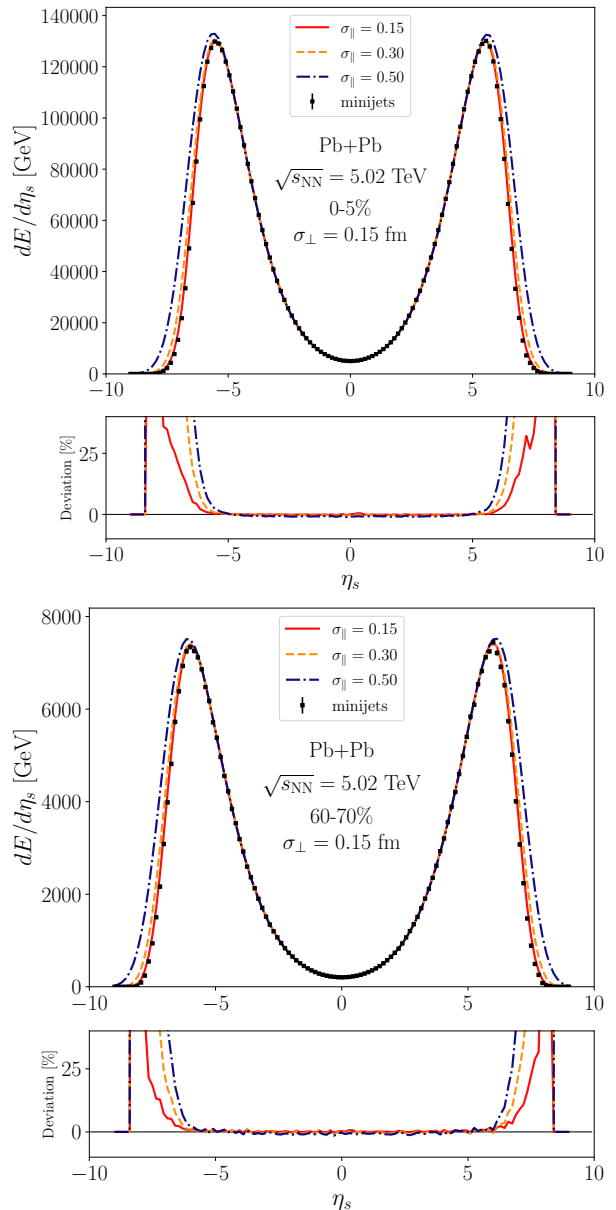

FIG. 11: Spacetime rapidity distribution of the event-averaged initial energy, $dE/d\eta_s$ as a function of η_s, at $\tau = \tau_0$ in 0-5 % central (a) and 60-70 % central (b) 5.02 TeV Pb+Pb collisions, obtained from the minijets before the smearing (markers) and after the smearing with a fixed transverse width $\sigma_\perp = 0.15$ fm and with different longitudinal widths $\sigma_\parallel$ (solid, dashed and dotted-dashed curves). The smaller panels show the relative difference between the smeared and unsmeared cases.

3. Averaging initial conditions

The above construction gives us the initial energy density event-by-event. As an example, the energy density distribution at $\tau = \tau_0$ obtained from a single event is plotted in the x-y and η_s-x planes in panels (a) and (b)
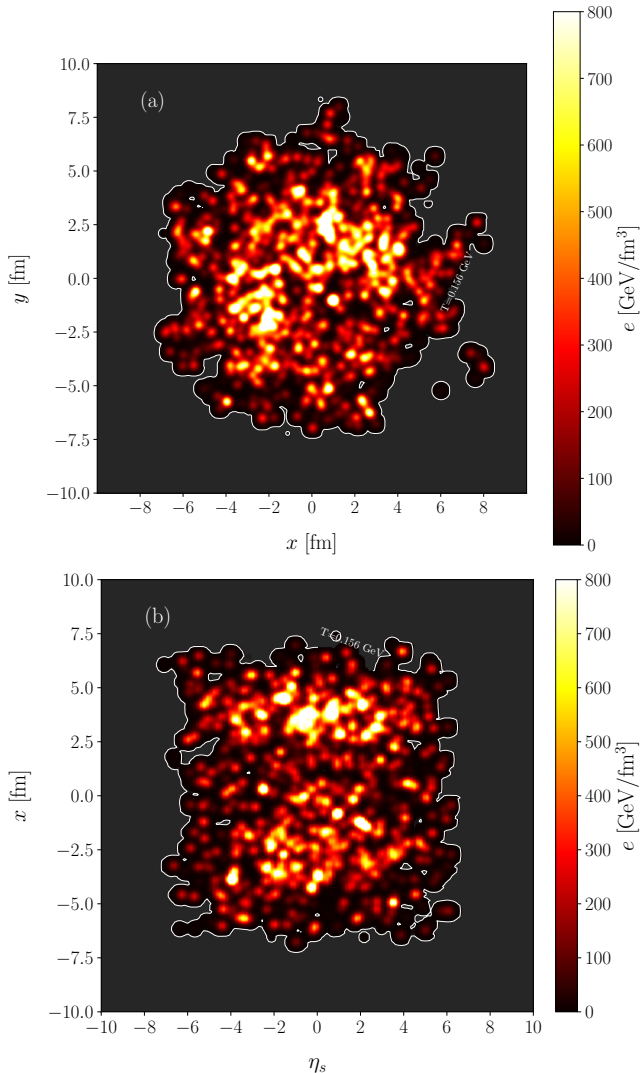
and the final hadron multiplicity have nearly a linear relation, and therefore averaging over the entropy-density profiles rather than over the energy-density profiles is a better approximation for obtaining the event-averaged final multiplicities, and their centrality dependence [28]. The difference here comes from the non-linear relation between the energy and entropy densities. The linear relation between the multiplicity and the initial entropy is somewhat broken by event-by-event fluctuations in the entropy production due to dissipation, but those fluctuations relative to total entropy production are typically small in central and semi-central collisions [17].

IV. RESULTS

In the following, we have applied MC-EKRT to 5.02 TeV and 2.76 TeV Pb+Pb, and 200 GeV Au+Au collisions. In particular, we explore here how the centrality and pseudorapidity dependence of charged particle multiplicity at different collision energies is affected by different choices of the Gaussian smearing and shear viscosity. We will also discuss the role of the energy conservation at different collision energies.

For each investigated collision system 100 000 minimum bias events were produced and sorted in centrality classes based on their initial transverse energy E_T. The Gaussian smearing widths were chosen to be $\sigma_\perp = 0.15$ or 0.4 fm in the transverse plane and the longitudinal smearing width was fixed to $\sigma_\parallel = 0.15$. The ratio of shear viscosity to entropy density η/s was taken either as constant, tuned to approximately reproduce the elliptic flow measurements at RHIC and LHC, or to follow the temperature dependent $\eta/s = param1$ from Ref. [17] (see Fig. 1 there).

The free parameters in the MC-EKRT model, namely K and $\kappa_{\rm sat}$, were tuned to approximately reproduce the centrality dependence of charged particle multiplicity at midrapidity. The saturation parameter $\kappa_{\rm sat}$ was kept the same for all systems, but the pQCD K-factor was tuned for each collision system separately. We note that the parameter values quoted here are specific to these realizations of MC-EKRT computation, and are different for different choices of e.g. smoothing and viscosity. Also event-by-event fluctuations would likely change these values.

A. Data comparison with event-averaged initial state

1. Charged particle pseudorapidity distribution

Figures 13, 14, and 15 show the charged particle pseudorapidity (η) distributions for $\sqrt{s_{NN}} = 5.02$ TeV Pb+Pb, 2.76 TeV Pb+Pb, and 200 GeV Au+Au collisions, respectively. The centrality classes are quoted in the figures. We show all the cases tested here, namely
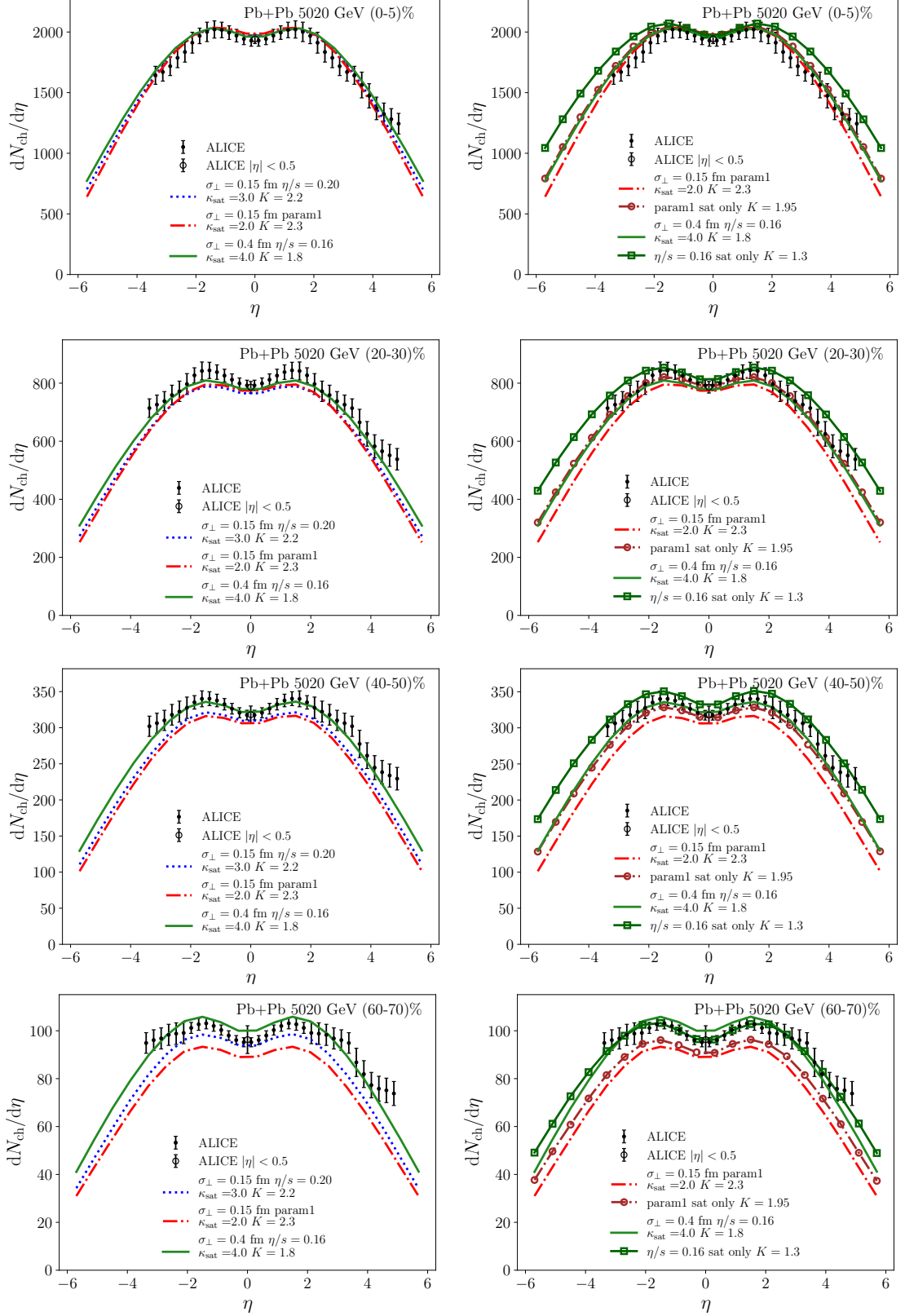

FIG. 12: Initial energy density profile above the QCD transition temperature $T_c = 0.156$ GeV [115] at $\tau = \tau_0$ computed from a single MC-EKRT event in the x-y plane (a), and in the η_s-x plane (b).

of Fig. 12, respectively. Here we, however, want to avoid computationally very intensive 3+1D event-by-event hydrodynamic simulations, and therefore compute event-averaged initial conditions. As explained in Sec. II F, we perform first the centrality selection according to the total initial transverse energy computed from the partons, and average the initial conditions within each centrality class. The hydrodynamic evolution is then computed for each event-averaged initial conditions, i.e. one hydrodynamic simulation per centrality class.

We first convert each event-by-event initial energy-density profile to an entropy-density profile using the EoS, and then average the entropy-density profiles and convert the averaged entropy density back to energy density. The reason for this is that the total initial entropy

FIG. 13: Charged particle multiplicity $dN_{ch}/d\eta$ as a function of pseudorapidity in Pb+Pb collisions at $\sqrt{s_{NN}} = 5.02$ TeV, compared with ALICE data [116] (filled markers) and [117] (open markers). Left panels show the results with all the filters on, and the curves with markers in the right panels show the results with only the saturation filter on. The solid green and dashed-dotted red curves are the same in the left and right panels.
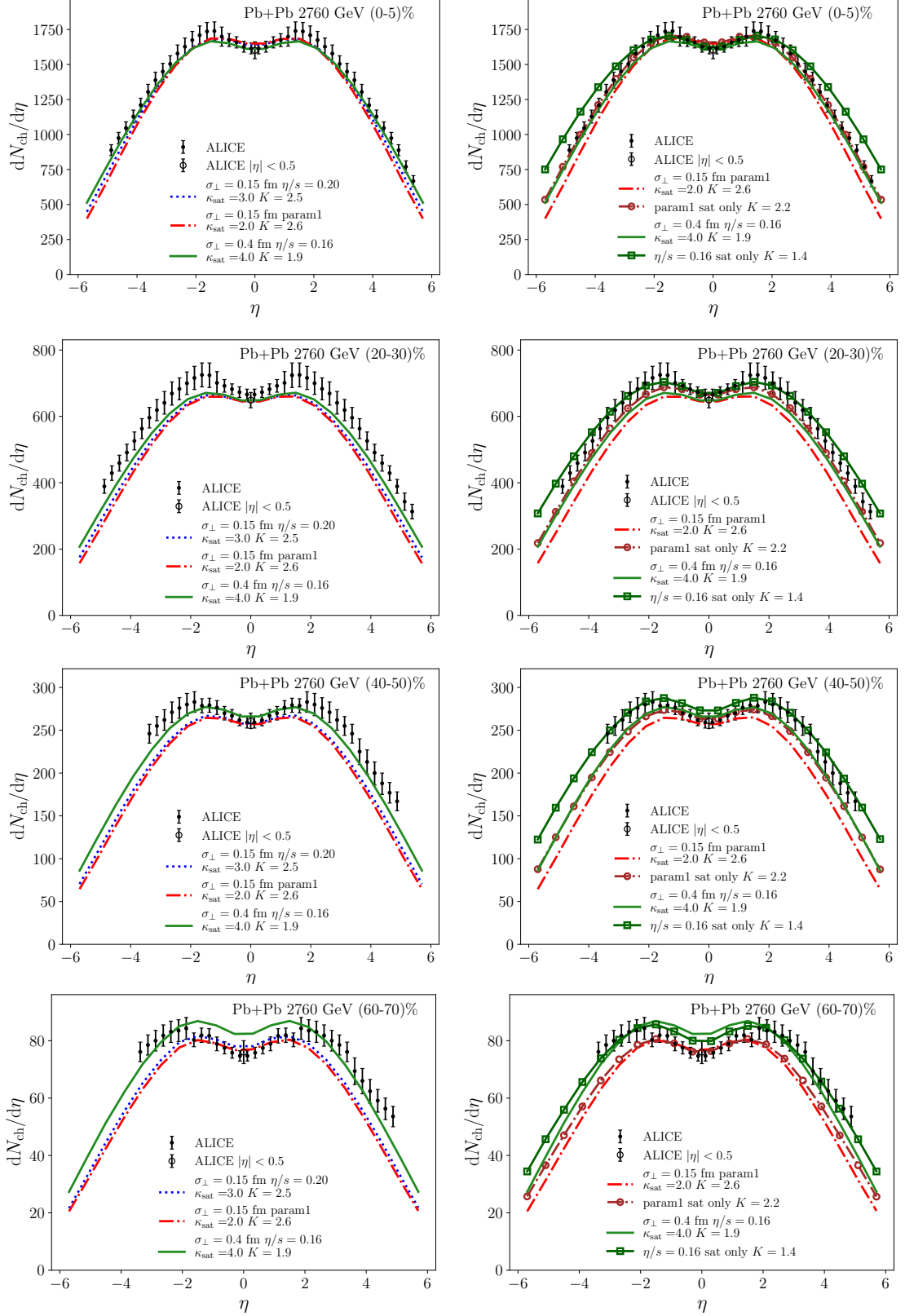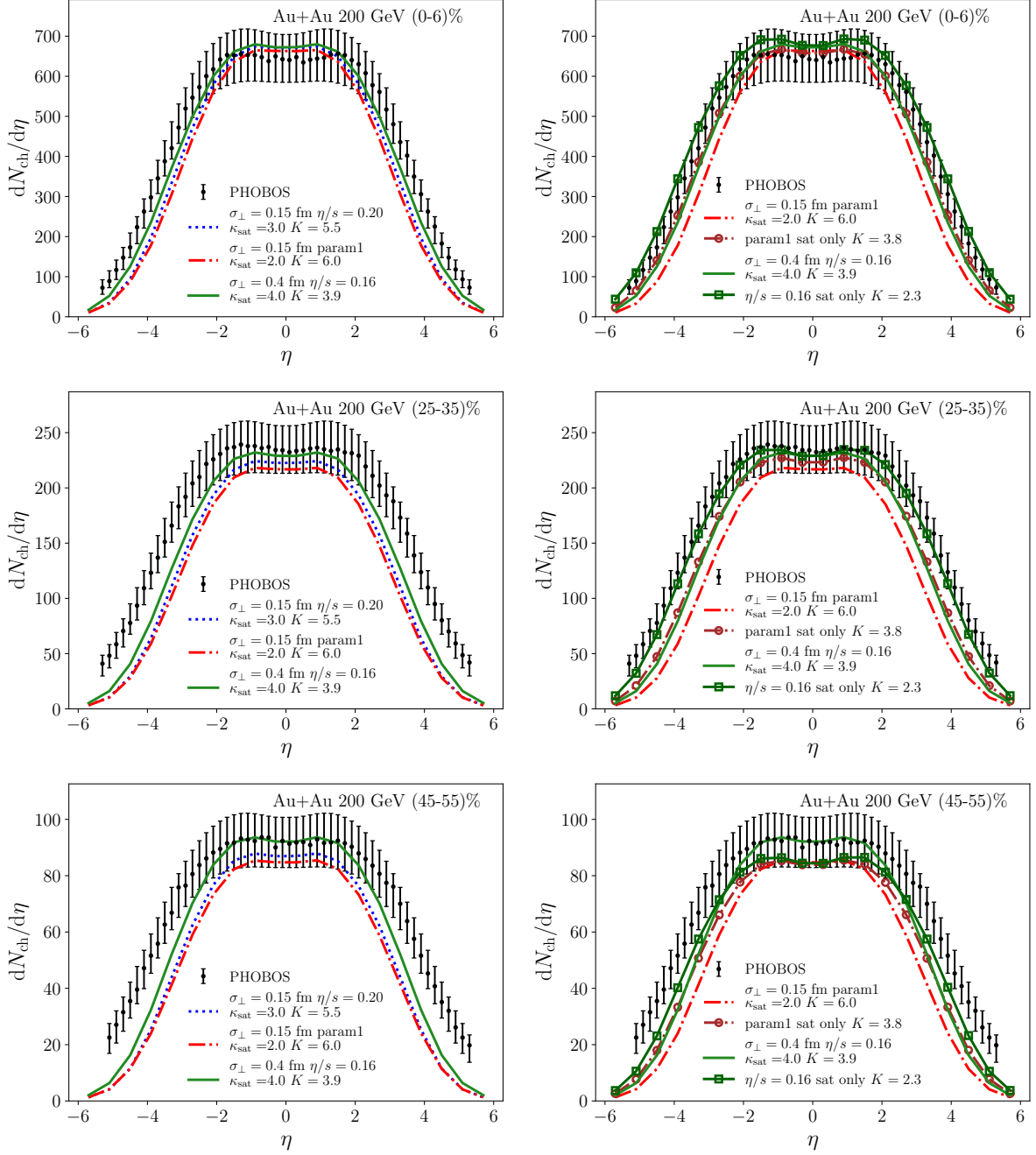
FIG. 14: Charged particle multiplicity $\mathrm{d}N_{\mathrm{ch}}/\mathrm{d}\eta$ as a function of pseudorapidity in Pb+Pb collisions at $\sqrt{s_{NN}} = 2.76$ TeV, compared with ALICE data [118] (filled markers) and [119] (open markers). Left panels show the results with all the filters on, and the curves with markers in the right panels show the results with only the saturation filter on. The solid green and dashed-dotted red curves are the same in the left and right panels.

FIG. 15: Charged particle multiplicity $dN_{ch}/d\eta$ as a function of pseudorapidity in Au+Au collisions at $\sqrt{s_{NN}} = 200$ GeV, compared with PHOBOS data [120]. Left panels show the results with all the filters on, and the curves with markers in the right panels show the results with only the saturation filter on. The solid green and dashed-dotted red curves are the same in the left and right panels.

$\sigma_\perp = 0.15$ fm with $\eta/s = 0.20$, $\sigma_\perp = 0.15$ fm with $\eta/s = param1$, and $\sigma_\perp = 0.4$ fm with $\eta/s = 0.16$. The values of κ_{sat} and K for each case are indicated in the figures. The left panels show the full results where saturation, energy conservation, and valence-quark number conservation are taken into account. The curves with

markers in the right panels show the results with saturation only, demonstrating the role of saturation in the energy conservation, as well as the role of the per-nucleon level energy conservation in narrowing the rapidity distributions.

The values for the K factors that are needed to re-

produce the data are increasing with decreasing collision energy. This is in line with the expectation that NLO corrections become increasingly important towards lower collision energy [66, 67]. We can, however, see that the centrality dependence of the multiplicity is well described by collision energy independent κ_{sat}. This is already a non-trivial result, even if we have some freedom to tune the centrality dependence by changing κ_{sat}. The range of the centrality dependence with different values of κ_{sat} is, as shown in Fig. 9, quite limited. Thus, the centrality dependence of multiplicity is relatively robust prediction of the MC-EKRT model, and the good agreement with the data is similar to the NLO EbyE EKRT model [17], where 2+1 D fluid dynamics was employed.

A significant new feature in the MC-EKRT model is that we can obtain full 3D initial conditions, and subsequently we can compute the pseudorapidity dependence of the charged particle multiplicity. The overall agreement with the rapidity spectra is encouragingly good. At both LHC energies we can essentially reproduce the measurements in all the centrality classes. Only in the most peripheral collisions with $|\eta| > 2$, we can start to see some more significant deviations from the shape of the measured rapidity distribution. In the most central collisions at RHIC the agreement is very similar as at the LHC. In peripheral collisions we start to get too narrow spectrum, but even then the agreement remains good up to $|\eta| \sim 2$.

The transverse smoothing range $\sigma_\perp$ and the η/s parametrization slightly affect both the centrality dependence and the width of the rapidity spectra. The energy per unit rapidity is independent of $\sigma_\perp$, but since the conversion from energy density to entropy density is non-linear, the final multiplicity depends on $\sigma_\perp$. As a result, the rapidity spectra get wider with larger smoothing range. Temperature dependence of η/s also affects the width of the rapidity distribution through the entropy production. If η/s increases with increasing temperature, the relative entropy production becomes larger at higher temperatures or energy densities, and the rapidity distribution becomes narrower than with a constant η/s. Even though the main features of the rapidity spectra are here coming from the MC-EKRT model, the finer details of the obtained spectra depend also on the details of the initialization and on the details of the fluid dynamical evolution.

In the right panels of Figs. 13, 14, and 15 we show the charged particle pseudorapidity distributions with saturation only, i.e. we do not explicitly impose the nucleon-level energy and valence-quark number conservations. As we can see from the figures, comparing the curves with and without the markers, the rapidity distributions become wider without the per-nucleon energy conservation. This is natural, as dijets with large rapidity carry a lot of energy, and are thus more constrained by the energy conservation. It is interesting to note that the saturation-only results can also reproduce the shape of the rapidity distribution in peripheral Au+Au collisions at RHIC.

On the other hand, the saturation-only distributions with $\kappa_{\mathrm{sat}} = 4$ at the LHC tend to get too wide in the most central collisions.

We have checked that with the saturation-only $\kappa_{\mathrm{sat}} = 4$ central-collision cases, i.e. with weaker saturation, the energy conservation of the contributing nucleons is violated on the average already by ~ 50 % at the LHC, and ~ 20 % at RHIC. Interestingly, however, with the saturation-only $\kappa_{\mathrm{sat}} = 2$ central-collision cases, i.e. with stronger saturation, the average violation is only ~ 5 % at the LHC, and energy is practically conserved at RHIC.

These results suggest that, given strong enough saturation, the total energy budget could be conserved even without a requirement of a tight per-nucleon energy conservation, supporting the view that the high-energy nuclear collisions can be described as collisions of two parton clouds rather than as a collection of sub-collisions of individual nucleons.

2. Charged particle elliptic flow

Figure 16 shows the pseudorapidity dependence of elliptic flow, the second-order Fourier coefficient $v_2\{4\}$ of the azimuthal angle distribution of charged hadrons, in semi-central 2.76 TeV Pb+Pb and 200 GeV Au+Au collisions. The model results are calculated using the 4-particle cumulant method [123]. Since our initial energy density profiles are averages over multiple events, $v_2\{\mathrm{EP}\} \approx v_2\{2\} \approx v_2\{4\}$ [2].

The η-differential flow is determined with respect to a reference flow vector, which is typically constructed from particles in a separate rapidity bin to avoid autocorrelations. For the comparison with the ALICE data [121], the reference flow vector is calculated using particles in the TPC pseudorapidity acceptance $|\eta_{\mathrm{ref}}| < 0.8$ and in addition there is also a p_T cut ($0.2 < p_T < 5.0$) GeV. When calculating $v_2(\eta)$ in the rapidity bins with $|\eta| > 2.0$, the particles in the η bin are correlated with the full reference flow vector. For the rapidity bins with $|\eta| < 2.0$, the particles with $\eta < 0$ are correlated with the positive-rapidity reference particles $0 < \eta_{\mathrm{ref}} < 0.8$, while the negative reference $-0.8 < \eta_{\mathrm{ref}} < 0$ is used for particles with $\eta > 0$. In the PHOBOS comparison [122], the reference flow for the $\eta < 0$ bins is determined from particles in the pseudorapidity range $0.1 < \eta_{\mathrm{ref}} < 2.0$ and the reference for $\eta > 0$ is determined from particles in the range $-2.0 < \eta_{\mathrm{ref}} < -0.1$.

As our average initial energy density profiles lack event-by-event fluctuations, at present the comparison to v_2 data has to be considered more qualitative than

---

[2] PHOBOS states in Ref. [122] that their event plane $v_2\{\mathrm{EP}\}$ results are most consistent with the 4-particle cumulant method, so we consider $v_2\{\mathrm{EP}\}$ and $v_2\{4\}$ to be comparable in this particular case.
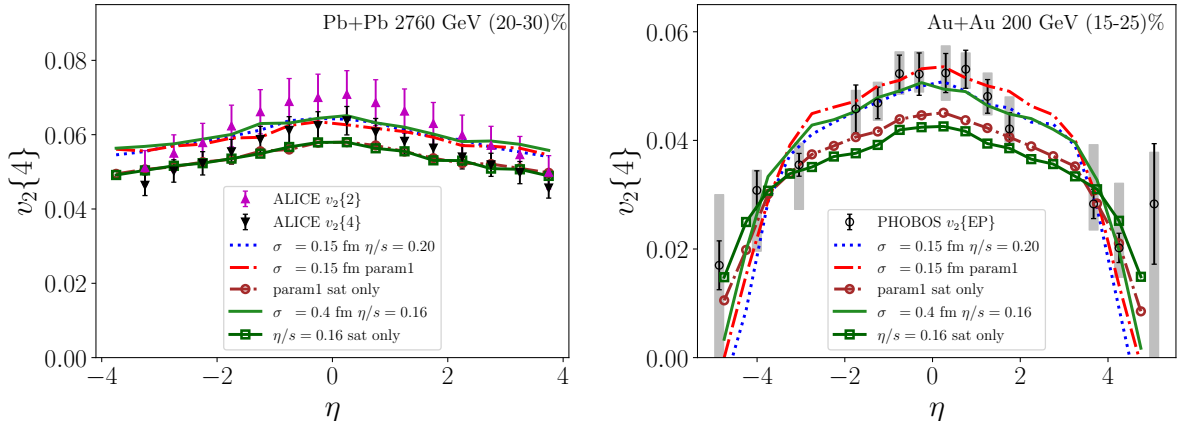
FIG. 16: Charged particle $v_2\{4\}$ as a function of pseudorapidity in Pb+Pb collisions at $\sqrt{s_{NN}} = 2.76$ TeV, in the 20-30 % centrality class, compared with ALICE data [121] (left panel), and in Au+Au collisions at $\sqrt{s_{NN}} = 200$ GeV, in the 15-25 % centrality class, compared with PHOBOS hit-based event plane v_2 data [122] (right panel). The curves without markers show the results with all filters on, and the ones with markers the saturation-only cases. The parameter setups and the curve labelings are the same as in Figs. 13-15.

quantitative in nature. Nevertheless, the currently observed trends look very promising; the magnitude of v_2 is already close to data for both investigated collision systems, and we observe stronger dependence on pseudorapidity at 200 GeV compared to 2.76 TeV, as is also suggested by the data. This steeper fall-off of $dv_2/d\eta$ at RHIC can be understood as a sign of incomplete conversion of spatial eccentricity into momentum anisotropy due to the shorter lifetime of the hot QCD medium at lower collision energies. This result is rather robust with respect to the implementation details of the MC-EKRT initialization. The largest effect is seen when relaxing the energy conservation requirement, which leads to a visible decrease in v_2, but in this case we have not tried to adjust η/s to reproduce the data.

B. Event-by-event fluctuations of the initial state eccentries

Even though we have not performed here event-by-event fluid dynamical evolution, we can still compute the initial state eccentricities event-by-event, and in particular examine the decorrelation of the eccentricities as a function of spacetime rapidity. The spatial eccentricity vector with the magnitude ϵ_2 pointing at the angle Ψ_2 can be defined as a complex number constructed from a weighted average,

$$\epsilon_2 e^{i2\Psi_2} = \frac{\sum_k w_k r_k^2 e^{i2\phi_k}}{\sum_k w_k r_k^2}$$
$$= \frac{\sum_k w_k r_k^2 (\cos(2\phi_k) + i\sin(2\phi_k))}{\sum_k w_k r_k^2}.$$

Here r and ϕ indicate the polar coordinates (radius and angle) in the transverse plane: $r^2 = \hat{x}^2 + \hat{y}^2$, $\cos(2\phi) =$

$(\hat{x}^2 - \hat{y}^2)/r^2$ and $\sin(2\phi) = 2\hat{x}\hat{y}/r^2$, where we have defined $\hat{x} = x - x_{cm}$ and $\hat{y} = y - y_{cm}$ with respect to the center-of-mass point $(x_{cm}, y_{cm}) = \left(\frac{\sum_k w_k x_k}{\sum_k w_k}, \frac{\sum_k w_k y_k}{\sum_k w_k} \right)$. The weight w_k is the initial energy density at $\tau = \tau_0$ in a hydro cell and the sum is over the cells in a transverse slice of the hydro grid which has the width $\Delta\eta_s$.

Once we have determined the eccentricities for each event, we can compute the Pearson correlation of the eccentricity magnitudes between different rapidity bins η_s and η_{s0},

$$c(\epsilon_2(\eta_s), \epsilon_2(\eta_{s0}))$$
$$= \frac{\langle (\epsilon_2(\eta_s) - \langle\epsilon_2(\eta_s)\rangle)(\epsilon_2(\eta_{s0}) - \langle\epsilon_2(\eta_{s0})\rangle) \rangle}{\sigma(\epsilon_2(\eta_s))\sigma(\epsilon_2(\eta_{s0}))}, \quad (70)$$

where $\langle\cdot\rangle$ indicates an average over events and σ is the corresponding standard deviation.

In Fig. 17 we show the event-averaged eccentricities and the Pearson correlations between the eccentricities at finite rapidity $\epsilon_2(\eta_s)$ and midrapidity $\epsilon_2(\eta_{s0} = 0)$ in Pb+Pb collisions at $\sqrt{s_{NN}} = 2.76$ TeV in the LHC and in Au+Au collisions at $\sqrt{s_{NN}} = 200$ GeV at RHIC. The rapidity bin width was chosen to be $\Delta\eta_s = 1.0$. The event-averaged eccentricities remain nearly constant close to midrapidity, but both at RHIC and LHC the eccentricity starts to increase at higher rapidities. We also see that if we relax the energy conservation, the mid-rapidity eccentricities decrease by ~ 10 % at the LHC, and ~ 15 % at RHIC, which explains the decrease in v_2 in the saturation-only cases in Fig. 16.

As seen in the right panel of Fig. 17, the Pearson correlation becomes weaker at higher rapidities, and at RHIC the eccentricity beyond $|\eta_s| \gtrsim 3.5$ is no longer correlated with midrapidity, while at the LHC the correlation spans a considerably larger rapidity range $|\eta_s| \lesssim 5.0$. The decreasing number of particles at RHIC compared to the
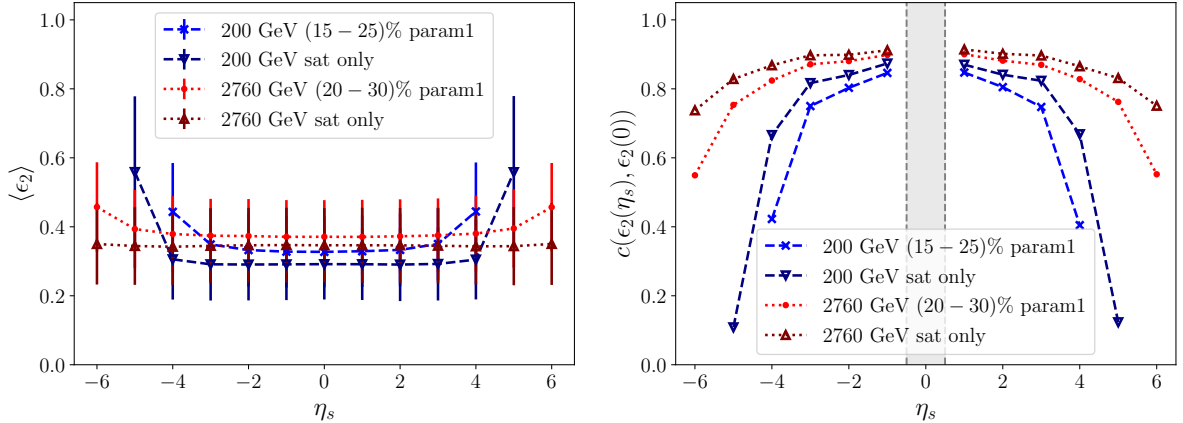
FIG. 17: Spacetime rapidity dependence of the event-averaged eccentricity (left panel) and the Pearson correlation (right panel) between $\epsilon_2(\eta_s)$ and $\epsilon_2(\eta_s = 0)$ (midrapidity bin indicated by the gray band) in 20-30 % central Pb+Pb collisions at $\sqrt{s_{NN}} = 2760$ GeV and in 15-25 % central Au+Au collisions at $\sqrt{s_{NN}} = 200$ GeV. The dashed blue and dotted red curves show the results with all filters on, and the dashed dark blue and dotted brown curves the saturation-only cases. The errorbars show the standard deviation of the calculation.

LHC, and also towards larger rapidities leads to larger fluctuations of eccentricity, and therefore also to a weaker correlation with midrapidity at RHIC and at large rapidities. In the saturation-only cases the correlation is stronger at large rapidities than in the fully filtered cases. To our understanding, also this is a multiplicity effect, originating from the increased multiplicities at larger rapidities.

We also note that the Pearson correlation from the EbyE initial conditions should not be directly compared to the rapidity dependence of elliptic flow in Fig. 16. The elliptic flow is computed from event-averaged initial conditions, and all the decorrelation effects disappear in the averaging. We rather expect that the decreasing multiplicity at larger rapidity leads to a shorter lifetime in the fluid evolution, and thus the conversion from eccentricity to elliptic flow is not completed at higher rapidities, and we get smaller v_2. In a full EbyE computation both the lifetime effect and the decorrelation effect would be present.

The CMS collaboration has defined the rapidity dependent correlation ratio [124] as

$$r_2 = \frac{\langle v_2(-\eta)v_2(\eta_{\mathrm{ref}}) \cos 2\left[\Psi_2(-\eta) - \Psi_2(\eta_{\mathrm{ref}})\right]\rangle}{\langle v_2(\eta)v_2(\eta_{\mathrm{ref}}) \cos 2\left[\Psi_2(\eta) - \Psi_2(\eta_{\mathrm{ref}})\right]\rangle}, \quad (71)$$

where the η bin is somewhere in the central rapidity region $0 < \eta < 2.5$, its negative-side counterpart is at $-\eta$, and the reference bin will be somewhere further away in forward rapidity $\eta_{\mathrm{ref}} > 3.0$ to reduce nonflow effects. Since we have performed full MC-EKRT + fluid dynamics simulations only for event-averaged initial profiles, we are not able to study event-by-event fluctuations of v_2. We can, however, estimate r_2 from the pre-averaging eccentricities, assuming $v_2(\eta) \approx k\epsilon_2(\eta_s)$ for some proportionality factor k:

$$r_2 \approx \frac{\langle \epsilon_2(-\eta_s)\epsilon_2(\eta_{s,\mathrm{ref}}) \cos 2\left[\Psi_2(-\eta_s) - \Psi_2(\eta_{s,\mathrm{ref}})\right]\rangle}{\langle \epsilon_2(\eta_s)\epsilon_2(\eta_{s,\mathrm{ref}}) \cos 2\left[\Psi_2(\eta_s) - \Psi_2(\eta_{s,\mathrm{ref}})\right]\rangle}, \quad (72)$$

where Ψ_2 is obtained from Eq. (70). Using the same replacement $v_2 \to \epsilon_2$ we can also investigate the "twist factor" $R_{n|n;2} \equiv R_2$, by the ATLAS collaboration [125] where the ratio is controlled by the cosine term:

$$R_2 \approx \frac{\langle \epsilon_2(-\eta_{s,\mathrm{ref}})\epsilon_2(-\eta_s)\epsilon_2(\eta_s)\epsilon_2(\eta_{s,\mathrm{ref}}) \cos 2\left[\Psi_2(-\eta_{s,\mathrm{ref}}) - \Psi_2(\eta_{s,\mathrm{ref}}) + (\Psi_2(-\eta_s) - \Psi_2(\eta_s))\right]\rangle}{\langle \epsilon_2(-\eta_{s,\mathrm{ref}})\epsilon_2(-\eta_s)\epsilon_2(\eta_s)\epsilon_2(\eta_{s,\mathrm{ref}}) \cos 2\left[\Psi_2(-\eta_{s,\mathrm{ref}}) - \Psi_2(\eta_{s,\mathrm{ref}}) - (\Psi_2(-\eta_s) - \Psi_2(\eta_s))\right]\rangle}. \quad (73)$$

We show the eccentricity correlation ratio r_2 and twist factor R_2 in Fig. 18 in 20-30 % central Pb+Pb collisions at $\sqrt{s_{NN}} = 2.76$ TeV and in 15-25 % central Au+Au col-

lisions at $\sqrt{s_{NN}} = 200$ GeV. Both r_2 and R_2 show a similar behavior as the Pearson correlator, i.e. decorrelation at larger rapidities, and the decorrelation is stronger at

RHIC than at the LHC. The decreasing trend of the calculated r_2 and R_2 is similar as seen in the CMS and ATLAS measurements, but the calculated r_2 and R_2 show slightly stronger correlations than the measurements do. However, as we do not perform event-by-event fluid dynamical evolution, a direct comparison is not really feasible here [38], but our results should be rather taken as qualitative.

V. CONCLUSIONS

We have developed a new MC-EKRT model for computing initial particle production in ultrarelativistic heavy-ion collisions. This is an extension of the EbyE EKRT model [17], which has very successfully predicted the midrapidity low-p_T observables from 200 GeV Au+Au collisions at RHIC to the top energy LHC Pb+Pb collisions. The essential new feature in the new Monte-Carlo framework is the implementation of the dynamical minijet-multiplicity-originating fluctuations in the saturation and particle production. Also energy/momentum conservation and valence-quark number conservation were implemented, together with a new type of spatially dependent nuclear PDFs that cope with the large density fluctuations present in an event-by-event study. As a result, the MC-EKRT model now gives a full 3-dimensional initial state that can be coupled to 3+1 D fluid dynamics.

We have applied the novel MC-EKRT framework to 5.02 TeV Pb+Pb, 2.76 TeV Pb+Pb, and 200 GeV Au+Au collisions. The 3+1 D spacetime evolution is computed with viscous relativistic hydrodynamics [73]. We have studied the uncertainties related to converting the partonic state, given by the MC-EKRT, to an initial state of fluid dynamics, and also discussed the role of energy conservation in rapidity distributions of charged particle multiplicities and elliptic flow coefficients.

Although the MC-EKRT initial state model gives the full 3–dimensional initial state that include all the EbyE fluctuations, we have here made only an exploratory study of the final observables. The main simplification here is that we have first computed the initial conditions by averaging a large number of EbyE MC-EKRT initial states for each centrality class, and then computed the fluid dynamical evolution only for the averaged initial conditions. Obviously, this limits the number of observables that we can study, but it also decreases the computational cost by a huge amount. The averaging of the initial conditions is performed in such a way that the final multiplicities resemble as closely as possible those that would be obtained by a full EbyE computation.

The comparison with the measured charged particle multiplicities at the LHC and RHIC shows that MC-EKRT can describe the centrality dependence of the multiplicity very well, practically at the same level as the earlier EbyE EKRT implementation. Moreover, the new framework describes the rapidity dependence as well.

The overall agreement with the measured shape of the rapidity spectra is very good. This is a non-trivial result, as it is a rather robust outcome from the MC-EKRT model, and essentially dominated by the pQCD minijet production and saturation. Note also that there is no parameter to directly control the rapidity distribution. Only in peripheral collisions at RHIC we start to see larger deviations from the data. Interestingly, we observed that when we give up the detailed nucleon-level energy conservation, the agreement with the data extends all the way to peripheral RHIC collisions. This might indicate that in the view that ultrarelativistic nuclear collision are rather collisions of parton clouds than collisions between individual nucleons, the nucleon-level energy conservation is an unrealistically strict condition.

We have also computed the rapidity dependence of elliptic flow, and the agreement with the LHC and RHIC data is good. The rapidity dependence of the computed v_2 is only slightly weaker than that of the data. Even though the computation of the flow coefficients without EbyE fluctuations should be viewed rather as qualitative than quantitative, the fact that the computed rapidity dependence of the elliptic flow is very similar to what is seen in the data is very promising. Moreover, we see that the EbyE initial state eccentricities at different rapidities are slightly decorrelated. As these decorrelations are not accounted for in the averaged initial state, our result suggests that eventually the computation of the true EbyE flow coefficients that include the decorrelations could show a slightly stronger rapidity dependence than the ones now computed from the averaged initial state.

As an outlook, we can see various exciting avenues along which the current MC-EKRT framework can be developed further. First, similarly to Refs. [66, 67], a well-defined NLO pQCD calculation for the integrated minijet cross section σ_{jet}^{ab}, which determines the multiplicity of the candidate dijets here, can and should be done, and also its snPDF and scale dependencies should be charted. Second, pQCD parton showering should be included as a dynamical way to distribute the initially produced parton's energy and momentum into the phase space. Third, also a more detailed spacetime picture of parton production along the lines of Ref. [114] should be studied, relaxing especially the assumption of all partons being produced at $z = 0$ and thus making the initial parton production more isotropic. Fourth, pre-thermal evolution, i.e. the effects of the isotropizing and thermalizing secondary collisions of the produced partons [126–137] should be considered. After all these developments, an extraction of the full initial energy-momentum tensor $T^{\mu\nu}$ for 3+1 D fluid dynamics could be more realistically done, and effects of e.g. initial velocity [36, 138, 139] and shear-stress tensor to observables studied. Finally, we note that the MC-EKRT framework provides a promising platform for jet-quenching studies, where both the QCD-matter initial conditions for fluid dynamics and the high-energy partons that are losing energy are consistently
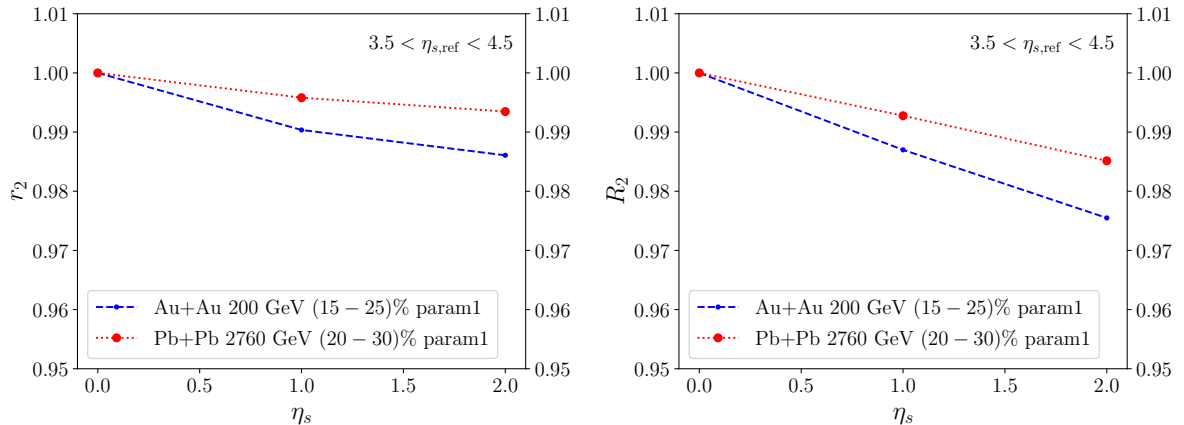
FIG. 18: Spacetime rapidity dependence of the correlation ratio r_2 (left panel) and the twist factor R_2 (right panel) in 20-30 % central Pb+Pb collisions at $\sqrt{s_{NN}} = 2760$ GeV and in 15-25 % central Au+Au collisions at $\sqrt{s_{NN}} = 200$ GeV.

obtained from the same computation, event-by-event.

[1] A. Bazavov et al. [HotQCD], Phys. Rev. D **90**, 094503 (2014) doi:10.1103/PhysRevD.90.094503 [arXiv:1407.6387 [hep-lat]].

[2] A. Bazavov, P. Petreczky and J. H. Weber, Phys. Rev. D **97**, no.1, 014510 (2018) doi:10.1103/PhysRevD.97.014510 [arXiv:1710.05024 [hep-lat]].

[3] S. Borsanyi, Z. Fodor, C. Hoelbling, S. D. Katz, S. Krieg and K. K. Szabo, Phys. Lett. B **730**, 99-104 (2014) doi:10.1016/j.physletb.2014.01.007 [arXiv:1309.5258 [hep-lat]].

[4] S. Borsanyi, G. Endrodi, Z. Fodor, A. Jakovac, S. D. Katz, S. Krieg, C. Ratti and K. K. Szabo, JHEP **11**, 077 (2010) doi:10.1007/JHEP11(2010)077 [arXiv:1007.2580 [hep-lat]].

[5] [ALICE], "The ALICE experiment – A journey through QCD," CERN-EP-2022-227, [arXiv:2211.04384 [nucl-ex]].

[6] P. Romatschke and U. Romatschke, Phys. Rev. Lett. **99**, 172301 (2007) doi:10.1103/PhysRevLett.99.172301 [arXiv:0706.1522 [nucl-th]].

[7] M. Luzum and P. Romatschke, Phys. Rev. C **78**, 034915 (2008) [erratum: Phys. Rev. C **79**, 039903 (2009)] doi:10.1103/PhysRevC.78.034915 [arXiv:0804.4015 [nucl-th]].

[8] P. Bozek, Phys. Rev. C **81**, 034909 (2010) doi:10.1103/PhysRevC.81.034909 [arXiv:0911.2397 [nucl-th]].

[9] B. Schenke, S. Jeon and C. Gale, Phys. Rev. Lett. **106**, 042301 (2011) doi:10.1103/PhysRevLett.106.042301 [arXiv:1009.3244 [hep-ph]].

[10] B. Schenke, S. Jeon and C. Gale, Phys. Rev. C **82**, 014903 (2010) doi:10.1103/PhysRevC.82.014903 [arXiv:1004.1408 [hep-ph]].

[11] B. Schenke, S. Jeon and C. Gale, Phys. Rev. C **85**, 024901 (2012) doi:10.1103/PhysRevC.85.024901 [arXiv:1109.6289 [hep-ph]].

[12] H. Song, S. A. Bass and U. Heinz, Phys. Rev. C **83**, 054912 (2011) [erratum: Phys. Rev. C **87**, no.1, 019902 (2013)] doi:10.1103/PhysRevC.83.054912 [arXiv:1103.2380 [nucl-th]].

[13] H. Niemi, G. S. Denicol, P. Huovinen, E. Molnar and D. H. Rischke, Phys. Rev. Lett. **106**, 212302 (2011) doi:10.1103/PhysRevLett.106.212302 [arXiv:1101.2442

[nucl-th]].

[14] C. Gale, S. Jeon, B. Schenke, P. Tribedy and R. Venu-gopalan, Phys. Rev. Lett. **110**, no.1, 012302 (2013) doi:10.1103/PhysRevLett.110.012302 [arXiv:1209.6330 [nucl-th]].

[15] H. Niemi, G. S. Denicol, P. Huovinen, E. Molnar and D. H. Rischke, Phys. Rev. C **86**, 014909 (2012) doi:10.1103/PhysRevC.86.014909 [arXiv:1203.2452 [nucl-th]].

[16] J. Noronha-Hostler, G. S. Denicol, J. Noronha, R. P. G. Andrade and F. Grassi, Phys. Rev. C **88**, no.4, 044916 (2013) doi:10.1103/PhysRevC.88.044916 [arXiv:1305.1981 [nucl-th]].

[17] H. Niemi, K. J. Eskola and R. Paate-lainen, Phys. Rev. C **93**, no.2, 024907 (2016) doi:10.1103/PhysRevC.93.024907 [arXiv:1505.02677 [hep-ph]].

[18] S. Ryu, J. F. Paquet, C. Shen, G. S. Denicol, B. Schenke, S. Jeon and C. Gale, Phys. Rev. Lett. **115**, no.13, 132301 (2015) doi:10.1103/PhysRevLett.115.132301 [arXiv:1502.01675 [nucl-th]].

[19] I. A. Karpenko, P. Huovinen, H. Petersen and M. Bleicher, Phys. Rev. C **91**, no.6, 064901 (2015) doi:10.1103/PhysRevC.91.064901 [arXiv:1502.01978 [nucl-th]].

[20] G. Giacalone, J. Noronha-Hostler, M. Luzum and J. Y. Ollitrault, Phys. Rev. C **97**, no.3, 034904 (2018) doi:10.1103/PhysRevC.97.034904 [arXiv:1711.08499 [nucl-th]].

[21] G. Nijs, W. van der Schee, U. Gürsoy and R. Snellings, Phys. Rev. C **103**, no.5, 054909 (2021) doi:10.1103/PhysRevC.103.054909 [arXiv:2010.15134 [nucl-th]].

[22] H. Hirvonen, K. J. Eskola and H. Niemi, Phys. Rev. C **106**, no.4, 044913 (2022) doi:10.1103/PhysRevC.106.044913 [arXiv:2206.15207 [hep-ph]].

[23] J. Novak, K. Novak, S. Pratt, J. Vredevoogd, C. Coleman-Smith and R. Wolpert, Phys. Rev. C **89**, no.3, 034917 (2014) doi:10.1103/PhysRevC.89.034917 [arXiv:1303.5769 [nucl-th]].

[24] J. E. Bernhard, J. S. Moreland, S. A. Bass, J. Liu and U. Heinz, Phys. Rev. C **94**, no.2, 024907 (2016) doi:10.1103/PhysRevC.94.024907 [arXiv:1605.03954 [nucl-th]].

[25] S. A. Bass, J. E. Bernhard and J. S. More-land, Nucl. Phys. A **967**, 67-73 (2017) doi:10.1016/j.nuclphysa.2017.05.052 [arXiv:1704.07671 [nucl-th]].

[26] J. E. Bernhard, J. S. Moreland and S. A. Bass, Nature Phys. **15**, no.11, 1113-1117 (2019) doi:10.1038/s41567-019-0611-8

[27] D. Everett *et al.* [JETSCAPE], Phys. Rev. C **103**, no.5, 054904 (2021) doi:10.1103/PhysRevC.103.054904 [arXiv:2011.01430 [hep-ph]].

[28] J. Auvinen, K. J. Eskola, P. Huovinen, H. Niemi, R. Paatelainen and P. Petreczky, Phys. Rev. C **102**, no.4, 044911 (2020) doi:10.1103/PhysRevC.102.044911 [arXiv:2006.12499 [nucl-th]].

[29] J. E. Parkkila, A. Onnerstad and D. J. Kim, Phys. Rev. C **104**, no.5, 054904 (2021) doi:10.1103/PhysRevC.104.054904 [arXiv:2106.05019 [hep-ph]].

[30] J. E. Parkkila, A. Onnerstad, S. F. Taghavi,

C. Mordasini, A. Bilandzic, M. Virta and D. J. Kim, Phys. Lett. B **835**, 137485 (2022) doi:10.1016/j.physletb.2022.137485 [arXiv:2111.08145 [hep-ph]].

[31] G. Nijs and W. van der Schee, [arXiv:2304.06191 [nucl-th]].

[32] C. Shen and B. Schenke, Phys. Rev. C **105**, no.6, 064905 (2022) doi:10.1103/PhysRevC.105.064905 [arXiv:2203.04685 [nucl-th]].

[33] P. Bozek and W. Broniowski, Phys. Rev. C **97**, no.3, 034913 (2018) doi:10.1103/PhysRevC.97.034913 [arXiv:1711.03325 [nucl-th]].

[34] P. Bozek and I. Wyskiel-Piekarska, Phys. Rev. C **85**, 064915 (2012) doi:10.1103/PhysRevC.85.064915 [arXiv:1203.6513 [nucl-th]].

[35] L. G. Pang, H. Petersen and X. N. Wang, Phys. Rev. C **97**, no.6, 064918 (2018) doi:10.1103/PhysRevC.97.064918 [arXiv:1802.04449 [nucl-th]].

[36] L. Pang, Q. Wang and X. N. Wang, Phys. Rev. C **86**, 024911 (2012) doi:10.1103/PhysRevC.86.024911 [arXiv:1205.5019 [nucl-th]].

[37] G. Denicol, A. Monnai and B. Schenke, Phys. Rev. Lett. **116**, no.21, 212301 (2016) doi:10.1103/PhysRevLett.116.212301 [arXiv:1512.01538 [nucl-th]].

[38] L. G. Pang, H. Petersen, G. Y. Qin, V. Roy and X. N. Wang, Eur. Phys. J. A **52**, no.4, 97 (2016) doi:10.1140/epja/i2016-16097-x [arXiv:1511.04131 [nucl-th]].

[39] J. Auvinen, J. E. Bernhard, S. A. Bass and I. Karpenko, Phys. Rev. C **97**, no.4, 044905 (2018) doi:10.1103/PhysRevC.97.044905 [arXiv:1706.03666 [hep-ph]].

[40] A. Mankolli *et al.* [JETSCAPE], [arXiv:2401.00402 [nucl-th]].

[41] D. Soeder, W. Ke, J. F. Paquet and S. A. Bass, [arXiv:2306.08665 [nucl-th]].

[42] H. Hirvonen, K. J. Eskola and H. Niemi, Phys. Rev. C **108**, no.3, 034905 (2023) doi:10.1103/PhysRevC.108.034905 [arXiv:2303.04517 [hep-ph]].

[43] H. Hirvonen, K. J. Eskola and H. Niemi, [arXiv:2404.02602 [hep-ph]].

[44] B. Schenke, P. Tribedy and R. Venu-gopalan, Phys. Rev. Lett. **108**, 252301 (2012) doi:10.1103/PhysRevLett.108.252301 [arXiv:1202.6646 [nucl-th]].

[45] K. J. Eskola, K. Kajantie, P. V. Ruuskanen and K. Tuominen, Nucl. Phys. B **570**, 379-389 (2000) doi:10.1016/S0550-3213(99)00720-8 [arXiv:hep-ph/9909456 [hep-ph]].

[46] K. J. Eskola, K. Kajantie and K. Tuominen, Phys. Lett. B **497**, 39-43 (2001) doi:10.1016/S0370-2693(00)01341-1 [arXiv:hep-ph/0009246 [hep-ph]].

[47] R. Paatelainen, K. J. Eskola, H. Niemi and K. Tuominen, Phys. Lett. B **731**, 126-130 (2014) doi:10.1016/j.physletb.2014.02.018 [arXiv:1310.3105 [hep-ph]].

[48] T. Pierog and K. Werner, Nucl. Phys. B Proc. Suppl. **196**, 102-105 (2009) doi:10.1016/j.nuclphysbps.2009.09.017 [arXiv:0905.1198 [hep-ph]].

[49] T. Pierog, I. Karpenko, J. M. Katzy, E. Yatsenko

and K. Werner, Phys. Rev. C **92**, no.3, 034906 (2015) doi:10.1103/PhysRevC.92.034906 [arXiv:1306.0121 [hep-ph]].

[50] K. Werner, B. Guiot, I. Karpenko and T. Pierog, Phys. Rev. C **89**, no.6, 064903 (2014) doi:10.1103/PhysRevC.89.064903 [arXiv:1312.1233 [nucl-th]].

[51] K. Werner, Phys. Rev. C **108**, no.6, 064903 (2023) doi:10.1103/PhysRevC.108.064903 [arXiv:2301.12517 [hep-ph]].

[52] K. Werner, Phys. Rev. C **109**, no.1, 014910 (2024) doi:10.1103/PhysRevC.109.014910 [arXiv:2306.10277 [hep-ph]].

[53] K. Werner and B. Guiot, Phys. Rev. C **108**, no.3, 034904 (2023) doi:10.1103/PhysRevC.108.034904 [arXiv:2306.02396 [hep-ph]].

[54] L. G. Pang, G. Y. Qin, V. Roy, X. N. Wang and G. L. Ma, Phys. Rev. C **91**, no.4, 044904 (2015) doi:10.1103/PhysRevC.91.044904 [arXiv:1410.8690 [nucl-th]].

[55] Y. Kanakubo, Y. Tachibana and T. Hirano, Phys. Rev. C **101**, no.2, 024912 (2020) doi:10.1103/PhysRevC.101.024912 [arXiv:1910.10556 [nucl-th]].

[56] Y. Kanakubo, Y. Tachibana and T. Hirano, Phys. Rev. C **105**, no.2, 024905 (2022) doi:10.1103/PhysRevC.105.024905 [arXiv:2108.07943 [nucl-th]].

[57] C. Bierlich, G. Gustafson, L. Lönnblad and H. Shah, JHEP **10**, 134 (2018) doi:10.1007/JHEP10(2018)134 [arXiv:1806.10820 [hep-ph]].

[58] P. Carzon, M. Martinez, M. D. Sievert, D. E. Wertepny and J. Noronha-Hostler, Phys. Rev. C **105**, no.3, 034908 (2022) doi:10.1103/PhysRevC.105.034908 [arXiv:1911.12454 [nucl-th]].

[59] O. Garcia-Montero, H. Elfner and S. Schlichting, Phys. Rev. C **109**, no.4, 044916 (2024) doi:10.1103/PhysRevC.109.044916 [arXiv:2308.11713 [hep-ph]].

[60] K. Kajantie, P. V. Landshoff and J. Lindfors, Phys. Rev. Lett. **59**, 2527 (1987) doi:10.1103/PhysRevLett.59.2527

[61] K. J. Eskola, K. Kajantie and J. Lindfors, Nucl. Phys. B **323**, 37-52 (1989) doi:10.1016/0550-3213(89)90586-5

[62] K. J. Eskola and K. Kajantie, Z. Phys. C **75**, 515-522 (1997) doi:10.1007/s002880050495 [arXiv:nucl-th/9610015 [nucl-th]].

[63] K. J. Eskola, H. Honkanen, H. Niemi, P. V. Ruuskanen and S. S. Rasanen, Phys. Rev. C **72**, 044904 (2005) doi:10.1103/PhysRevC.72.044904 [arXiv:hep-ph/0506049 [hep-ph]].

[64] P. F. Kolb, U. W. Heinz, P. Huovinen, K. J. Eskola and K. Tuominen, Nucl. Phys. A **696**, 197-215 (2001) doi:10.1016/S0375-9474(01)01114-9 [arXiv:hep-ph/0103234 [hep-ph]].

[65] H. Niemi, K. J. Eskola and P. V. Ruuskanen, Phys. Rev. C **79**, 024903 (2009) doi:10.1103/PhysRevC.79.024903 [arXiv:0806.1116 [hep-ph]].

[66] K. J. Eskola and K. Tuominen, Phys. Rev. D **63**, 114006 (2001) doi:10.1103/PhysRevD.63.114006 [arXiv:hep-ph/0010319 [hep-ph]].

[67] K. J. Eskola and K. Tuominen, Phys. Lett. B **489**, 329-336 (2000) doi:10.1016/S0370-2693(00)00946-1 [arXiv:hep-ph/0002008 [hep-ph]].

[68] H. Niemi, K. J. Eskola, R. Paatelainen and K. Tuominen, Phys. Rev. C **93**, no.1, 014912 (2016) doi:10.1103/PhysRevC.93.014912 [arXiv:1511.04296 [hep-ph]].

[69] K. J. Eskola, H. Niemi, R. Paatelainen and K. Tuominen, Phys. Rev. C **97**, no.3, 034911 (2018) doi:10.1103/PhysRevC.97.034911 [arXiv:1711.09803 [hep-ph]].

[70] H. Niemi, K. J. Eskola, R. Paatelainen and K. Tuominen, Nucl. Phys. A **982**, 443-446 (2019) doi:10.1016/j.nuclphysa.2018.10.013 [arXiv:1807.02378 [nucl-th]].

[71] I. Helenius, K. J. Eskola, H. Honkanen and C. A. Salgado, JHEP **07**, 073 (2012) doi:10.1007/JHEP07(2012)073 [arXiv:1205.5359 [hep-ph]].

[72] The MC-EKRT code will be available at url:github.com/mialkuha/MC-EKRT

[73] E. Molnar, H. Holopainen, P. Huovinen and H. Niemi, Phys. Rev. C **90**, no.4, 044904 (2014) doi:10.1103/PhysRevC.90.044904 [arXiv:1407.8152 [nucl-th]].

[74] R. Paatelainen, K. J. Eskola, H. Holopainen and K. Tuominen, Phys. Rev. C **87**, no.4, 044904 (2013) doi:10.1103/PhysRevC.87.044904 [arXiv:1211.0461 [hep-ph]].

[75] C. Loizides, J. Kamin and D. d'Enterria, Phys. Rev. C **97**, no.5, 054910 (2018) [erratum: Phys. Rev. C **99**, no.1, 019901 (2019)] doi:10.1103/PhysRevC.97.054910 [arXiv:1710.07098 [nucl-ex]].

[76] C. W. De Jager, H. De Vries and C. De Vries, Atom. Data Nucl. Data Tabl. **14**, 479-508 (1974) [erratum: Atom. Data Nucl. Data Tabl. **16**, 580-580 (1975)] doi:10.1016/S0092-640X(74)80002-1

[77] H. De Vries, C. W. De Jager and C. De Vries, Atom. Data Nucl. Data Tabl. **36**, 495-536 (1987) doi:10.1016/0092-640X(87)90013-1

[78] R. D. Woods and D. S. Saxon, Phys. Rev. **95**, 577-578 (1954) doi:10.1103/PhysRev.95.577

[79] C. Loizides, J. Nagle and P. Steinberg, SoftwareX **1-2**, 13-18 (2015) doi:10.1016/j.softx.2015.05.001 [arXiv:1408.2549 [nucl-ex]].

[80] J. R. Cudell *et al.* [COMPETE], Phys. Rev. Lett. **89**, 201801 (2002) doi:10.1103/PhysRevLett.89.201801 [arXiv:hep-ph/0206172 [hep-ph]].

[81] G. Antchev *et al.* [TOTEM], Eur. Phys. J. C **79**, no.2, 103 (2019) doi:10.1140/epjc/s10052-019-6567-0 [arXiv:1712.06153 [hep-ex]].

[82] X. N. Wang and M. Gyulassy, Phys. Rev. D **44**, 3501-3516 (1991) doi:10.1103/PhysRevD.44.3501

[83] S. Chekanov *et al.* [ZEUS], Eur. Phys. J. C **24**, 345-360 (2002) doi:10.1007/s10052-002-0953-7 [arXiv:hep-ex/0201043 [hep-ex]].

[84] K. J. Eskola, C. A. Flett, V. Guzey, T. Löytäinen and H. Paukkunen, Phys. Rev. C **106**, no.3, 035202 (2022) doi:10.1103/PhysRevC.106.035202 [arXiv:2203.11613 [hep-ph]].

[85] C. A. Flett, "Exclusive Observables to NLO and Low x PDF Phenomenology at the LHC," Ph.D. thesis, University of Liverpool, 2021

[86] X. N. Wang, Phys. Rev. D **43**, 104-112 (1991) doi:10.1103/PhysRevD.43.104

[87] L. Durand and P. Hong, Phys. Rev. Lett. **58**, 303-306 (1987) doi:10.1103/PhysRevLett.58.303

[88] E. Eichten, I. Hinchliffe, K. D. Lane and

C. Quigg, Rev. Mod. Phys. **56**, 579-707 (1984) doi:10.1103/RevModPhys.56.579

[89] I. Sarcevic, S. D. Ellis and P. Carruthers, Phys. Rev. D **40**, 1446 (1989) doi:10.1103/PhysRevD.40.1446

[90] K. J. Eskola, H. Paukkunen and C. A. Salgado, JHEP **04**, 065 (2009) doi:10.1088/1126-6708/2009/04/065 [arXiv:0902.4154 [hep-ph]].

[91] K. J. Eskola, P. Paakkinen, H. Paukkunen and C. A. Salgado, Eur. Phys. J. C **77**, no.3, 163 (2017) doi:10.1140/epjc/s10052-017-4725-9 [arXiv:1612.05741 [hep-ph]].

[92] K. J. Eskola, P. Paakkinen, H. Paukkunen and C. A. Salgado, Eur. Phys. J. C **82**, no.5, 413 (2022) doi:10.1140/epjc/s10052-022-10359-0 [arXiv:2112.12462 [hep-ph]].

[93] I. Helenius, M. Walt and W. Vogelsang, Phys. Rev. D **105**, no.9, 094031 (2022) doi:10.1103/PhysRevD.105.094031 [arXiv:2112.11904 [hep-ph]].

[94] R. Abdul Khalek, R. Gauld, T. Giani, E. R. Nocera, T. R. Rabemananjara and J. Rojo, Eur. Phys. J. C **82**, no.6, 507 (2022) doi:10.1140/epjc/s10052-022-10417-7 [arXiv:2201.12363 [hep-ph]].

[95] P. Duwentäster, T. Ježo, M. Klasen, K. Kovařík, A. Kusina, K. F. Muzakka, F. I. Olness, R. Ruiz, I. Schienbein and J. Y. Yu, Phys. Rev. D **105**, no.11, 114043 (2022) doi:10.1103/PhysRevD.105.114043 [arXiv:2204.09982 [hep-ph]].

[96] K. J. Eskola, Z. Phys. C **51**, 633-642 (1991) doi:10.1007/BF01565590

[97] S. R. Klein and R. Vogt, Phys. Rev. Lett. **91**, 142301 (2003) doi:10.1103/PhysRevLett.91.142301 [arXiv:nucl-th/0305046 [nucl-th]].

[98] R. Vogt, Phys. Rev. C **70**, 064902 (2004) doi:10.1103/PhysRevC.70.064902

[99] L. Frankfurt, V. Guzey and M. Strikman, Phys. Rept. **512**, 255-393 (2012) doi:10.1016/j.physrep.2011.12.002 [arXiv:1106.2091 [hep-ph]].

[100] S. Dulat, T. J. Hou, J. Gao, M. Guzzi, J. Huston, P. Nadolsky, J. Pumplin, C. Schmidt, D. Stump and C. P. Yuan, Phys. Rev. D **93**, no.3, 033006 (2016) doi:10.1103/PhysRevD.93.033006 [arXiv:1506.07443 [hep-ph]].

[101] A. Buckley, J. Ferrando, S. Lloyd, K. Nordström, B. Page, M. Rüfenacht, M. Schönherr and G. Watt, Eur. Phys. J. C **75**, 132 (2015) doi:10.1140/epjc/s10052-015-3318-8 [arXiv:1412.7420 [hep-ph]].

[102] H. Hirvonen, M. Kuha, J. Auvinen, K. J. Eskola, Y. Kanakubo, H. Niemi, work in progress

[103] S. Chatrchyan *et al.* [CMS], Eur. Phys. J. C **74**, no.7, 2951 (2014) doi:10.1140/epjc/s10052-014-2951-y [arXiv:1401.4433 [nucl-ex]].

[104] G. S. Denicol, H. Niemi, E. Molnar and D. H. Rischke, Phys. Rev. D **85**, 114047 (2012) [erratum: Phys. Rev. D **91**, no.3, 039902 (2015)] doi:10.1103/PhysRevD.85.114047 [arXiv:1202.4551 [nucl-th]].

[105] W. Israel and J. M. Stewart, Annals Phys. **118**, 341-372 (1979) doi:10.1016/0003-4916(79)90130-1

[106] E. Molnár, H. Niemi, G. S. Denicol and D. H. Rischke, Phys. Rev. D **89**, no.7, 074010 (2014) doi:10.1103/PhysRevD.89.074010 [arXiv:1308.0785 [nucl-th]].

[107] G. S. Denicol, T. Koide and D. H. Rischke, Phys. Rev. Lett. **105**, 162501 (2010) doi:10.1103/PhysRevLett.105.162501 [arXiv:1004.5013 [nucl-th]].

[108] P. Huovinen and P. Petreczky, Nucl. Phys. A **837**, 26-53 (2010) doi:10.1016/j.nuclphysa.2010.02.015 [arXiv:0912.2541 [hep-ph]].

[109] P. Huovinen, Eur. Phys. J. A **37**, 121-128 (2008) doi:10.1140/epja/i2007-10611-3 [arXiv:0710.4379 [nucl-th]].

[110] J. P. Boris and D. L. Book, J. Comput. Phys. **11**, 38 (1973).

[111] E. Molnar, H. Niemi and D. H. Rischke, Eur. Phys. J. C **65**, 615-635 (2010) doi:10.1140/epjc/s10052-009-1194-9 [arXiv:0907.2583 [nucl-th]].

[112] F. Cooper and G. Frye, Phys. Rev. D **10**, 186 (1974) doi:10.1103/PhysRevD.10.186

[113] F. Debbasch, W. A. van Leeuwen, Physica A **388**, 1079-1104 (2009).

[114] K. J. Eskola and X. N. Wang, Phys. Rev. D **49**, 1284-1292 (1994) doi:10.1103/PhysRevD.49.1284 [arXiv:nucl-th/9307011 [nucl-th]].

[115] A. Bazavov *et al.* [HotQCD], Phys. Lett. B **795**, 15-21 (2019) doi:10.1016/j.physletb.2019.05.013 [arXiv:1812.08235 [hep-lat]].

[116] J. Adam *et al.* [ALICE], Phys. Lett. B **772**, 567-577 (2017) doi:10.1016/j.physletb.2017.07.017 [arXiv:1612.08966 [nucl-ex]].

[117] J. Adam *et al.* [ALICE], Phys. Rev. Lett. **116**, no.22, 222302 (2016) doi:10.1103/PhysRevLett.116.222302 [arXiv:1512.06104 [nucl-ex]].

[118] E. Abbas *et al.* [ALICE], Phys. Lett. B **726**, 610-622 (2013) doi:10.1016/j.physletb.2013.09.022 [arXiv:1304.0347 [nucl-ex]].

[119] K. Aamodt *et al.* [ALICE], Phys. Rev. Lett. **106**, 032301 (2011) doi:10.1103/PhysRevLett.106.032301 [arXiv:1012.1657 [nucl-ex]].

[120] B. B. Back, M. D. Baker, D. S. Barton, R. R. Betts, M. Ballintijn, A. A. Bickley, R. Bindel, A. Budzanowski, W. Busza and A. Carroll, *et al.* Phys. Rev. Lett. **91**, 052303 (2003) doi:10.1103/PhysRevLett.91.052303 [arXiv:nucl-ex/0210015 [nucl-ex]].

[121] J. Adam *et al.* [ALICE], Phys. Lett. B **762**, 376-388 (2016) doi:10.1016/j.physletb.2016.07.017 [arXiv:1605.02035 [nucl-ex]].

[122] B. B. Back *et al.* [PHOBOS], Phys. Rev. C **72**, 051901 (2005) doi:10.1103/PhysRevC.72.051901 [arXiv:nucl-ex/0407012 [nucl-ex]].

[123] A. Bilandzic, R. Snellings and S. Voloshin, Phys. Rev. C **83**, 044913 (2011) doi:10.1103/PhysRevC.83.044913 [arXiv:1010.0233 [nucl-ex]].

[124] V. Khachatryan *et al.* [CMS], Phys. Rev. C **92**, no.3, 034911 (2015) doi:10.1103/PhysRevC.92.034911 [arXiv:1503.01692 [nucl-ex]].

[125] M. Aaboud *et al.* [ATLAS], Eur. Phys. J. C **78**, no.2, 142 (2018) doi:10.1140/epjc/s10052-018-5605-7 [arXiv:1709.02301 [nucl-ex]].

[126] K. J. Eskola, K. Kajantie and J. Lindfors, Phys. Lett. B **214**, 613-616 (1988) doi:10.1016/0370-2693(88)90130-X

[127] Z. Xu and C. Greiner, Phys. Rev. C **71**, 064901 (2005) doi:10.1103/PhysRevC.71.064901 [arXiv:hep-ph/0406278 [hep-ph]].

[128] A. Kurkela and E. Lu, Phys. Rev. Lett. **113**, no.18, 182301 (2014) doi:10.1103/PhysRevLett.113.182301 [arXiv:1405.6318 [hep-ph]].

[129] A. Kurkela and Y. Zhu, Phys. Rev. Lett. **115**, no.18, 182301 (2015) doi:10.1103/PhysRevLett.115.182301 [arXiv:1506.06647 [hep-ph]].

[130] A. Kurkela, A. Mazeliauskas, J. F. Paquet, S. Schlichting and D. Teaney, Phys. Rev. C **99**, no.3, 034910 (2019) doi:10.1103/PhysRevC.99.034910 [arXiv:1805.00961 [hep-ph]].

[131] A. Kurkela and A. Mazeliauskas, Phys. Rev. D **99**, no.5, 054018 (2019) doi:10.1103/PhysRevD.99.054018 [arXiv:1811.03068 [hep-ph]].

[132] A. Kurkela, A. Mazeliauskas, J. F. Paquet, S. Schlichting and D. Teaney, Phys. Rev. Lett. **122**, no.12, 122302 (2019) doi:10.1103/PhysRevLett.122.122302 [arXiv:1805.01604 [hep-ph]].

[133] A. Kurkela and A. Mazeliauskas, Phys. Rev. Lett. **122**, 142301 (2019) doi:10.1103/PhysRevLett.122.142301 [arXiv:1811.03040 [hep-ph]].

[134] X. Du and S. Schlichting, Phys. Rev. D **104**, no.5, 054011 (2021) doi:10.1103/PhysRevD.104.054011 [arXiv:2012.09079 [hep-ph]].

[135] X. Du and S. Schlichting, Phys. Rev. Lett. **127**, no.12, 122301 (2021) doi:10.1103/PhysRevLett.127.122301 [arXiv:2012.09068 [hep-ph]].

[136] P. Carzon, M. Martinez, J. Noronha-Hostler, P. Plaschke, S. Schlichting and M. Sievert, Phys. Rev. C **108**, no.6, 064905 (2023) doi:10.1103/PhysRevC.108.064905 [arXiv:2301.04572 [nucl-th]].

[137] F. Zhou, J. Brewer and A. Mazeliauskas, [arXiv:2402.09298 [hep-ph]].

[138] M. Gyulassy, I. Vitev, X. N. Wang and P. Huovinen, Phys. Lett. B **526**, 301-308 (2002) doi:10.1016/S0370-2693(02)01157-7 [arXiv:nucl-th/0109063 [nucl-th]].

[139] M. Okai, K. Kawaguchi, Y. Tachibana and T. Hirano, Phys. Rev. C **95**, no.5, 054914 (2017) doi:10.1103/PhysRevC.95.054914 [arXiv:1702.07541 [nucl-th]].

[140] K. J. Eskola, K. Kajantie, P. V. Ruuskanen and K. Tuominen, Phys. Lett. B **543**, 208-216 (2002) doi:10.1016/S0370-2693(02)02457-7 [arXiv:hep-ph/0204034 [hep-ph]].

PV

EFFECTS OF SATURATION AND FLUCTUATING HOTSPOTS FOR FLOW OBSERVABLES IN ULTRARELATIVISTIC HEAVY-ION COLLISIONS

by

Henry Hirvonen, Mikko Kuha, Jussi Auvinen, Kari J. Eskola, Yuuka Kanakubo and Harri Niemi.

Effects of saturation and fluctuating hotspots for flow observables in ultrarelativistic heavy-ion collisions

Henry Hirvonen, Mikko Kuha, Jussi Auvinen, Kari J. Eskola, Yuuka Kanakubo, Harri Niemi

University of Jyväskylä, Department of Physics, P.O. Box 35, FI-40014 University of Jyväskylä, Finland, and Helsinki Institute of Physics, P.O.Box 64, FI-00014 University of Helsinki, Finland

We investigate the effects of saturation dynamics on midrapidity flow observables by adding fluctuating hotspots into the novel Monte Carlo EKRT (MC-EKRT) event generator for high-energy nuclear collisions. We demonstrate that the intensity of the saturation effects significantly affects the ratio between the flow coefficients v_3 and v_2 at the LHC. Adding a hotspot substructure to the nucleons enhances the saturation effects and improves the agreement with the measured data. We show that the collision-energy dependence of the flow coefficients obtained using the MC-EKRT initial states with hotspots is improved in comparison with the earlier event-by-event EKRT model. In addition, we present the results for the charged hadron multiplicity distribution in Pb+Pb collisions at the LHC, and show that the minijet-multiplicity originating fluctuations of the saturation scale included in MC-EKRT, as well as the presence of hotspots, are necessary for describing the measured large-multiplicity tail in the distribution.

I. INTRODUCTION

The highest-energy nucleus-nucleus collisions, ultrarelativistic heavy-ion collisions, which are currently performed at the CERN Large Hadron Collider (LHC) and at the Brookhaven National Laboratory (BNL) Relativistic Heavy Ion Collider (RHIC), aim at determining the properties of the nearly net-baryon-free hot Quark-Gluon Plasma (QGP). One also strives for a detailed understanding of the strong-interaction dynamics that is responsible for the creation and further evolution of the QGP in these collisions. See e.g. Ref. [1] for a review.

According to lattice simulations of Quantum Chromodynamics (QCD, the theory of the strong interaction) the strongly-interacting matter takes the form of the QGP at high temperatures of $T \gtrsim 150 - 160$ MeV [2, 3] at a vanishing baryochemical potential. Quarks and gluons can be produced in ultrarelativistic heavy-ion collisions from the kinetic energy of the colliding nuclei so copiously that the effective temperature (energy over particle ratio) of the system clearly exceeds 160 MeV. In these conditions, the normal formation of the color-confined, color-singlet bound states, hadrons, is momentarily inhibited, and a nearly-thermalized QGP, where the degrees of freedom are colored gluons, quarks and antiquarks, can be formed. The subsequent spacetime evolution stages of such a QCD matter – the expansion and cooling of the QGP, the cross-over transition to a hadron gas, followed by the expansion and cooling of the hadron gas – as well as the simultaneous appearance of the QGP and hadron-gas phases in different density regions of the expanding system, are describable in terms of relativistic dissipative fluid dynamics [4–27]. While QCD is a cornerstone of the Standard Model of particle physics, relativistic fluid dynamics has become a standard tool in the analysis of heavy-ion observables.

The determination of the QCD matter properties, such as its equation of state and transport properties like the shear and bulk viscosities, from the measured LHC and RHIC observables is a highly challenging task. Clearly, a precise determination requires a simultaneous analysis of as many heavy-ion observables as possible, from as many collision systems and collision energies as possible – a "global analysis" of heavy-ion observables [11, 14, 17, 28]. A proper statistical analysis, Bayesian inference [26, 29–40] is necessary for setting well-defined uncertainties to the extracted matter properties. Interestingly, neural networks are currently making it possible to include also statistics-expensive observables, such as complicated rare flow correlators, into the global analysis [41, 42] (see also Ref. [43]).

The mentioned global analyses of heavy-ion observables are based on a fluid-dynamical description, which takes initial densities and flow velocities of the produced QCD matter as initial conditions. One either parametrizes these initial conditions [26, 29–33, 35–40, 44] or tries to compute them from a QCD dynamical model for the initial production of gluons and quarks [14, 17, 28, 38]. In both cases there is some number of fit parameters that characterize the initial states, and these will obviously be correlated with the actual QCD-matter properties extracted from the data via Bayesian inference. It is therefore important to model the QCD-matter initial states based on QCD dynamics as far as is possible, in order to understand the dominant particle production mechanism, to reduce the uncertainties in the extraction of the initial states, and to have predictive power for moving from one system to another.

The EKRT (Eskola-Kajantie-Ruuskanen-Tuominen) model [17, 45–47], which treats the nuclear collisions as collisions of parton clouds, and supplements a perturbative QCD (pQCD) calculation for the production of few-GeV partons (minijets) [48, 49] with a collinear factorization -inspired QCD saturation mechanism [17, 47] for regulating the small-p_T minijet production (p_T being transverse momentum), is an example of such a QCD-based initial state modeling with predictive power. The event-by-event (EbyE) version of the model, EbyE-EKRT [17],

has been quite successful in explaining a large collection of heavy-ion bulk observables at the LHC and RHIC [17, 28, 34, 50–52]. The latest progress here is the novel MC-EKRT event generator (MC for Monte Carlo), introduced recently in Ref. [53], and employed in the present article.

The new features in MC-EKRT [53] relative to EbyE-EKRT [17] are that now the produced partonic system contains local fluctuations of the minijet multiplicity, which in turn induce dynamical fluctuations to the saturation controlling the initial parton production. Also per-nucleon conservation of energy and valence-quark numbers are accounted for. MC-EKRT also introduces a new type of spatially dependent nuclear parton distribution functions (snPDFs) that are specific to the nucleon configuration in each event and can cope with the largest density fluctuations of the nucleon densities. Thanks to these new features, MC-EKRT gives initial conditions for full 3+1 D EbyE fluid-dynamics, and thus enables the studies of rapidity-dependent observables, such as rapidity distributions of yields and flow coefficients of charged hadrons in Pb+Pb collisions at the LHC and at the highest-energy Au+Au collisions at RHIC – see Ref. [53].

In this paper, we employ the new MC-EKRT framework for computing event-by-event initial conditions for 2+1 D dissipative shear- and bulk-viscous second-order transient fluid-dynamics in the mid-rapidity unit of 5.02 and 2.76 TeV Pb+Pb collisions at the LHC. In particular, we study the sensitivity of the flow coefficients v_n to the model details, such as the nucleonic width and substructure, the Gaussian smearing in coupling the individual minijets to continuous fluid dynamics, as well as the order in which we do the minijet filtering based on saturation and conservation of energy. In addition, we show how the added minijet multiplicity fluctuations are the piece formerly missing from EbyE-EKRT in explaining the behaviour of the charged multiplicity distributions in the most central collisions. The recently developed neural networks for predicting flow observables directly from the initial energy density event-by-event [41, 42], are also utilized. As the main result of this paper, we show that a detailed simultaneous description of the v_n's requires saturation to be the driving QCD mechanism for initial parton production. In particular, this result calls for further nucleonic substructure – hotspots – to be introduced in MC-EKRT. We also implement these in MC-EKRT and discuss their interesting interplay with saturation, in describing the v_2/v_3 ratio as well as in explaining the measured charged multiplicity distributions.

II. MC-EKRT INITIAL STATE FOR FLUID DYNAMICS

A. Minijet sampling

The MC-EKRT event generator of Ref. [53] produces partonic initial states, i.e. saturated systems of gluons and quarks with $p_T \gtrsim p_0 \sim 1$ GeV, that can be fed as ini-

tial conditions to 3+1 D event-by-event fluid-dynamical simulations. The generation of such MC-EKRT initial states proceeds via the following steps (for details, see Ref. [53]):

First, the nucleon configurations of the colliding (here spherically symmetric) nuclei A and B are generated by sampling the standard 2-parameter Woods-Saxon distribution, and by requiring an exclusion radius of 0.4 fm. A squared impact parameter b_{AB}^2 for the $A+B$ collision, defining the distance between the centers of masses of the colliding nuclei, is sampled from a uniform distribution. In the absence of hotspots (i.e. without sub-nucleonic density fluctuations), the $A+B$ collision is triggered using MC Glauber-like black-disc nucleons with a trigger cross section identical to the inelastic nucleon-nucleon cross section $\sigma_{\text{inel}}^{NN}$, which is obtained from the measured total and elastic nucleon-nucleon cross sections as a function of the nucleon-nucleon center-of-momentum (cms) system energy $\sqrt{s_{NN}}$ [54, 55].

Once the $A+B$ collision is triggered, MC-EKRT does not consider nucleonic sub-collisions at all but pictures the entire nuclear collision as a collision of two extensive parton clouds. For distributing the parton sub-clouds spatially around each nucleon, MC-EKRT assumes a Gaussian thickness function,

$$T_N(\bar{s}) = \frac{1}{2\pi\sigma_N^2} \exp\left(-\frac{|\bar{s}|^2}{2\sigma_N^2}\right), \quad (1)$$

with a width parameter $\sigma_N = \sigma_N(\sqrt{s_{NN}})$ that is obtained from exclusive photo-production of J/Ψ in photon-proton collisions at HERA [56, 57]. Then, multiple dijet production, i.e. the number of independent dijets with jet transverse momentum $p_T \geq p_0 = 1$ GeV, that is assigned to originate from each ab pair, is sampled from a Poissonian probability distribution with a mean

$$\bar{N}_{\text{jets}}^{ab} = T_{NN}(\bar{b}_{ab}) \, \sigma_{\text{jet}}^{ab}(p_0, \sqrt{s_{NN}}, \{\bar{s}_a\}, \{\bar{s}_b\}), \quad (2)$$

where $T_{NN}(\bar{b}_{ab})$ is the nucleonic overlap function and $\bar{b}_{ab}$ is the impact parameter between the nucleons a and b, while σ_{jet}^{ab} is the integrated pQCD (mini)jet cross section, which MC-EKRT computes using the novel snPDFs for a and b, and all possible leading-order (LO) partonic $2 \to 2$ sub-processes. A cms-energy dependent multiplicative K-factor is introduced to σ_{jet}^{ab} as a free fit parameter, to account for the missing higher order contributions. The (mini)jet cross section depends on the transverse momentum cut-off parameter p_0, on the cms energy $\sqrt{s_{NN}}$, as well as on the transverse locations $\bar{s}_a$ and $\bar{s}_b$ of a and b in the nucleon-configurations of A and B, indicated here with $\{\bar{s}_a\}$ and $\{\bar{s}_b\}$.

As explained in detail Ref. [53], the novel snPDFs are now nucleon-configuration specific and account for the nuclear modifications of each nucleon's PDFs caused by all other nucleons in the nucleus. In other words, the MC-EKRT snPDFs are nucleon-specific and nucleon-configuration specific. Also noteworthy is that these

novel snPDFs can fully cope with the event-by-event density fluctuations, which was not the case with the formerly developed spatial nPDFs, such as those in Ref. [58]. The MC-EKRT snPDFs are normalized (averaging over all nucleons in each nucleus and over a large number of nuclei) to the spatially averaged nuclear PDF modifications of the EPS09LO set [59], and CT14LO [60] are employed for the free proton PDFs.

Finally, the transverse location for each produced dijet is sampled from the product of the two overlap functions T_N, whose transverse integral gives the usual overlap function T_{NN}. The kinematic variables and the flavor chemistry of the produced partons, along with identifying the valence quark-consuming processes, is sampled from the differential jet sub-cross sections, as explained in Ref. [53].

B. Minijet filtering

The next, and decisive, step in MC-EKRT is the filtering of the excessive candidate-dijets, based on the EKRT saturation [17, 45–47] and conservation of energy and valence quark numbers. As explained in [17, 47, 53] saturation here is expected to occur when all the higher-order $(n > 2) \rightarrow 2$ parton processes start to dominate over the $2 \rightarrow 2$ ones. For maintaining collinear factorization at the highest values of jet transverse momenta, the filterings are performed in the order of decreasing factorization scale, which here is the jet p_T. Then, the highest-p_T partons can remain in the system while the lower-p_T ones may get filtered away.

For the saturation filtering, MC-EKRT assigns a transverse radius $1/(\kappa_{\mathrm{sat}} p_T)$ for each dijet candidate, where κ_{sat} is a packing factor, a free parameter to be fitted from the data. The transverse position of each candidate dijet is kept track of, and a candidate dijet gets filtered away if it overlaps with any of the previously accepted dijets. As shown in Ref. [53], after the saturation filtering the p_T distribution of surviving partons is not anymore sensitive to the original cut-off parameter p_0 but now saturation is the dynamical and local regulation mechanism for these distributions. This is the major difference to the traditional minijet eikonal models (and models alike) which are employed in event generators describing multiparton interactions, such as HIJING [61].

Similarly, MC-EKRT keeps track of all the longitudinal momentum fractions and valence quarks drawn out from their mother nucleons by the candidate dijets. If the candidate dijet would make its mother nucleon exceed its energy or valence-quark budget, again checking the dijet candidates in the order of decreasing p_T, then that dijet candidate gets filtered away. In the EKRT framework, in the spirit of suggesting saturation as the dominant QCD-mechanism that regulates and controls initial parton production in highest-energy nuclear collisions, the default is to do the saturation filtering first, and only then the energy and valence-quark number con-

servation filterings. There is, however, an option in the code which we utilize and consequences we study in this paper, to have all the filterings done simultaneously.

C. Nucleon substructure and hotspot trigger

The fluctuating substructure to the nucleons of the MC-EKRT framework is implemented as follows. While there is clear evidence that the nucleon substructure is necessary for describing the measured incoherent J/ψ photo-production [62], the situation is less clear in heavy-ion collisions. The global analyses performed in Refs. [37, 44] provide a slight preference towards the inclusion of the nucleon substructure, but the evidence is not conclusive. However, these analyses use the T$_\mathrm{R}$ENTo [63] initial state model, in which the effect of the substructure can partly be compensated with other initial state parameters.

In the MC-EKRT model, the addition of the nucleon substructure enhances the saturation effects since it confines the minijet production into more localized transverse regions. This leads to a change in the initial geometry, which might have an impact on the flow observables. The nucleon substructure is implemented by introducing Gaussian hotspots to the nucleon thickness function:

$$T_N(\bar{s}) = \frac{1}{N_h} \sum_{i=1}^{N_h} \frac{1}{2\pi\sigma_h^2} \exp\left(-\frac{\left|\bar{s} - \bar{s}_i^h\right|^2}{2\sigma_h^2}\right), \qquad (3)$$

where N_h is the number of hotspots, and σ_h is the width of the hotspot. In this article, $N_h = 3$ is always used when the nucleon substructure is enabled. The hotspot locations $\bar{s}_i^h$ are sampled from a 2-dimensional Gaussian distribution with a width σ_s. The total nucleon width σ_N is then related to the hotspot widths via $\sigma_N^2 = \sigma_s^2 + \sigma_h^2$. Therefore, only two of the three widths are independent. As in Refs. [53, 57, 64], the energy dependence of the total nucleon width is parametrized as $\sigma_N = \sqrt{b}$ with

$$b/\mathrm{GeV}^{-2} = b_0 + 4\alpha_P' \log\left(\frac{W}{W_0}\right). \qquad (4)$$

where $W = \sqrt{s_{NN}}$, and b_0, α_P' and W_0 are fit parameters. In the present paper, our default choice of parameters, based on the H1 measurements [64], are $b_0 = 4.63$, $\alpha_P' = 0.164$ and $W_0 = 90$ GeV. This corresponds to $\sigma_N = 0.517$ fm for 2.76 TeV, and $\sigma_N = 0.532$ fm for 5.023 TeV collision energies.

In principle, the nucleon substructure needs to be accounted for when performing the triggering of the nuclear collision event [65, 66] since otherwise there might be events where the collision is accepted even though there is no hadronic interaction. As mentioned before, without any substructure, the triggering is done by assuming hard-sphere scattering between two nucleons. The event is accepted if the distance $d_{\min}^{NN}$ between any nucleons

$a \in A$ and $b \in B$ satisfy

$$d_{\min}^{NN} < \sqrt{\frac{\sigma_{\text{inel}}^{NN}}{\pi}}, \qquad (5)$$

where $\sigma_{\text{inel}}^{NN}$ is the inelastic nucleon-nucleon cross section. The same kind of geometrical criterion can be extended to account for the locations of the hotspots. That is, the triggering with the nucleon substructure is done based on the minimum distance between two colliding hotspots $d_{\min}^{HS}$, i.e.

$$d_{\min}^{HS} < \sqrt{\frac{\sigma_{HS}}{\pi}}, \qquad (6)$$

where σ_{HS} is an effective hotspot-hotspot cross section fitted to reproduce the same nucleus-nucleus cross section as obtained with condition (5). Therefore, the value of σ_{HS} will depend on the hotspot sampling-width σ_s and the collision system.

Even though in principle hotspot triggering could have a notable impact, we have noticed that in most cases all the measured observables remain nearly unchanged in the 0-80% centrality range. The largest effects are most visible in the most peripheral charged particle multiplicity region, where usually no measured data are given. In the 60-80% centralities, the differences in charged particle multiplicities are only a few percent at most. However, since in MC-EKRT we sample dijets from the same nucleon configuration until at least one is produced in a collision, the addition of hotspot triggering there speeds up the generation of the initial states.

D. Initialization of fluid dynamics

The initial condition of fluid dynamics is the energy-momentum tensor $T^{\mu\nu}$ at some initial proper time τ_0. However, MC-EKRT produces a list of massless partons with known momentum rapidities y_i, transverse momenta $\mathbf{p}_{Ti}$, and transverse coordinates $\mathbf{x}_{\perp,0i}$. Thus, the partons need to be propagated to the τ_0 surface and converted to the components of the energy-momentum tensor. Here we assume that all the partons are produced at the longitudinal location $z_i = 0$ at time $t = 0$, and that they propagate as free particles to the proper time $\tau_0 = 0.2$ fm. Therefore, spacetime and momentum rapidities are equivalent, i.e. $\eta_{s,i} = y_i$. The spacetime coordinates of the parton i are then $(\tau_0, \mathbf{x}_{\perp i}(\tau_0), \eta_{s,i})$ where $\mathbf{x}_{\perp i}(\tau_0) = \mathbf{x}_{\perp,0i} + \tau_0 \mathbf{p}_{Ti}/p_{Ti}$.

The components of the energy-momentum tensor in the $\tau - \eta_s$ coordinates are obtained as in Ref. [53],

$$T^{\alpha\beta}(x^\alpha) = \sum_i \int d^2\mathbf{p}_T dy \frac{p^\alpha p^\beta}{p^\tau} \frac{1}{\tau} \cosh(y - \eta_s) \qquad (7)$$

$$\times \delta^{(2)}(\mathbf{x}_\perp - \mathbf{x}_{\perp i})\delta(\eta_s - \eta_{s,i})\delta^{(2)}(\mathbf{p}_T - \mathbf{p}_{Ti})\delta(y - \eta_s),$$

where the four-momentum $p^\alpha = (p^\tau, \mathbf{p}_T, p^\eta)$ at a space-time location $x^\alpha = (\tau, \mathbf{x}_\perp, \eta_s)$ is given by

$$p^\alpha = \begin{pmatrix} p_T \cosh(y - \eta_s) \\ \mathbf{p}_T \\ \tau^{-1} p_T \sinh(y - \eta_s) \end{pmatrix}. \qquad (8)$$

Depositing all energy and momentum of a parton into a single cell on a hydro grid as suggested by the delta functions appearing in Eq. (7) would lead to extreme fluctuations in energy and momentum densities. To obtain smooth density distributions, smearing is required. Here we are performing 2+1 D hydrodynamic simulations, where a natural choice is to let all partons that are produced in the midrapidity window Δy contribute to the fluid dynamical initial state. That is, in Eq. (7) we replace $\delta(\eta_s - \eta_{s,i}) \to \theta(\Delta y/2 - |\eta_{s,i}|)/\Delta y$, where θ is the Heaviside theta function. Here we use $\Delta y = 1.0$, but we have tested that the final results are practically insensitive to the choice of Δy as long as $0.5 \leq \Delta y \leq 2.0$. The smearing in the transverse (x, y) plane is performed by replacement $\delta^{(2)}(\mathbf{x}_\perp - \mathbf{x}_{\perp i}) \to g_\perp(\mathbf{x}_\perp; \mathbf{x}_{\perp i})$, where

$$g_\perp(\mathbf{x}_\perp; \mathbf{x}_{\perp i}) = \frac{C_\perp}{2\pi\sigma_\perp^2} \exp\left[-\frac{(\mathbf{x}_\perp - \mathbf{x}_{\perp i})^2}{2\sigma_\perp^2}\right] \qquad (9)$$

is a Gaussian distribution with transverse smearing width $\sigma_\perp$ which is normalized as

$$\int d^2\mathbf{x}_\perp g_\perp(\mathbf{x}_\perp; \mathbf{x}_{\perp i}) = 1. \qquad (10)$$

The computation cost is reduced by imposing a $\pm 3\sigma_\perp$ cut-off on the smearing range, and the coefficient $C_\perp$ takes care of the unit normalization.

As in Ref. [53], we only consider the local rest frame energy density e when initializing the fluid dynamical system, i.e. we neglect the initial transverse velocity and the initial components of the shear-stress tensor. Therefore, the initialization is determined by

$$T^{\tau\tau}(\tau_0, \mathbf{x}_\perp, \Delta y) =$$
$$\frac{1}{\tau_0 \Delta y} \sum_i p_{Ti} g_\perp(\mathbf{x}_\perp; \mathbf{x}_{\perp i})\theta(\Delta y/2 - |y_i|), \qquad (11)$$

which in this case coincides with e. The remaining components are then obtained, using the equation of state, as $T^{ij} = P(e)\delta^{ij}$.

Finally, we emphasize that even if we utilize only the midrapidity minijets in computing the above initial conditions, the underlying MC-EKRT event generation is fully 3 D. Thus, the midrapidity initial conditions are influenced also by the finite-rapidity effects in saturation and in energy conservation.

III. FLUID SIMULATION FRAMEWORK

The simulations performed in this article focus on midrapidity observables and therefore we assume that the

longitudinal expansion of the system is boost invariant. The same framework as in Ref. [28] is used, i.e. we evolve the initially formed strongly interacting matter using dissipative fluid dynamics, and compute the final particle spectra at the dynamical decoupling surface. Additionally, the neural networks trained in Ref. [41] are utilized for significantly decreasing the computation time of the simulations. In this section, we give a brief recapitulation of each aspect of the framework.

A. Fluid dynamics

Fluid dynamics is based on the local conservation laws for energy, momentum, and conserved charges. Here we neglect the conserved charges, in which case the conservation law for the energy-momentum tensor, $\partial_\mu T^{\mu\nu} = 0$, controls the dynamics. The energy-momentum tensor can be decomposed with respect to 4-velocity u^μ as

$$T^{\mu\nu} = e u^\mu u^\nu - P \Delta^{\mu\nu} + \pi^{\mu\nu}, \qquad (12)$$

where $\Delta^{\mu\nu} = g^{\mu\nu} - u^\mu u^\nu$ is a projection operator, $P = -\frac{1}{3}\Delta_{\mu\nu}T^{\mu\nu}$ is the total isotropic pressure, $e = T^{\mu\nu}u_\mu u_\nu$ is the local rest frame energy density, and $\pi^{\mu\nu} = T^{\langle\mu\nu\rangle}$ is the shear-stress tensor. The angular brackets denote the symmetric, traceless part of the tensor that is orthogonal to the fluid 4-velocity. Here the fluid velocity is defined in the Landau frame, i.e. $T^\mu_\nu u^\nu = e u^\mu$. The bulk viscous pressure is defined as the deviation of the isotropic pressure P from the equilibrium pressure P_0, i.e. $\Pi = P - P_0$. The equilibrium pressure is given by the equation of state (EoS) of the QCD matter at zero baryon density, $P_0 = P_0(e)$. In this work, we use the s95p-v1 parametrization [67] for the EoS, which includes the partial chemical decoupling at $T_{\text{chem}} = 155$ MeV. The partial chemical decoupling is implemented by adding temperature-dependent chemical potentials for each hadron in the hadronic part of the EoS [68–70].

The conservation laws together with the EoS are enough to solve the evolution in equilibrium, but additional constraints are needed when dissipative effects are present. The dissipative parts of the energy-momentum tensor are the shear-stress tensor and the bulk viscous pressure. In the formalism by Israel and Stewart [71], the equations of motion for dissipative parts take a form

$$\tau_\Pi \frac{d}{d\tau}\Pi + \Pi = -\zeta\theta - \delta_{\Pi\Pi}\Pi\theta + \lambda_{\Pi\pi}\pi^{\mu\nu}\sigma_{\mu\nu}, \qquad (13)$$

$$\begin{aligned} \tau_\pi \frac{d}{d\tau}\pi^{\langle\mu\nu\rangle} + \pi^{\mu\nu} =\ & 2\eta\sigma^{\mu\nu} + 2\tau_\pi \pi_\alpha^{\langle\mu}\omega^{\nu\rangle\alpha} \\ & -\delta_{\pi\pi}\pi^{\mu\nu}\theta - \tau_{\pi\pi}\pi_\alpha^{\langle\mu}\sigma^{\nu\rangle\alpha} \\ & +\varphi_7\pi_\alpha^{\langle\mu}\pi^{\nu\rangle\alpha} + \lambda_{\pi\Pi}\Pi\sigma^{\mu\nu}, \end{aligned} \qquad (14)$$

where $\theta = \nabla_\mu u^\mu$ is the expansion rate, $\sigma^{\mu\nu} = \nabla^{\langle\mu}u^{\nu\rangle}$ is the strain-rate tensor, and $\omega^{\mu\nu} = \frac{1}{2}\left(\nabla^\mu u^\nu - \nabla^\nu u^\mu\right)$ is the vorticity tensor. The first-order transport coefficients η and ζ are called shear and bulk viscosity respectively. In a 14-moment approximation to the massless gas [72–75], the first-order transport coefficients are related to the shear and bulk relaxation times as

$$\tau_\pi = \frac{5\eta}{e + P_0}, \quad \tau_\Pi = \left(15\left(\frac{1}{3} - c_s^2\right)^2 (e + P_0)\right)^{-1}\zeta, \quad (15)$$

and the remaining second-order transport coefficients are

$$\begin{aligned} &\delta_{\Pi\Pi} = \frac{2}{3}\tau_\Pi, \quad \lambda_{\Pi\pi} = \frac{8}{5}\left(\frac{1}{3} - c_s^2\right)\tau_\Pi, \quad \delta_{\pi\pi} = \frac{4}{3}\tau_\pi, \\ &\tau_{\pi\pi} = \frac{10}{7}\tau_\pi, \quad \varphi_7 = \frac{9}{70P_0}, \quad \lambda_{\pi\Pi} = \frac{6}{5}\tau_\pi, \end{aligned} \qquad (16)$$

where c_s is the speed of sound. The specific shear viscosity η/s and specific bulk viscosity ζ/s are from the $\eta/s = dyn$ parametrization introduced in Ref. [28].

B. Decoupling and particle spectra

The fluid dynamic evolution is continued until reaching the kinetic decoupling surface. Here the decoupling surface is determined by the dynamical decoupling conditions

$$\text{Kn} = \tau_\pi\theta = C_{\text{Kn}} \qquad (17)$$

$$\frac{\gamma\tau_\pi}{R} = C_R, \qquad (18)$$

where Kn is the Knudsen number, γ is the Lorentz gamma factor, and the coefficients C_{Kn} and C_R are proportionality constants of $\mathcal{O}(1)$ which are fitted to the measured data. Here, values $C_{\text{Kn}} = 0.8$ and $C_R = 0.15$ are used according to Ref. [28]. The size of the system R is defined as

$$R = \sqrt{\frac{A}{\pi}}, \qquad (19)$$

where A is the area in the transverse (x, y) plane where $\text{Kn} < C_{\text{Kn}}$. Additionally, the decoupling is forced to happen in the hadronic phase of the QCD matter, i.e. when $T < 150$ MeV. Given these conditions the decoupling surface is determined using the Cornelius algorithm [76].

At the decoupling surface Σ with the directed surface element $d\Sigma_\mu$, the Lorentz-invariant particle spectrum for particle type i is computed according to the Cooper-Frye integral,

$$E\frac{d^3 N_i}{d^3 k} = \int_\Sigma d\Sigma_\mu k^\mu f_i(x, k), \qquad (20)$$

where E and k^μ are particles energy and 4-momentum, respectively. The distribution function for particle species i is decomposed into in- and out-of-equilibrium parts as $f_i = f_{0i} + \delta f_i$, where the equilibrium part is given by

$$f_{0i}(x,k) = \left[\exp\left(\frac{k_i^\mu u_\mu - \mu_i}{T}\right) \pm 1 \right]^{-1}, \qquad (21)$$

where $+(-)$ sign is for fermions (bosons), and μ_i is the chemical potential. Here, the viscous corrections to the equilibrium distribution are of the form [6, 77–79]

$$\delta f_i = - f_{0i}\tilde{f}_{0i}\frac{C_{bulk}}{T}\left[\frac{m^2}{3E_k} - \left(\frac{1}{3} - c_s^2\right)E_k\right]\Pi$$
$$+ \frac{f_{0i}\tilde{f}_{0i}}{2T^2(e+P_0)}\pi^{\mu\nu}k_\mu k_\nu, \qquad (22)$$

with $\tilde{f}_{0i} = 1 \pm f_{0i}$ (+ for bosons and − for fermions) and the coefficient

$$\frac{1}{C_{bulk}} = \sum_i \frac{g_i m_i^2}{3T} \int \frac{\mathrm{d}^3\mathbf{k}}{(2\pi)^3 k^0} f_{0i}\tilde{f}_{0i}\left[\frac{m_i^2}{3E_k} - \left(\frac{1}{3} - c_s^2\right)E_k\right], \qquad (23)$$

where g_i is the degeneracy factor. After computing the spectra from Eq. (20), the 2- and 3-body decays of unstable particles are computed as in Ref. [80].

C. Neural Networks

To reduce the computational cost of the simulations, deep convolutional neural networks trained in Ref. [41] are utilized here for predicting final state event-by-event observables at midrapidity. Each neural network takes the discretized initial energy density profile in the transverse-coordinate (x, y) plane as an input, and outputs one p_T-integrated observable. Separate neural networks are used to predict flow coefficients v_n, charged particle multiplicities $dN_{\mathrm{ch}}/d\eta$, and mean transverse momenta $[p_T]$. Predicting flow observables with neural networks is many orders of magnitude faster than performing full hydrodynamic simulations. For example, predicting results for 10 million events takes only around 20 hours with Nvidia Tesla V100 GPU.

As the training data for the neural networks is from Ref. [28], and the predictions made using these networks emulate the same dynamics as the training data, the viscosities η/s, and ζ/s, and other parameters affecting the fluid-dynamical evolution are the same ones as in Ref. [28].

In Ref. [41], it was demonstrated that the neural networks work accurately when using the EbyE version of the EKRT model. However, it is non-trivial that the accuracy of the neural networks, which are trained by the EbyE-EKRT data from Ref. [28], and *not* from MC-EKRT, would extend to the MC-EKRT initial states with hotspots, where the initial geometry can be significantly different. Therefore, the neural networks were validated by generating 10k MC-EKRT initial states and comparing the neural network predictions against 2+1 D fluid dynamical simulations for the 5.023 TeV Pb+Pb collision system. The validation tests for the flow coefficients

v_2, v_3, and v_4 are shown in Fig. 1. The initial state parameters used in the validation test were $\kappa_{\mathrm{sat}} = 2.5$, $K = 2.2$, $\sigma_\perp = 0.4$ fm, and $\sigma_h = 0.2$ fm. The obtained excellent agreement between the fluid dynamical simulations and neural network predictions illustrates the versatility of the neural networks with different initial conditions. Additionally, we have verified that the accuracy of the employed neural networks remains good for other training observables as well.

IV. RESULTS

In this section, we present the results of fluid-dynamical simulations with MC-EKRT initial states for midrapidity bulk observables, and compare the results against the earlier EbyE EKRT work [28]. All the fluid dynamical results are generated using our neural networks, and they contain 50k collision events, except the multiplicity distribution results which are obtained from 150k events. As discussed in Sec. III C, the neural network results correspond to the fluid dynamical simulations with the matter properties and decoupling parameters from Ref. [28]. Therefore, any differences between the presented results are due to differences in the initial states.

When examining the effects of the initial state through final state observables, it is important to remember that some observables are highly sensitive to the properties of the matter. For instance, the magnitude of flow coefficients is significantly influenced by the shear viscosity to entropy density ratio η/s. In contrast, the ratios of flow coefficients are less sensitive to such details, particularly the ratio between v_3 and v_2, which can provide valuable insights into the geometry and structure of the initial state [82].

The effect of the Gaussian smearing width $\sigma_\perp$ is demonstrated in Fig. 2, where the ratios of the flow coefficients v_2, v_3, and v_4 in 5.023 TeV Pb+Pb collision system are shown as a function of centrality for different smearing widths. The MC-EKRT initial state parameters are set to $\kappa_{\mathrm{sat}} = 1.4$, and $K = 2.5$. Nucleon substructure is not included in these plots. As can be seen in the left panel, the magnitude of flow is sensitive to the Gaussian smearing width $\sigma_\perp$. However, $\sigma_\perp$ has only little impact on the ratios between the flow coefficients, as shown by the middle and right panels. Therefore, the parameter $\sigma_\perp$ is influencing the flow coefficients in a similar manner as the shear viscosity. Here, and in what follows, we adjust $\sigma_\perp$ to obtain the measured v_2 in mid-central collisions for all different MC-EKRT results. However, we want to emphasize that this is only done to illustrate the capabilities and uncertainties of MC-EKRT. To get the best overall fit to all different observables, a global analysis is needed, but this is beyond the purpose of this study.

An intriguing aspect of the MC-EKRT model is the interplay between the saturation and conservation-law
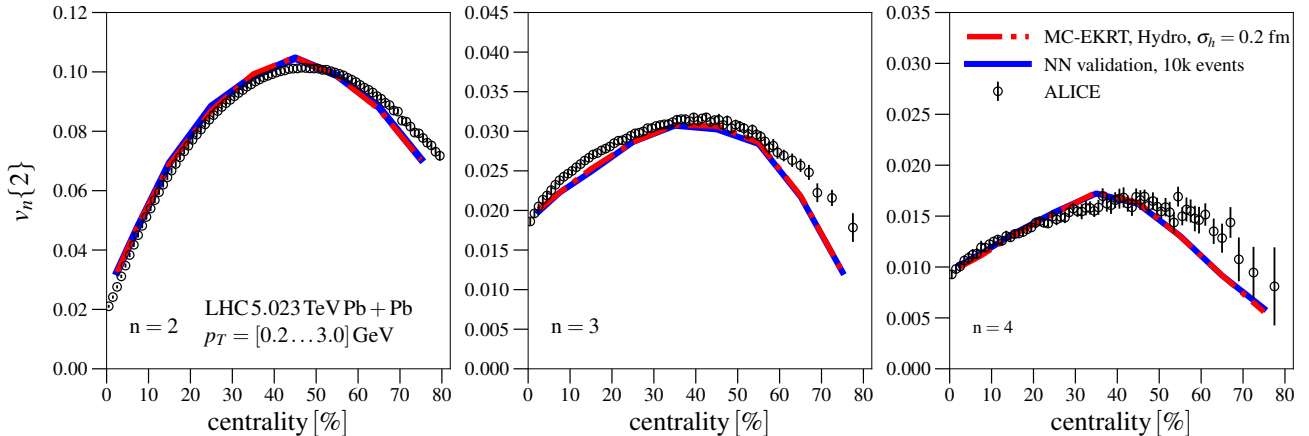
FIG. 1: Neural network validation test for the flow coefficients $v_2\{2\}, v_3\{2\}$, and $v_4\{2\}$ in 5.023 TeV Pb+Pb collisions. The networks were trained with the EbyE-EKRT data from Ref. [28] as described in Ref. [41]. The hydro results and the neural network validation results were obtained from 10k MC-EKRT initial states which included hotspots and multiplicity fluctuations that were not present in the training data. The measured data are from the ALICE Collaboration [81].
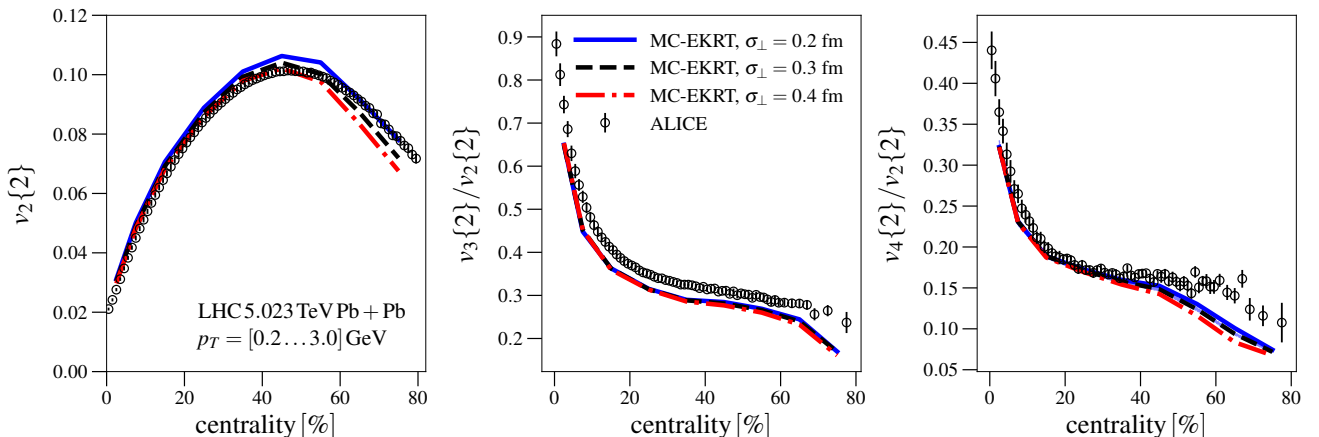

FIG. 2: The effect of the Gaussian smearing width $\sigma_\perp$ on the two-particle flow coefficient $v_2\{2\}$ (left panel) and the ratios $v_3\{2\}/v_2\{2\}$ (middle panel), and $v_4\{2\}/v_2\{2\}$ (right panel) in 5.023 TeV Pb+Pb collisions. No nucleon substructure is included here. The experimental data for the ratios are computed based on the ALICE measurements for the two-particle flow coefficients [81].

filters. The impact of different filters on the flow coefficients in 5.023 TeV Pb+Pb collisions is illustrated in Fig. 3. In all these scenarios, a value of $K = 2.5$ is used, while the saturation parameter κ_{sat} is adjusted to achieve roughly identical charged particle multiplicities in central collisions. This corresponds to $\kappa_{sat} = 1.3$ for the saturation-only case, and $\kappa_{sat} = 1.4$ for the other cases. The nucleon width is set according to the default parametrization from Eq. (4), i.e. $\sigma_N = 0.53$ fm, and no nucleon substructure is introduced. For the saturation-first case $\sigma_\perp = 0.3$ fm, for the case with all filters at the same time $\sigma_\perp = 0.4$ fm, and for the saturation-only case $\sigma_\perp = 0.3$ fm.

The most notable feature in Fig. 3 is the significant impact of saturation on the ratio between v_3 and v_2. The

case with only saturation reproduces the measured v_2 and v_3 most accurately, while the simultaneous application of all the filters leads to a clear underestimation of v_3. When saturation is applied before other filters, the results approach those of the saturation-only scenario, as anticipated. The discrepancies in the v_3/v_2 ratio arise from the geometrical differences in saturation and momentum conservation. Saturation does not allow geometrical overlap in the transverse plane. This leads to a more evenly distributed energy density profile. Energy conservation, on the other hand, gives no direct geometrical constraints. The stronger the saturation the more the eccentricity ε_2 is suppressed compared to the eccentricity ε_3. The reduced eccentricity ε_2 can be compensated by decreasing the smearing width $\sigma_\perp$ so that the elliptic flow v_2 remains
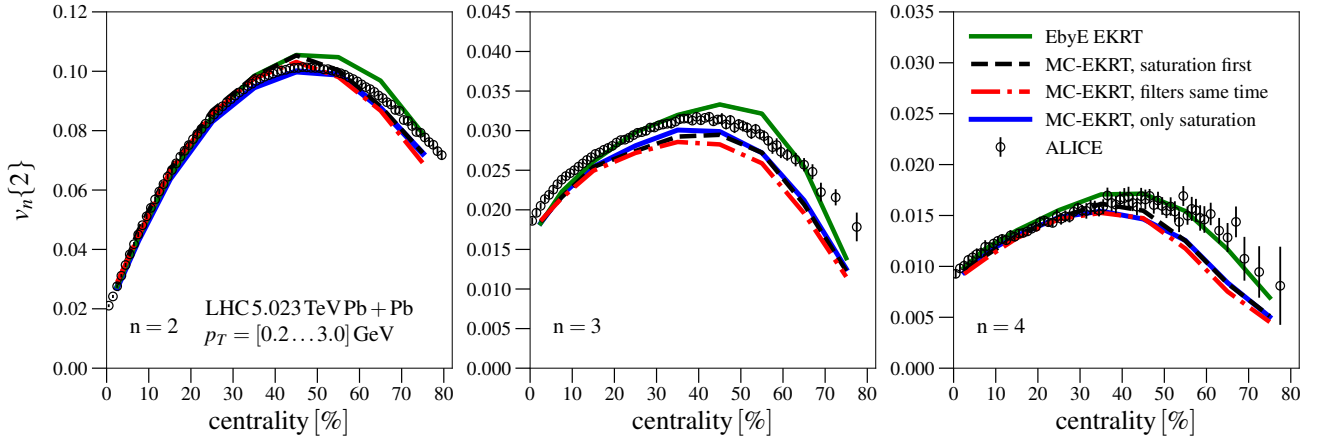
FIG. 3: The flow coefficients $v_n\{2\}$ as a function of centrality for 5.023 TeV Pb+Pb collisions. The simulation results with different MC-EKRT filter settings are compared against the ALICE measurements [81], and the EbyE-EKRT results from Ref. [28]. No nucleon substructure was included here.
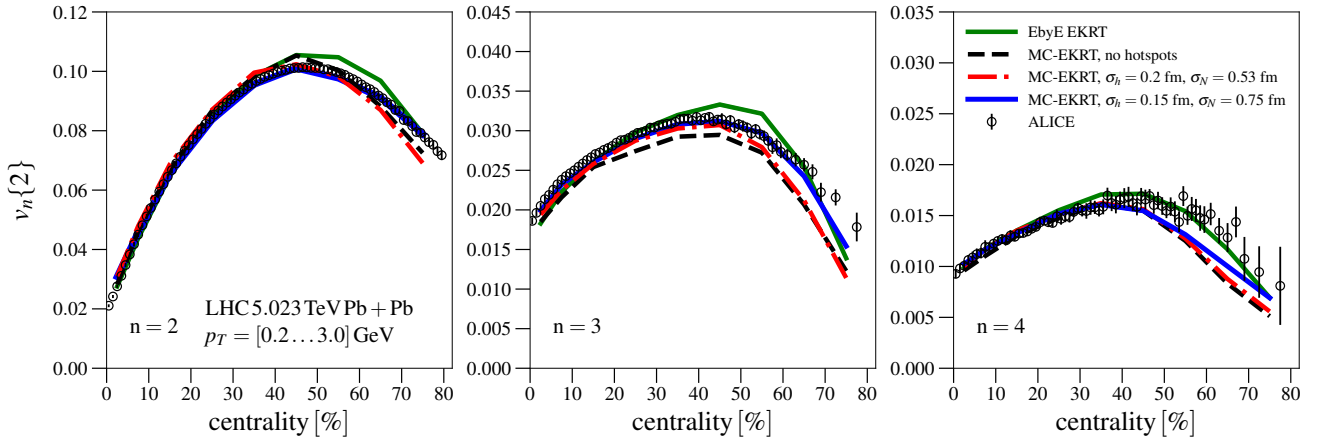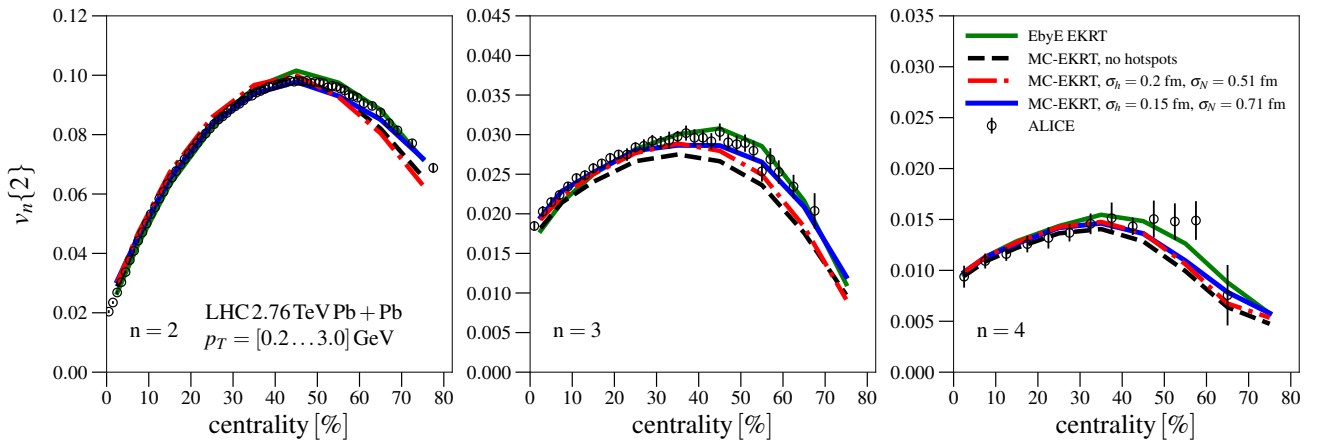

FIG. 4: The flow coefficients $v_n\{2\}$ as a function of centrality for 5.023 TeV Pb+Pb collisions. The MC-EKRT results with and without nucleon substructure are compared against the ALICE measurements [81], and the EbyE-EKRT results from Ref. [28].

FIG. 5: The flow coefficients $v_n\{2\}$ as a function of centrality for 2.76 TeV Pb+Pb collisions. The MC-EKRT results with and without nucleon substructure are compared against the ALICE measurements [81], and the EbyE-EKRT results from Ref. [28].

nearly unchanged, while ε_3 increases. This is reflected in the shown flow coefficients. It is also noteworthy that the v_3/v_2 ratio is very similar between the MC-EKRT model with only saturation and the EbyE-EKRT model, which does not explicitly include momentum conservation. Since strong saturation appears to be necessary for matching the measured v_3/v_2 ratio, we will now focus exclusively on the scenarios where saturation is applied first, followed by the conservation filters. This approach is also theoretically justified because, in principle, saturation should inherently account for conservation laws. However, achieving this would require implementing saturation through momentum-conserving multiparton distributions to all orders, which is not practically feasible.

Since saturation is sensitive to the nuclear overlap $T_A T_B$ (nuclear thickness function T_A is the sum of T_Ns), the hotspots introduce interesting dynamics. With the hotspots, T_A can reach ~ 10 times higher values than with the average nucleon geometry. Therefore, one would expect the saturation strength and the v_3/v_2 ratio to increase when hotspots are included.

The effect of hotspots on the flow coefficients is illustrated in Fig. 4, which compares two different hotspot parametrizations. The first parametrization uses the default nucleon width from parametrization Eq. (4), together with hotspots with width $\sigma_h = 0.2$ fm. In this case, the MC-EKRT parameters are set to $\kappa_{\rm sat} = 2.5$, $K = 2.2$, and $\sigma_\perp = 0.4$ fm. For the second parametrization, the nucleon width is obtained from Eq. (4), but this time a significantly stronger energy dependence with $\alpha' = 0.6$ is used. This corresponds to a nucleon width $\sigma_N = 0.75$ fm for 5.023 TeV collision energy. This nucleon width is in line with the many global analyses, where values in the range $\sim 0.6 - 1.0$ fm are preferred [33, 37, 44, 83]. With a wider nucleon, a narrower hotspot with $\sigma_h = 0.15$ fm is used together with parameters $\kappa_{\rm sat} = 2.5$, $K = 2.4$, and $\sigma_\perp = 0.25$ fm. The saturation-first case from Fig. 3 is here left as a reference curve.

As expected, the addition of hotspots appears to increase the v_3/v_2 ratio. The best overall fit to the measurements is obtained with the narrow hotspots, i.e. $\sigma_h = 0.15$ fm, corresponding thus to the strongest saturation. In this case, the centrality dependence of v_2, and v_3 matches nearly perfectly to the ALICE measurements [81], while maintaining a good agreement for v_4. These findings suggest that the interplay between hotspots and saturation is crucial for the simultaneous description of the flow coefficients and especially of the v_3/v_2 ratio.

In Fig. 5, the flow coefficients are shown for 2.76 TeV Pb+Pb collisions. The different curves correspond to the same cases as in Fig. 4, but the K factor is adjusted to obtain a reasonable agreement with the measured charged particle multiplicity. The obtained values are $K = 2.5$ for the $\sigma_h = 0.2$ fm case, while the $\sigma_h = 0.15$ fm and the no-hotspots cases both use $K = 2.7$. The agreement between the data and the results is quite similar to the

5.023 TeV collision energy results. At both energies, the narrow-hotspot case with $\sigma_h = 0.15$ fm can describe the measured flow coefficients well, while the centrality dependence of v_2 is slightly off for the $\sigma_h = 0.2$ fm case. From Figs. 4 and 5 it can be seen that MC-EKRT with the nucleon substructure captures the energy dependence of the flow coefficients significantly better than the EbyE-EKRT model.

In Fig. 6, the charged particle multiplicity as a function of centrality is shown for the same initial state parametrizations in 2.76 TeV and 5.023 TeV Pb+Pb collisions. The agreement between the results and the ALICE measurements [84, 85] is good in all cases, even though there are some minor discrepancies in the centrality behavior. The initial state without hotspots seems to produce slightly too weak a centrality dependence, while, with the hotspots, the centrality dependence is a bit too steep. However, these are small differences, and further improvements could be obtained by fine-tuning the matter properties and initial state parameters.

The MC-EKRT approach adds minijet-multiplicity originating saturation-scale fluctuations to the EKRT initial state. These fluctuations, together with hotspot fluctuations, should in principle increase the hadron multiplicity fluctuations in the most central collisions. This effect is studied in Fig. 7, where the charged hadron multiplicity distributions from MC-EKRT with and without hotspots are compared against the EbyE-EKRT results, which do not contain multiplicity-originating fluctuations of the saturation scale or hotspots. To make the results comparable with the V0 amplitude measured by ALICE [86], they are normalized to have approximately the same mean as the V0 amplitude. As shown also in Ref. [17], the EbyE-EKRT results almost completely miss the high-multiplicity tail in the distribution. The addition of the further saturation scale fluctuations indeed enhances the high-multiplicity tail in the distribution, and therefore improves the agreement with the measurements as one would expect. The addition of the hotspots is important also for this observable, as it increases the fluctuations and high-multiplicity tail further, leading to a very good agreement with the ALICE data.

V. CONCLUSIONS

In this article, we have studied the effects of the MC-EKRT initial states on midrapidity flow observables. The computationally slow fluid dynamics simulations were replaced with the neural networks, that could predict flow observables directly from the initial state. The networks used here did not contain any information about the MC-EKRT initial states. Even so, the neural networks did accurately describe the flow observables, emphasizing the versatility and usefulness of the neural networks.

We found that essentially the strength of saturation controls the ratio between two-particle flow coefficients v_3/v_2. Without any nucleon substructure, the measured
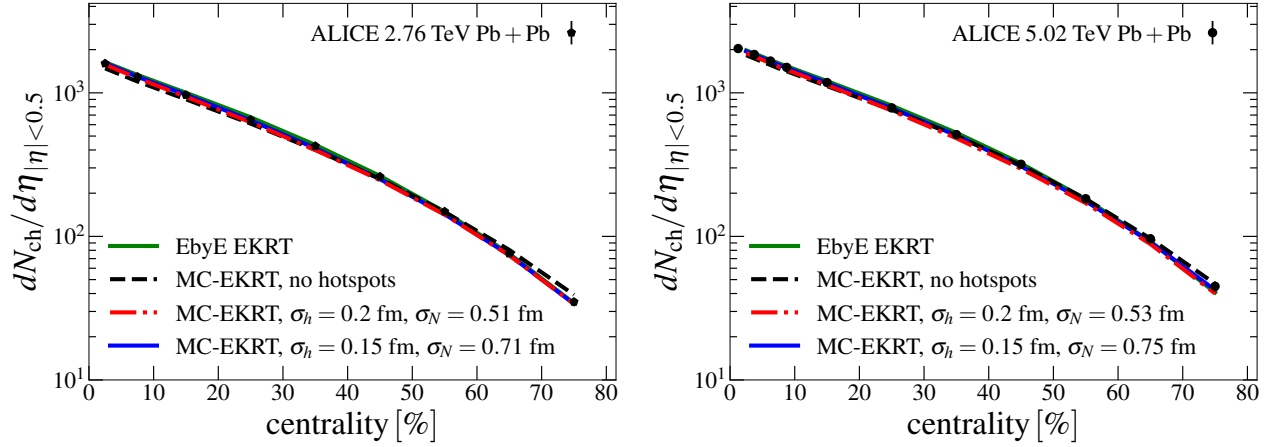
FIG. 6: The charged particle multiplicity as a function of centrality in 2.76 TeV (left panel), and 5.023 TeV (right panel) Pb+Pb collisions. The MC-EKRT results with and without nucleon substructure are compared against the ALICE measurements [84, 85], and the EbyE-EKRT results from Ref. [28].
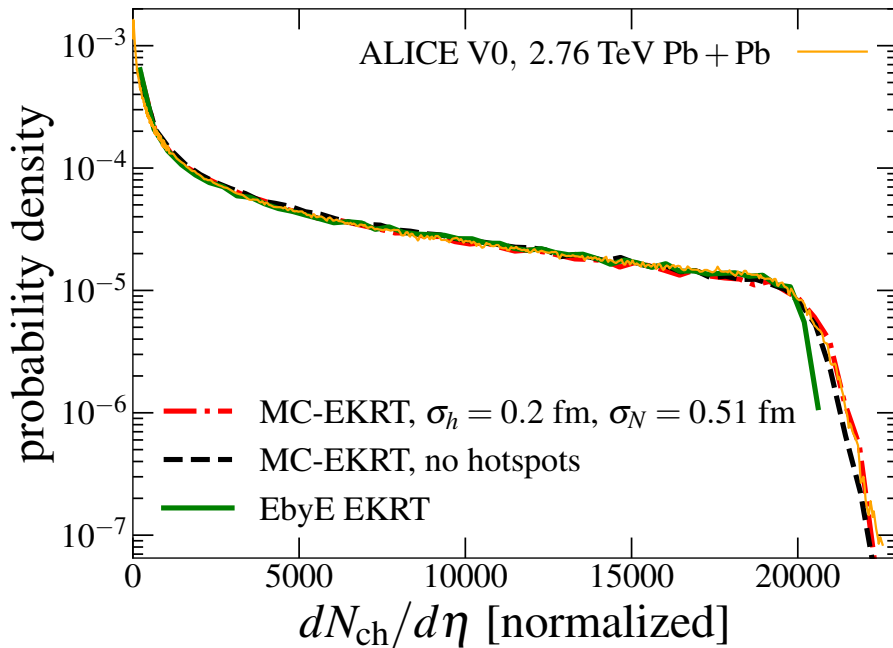

FIG. 7: The probability distribution of charged particle multiplicity for 2.76 TeV Pb+Pb collisions. The MC-EKRT results with and without nucleon substructure are compared against the parametrization of the ALICE V0 amplitude read off from Ref. [86], and the EbyE-EKRT results from Ref. [28].

data preferred that no local momentum conservation was enforced, so that the saturation would be the only effect that regulates the initial low-p_T parton production. The addition of the nucleon substructure enhanced the saturation strength, and led to a good agreement with the measured data, even with the local momentum conservation imposed. Our flow coefficient results lend support to having relatively narrow hotspots in a relatively wide nucleon, and rather systematically saturation as the de-

cisive QCD mechanism for regulating the initial parton production.

The results from the MC-EKRT initial state with the nucleon substructure managed to improve the agreement with the LHC measurements relative to the previous EbyE-EKRT model. The novel MC-EKRT model now captures the measured energy dependence of the flow coefficients better, while the added saturation scale fluctuations and the inclusion of hotspots systematically im-

proves the agreement with the measured multiplicity distribution in the most central collisions.

Overall, the MC-EKRT results presented here show an excellent agreement with the data for the flow coefficients and the charged particle multiplicity. We want to note that this was achieved even without adjusting the QCD matter properties or the dynamical decoupling conditions from previous works, and therefore this acts as a baseline for what can be achieved. More detailed global analysis with more observables and collision systems should be done to constrain the QCD matter properties. Additionally, at the lower collision energies, the finite longitudinal overlap area in the initial collision together with the initial transverse flow can play an important role in the simulations. These aspects were not considered here, but are left as future work.

Acknowledgments

[1] [ALICE], "The ALICE experiment – A journey through QCD," CERN-EP-2022-227, [arXiv:2211.04384 [nucl-ex]].

[2] A. Bazavov, P. Petreczky and J. H. Weber, Phys. Rev. D **97**, no.1, 014510 (2018) doi:10.1103/PhysRevD.97.014510 [arXiv:1710.05024 [hep-lat]].

[3] S. Borsanyi, Z. Fodor, C. Hoelbling, S. D. Katz, S. Krieg and K. K. Szabo, Phys. Lett. B **730**, 99-104 (2014) doi:10.1016/j.physletb.2014.01.007 [arXiv:1309.5258 [hep-lat]].

[4] P. Romatschke and U. Romatschke, Phys. Rev. Lett. **99**, 172301 (2007) doi:10.1103/PhysRevLett.99.172301 [arXiv:0706.1522 [nucl-th]].

[5] M. Luzum and P. Romatschke, Phys. Rev. C **78**, 034915 (2008) [erratum: Phys. Rev. C **79**, 039903 (2009)] doi:10.1103/PhysRevC.78.034915 [arXiv:0804.4015 [nucl-th]].

[6] P. Bozek, Phys. Rev. C **81**, 034909 (2010) doi:10.1103/PhysRevC.81.034909 [arXiv:0911.2397 [nucl-th]].

[7] P. Bozek and I. Wyskiel-Piekarska, Phys. Rev. C **85**, 064915 (2012) doi:10.1103/PhysRevC.85.064915 [arXiv:1203.6513 [nucl-th]].

[8] B. Schenke, S. Jeon and C. Gale, Phys. Rev. Lett. **106**, 042301 (2011) doi:10.1103/PhysRevLett.106.042301 [arXiv:1009.3244 [hep-ph]].

[9] B. Schenke, S. Jeon and C. Gale, Phys. Rev. C **82**, 014903 (2010) doi:10.1103/PhysRevC.82.014903 [arXiv:1004.1408 [hep-ph]].

[10] B. Schenke, S. Jeon and C. Gale, Phys. Rev. C **85**, 024901 (2012) doi:10.1103/PhysRevC.85.024901 [arXiv:1109.6289 [hep-ph]].

[11] H. Song, S. A. Bass and U. Heinz, Phys. Rev. C **83**, 054912 (2011) [erratum: Phys. Rev. C **87**, no.1, 019902 (2013)] doi:10.1103/PhysRevC.83.054912 [arXiv:1103.2380 [nucl-th]].

[12] H. Niemi, G. S. Denicol, P. Huovinen, E. Molnar and D. H. Rischke, Phys. Rev. Lett. **106**, 212302 (2011) doi:10.1103/PhysRevLett.106.212302 [arXiv:1101.2442 [nucl-th]].

[13] L. Pang, Q. Wang and X. N. Wang, Phys. Rev. C **86**, 024911 (2012) doi:10.1103/PhysRevC.86.024911 [arXiv:1205.5019 [nucl-th]].

[14] C. Gale, S. Jeon, B. Schenke, P. Tribedy and R. Venugopalan, Phys. Rev. Lett. **110**, no.1, 012302 (2013) doi:10.1103/PhysRevLett.110.012302 [arXiv:1209.6330 [nucl-th]].

[15] H. Niemi, G. S. Denicol, P. Huovinen, E. Molnar and D. H. Rischke, Phys. Rev. C **86**, 014909 (2012) doi:10.1103/PhysRevC.86.014909 [arXiv:1203.2452 [nucl-th]].

[16] J. Noronha-Hostler, G. S. Denicol, J. Noronha, R. P. G. Andrade and F. Grassi, Phys. Rev. C **88**, no.4, 044916 (2013) doi:10.1103/PhysRevC.88.044916 [arXiv:1305.1981 [nucl-th]].

[17] H. Niemi, K. J. Eskola and R. Paatelainen, Phys. Rev. C **93**, no.2, 024907 (2016) doi:10.1103/PhysRevC.93.024907 [arXiv:1505.02677 [hep-ph]].

[18] G. Denicol, A. Monnai and B. Schenke, Phys. Rev. Lett. **116**, no.21, 212301 (2016) doi:10.1103/PhysRevLett.116.212301 [arXiv:1512.01538 [nucl-th]].

[19] S. Ryu, J. F. Paquet, C. Shen, G. S. Denicol, B. Schenke, S. Jeon and C. Gale, Phys. Rev. Lett. **115**, no.13, 132301 (2015) doi:10.1103/PhysRevLett.115.132301 [arXiv:1502.01675 [nucl-th]].

[20] L. G. Pang, H. Petersen, G. Y. Qin, V. Roy and X. N. Wang, Eur. Phys. J. A **52**, no.4, 97 (2016)

doi:10.1140/epja/i2016-16097-x [arXiv:1511.04131 [nucl-th]].

[21] I. A. Karpenko, P. Huovinen, H. Petersen and M. Bleicher, Phys. Rev. C **91**, no.6, 064901 (2015) doi:10.1103/PhysRevC.91.064901 [arXiv:1502.01978 [nucl-th]].

[22] G. Giacalone, J. Noronha-Hostler, M. Luzum and J. Y. Ollitrault, Phys. Rev. C **97**, no.3, 034904 (2018) doi:10.1103/PhysRevC.97.034904 [arXiv:1711.08499 [nucl-th]].

[23] P. Bozek and W. Broniowski, Phys. Rev. C **97**, no.3, 034913 (2018) doi:10.1103/PhysRevC.97.034913 [arXiv:1711.03325 [nucl-th]].

[24] L. G. Pang, H. Petersen and X. N. Wang, Phys. Rev. C **97**, no.6, 064918 (2018) doi:10.1103/PhysRevC.97.064918 [arXiv:1802.04449 [nucl-th]].

[25] A. Sakai, K. Murase and T. Hirano, Phys. Rev. C **102**, no.6, 064903 (2020) doi:10.1103/PhysRevC.102.064903 [arXiv:2003.13496 [nucl-th]].

[26] G. Nijs, W. van der Schee, U. Gürsoy and R. Snellings, Phys. Rev. C **103**, no.5, 054909 (2021) doi:10.1103/PhysRevC.103.054909 [arXiv:2010.15134 [nucl-th]].

[27] C. Shen and B. Schenke, Phys. Rev. C **105**, no.6, 064905 (2022) doi:10.1103/PhysRevC.105.064905 [arXiv:2203.04685 [nucl-th]].

[28] H. Hirvonen, K. J. Eskola and H. Niemi, Phys. Rev. C **106**, no.4, 044913 (2022) doi:10.1103/PhysRevC.106.044913 [arXiv:2206.15207 [hep-ph]].

[29] J. Novak, K. Novak, S. Pratt, J. Vredevoogd, C. Coleman-Smith and R. Wolpert, Phys. Rev. C **89**, no.3, 034917 (2014) doi:10.1103/PhysRevC.89.034917 [arXiv:1303.5769 [nucl-th]].

[30] J. E. Bernhard, J. S. Moreland, S. A. Bass, J. Liu and U. Heinz, Phys. Rev. C **94**, no.2, 024907 (2016) doi:10.1103/PhysRevC.94.024907 [arXiv:1605.03954 [nucl-th]].

[31] S. A. Bass, J. E. Bernhard and J. S. Moreland, Nucl. Phys. A **967**, 67-73 (2017) doi:10.1016/j.nuclphysa.2017.05.052 [arXiv:1704.07671 [nucl-th]].

[32] J. E. Bernhard, J. S. Moreland and S. A. Bass, Nature Phys. **15**, no.11, 1113-1117 (2019) doi:10.1038/s41567-019-0611-8

[33] D. Everett *et al.* [JETSCAPE], Phys. Rev. C **103**, no.5, 054904 (2021) doi:10.1103/PhysRevC.103.054904 [arXiv:2011.01430 [hep-ph]].

[34] J. Auvinen, K. J. Eskola, P. Huovinen, H. Niemi, R. Paatelainen and P. Petreczky, Phys. Rev. C **102**, no.4, 044911 (2020) doi:10.1103/PhysRevC.102.044911 [arXiv:2006.12499 [nucl-th]].

[35] J. E. Parkkila, A. Onnerstad and D. J. Kim, Phys. Rev. C **104**, no.5, 054904 (2021) doi:10.1103/PhysRevC.104.054904 [arXiv:2106.05019 [hep-ph]].

[36] J. E. Parkkila, A. Onnerstad, S. F. Taghavi, C. Mordasini, A. Bilandzic, M. Virta and D. J. Kim, Phys. Lett. B **835**, 137485 (2022) doi:10.1016/j.physletb.2022.137485 [arXiv:2111.08145 [hep-ph]].

[37] G. Nijs and W. van der Schee, [arXiv:2304.06191 [nucl-th]].

[38] J. Auvinen, J. E. Bernhard, S. A. Bass and I. Karpenko, Phys. Rev. C **97**, no.4, 044905 (2018) doi:10.1103/PhysRevC.97.044905 [arXiv:1706.03666 [hep-ph]].

[39] A. Mankolli *et al.* [JETSCAPE], [arXiv:2401.00402 [nucl-th]].

[40] D. Soeder, W. Ke, J. F. Paquet and S. A. Bass, [arXiv:2306.08665 [nucl-th]].

[41] H. Hirvonen, K. J. Eskola and H. Niemi, Phys. Rev. C **108**, no.3, 034905 (2023) doi:10.1103/PhysRevC.108.034905 [arXiv:2303.04517 [hep-ph]].

[42] H. Hirvonen, K. J. Eskola and H. Niemi, [arXiv:2404.02602 [hep-ph]].

[43] H. Huang, B. Xiao, Z. Liu, Z. Wu, Y. Mu and H. Song, Phys. Rev. Res. **3**, no.2, 023256 (2021) doi:10.1103/PhysRevResearch.3.023256 [arXiv:1801.03334 [nucl-th]].

[44] J. S. Moreland, J. E. Bernhard and S. A. Bass, Phys. Rev. C **101**, no.2, 024911 (2020) doi:10.1103/PhysRevC.101.024911 [arXiv:1808.02106 [nucl-th]].

[45] K. J. Eskola, K. Kajantie, P. V. Ruuskanen and K. Tuominen, Nucl. Phys. B **570**, 379-389 (2000) doi:10.1016/S0550-3213(99)00720-8 [arXiv:hep-ph/9909456 [hep-ph]].

[46] K. J. Eskola, K. Kajantie and K. Tuominen, Phys. Lett. B **497**, 39-43 (2001) doi:10.1016/S0370-2693(00)01341-1 [arXiv:hep-ph/0009246 [hep-ph]].

[47] R. Paatelainen, K. J. Eskola, H. Niemi and K. Tuominen, Phys. Lett. B **731**, 126-130 (2014) doi:10.1016/j.physletb.2014.02.018 [arXiv:1310.3105 [hep-ph]].

[48] K. Kajantie, P. V. Landshoff and J. Lindfors, Phys. Rev. Lett. **59**, 2527 (1987) doi:10.1103/PhysRevLett.59.2527

[49] K. J. Eskola, K. Kajantie and J. Lindfors, Nucl. Phys. B **323**, 37-52 (1989) doi:10.1016/0550-3213(89)90586-5

[50] H. Niemi, K. J. Eskola, R. Paatelainen and K. Tuominen, Phys. Rev. C **93**, no.1, 014912 (2016) doi:10.1103/PhysRevC.93.014912 [arXiv:1511.04296 [hep-ph]].

[51] K. J. Eskola, H. Niemi, R. Paatelainen and K. Tuominen, Phys. Rev. C **97**, no.3, 034911 (2018) doi:10.1103/PhysRevC.97.034911 [arXiv:1711.09803 [hep-ph]].

[52] H. Niemi, K. J. Eskola, R. Paatelainen and K. Tuominen, Nucl. Phys. A **982**, 443-446 (2019) doi:10.1016/j.nuclphysa.2018.10.013 [arXiv:1807.02378 [nucl-th]].

[53] M. Kuha, J. Auvinen, K. J. Eskola, H. Hirvonen, Y. Kanakubo and H. Niemi, [arXiv:2406.17592 [hep-ph]].

[54] J. R. Cudell *et al.* [COMPETE], Phys. Rev. Lett. **89**, 201801 (2002) doi:10.1103/PhysRevLett.89.201801 [arXiv:hep-ph/0206172 [hep-ph]].

[55] G. Antchev *et al.* [TOTEM], Eur. Phys. J. C **79**, no.2, 103 (2019) doi:10.1140/epjc/s10052-019-6567-0 [arXiv:1712.06153 [hep-ex]].

[56] S. Chekanov *et al.* [ZEUS], Eur. Phys. J. C **24**, 345-360 (2002) doi:10.1007/s10052-002-0953-7 [arXiv:hep-ex/0201043 [hep-ex]].

[57] K. J. Eskola, C. A. Flett, V. Guzey, T. Löytäinen and H. Paukkunen, Phys. Rev. C **106**, no.3, 035202 (2022) doi:10.1103/PhysRevC.106.035202 [arXiv:2203.11613 [hep-ph]].

[58] I. Helenius, K. J. Eskola, H. Honkanen and C. A. Salgado,

JHEP **07**, 073 (2012) doi:10.1007/JHEP07(2012)073 [arXiv:1205.5359 [hep-ph]].

[59] K. J. Eskola, H. Paukkunen and C. A. Salgado, JHEP **04**, 065 (2009) doi:10.1088/1126-6708/2009/04/065 [arXiv:0902.4154 [hep-ph]].

[60] S. Dulat, T. J. Hou, J. Gao, M. Guzzi, J. Huston, P. Nadolsky, J. Pumplin, C. Schmidt, D. Stump and C. P. Yuan, Phys. Rev. D **93**, no.3, 033006 (2016) doi:10.1103/PhysRevD.93.033006 [arXiv:1506.07443 [hep-ph]].

[61] X. N. Wang and M. Gyulassy, Phys. Rev. D **44**, 3501-3516 (1991) doi:10.1103/PhysRevD.44.3501

[62] H. Mäntysaari and B. Schenke, Phys. Rev. Lett. **117**, no.5, 052301 (2016) doi:10.1103/PhysRevLett.117.052301 [arXiv:1603.04349 [hep-ph]].

[63] J. S. Moreland, J. E. Bernhard and S. A. Bass, Phys. Rev. C **92** (2015) no.1, 011901 doi:10.1103/PhysRevC.92.011901 [arXiv:1412.4708 [nucl-th]].

[64] A. Aktas *et al.* [H1], Eur. Phys. J. C **46**, 585-603 (2006) doi:10.1140/epjc/s2006-02519-5 [arXiv:hep-ex/0510016 [hep-ex]].

[65] C. Loizides, Phys. Rev. C **94**, no.2, 024914 (2016) doi:10.1103/PhysRevC.94.024914 [arXiv:1603.07375 [nucl-ex]].

[66] P. Bożek, W. Broniowski, M. Rybczynski and G. Stefanek, Comput. Phys. Commun. **245**, 106850 (2019) doi:10.1016/j.cpc.2019.07.014 [arXiv:1901.04484 [nucl-th]].

[67] P. Huovinen and P. Petreczky, Nucl. Phys. A **837**, 26-53 (2010) doi:10.1016/j.nuclphysa.2010.02.015 [arXiv:0912.2541 [hep-ph]].

[68] H. Bebie, P. Gerber, J. L. Goity and H. Leutwyler, Nucl. Phys. B **378**, 95-128 (1992) doi:10.1016/0550-3213(92)90005-V

[69] T. Hirano and K. Tsuda, Phys. Rev. C **66**, 054905 (2002) doi:10.1103/PhysRevC.66.054905 [arXiv:nucl-th/0205043 [nucl-th]].

[70] P. Huovinen, Eur. Phys. J. A **37**, 121-128 (2008) doi:10.1140/epja/i2007-10611-3 [arXiv:0710.4379 [nucl-th]].

[71] W. Israel and J. M. Stewart, Annals Phys. **118**, 341-372 (1979) doi:10.1016/0003-4916(79)90130-1

[72] G. S. Denicol, T. Koide and D. H. Rischke, Phys. Rev. Lett. **105**, 162501 (2010) doi:10.1103/PhysRevLett.105.162501 [arXiv:1004.5013 [nucl-th]].

[73] G. S. Denicol, H. Niemi, E. Molnar and D. H. Rischke, Phys. Rev. D **85**, 114047 (2012) [erratum: Phys. Rev. D **91**, no.3, 039902 (2015)] doi:10.1103/PhysRevD.85.114047 [arXiv:1202.4551 [nucl-th]].

[74] E. Molnár, H. Niemi, G. S. Denicol and D. H. Rischke, Phys. Rev. D **89**, no.7, 074010 (2014) doi:10.1103/PhysRevD.89.074010 [arXiv:1308.0785 [nucl-th]].

[75] G. S. Denicol, S. Jeon and C. Gale, Phys. Rev. C **90**, no.2, 024912 (2014) doi:10.1103/PhysRevC.90.024912 [arXiv:1403.0962 [nucl-th]].

[76] P. Huovinen and H. Petersen, Eur. Phys. J. A **48**, 171 (2012) doi:10.1140/epja/i2012-12171-9 [arXiv:1206.3371 [nucl-th]].

[77] A. Hosoya and K. Kajantie, Nucl. Phys. B **250**, 666-688 (1985) doi:10.1016/0550-3213(85)90499-7

[78] S. Gavin, Nucl. Phys. A **435**, 826-843 (1985) doi:10.1016/0375-9474(85)90190-3

[79] C. Sasaki and K. Redlich, Phys. Rev. C **79**, 055207 (2009) doi:10.1103/PhysRevC.79.055207 [arXiv:0806.4745 [hep-ph]].

[80] J. Sollfrank, P. Koch and U. W. Heinz, Z. Phys. C **52**, 593-610 (1991) doi:10.1007/BF01562334

[81] S. Acharya *et al.* [ALICE], JHEP **07**, 103 (2018) doi:10.1007/JHEP07(2018)103 [arXiv:1804.02944 [nucl-ex]].

[82] E. Retinskaya, M. Luzum and J. Y. Ollitrault, Phys. Rev. C **89**, no.1, 014902 (2014) doi:10.1103/PhysRevC.89.014902 [arXiv:1311.5339 [nucl-th]].

[83] G. Nijs, W. van der Schee, U. Gürsoy and R. Snellings, Phys. Rev. Lett. **126**, no.20, 202301 (2021) doi:10.1103/PhysRevLett.126.202301 [arXiv:2010.15130 [nucl-th]].

[84] K. Aamodt *et al.* [ALICE], Phys. Rev. Lett. **106**, 032301 (2011) doi:10.1103/PhysRevLett.106.032301 [arXiv:1012.1657 [nucl-ex]].

[85] J. Adam *et al.* [ALICE], Phys. Rev. Lett. **116**, no.22, 222302 (2016) doi:10.1103/PhysRevLett.116.222302 [arXiv:1512.06104 [nucl-ex]].

[86] B. Abelev *et al.* [ALICE], Phys. Rev. C **88**, no.4, 044909 (2013) doi:10.1103/PhysRevC.88.044909 [arXiv:1301.4361 [nucl-ex]].